Engineering near-Earth asteroid resources using the orbital siphon effect

Andrea Viale

Submitted in fulfilment of the requirements for the
Degree of Doctor of Philosophy

James Watt School of Engineering
College of Science and Engineering
University of Glasgow

March 2021

Abstract

Exploitation of the resources available in space is one of the key challenges for future space exploration. Many of these resources have been recognized as potentially low-cost alternatives to those launched from Earth. In particular, near-Earth asteroids are among the easiest objects to reach and could provide resources such as water, liquid propellants electrolysed form water, semiconductors, and metals. Several studies have shown that a useful quantity of accessible resources may be available to be transferred into Earth orbit with transfer energies lower than that required to exploit material from the Moon. To address this problem, different scenarios can be envisaged to transfer material to Earth orbit or Halo orbits, such as transport of the entire asteroid or transport of mined material, the optimal choice depending on the particular asteroid of interest. A further possibility is *in situ* manufacturing using asteroid resources, for example to assemble space-structures directly nearby the asteroid or to process water for propellants or life support.

Motivated by this growing interest in asteroid resource exploitation, this thesis investigates a novel strategy to deliver a fraction of the asteroid mass into orbit about the asteroid or to escape. The analysis has its roots in the idea of leveraging the rotational kinetic energy of a rotating body to lift material, for example with the concept of the space elevator. The elevator is envisaged as a tethered structure to connect a mass in synchronous (or higher) orbit and the surface of the body. The tether is in equilibrium by the balance of centripetal and gravitational forces acting on it; the payload, i.e. mass extracted from the asteroid, is then lifted to the desired altitude along the tether and, if synchronous orbit is reached, the payload could increase its altitude without further work required.

A direct evolution of the space elevator is the orbital siphon concept which is the foundation of this thesis. In this case, rather than a single payload ascending along the tether, a chain of tether-connected masses is envisaged, where the centrifugal-induced pull due to the body's spin can overcome the gravitational force on the payloads, eventually allowing payloads to escape. A chain of payloads can therefore be envisaged to provide a continuous mass flow from the surface of a rotating asteroid into orbit (siphon effect): new payloads are connected to the chain while the top payloads are removed and released into orbit, without the need for external work to be done.

The siphon, as with the space elevator, can in principle be used as a payload-raising mecha-

nism on any rotating body. However, contrary to the space elevator, the siphon does not require external work to lift asteroid material below synchronous altitude. In support of mining operations, the siphon can be used to raise mined material to a collecting/processing station in orbit around the asteroid or directly connected to the siphon. Alternatively, the siphon can be used to release material to escape, without the need to use propellant-based methods.

This thesis therefore will investigate the dynamics of an orbital siphon anchored at an asteroid and examine a range of applications in the context of asteroid manipulation and resource exploitation. Long-term effects of the siphon operation are discussed, showing that this device allows a significant quantity of mass to be raised to orbit or to escape. It is shown that an optimal siphon length can be chosen, such that the extracted mass is maximised. Key variables, such as achievable mass flow rates, tension on the tethers, timescales and anchor forces are discussed.

It is demonstrated that the oscillations of this device resulting from Coriolis forces are damped and the siphon will eventually align with the local vertical if mass is released to a collecting spacecraft connected at the top of the siphon. Moreover, it is proposed that the siphon dynamics could be leveraged to deliver resource payloads to stable equilibria about the asteroid, with a smaller Δv than direct transfer from the surface, which may be beneficial in a long-term mining scenario. Effects of an irregular gravity field on the siphon dynamics are also examined, using polyhedral shape models of two candidate asteroids. The siphon effect is still generated for the candidate asteroids analysed, even with motion of the anchoring system on the asteroid surface, thus allowing the mining location to be moved without interrupting the flow of material to the collecting spacecraft.

If a large quantity of material is released to escape, the siphon effect may also be exploited to induce a small variation to the heliocentric velocity of a potentially hazardous asteroid for impact risk mitigation. It is shown that typical Δv on the order of $1\,\mathrm{cm\,s^{-1}}$ can be achieved within a time window of a decade. Finally, use of the orbital siphon to generate artificial cavities for habitats or storage of mined material is discussed.

Contents

List of Tables

List of Figures

Acknowledgements

First and foremost, I would like to thank my supervisors Prof Colin McInnes and Dr Matteo Ceriotti. Your guidance and support have been invaluable for the preparation of this thesis and your knowledge and advices inspired me to become a better researcher.

I would also like to acknowledge the School of Engineering of the University of Glasgow without whom I would not have been able to pursue my PhD.

Thanks to all my colleagues and friends in our research group, for useful discussions and fun moments together. In particular, I would like to express my gratitude to my office mates Callum, Federica, Zonghxu, Malcolm and Masaki for your useful inputs and for creating the perfect research environment. Special thanks to my colleague and friend Gilles, for his countless ideas on everything which is space-related and for always supporting and encouraging me. You all helped me to make this an invaluable experience both professionally and personally. A thanks also goes to each student, researcher and professor I met during this three years, at the University and at conferences, for helping me to grow as a scholar.

On a more personal side, I am incredibly thankful to all my friends in Glasgow that helped me to settle, have a great time in Scotland and relax from work. Many thanks to all the Paesano folks and my deepest gratitude to my friend João, the ultimate Linux guru, for successfully converting me to the world of terminals and bash scripts.

Life in Glasgow would not have been the same without the folks at the Piping Center. Thanks to my bagpipe teacher Danny, the best bagpiper ever, for helping me to learn this epic instrument in Scotland. Thanks to Peter and Martin, for your kindness and help. I would also like to thank all my friends at the Choral Society. Singing at four concerts at the University Chapel was a truly amazing experience. All the rehearsals were for me a moment of great fun and relax from work.

I would also like to thank all my friends in Chirignago and the CIT folks, who supported and encouraged me during my stay abroad. Thanks to my doctoral fellow Marco for amazing high-entropy discussions and useful inputs on some differential issues in this thesis. Isabella, thanks for your support and patience during these last months while writing this thesis.

Last, but not least, I am extremely grateful to my parents and my brother who always believed in me and supported me in all my choices. This thesis is dedicated to you.

Nomenclature

This section contains only the main symbols used on this thesis. The author attempted to use the symbols consistently throughout the thesis. Some symbols have duplicate meanings but the appropriate one should be clear from the context.

Acronyms

CEP	Center equilibrium point
CS	Collecting Spacecraft
CW	Clohessy-Wiltshire
DEM	Discrete element method
EP	Equilibrium point
ESA	European Space Agency
DS	Descending side
JAXA	Japan Aerospace Exploration Agency
LS	Lifting side
MR	Multiple release
NASA	National Aeronautics and Space Administration
NEA	Near-Earth asteroid
PM	Payload mass
PO	Periodic orbit
SEP	Saddle equilibrium point
SR	Single release

Symbols

A	Siphon cross section, m^2
b	Inner cavity radius, m
c	Cohesion, Pa
c^*	Critical cohesion,Pa

C	Jacobi constant
C	Damping factor, Ns
D	Ratio between m_{ds} and m_{ls}
E	Young's modulus, N
E	Energy, J
$\mathscr{E}$	Energy per unit mass, J/kg
f	force, N
f^*	Radial force on the siphon for $n \to \infty$, N
f_{cont}	Radial force on a siphon modelled as continuous mass distribution, N
G	Gravitational constant, $6.67 \times 10^{-11}\,\text{m}^3\,\text{kg}^{-1}\,\text{s}^{-2}$
h	Distance between first payload mass and asteroid surface, m
H	Distance between primary and secondary centre-of-mass, m
I	Moment of inertia, kg m^2
l	Distance between consecutive payload masses, m
K	Kinetic energy, J
L	Siphon length, m
L_{eq}	Siphon equilibrium length, m
m	mass, kg
m	Secondary mass (Chapter 6), kg
$\dot{m}_{avg}$	Average mass flow rate, kg/s
M	Asteroid mass, kg
M_{cs}	Collecting spacecraft mass, kg
n	Number of payload masses
p	Pressure, Pa
P	Gravitational potential energy, J
$\mathbf{r}$	Position vector
R	Asteroid radius, m
S	Tether cross section, m^2
t	time, s
T	Torque, N m
U	Effective potential J/kg
v	velocity, m/s
V	Gravitational potential J/kg
W	Work per unit mass, J/kg
α	Larger semimajor axis, ellipsoidal asteroid, m
β	Intermediate semimajor axis, ellipsoidal asteroid, m
γ	Smaller semimajor axis, ellipsoidal asteroid, m
δM	Payload mass, kg

Δv	Velocity change, m/s
ε	Strain
$\dot{\varepsilon}$	Strain rate, s^{-1}
ϕ	Longitude
ϕ_A	Anchor longitude
Γ	Longitude
μ	Siphon linear density, kg/m
ν	Poisson's ratio
Ψ	Polygamma function
ρ	Asteroid density, kg/m^3
ϱ	Radial distance from centre, m
σ	Stress tensor, Pa
θ	Siphon equatorial angle
θ_{eq}	Siphon equilibrium angle
Θ	Co-latitude
τ	Tension, Pa
ξ_m	Extracted mass ratio
ω	Asteroid angular velocity, rad/s
ω_{crit}	Critical angular velocity, rad/s

Superscripts and subscripts

$\bar{\square}$	Non-dimensional variable
$\hat{\square}$	unit vector
$\square_0$	Initial condition
$\square_{ls}$	Lifting side
$\square_{ds}$	Descending side
$\square_p$	Primary
$\square_s$	Secondary
$\square_c$	Centrifugal
$\square_g$	Gravitational

Operators and other notations

$\dot{\square}$	First derivative with respect to time
$\ddot{\square}$	Second derivative with respect to time
$\cdot$	Scalar product
$\times$	Vectorial product

$\nabla\square$	Gradient
$\mathscr{O}(\square)$	Order of magnitude
$\|\square\|$	Euclidean norm
$\mathbf{H}_{\square}$	Hessian matrix
h.o.t.	Higher order terms

Declaration

I, the undersigned Andrea Viale hereby declare that I am the sole author of this thesis. To the best of my knowledge this thesis contains no material previously published by any other person except where due acknowledgment has been made. This thesis contains no material which has been accepted as part of the requirements of any other academic degree or non-degree program, in English or in any other language.

Date: March 26, 2021

Chapter 1

Introduction

Interest towards near-Earth asteroids (NEAs) has been growing significantly over the past few decades. NEAs are a subset of the near-Earth object class, including any asteroid or comet that has a perihelion distance of less than 1.3 Astronomical Units.

There are three main factors behind the interest towards NEAs. Firstly they represent the most direct remnants of the early Solar System [15] and study of them could shed light on planet formation. Moreover, some asteroids may contain chemical compounds that could have been precursors to life on Earth [24]. Secondly, a fraction of NEAs have been classified as potentially hazardous, due to their close approaches to Earth. As of October 2020, 2132 NEAs have been classified as potentially hazardous and 156 of these have a diameter larger than one kilometre[1]. An object of this size would have enough energy to deliver catastrophic damage to our civilisation. Impact craters on Earth provide evidence that such events have already happened in the past, with dramatic consequences [137]. For example, it is believed that the crater Chicxulub in Yucatan was caused by a ten-kilmetre-wide asteroid, responsible for an extinction 65 million years ago [46]. The third reason behind the interests in NEAs is related to the resources available from these objects. A variety of materials can be found on asteroids, ranging from water, volatiles, metals and semiconductors, that could be useful to support future space activities [110]. For example, materials such as iron, nickel, cobalt, manganese and titanium could be used for construction of space infrastructures, such as space habitats, solar power stations or deep-space transportation bases. Other resources such as hydrogen and oxygen from water can be used to produce propellants or for life-support. Precious metals such as gold or platinum can also be found. These resources in principle make NEAs extremely valuable.

For all these reasons, identification, classification and orbit determination of NEAs is crucial. As of 9th November 2020, 24172 NEAs have been discovered (see Fig. 1.1). Among those, 890 NEAs have a diameter larger than 1 km. However, smaller objects with a diameter on the order of 100 m or less are difficult to detect and therefore it is believed that the actual population of NEAs is much larger. Estimation models have been developed to assess the actual distribution

[1] From `https://cneos.jpl.nasa.gov/`. Last access: 29th October 2020.

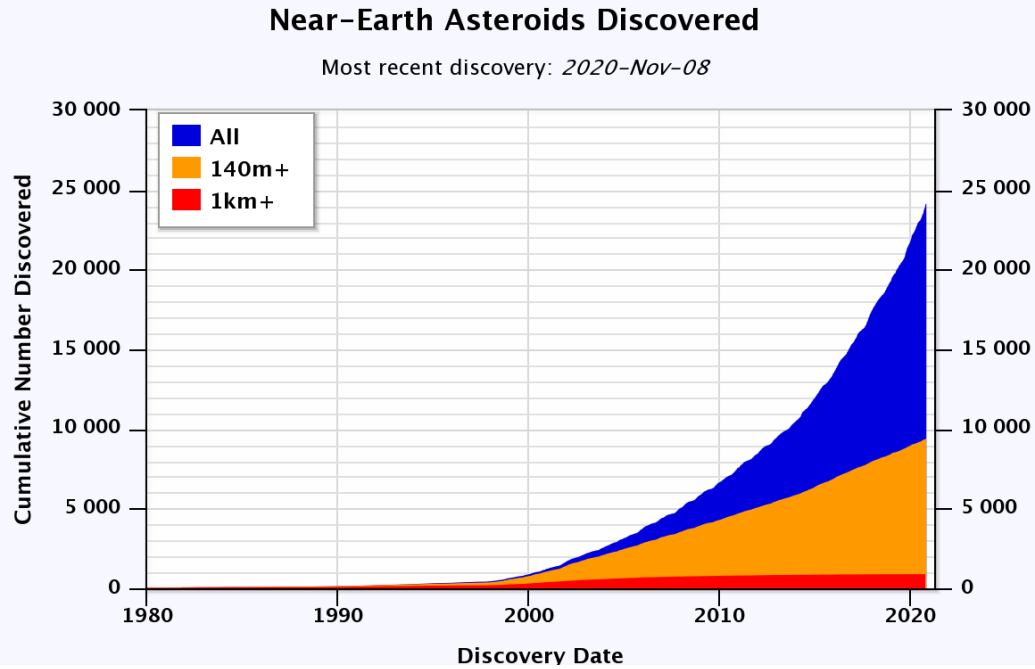

FIGURE 1.1: Cumulative number of discovered NEAs over time. Credits: Alan B. Chamberlin - Jet Propulsion Laboratory, NASA.

of NEAs. For example, according to Ref. [134], the NEAs population is estimated to comprise 413 ± 100 million asteroids and only 29% of the objects with a diameter of less than 140 m have been discovered so far. It is clear that an abundance of invaluable natural resources might be available in the Solar System.

However, large-scale mining operations on asteroids or their deflection is undoubtedly challenging, requiring macro-scale manipulation of these objects. The majority of missions to asteroids performed so far involved close approaches for scientific analysis, while only a few involved micro-scale manipulations (such as sample-return missions). Macro-scale manipulation of asteroids has not been performed so far and most of the techniques considered have only been conceptualised in simulation, including those proposed in this thesis. A novel asteroid manipulation technique is therefore presented in this thesis, and a range of applications in the context of asteroid mining and deflection are discussed. Before introducing the idea at the core of the thesis, a brief overview of past and current missions to asteroids is provided, followed by a review of the state-of-the-art on asteroid manipulation concepts.

1.1 Exploration of asteroids: an overview of past and current missions

The first spacecraft to visit an asteroid was the NASA mission Galileo, launched in 1989. Galileo completed a successful flyby of the asteroids 951 Gaspra and 243 Ida, providing for the first time

a close range image of an asteroid [52, 73]. The NASA spacecraft Clementine was launched in 1994 to make close observations of the Moon and the NEA 1620 Geographos, however the flyby of the asteroid was not possible due to a computer failure [95]. In 1997 the spacecraft NEAR made a close approach to the asteroid Mathilde and one year later reached the asteroid Eros, completing 230 orbits about it and then touched down on its surface. The spacecraft was still operational after landing, thus becoming the first spacecraft to soft-land on an asteroid [145]. Three years later, the spacecraft Cassini, directed to Jupiter and Saturn, approached the asteroid 2685 Masaursky, however it only returned a poor quality image [133]. On July 1999 the NASA Deep Space 1 probe successfully completed a flyby of the asteroid 9969 Braille with a closest approach distance of just 28.3 km [108]. Unfortunately, it released some low-quality images of the asteroid, due to a computer failure.

In February 1999, the NASA Stardust mission was launched with the primary aim of collecting samples from the coma of comet Wild 2 and also collecting cosmic dust and returning the samples back to Earth [18]. It was the first small body sample-return mission. Before reaching the comet, Stardust also successfully completed a flyby of the asteroid 5535 Annefrank and tested the manoeuvres required for the comet flyby. The JAXA spacecraft Hayabusa was the first to attempt a sample-return mission to an asteroid. Launched in 2003, it reached the asteroid Itokawa in September 2005, sampled some regolith from the asteroid and returned the material back to Earth. Approximately 1500 grains of material were collected, with sizes on the order of 10 micrometers and a total mass of less than 1 gram. Hayabusa also released the lander Minerva in an attempt to land on the surface, however after an accidental command it reached escape velocity [162]. In 2004, ESA launched the Rosetta mission with its primary lander module Philae to perform a study of the comet 67P/Churymov-Gerasimenko. Philae performed the first successful landing on a comet and, before arrival at the comet, Rosetta performed flybys of the asteroids 21 Lutetia and 2867 Steins [44]. In 2005, NASA launched Deep Impact, with the aim to analyse the composition of the comet 9P/Tempel by releasing an impactor onto the comet. The mission was successful, with the impactor hitting the comet surface at a relative speed of $10.3\,\mathrm{km\,s^{-1}}$ [109] (Fig. 1.2a shows the impact plume as photographed by the high-resolution camera onboard the carrier spacecraft). After the mission to 9P/Tempel was completed, it was proposed to retarget the spacecraft towards the asteroid 2002 GT, however, communication with the spacecraft was lost in 2013 and the mission aborted before reaching the asteroid [50]. In 2006 the New Horizon mission imaged the main-belt asteroid 132524 APL on its journey towards Pluto. In 2019, New Horizon reached the contact binary 486958 Arrokoth, which became the farthest object in the Solar System ever visited by a spacecraft [129]. The NASA Dawn spacecraft reached and orbited the two largest asteroids in the main belt, Vesta in 2011 and Ceres in 2015. Dawn was the first spacecraft to successfully orbit two asteroids and the first NASA mission to use ion propulsion for an exploratory mission, which enabled the spacecraft to enter and leave the orbit of Vesta [111]. The Chinese probe Chang'e 2 completed a flyby of the

asteroid 4179 Toutatis in 2012 after orbiting the Moon and reaching the Sun-Earth Lagrangian point L_2 to test the Chinese tracking and control network [72]. In 2013 an ambitious NASA mission was considered to retrieve a four-metre boulder from the surface of an asteroid and bring it to a stable lunar orbit, for further analysis via robotic probes or a future crewed mission. However, the Asteroid Redirect Mission, as the mission was initially termed, was cancelled due to insufficient funding [41].

In 2018 the probe Hayabusa 2, operated by JAXA, surveyed and took samples from the asteroid 162173 Ryugu, making it the second sample-return mission, after the first Hayabusa mission. The samples are expected to return to Earth at the end of 2020. The spacecraft also carried four small rovers, released to the asteroid to study its surface [57]. In 2016 the third sample-return mission, OSIRIS-REx, was launched by NASA en route to the asteroid 101955 Bennu. The probe successfully touched the surface and collected a sample via its extendable arm (Fig. 1.2b) and it is expected to return the sample back to Earth in September 2023 [70].

Several additional asteroid missions are planned. In particular, the Double Asteroid Redirection Test (DART) is a technology demonstrator to be launched in July 2021, to test a kinetic impactor and subsequent deflection [63]. The target of the mission, 65803 Didymos, is a binary asteroid system, and DART will impact onto the smaller asteroid (Didymos B) at a relative speed of $6\,\mathrm{km\,s^{-1}}$. With its mass of 500 kg, DART is expected to change the orbit speed of Didymos by about $0.4\,\mathrm{mm\,s^{-1}}$, which will lead to a small change in the trajectory of the asteroid system centre-of-mass, eventually causing a displacement in the long term. The actual measurement of the velocity change and assessment of orbit deflection will be made by the ESA spacecraft Hera, that will arrive at Didymos in 2027, five years after DART's impact [88].

A technical progression in the asteroid missions can be noted, from flybys to orbiter, then lander and sample return missions. This set the scene for future large-scale asteroid manipulation mission concepts, which will be discussed in the next section.

1.2 Asteroid manipulation

The term *asteroid manipulation* is used here to indicate all possible forms of interactions between an artificial device (e.g., a spacecraft) and the asteroid. Most past missions discussed in Sec. 1.1 involved asteroid flybys for scientific exploration, without any physical interaction between the spacecraft and the asteroid. The three sample-return missions Hayabusa, Hayabusa 2 and OSIRIS-REx represent initial micro-scale examples of asteroid manipulation, as they involve the interaction between the spacecraft and the asteroid for the collection of regolith, in this case for scientific purposes. The planned DART mission is an example of macro-scale asteroid manipulation, as it aims at changing the orbit of an asteroid.

On the basis of such interest towards asteroid, several additional manipulation techniques have been considered, not only for scientific purposes (e.g., collection of samples) but also for

(a) (b)

FIGURE 1.2: Examples of minor object manipulation missions. (a): Head-on collision of Deep Impact impactor with comet 9P/Tempel, imaged by the spacecraft high resolution camera. Credits : NASA/JPL-Caltech/UMD. (b): *Touch-and-go* manoeuvre by the OSIRIS-REx spacecraft with the asteroid 101955 Bennu. The acquisition mechanism collected at least 60 g of asteroid regolith. Credits: NASA/Goddard/University of Arizona

large-scale engineering operations such as mining or deflection. A review of the main manipulation concepts available in the literature is presented in the following sections, starting from mining methods and then moving to deflection techniques. A separate section is then dedicated to a discussion on the creation of artificial internal cavities for material storage or human habitats. Such review is necessary to contextualise the novel asteroid manipulation techniques that will be discussed later in this thesis.

1.2.1 Mining techniques

Similar to terrestrial mines, mining operations on an asteroid will likely involve the following phases [163]:

1. Prospecting. Mapping/scanning operations to establish the quantity of material that can be extracted and the location of such material.

2. Excavation. Removal of material from the asteroid.

3. Transportation. Transfer the excavated material from the ore site to a collection / processing site.

4. Processing. Transformation of the raw material into a form required for the refining process. For example, this phase may include breaking boulders into smaller fragments for transportation.

5. Refining. Extraction of important resources from the processed material.

6. Storage. Move the processed/refined material into a safe, stable location on the asteroid (or in orbit around the asteroid) for later use or transfer to Earth.

Contrary to terrestrial mining, however, the micro-gravity environment will challenge most (if not all) of these phases. For example, an asteroid such as Bennu (see Table 2.1 for physical properties) has an escape speed at the surface of approximately $0.2\,\mathrm{m\,s^{-1}}$. Any object travelling at a larger speed is released to escape. Hence, for example, any locomotion system that is not firmly attached to the surface will have to move at speeds on the order of tens of centimetre per second, thus posing constraints on mining throughputs. Also, many asteroids are believed to be rubble-piles, i.e., loose aggregates of grains and boulders held together by weak cohesion [104, 117]. Thus, any phase requiring anchoring to the surface will be challenging.

A proposed method to avoid anchoring to the surface involves the use of solar concentrators or lasers. McInnes proposed to use solar concentrators to reflect sunlight onto the asteroid surface and sublimate material [82]. The sublimated material can then be collected and processed. If the asteroid is metal-rich, part of the extracted material may be used to manufacture additional reflector surface, thus enhancing the extraction process. A similar concept has been proposed by Vasile et al. [141], which involves sublimation of asteroid material using lasers.

Alternatively, the entire asteroid can be encapsulated into a film bag with ports that permit the introduction of telescopic optics to deliver highly concentrated solar thermal power on the surface of the asteroid [36, 94, 123, 124]. The heat resulting from the solar radiation can excavate the asteroid via ablation and volatiles are forced to outgas into the encapsulating bag. In this scenario, the size of the infrastructure needed to encapsulate the asteroid scales with the asteroid size. Sercel [123] claims that a thousand-tonne asteroid can be entirely mined within a few months.

Methods involving encapsulation may require complete de-spin of the asteroid for easier extraction and storage of the resources. This can be achieved by placing a thruster at the asteroid equator and applying a torque opposite to the asteroid rotation [118]. For example, placing a 5 N thruster at the equator of an asteroid with a radius of 100 m, density $2000\,\mathrm{kg\,m^{-3}}$ and 5 h rotation period would require 4 months for complete de-spin [118]. Kang et al. [61, 62] suggest to use an actively controlled space tug to increase the asteroid rotation period. A spacecraft is connected to the asteroid via a tether and control is achieved via two strategies. Pure tension control is achieved by varying the tether length and converting the asteroid rotational kinetic energy into potential energy as the tether length is increased. However, it is shown that this method alone is not sufficient to completely de-spin the asteroid. A hybrid control strategy is then proposed by adding a thrust control to the tethered spacecraft which will lead to a complete de-spin of the asteroid.

On the contrary, asteroid spin-up has also been proposed to enhance asteroid disruption, to facilitate scientific analysis of the asteroid internal structure and composition or to increase the

surface-to-mass ratio for easier exploitation of their resources using solar concentrator technologies [11, 12]. The concept is to spin a satellite connected at the asteroid pole with a tether in a dumbbell-like configuration. Angular momentum is transferred to the the asteroid by spinning the tethered system in a direction opposite to the desired rotation direction. The asteroid rotation rate must be large enough such that the internal stresses overcome the critical stress required for disruption. It is shown that a 200-metre diameter asteroid can be spun-up and disrupted in less than 5 years using a tether centrifuge of a few tens of kilometres and using less than 20 tonne of overall system [12].

Separation or concentration of asteroid regolith according to size or composition may be required for large-scale *in situ* resource utilisation. To this end, it is proposed in Ref. [161] to launch material from the asteroid surface and exploit solar radiation pressure to passively sort it as a function of the grain size or density. Collection of the material can then be performed either on the asteroid surface (if the ejection speed is below escape speed) or on-orbit, using an orbiting collector. Garcia Yarnoz et al. [161] suggest that the method has a potential high throughput and can be useful for an initial preconcentration of regolith grains prior to more complex processing methods, although the effectiveness of this method would greatly depend on the properties of the material, inter-particle forces and the ability of surface rovers to move in micro-gravity environment.

Mass drivers have also been proposed to control the asteroid rotational state or deflect its trajectory. In this case, a mass is launched from the asteroid surface, thus exerting a force on the asteroid to conserve the overall linear momentum of the system. Larger reaction forces can be achieved using larger masses or launch speeds [17]. With release speeds smaller than escape velocity, material can be transferred to an orbiting station for storage [87].

Asteroids containing magnetic material can be manipulated using an electromagnetic excavator. Covey [31] proposes an apparatus made of a tube holding a series of magnetic coils, creating an electromagnetic field which will attract ferromagnetic materials contained in the asteroid regolith. Due to the microgravity environment, a relatively weak magnetic field (with respect, for example, to Earth applications) can be applied to effectively convey particles. The author notes that no anchoring is required for such operation as the forces pulling the regolith should be enough to keep the device in contact with the surface. Possible additional applications of the electromagnetic excavator are for drilling and thrusting (in the latter case the device would work as a mass driver). Similar concepts are presented in Refs. [2, 3]. In this case the idea is to apply a rectangular two-phase voltage between parallel screen electrodes with some openings mounted at the lower end of a tube. Particles agitated by the resulting electrostatic forces are captured when passing through the screen electrode openings. Other sampling/excavation mechanisms have been proposed, using tethers [57, 81], adhesive materials [64, 89] or brush-wheel devices [14, 91].

Among the main issues for most asteroid-manipulation methods is the transportation of

mined material to a collector or its temporary storage for processing. In fact, the problem of gathering material from the surface for later processing is still largely unexplored. This may become a crucial issue especially in a long-term mining scenario. Direct launch of material to orbit (for example using mass drivers) is affected by uncertainties when launching material from the surface (due to perturbations such as an irregular gravity field). Uncertainties in the initial condition at launch might challenge in-orbit collection of material within the low-gravity environment at asteroids. A novel asteroid manipulation concept is presented in this thesis (Chapters 3, 4, 5), where a tethered device is used for propellantless transfer of material from the surface to a collecting station. Such a device physically connects a point on the asteroid surface to the collecting station, thus avoiding any targeting issues. Moreover, as will be shown, by releasing the collected mass to escape, this device can be used for deflecting the asteroid trajectory.

1.2.2 Deflection techniques

Most proposed approaches for the deflection of potentially hazardous asteroids are characterised by momentum exchange between the asteroid and a reaction mass, in order to alter the asteroid trajectory. The most discussed deflection solutions include kinetic impactor, nuclear detonation, laser ablation, gravity tractor, ion-beam shepherd, asteroid thrusting, mass drivers, methods based on changes on the thermo-optical properties of the surface and tether-based methods.

The kinetic impactor method consists of impacting a spacecraft onto the asteroid surface [114]. Due to the small mass of the spacecraft with respect to the asteroid, the momentum exchanged is mainly due to the high relative velocity between the spacecraft and the target asteroid. Part of the exchanged momentum also comes from the impact ejecta. Better performance can be achieved with impact from retrograde orbits, in terms of impact speed and required mass [83]. Belonging to the same category is the *smart cloud* deflection technique [42]. The "cloud" is a large number of nano-size spacecrafts released at high relative speed towards the asteroid. The impact of these small units with the asteroid creates an artificial drag, and therefore an associated thrust onto the asteroid. By selecting a proper number of nano spacecrafts, the resulting thrust can be large enough to change the asteroid orbit in the long term. This technique can reduce the risk for catastrophic fragmentation that might occur with the impact of a spacecraft or projectile onto the asteroid.

Deflection via nuclear detonation is achieved by a nuclear explosion at a given stand-off distance from the asteroid surface. The explosion causes local ablation of the asteroid surface and the momentum due to the expelled ejecta induces a modification of the asteroid trajectory. This method has been considered to be especially effective for large asteroids and short lead times [157]. However, possible fracturing of the asteroid may cause unwanted outcomes and, therefore, knowledge of the shape and composition of the asteroid is crucial for this method. Moreover, the use of nuclear detonation in space is clearly still controversial [112].

Laser ablation deflection is achieved by illuminating the surface of an asteroid with high

intensity laser light. The absorbed energy induces sublimation of the asteroid material thus generating a plume of ejecta. The flow of released material, if properly controlled, produces a thrust that can be used to modify the trajectory of the asteroid or its rotational state [138, 144].

With the gravity tractor technique, a spacecraft (or a spacecraft formation) hovers in proximity to the asteroid using low-thrust propulsion, causing an acceleration of the centre-of-mass of the asteroid-spacecraft system [75].

Similarly, for the ion-beam shepherd concept the idea is to perturb the asteroid using a collimated beam of plasma [13]. A second propulsion system is required to offset the momentum transferred to the asteroid. For small asteroids (with a diameter smaller than 100 m) the required spacecraft mass is one order of magnitude smaller than the gravity tractor [13], whereas comparable performances is observed for asteroids larger than 2 km.

With direct thrusting [118] the entire asteroid is turned into a spacecraft, with a set of thrusters positioned on the asteroid surface applying continuous thrust. This method requires that the asteroid is firstly de-spun, to avoid a periodic change of the applied force direction. Clearly, the required thrust level scales up with the asteroid size, thus making this method suitable only for smaller asteroids.

Spitale [127] proposes to modify the thermo-optical properties of the asteroid using the Yarkovsky effect. This effect is caused by the anisotropic emission of photons which produces a slight force with magnitude proportional to the temperature contrast across the asteroid. Changing the albedo of the asteroid surface (e.g., by means of paints) changes the intensity of such acceleration. This method requires timescales on the order of 100 years to achieve significant deflections [127].

Another proposed deflection method is based on mass drivers [4, 96]. In this case, material collected from the asteroid is used as a reaction mass to be accelerated and released to escape to induce a change in velocity of the asteroid. A significant advantage of this method is that the reaction mass is provided *in situ*, therefore significantly reducing the launched mass of the deflection system. Based on this concept, it is proposed in Ref. [16] to achieve deflection by multiple ejection of boulders from an asteroid.

Finally, another class of methods for deflection is based on the use of tethers. French et al. [40] propose to connect a long tether and ballast to an asteroid to alter the centre-of-mass of the system and therefore its orbit. Diversion can be enhanced by cutting the tether at an appropriate time after attachment to the asteroid [79].

The methods described can be divided into two main categories. Kinetic impactor and nuclear detonation are single-event deflection methods, as the entire momentum transfer is applied at single time. Although the scale of momentum transfer can be large (such as in the nuclear detonation method), there is a single opportunity for the deflection: in case of failure (e.g., insufficient velocity change, unwanted asteroid fragmentation) a new mission has to be rescheduled. In contrast, all the other methods permit continuous corrections, even though they might

require longer timeframes for implementation. Moreover, many of the proposed methods will likely require a large mass of propellant or reaction mass to be delivered from Earth. Table 1.1 presents a summary of all the state-of-the-art asteroid manipulation and deflection techniques here discussed.

In this thesis, a novel asteroid deflection method will be discussed in Chapter 6. This method can be classified as a tethered-mass driver and, as with other mass driver methods discussed, it involves the use of asteroid mass as reaction mass. Similarly to a mass driver, this manipulation device accelerates mass from the surface of the body to escape. However, it leverages the rotational kinetic energy of the asteroid itself to release asteroid material to escape. Moreover, it can be adapted to be both single-event and multiple-event.

1.2.3 Asteroids as space habitats

Asteroid manipulation may also be beneficial for the developement of human space settlements [77]. In fact, among the main requirements for long-term sustainability of life in space are radiation shielding and artificial gravity. Internal asteroid caverns would provide a natural protection against cosmic rays and the solar wind. Contrary to other habitat concepts (such as O'Neill cylinders at the Lagrangian points [97]), an advantage of asteroids is that material for shielding is already available *in situ* and does not have to be sourced elsewhere. According to a study in Ref. [51] the minimum level of gravity to provide adequate perception of the upright direction for humans is approximately 0.15 g. Two main methods have been proposed to obtain artificial gravity. The first consists in spinning up the entire asteroid such that the required level of artificial gravity is obtained on the lateral surface of an internal cylindrical cavity [77]. However, rotation periods on the order of 1 minute are required to generate 0.15 g on a cylindrical cavern with radius of 100 m [77] and the asteroid may not sustain the body loads due to the rotation rate. In fact, most asteroids with a size above a hundred meter radius are believed to be gravity-dominated rubble piles with zero or negligible tensile strength [104]. Also, asteroid rotation periods are usually above 2.2 hours [104] and the spin up process may require significant amount of energy due to the large inertia of the body. An alternative method to generate artificial gravity would be to spin up a cylindrical or toroidal structure inside the cavity. In this way, the rotation of the space habitat is decoupled from that of the asteroid and therefore the requirement to spin up the entire asteroid is eliminated. Moreover, the microgravity environment at the outer asteroid surface is preserved, which may be advantageous for manufacturing infrastructures. Furthermore, excavation of asteroid interiors would be beneficial in a mining scenario, if the resources to be processed are naturally at a certain depth from the surface. For example, in carbonaceous asteroids, water may be available in the form of fluid inclusions [116] and may also be trapped underneath the surface, where the thermal inertia is larger and the diurnal variation of the temperature becomes negligible, so that water does not evaporate. Also, in the low-gravity environment of the asteroid, an internal cavern would offer a confined environment for storage

TABLE 1.1: Summary of state-of-the art methods for asteroid manipulation.

	Main applications	References	Remarks
Solar concentrator	excavation deflection	[82] [139]	Reflect sunlight onto the asteroid surface and sublimate material.
Laser ablation	spin control deflection	[43, 144] [100, 138, 140]	Asteroid surface is illuminated with a high intensity laser light. The absorbed energy induces sublimation of the asteroid material thus generating a plume of ejecta.
Electromagnetic waves	excavation	[31]	An electromagnetic field is generated to convey asteroid regolith into a collector.
Tethers	spin control excavation surface locomotion deflection	[11, 12, 62] [81] [26] [40, 79]	Tethers permit exchange of forces or momentum between the asteroid and a counterweight.
Mass driver	spin control deflection transportation	[17] [4, 16, 17, 96] [87]	A mass is launched from the asteroid surface, thus exerting a force on the asteroid to conserve the overall linear momentum of the system.
Solar radiation pressure	sorting	[161]	Launch material from the asteroid surface and exploit solar radiation pressure to passively sort it as a function of the grain size or density.
Thrusters	spin control deflection	[118] [118]	Thrusters can be used to exert a net force on the asteroid for deflection. Also, a non-zero torque with respect to the centre-of-mass changes the rotational state of the asteroid.
Kinetic impactor	deflection	[42, 83, 114]	Impact a mass onto the asteroid surface to exchange linear momentum
Nuclear detonation	deflection	[157]	Nuclear explosion at a given stand-off distance from the asteroid surface. Deflection caused by momentum of the expelled ejecta.
Gravity tractor	deflection	[75, 156]	A spacecraft hovers in proximity to the asteroid using low-thrust propulsion, causing an acceleration of the centre-of-mass of the asteroid-spacecraft system.
Ion-beam shepherd	deflection	[13]	Perturbs the asteroid using a collimated beam of plasma.
Modify surface thermo-optical properties	deflection	[127]	The intensity of the perturbing acceleration is changed by modifying the albedo of the asteroid surface, e.g., by means of paints.

of mined or processed material, such as propellant manufactured from asteroid-mined water.

An application of the asteroid manipulation concept defined in Chapters 3, 4 and 5 is proposed in Chapter 7 for creation of an asteroid internal cavern.

1.2.4 Commercial interest in asteroid resources and legal regulations

On the basis of this interest in asteroid manipulation and space resource exploitation, legal treaties have recently been signed to establish clear regulation with respect to asteroid mining. In 2015, the US Commercial Space Launch Competitiveness Act [10] stated that "A US citizen engaged in commercial recovery of an asteroid resource or a space resource shall be entitled to any asteroid resource or space resource obtained", thus giving US space companies the right to own and use materials from any celestial body. Prior to this, the Outer Space Treaty (1967) considered outer space as "the province of mankind" and gave countries the freedom to access all celestial bodies [45].

Luxembourg became the first European country to allow a company to own any resource they extract from a space resource and showed interest in creating a legal framework and incentives for companies involved in this sector. Japan, Portugal and the United Arab Emirate entered into cooperation agreements with Luxembourg for mining operations on celestial bodies. China is planning to use an asteroid as the base for a permanent space station, and also India is showing interest in space resources [78].

The first asteroid mining company, Planetary Resources, was founded in 2012. Planetary Resources aimed at developing a robotic asteroid mining-industry, operating on the basis of a long-term strategic plan. They planned to first launch space telescopes to locate the best targets among NEAs, and then establish a fully automated asteroid mining operation. In addition, they envisioned production of water for an orbital propellant depot. In 2019, Planetary Resources was acquired by Consensys in 2018, a blockchain software company, and pivoted to other applications. However, other firms have has been established since then, such as Deep Space Industries (now acquired by Bradford Space), Ispace, Kleos Space and Deltion Innovation. [78].

1.3 The orbital siphon

In this thesis a novel asteroid manipulation concept, called *orbital siphon* is investigated in detail. The concept of the orbital siphon, firstly introduced by Davis and elaborated by McInnes [85], has its roots in the idea of leveraging the rotational kinetic energy of a rotating body to overcome its gravity. The idea itself was initially developed by Tsiolovski [101, 135] then improved by Artsutanov [7] and Pearson [28, 102] with the concept of *space elevator*, a tethered structure to raise payloads from a rotating body. Before introducing the orbital siphon concept in detail, and its application for asteroid manipulation, a brief overview on the space elevator concept and tethered structures in space is provided.

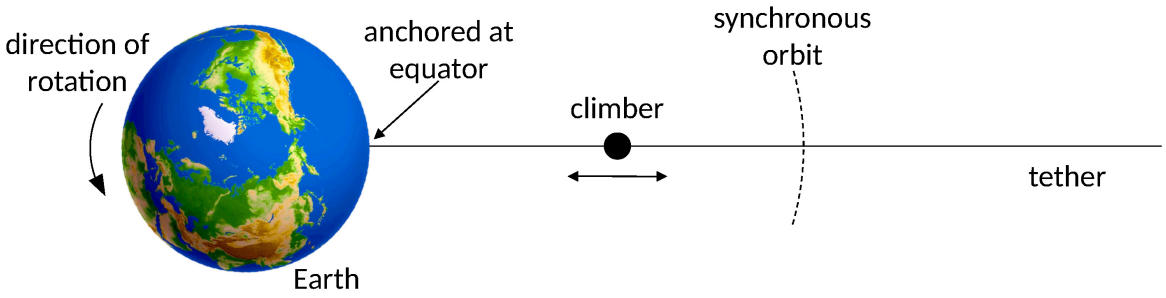

FIGURE 1.3: Space elevator.

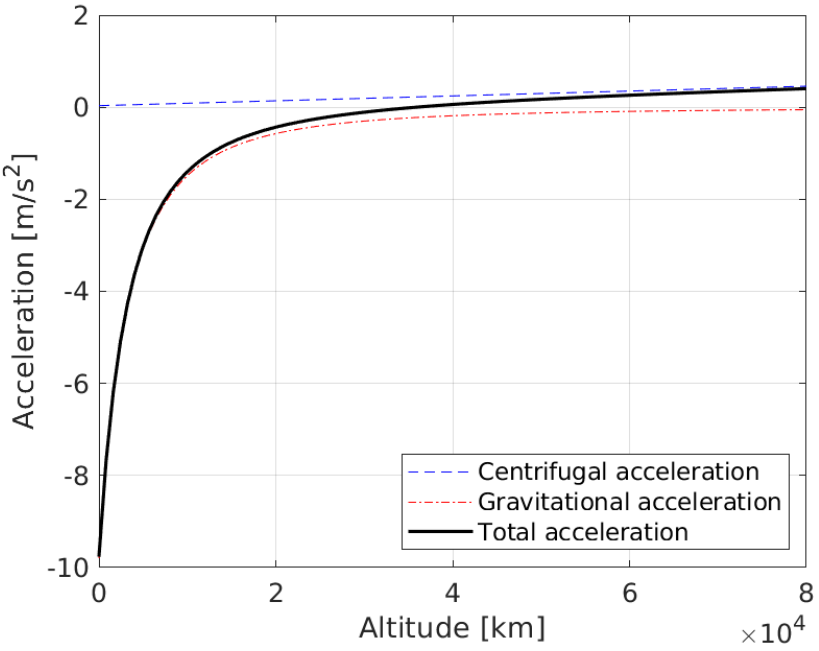

FIGURE 1.4: Centrifugal (blue dashed line), gravitational (red dot-dashed line) and total (black line) acceleration acting on the climber of a space elevator anchored to Earth's equator, as a function of altitude.

1.3.1 The space elevator

The space elevator was initially proposed as a new method to access space from Earth, as an alternative to rockets. The elevator comprises a tether anchored at the equator of the Earth and extending above geosynchronous orbit (Fig. 1.3). The tether is subjected to gravitational force and to the centrifugal-induced force due to the rotation of the Earth, the two forces having opposite directions. If the tether is long enough, the centrifugal-induced force acting on the tether exceeds the gravitational force and the tether remains balanced. For terrestrial applications, equilibrium of the forces is achieved with a tether length of approximately 144 000 km [102], although this distance can be reduced using a counterweight [38]. Once the cable is deployed, it can be ascended by a climber. Figure 1.4 shows the gravitational and centrifugal-induced acceleration acting on the climber as a function of altitude, for a space elevator anchored to the Earth's

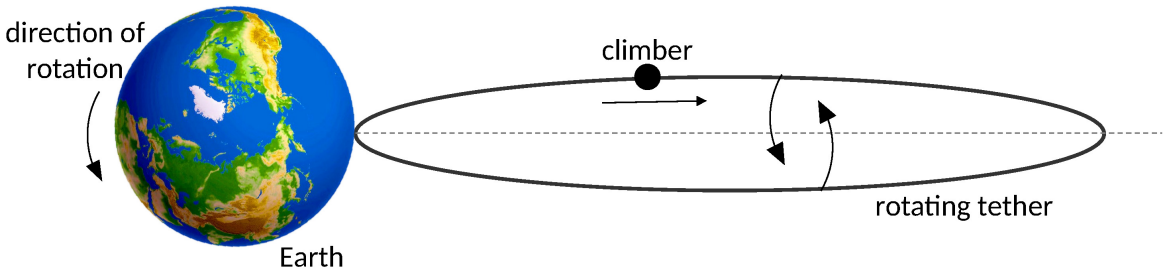

FIGURE 1.5: Rotating space elevator.

equator. Below synchronous orbit, the gravitational force is predominant and external energy must be supplied to the climber. Once the climber reaches synchronous orbit, the centrifugal-induced force overcomes the gravitational force and therefore the centrifugal-induced force is sufficient to lift the climber along the cable. If the climber proceeds far enough along the cable, it would have sufficient mechanical energy to escape from Earth by simply detaching from the tether. A wide range of studies are available in the literature, investigating design, materials, tether oscillation anchor location and stability [30, 38, 84, 105, 106, 153, 158–160] mainly for Earth applications. The most critical component of the space elevator is the tether, requiring a material with high strength and low density [106]. To date, the only two material candidates for this structure for terrestrial application are carbon nanotubes [58] and diamond nanothreads [39]. Better performances can be achieved by tapering the tether to have a uniform tensile stress profile [102]. Applications to other systems such as the Moon [71] or Mars moons [154] have also been proposed.

Knudsen and Golubovic [66, 67] tried to solve the issue of supplying energy to the climber below synchronous orbit. To this end, they elaborated an interesting solution called the *rotating space elevator*. In this case, the elevator is a *double* rotating tether, as represented in Fig. 1.5. It is observed that, for the proper tether shape and cable rotation speed, a climber does not require external propulsion to be transported above synchronous orbit, as the resulting Coriolis forces on the climber would propel the climber. However, despite the interesting underlying physics, the authors show that the motion of the climber may induce a morphological transition of the elevator cable to a chaotic state.

Interest towards the space elevator has motivated research for applications of tethered systems to asteroids. Mashayekhi et al. [80] studied the oscillations of a tether attached at an asteroid, taking into account higher order terms in the gravitational potential. Zhong et al. [166, 167] studied the stability of artificial equilibrium points of a tethered probe system anchored to an asteroid. Burov et al. [21] found the allowed location of the tether anchor that corresponds to a given spacecraft position around an asteroid. Other similar studies on the dynamics of pendulums anchored to asteroids can be found in Refs. [5, 19, 20].

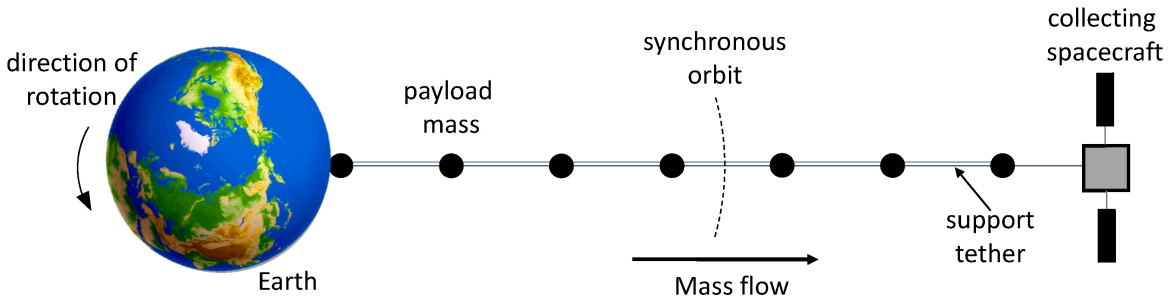

FIGURE 1.6: Orbital siphon.

1.3.2 The orbital siphon and the siphon effect

The orbital siphon is a discrete version of the space elevator. The concept was firstly introduced by Davis and elaborated by McInnes in Refs. [85, 86]. The initial idea for the siphon occurred to Davis as a thought experiment. He imagined a series of diggers extracting resources from an asteroid and transporting the collected material to a collection site at the asteroid equator. As more material is excavated, the conical heap of collected material would grow until the top of the heap reaches the synchronous orbit and material would escape due to the excess of centrifugal forces [85]. This idea then evolved imagining a chain of masses deployed vertically from the equator rather then the heap and sliding on a support structure (Fig. 1.6). Each mass of the chain will experience gravitational and centrifugal-induced forces, in addition to the tension forces from the nearest neighbours in the chain. In particular, masses below synchronous orbit will experience a larger gravitational force and above synchronous orbit will experience a larger centrifugal-induced force. As in the space elevator, for an appropriate number of masses, the chain can be configured to remain in equilibrium, such that the net force acting on the chain is balanced. If the length of the chain is larger than that required for the equilibrium there will be an excess of centrifugal-induced force acting on the masses above synchronous orbit. An *orbital siphon effect* can then be established, where a new payload is added at the bottom of the chain while the upper payload is released to a collecting spacecraft or to orbit, such that the total length of the chain does not change.

The siphon can then be though as a machine that converts the rotational kinetic energy of a body into translational kinetic energy. Contrary to the rotating space elevator approach, in this case there is no need to set the tether into rotation to generate Coriolis-induced lifting forces. Here, the net outwards force on the chain of masses is used to overcome the gravitational attraction to the central body and lift material. Authors in Ref. [85, 86] studied the the length of a siphon anchored to Earth that guarantees radial equilibrium and observed, as expected, that as the number of masses increases the equilibrium length approaches that of a space elevator, as defined in Ref. [102].

Longsdon [74] pictured an equivalent concept for fluids, where a pipeline is used instead of a chain of masses, to raise sea water above synchronous Earth orbit. Speculatively, he showed

that the water flux may drive turbines to generate power.

1.4 Application to asteroids and thesis objectives

The siphon, as with the space elevator, can be in principle used as a payload-raising mechanism on any rotating body. For a fixed body mass, the smaller the rotation period, the smaller the required siphon length to generate the siphon effect. For long-term siphon operations, it is expected that the rotation period of the body will increase over time, as more rotational kinetic energy is converted into translational kinetic energy to raise payload resources. The main objective of this thesis is therefore to study the behaviour of an orbital siphon anchored to an asteroid and consider three applications in the context of asteroid manipulation: asteroid mining, asteroid deflection, and creation of artificial internal cavities, as introduced in Sections 1.2.1, 1.2.2 and 1.2.3 respectively.

In support of mining operations, the siphon can be used to raise mined material to a collecting/processing station in orbit around the asteroid or directly connected to the siphon. Alternatively, the siphon can be used to release material to escape, without the need to use propellant-based methods or a mass driver. If a large quantity of material is released to escape, the siphon may also be used as a deflection tool. In this case, the main advantage over traditional deflection methods is that the reaction mass used for deflection is collected *in situ* and does not have to be provided from Earth. Eventually, the siphon could be used for excavation of an internal cavity underneath the asteroid surface. In this case, wasted material would be delivered to the siphon to be released to escape.

To achieve the main objective of the thesis, the following goals are also set:

- Undertake a detailed and systematic investigation of the dynamics of the orbital siphon concept and its interaction with a rotating asteroid.
- For large-scale mining operations, identify any upper bound on the maximum mass that can be extracted from the asteroid using the siphon effect, using different strategies (e.g., fixed or variable siphon length).
- Investigate the effect of the Coriolis forces due to the motion of the chain.
- Study the effect of a counterweight or mass collector at the top of the siphon.
- Discuss the transfer of payload material to stable equilibrium points about an asteroid or stable periodic orbit, for temporary storage or processing.
- Consider the effect of the irregular gravitational field of an asteroid on the dynamics of the orbital siphon.

- For deflection applications, investigate the achievable velocity change that can be imparted to an asteroid using the siphon and compare this with state-of-the-art deflection methods.
- For asteroid habitat applications, investigate the variation of the internal stresses on the asteroid during siphon operation and consider the material strength requirements to avoid collapse of the inner cavity.

1.4.1 Key contributions

This thesis presents the first rigorous and systematic investigation of the mechanics of the orbital siphon. It is shown that the siphon can be exploited in the context of asteroid manipulation to lift a significant quantity of mined mass to escape. Upper bounds on the maximum extractable mass are calculated in detail. The effects of the irregular gravitational field of the asteroid on the siphon dynamics is considered in detail and it is shown that the siphon can be self-supported, without the need for additional rigid supports (e.g., trusses), thus reducing the required infrastructural mass. In the context of asteroid mining, a novel sorting method is proposed, called the *centrifugal tower*, in which the centrifugal-induced force at the top of the siphon is exploited to sort the lifted regolith by size. Furthermore, the orbital siphon is proposed as a novel asteroid deflection method. Finally, in the context of asteroid habitats, this thesis analyses the use of the orbital siphon for excavation of internal cavities inside asteroids. The cavity can be used as a confined environment for material storage or, more speculatively, to host a space station, with the asteroid acting as natural radiation shield. Using simplifying assumptions, the internal stresses on the boundaries of the cavity are calculated and it is shown that a regolith cohesive strength as low as 4 Pa (for a candidate asteroid) is sufficient to avoid disruption of the internal cavity due to siphon operation.

1.5 Thesis outline

The thesis is divided into eight chapters. The initial chapters are focused on the siphon dynamics and its interaction with the asteroid (Chapters 3,4,5), whereas the final chapters study applications for asteroid deflection (Chapters 6) and the creation of artificial internal cavities (Chapter 7).

- Chapter 2 provides an overview of the asteroid gravitational environment for the different asteroid shape models used in this thesis. The concept of effective potential is introduced, which combines the effect of the gravitational force and centrifugal-induced force in an asteroid-fixed rotating frame.
- Chapter 3 investigates the dynamics of a siphon anchored to a spherical asteroid, with payload masses sliding without friction on a rigid support structure. The effects of the

collecting spacecraft are not taken into account and it is assumed that the siphon releases asteroid material into orbit or escape. Adopting simplifying assumptions, the underlying dynamics of the problem is entirely analytical and is investigated in detail. The variation of the asteroid angular velocity as a function of the mass removed is found. Conditions to release material to bound orbit around the asteroid or escape are found. The amount of mass extractable from the asteroid is discussed, according to a range of strategies. Candidate asteroids and extraction timescales are discussed. The contents of this chapter have been partly published in the *Proceedings of the Royal Society, Part A* [149].

- Chapter 4 takes into account the effect of the Coriolis forces during siphon operation and investigates the rotational dynamics of a siphon anchored at the equator, with a mass collector connected at the top of the siphon. The asteroid is modelled as a triaxial ellipsoid and the effect of different anchor longitudes along the equator is discussed. Eventually, a method to transfer the collected material to stable equilibrium points or retrograde orbits for temporary storage is proposed. The contents of this chapter have been published in *Acta Astronautica* [146].

- Chapter 5 investigates the dynamics of a non-rigid orbital siphon, modelled as a n-body tethered structure arranged as a conveyor belt. Tethers connecting consecutive payloads are modelled as spring-dashpot connections. Contrary to previous chapters, the dynamics is extended to the three-dimensional space and the modelling of the gravitational field is enhanced by using polyhedron shape models of two NEAs. Also, the dynamics of a siphon with moving anchors is considered. The contents of this chapter have been published in the *Journal of Guidance, Control and Dynamics* [150].

- Chapter 6 investigates an application of the orbital siphon for asteroid deflection. The key concept is to collect material lifted by the siphon and use it as a reaction mass to be released to change the asteroid velocity. Two different release strategies are defined and discussed. The optimal siphon length required to maximise the deflection Δv is found. The contents of this chapter have been published in the *Journal of Spacecrafts and Rockets* [147].

- Chapter 7 proposes to use the siphon effect to remove material from an asteroid interior and create a cavity inside the asteroid, to host habitats or for storage of mined materials. As in Chapter 3, the variation of the angular velocity of the asteroid as a function of the mass removed is considered, assuming that the internal cavity retains a spherical shape. Then, assuming elastic material behaviour, the variation of the internal stresses on the asteroid is considered and the regions that are most sensitive to structural failure are identified. Contents of this chapter have been published in *Advances in Space Research* [148].

- Chapter 8 concludes the thesis and provides a summary of the main findings. Moreover,

limitations of the current analysis are discussed, as well as proposed direction for future work.

1.6 Publications

The contents of this thesis have been published or submitted for publication in five journal articles, as follows:

- Viale A., Ceriotti M, McInnes C., Analytical mechanics of asteroid disassembly using the Orbital Siphon effect, *Proceedings of the Royal Society of London Series A*, 474.2220 (2018): 20180594, https://doi.org/10.1098/rspa.2018.0594.
- Viale A., Ceriotti M, McInnes C., Dynamics of a non-rigid Orbital Siphon anchored at a near-Earth asteroid, *Journal of Guidance Control and Dynamics* 43.11 (2020): 1998-2012, https://doi.org/10.2514/1.G004894.
- Viale A., Ceriotti M., McInnes C., Dynamics of an orbital siphon anchored to a rotating ellipsoidal asteroid for resource exploitation, *Acta Astronautica* 177 (2020): 561-576, https://doi.org/10.1016/j.actaastro.2020.08.001.
- Viale A., Ceriotti M., Bailet G., McInnes C., Asteroid deflection by leveraging rotational self-energy, *Journal of Spacecrafts and Rockets*, (2021), https://doi.org/10.2514/1.A34889.
- Viale A., Ceriotti M., Bailet G., McInnes C., Excavation of artificial caverns inside asteroids by leveraging rotational self-energy, *Advances in Space Research*, (2021), https://doi.org/10.1016/j.asr.2021.02.021.

In addition, the following conference papers were presented:

- Viale A., McInnes C., Ceriotti M., Disassembly of near- Earth asteroids by leveraging rotational self energy, *69th International Astronautical Congress*, Bremen, Germany, 1-5 Oct 2018, IAC-18-D4.3-18, ISBN 9781510881655, http://eprints.gla.ac.uk/168724/.
- Viale A., McInnes C., Ceriotti M., Orbital Siphon at a near-Earth Asteroid, *2019 AAS/AIAA Astrodynamics Specialist Conference*, Portland, ME, USA, 11-15 Aug 2019, http://eprints.gla.ac.uk/191709/.

Chapter 2

Asteroid effective potential models

This chapter discusses the equations and the mathematical models to represent the main properties of an asteroid effective gravitational potential (or simply *effective potential*) for some mass distribution as used throughout this thesis. The term *effective* is used to indicate that the gravitational potential is amended to include the effects of the centrifugal-induced potential, due to the asteroid rotation. In fact, most of the analysis in this thesis is performed in an asteroid-fixed reference frame and it is therefore useful to combine the gravitational potential and centrifugal-induced potential into a single effective potential. Knowledge of the gradient of the effective potential is then necessary to derive the net acceleration acting on a point mass in the vicinity of the asteroid. The effective potential equations are presented for three particular mass distributions: spherical, ellipsoidal and polyhedral mass distribution. These three mass distributions will be used in subsequent chapters to model the asteroid shape and study the orbital siphon dynamics. In particular the asteroid effective potential permits the calculation of the net forces acting on the siphon and the study of the dynamics of material released from the siphon. Basic dynamical properties stemming from the effective potential calculated for these mass distributions are discussed, in particular, the integral of motion, zero-velocity curves, the location of equilibrium points and their stability.

2.1 Assumptions and definitions

Consider a mass distribution $\mathscr{M}$ spinning with angular velocity $\boldsymbol{\omega} > 0$ with respect to some arbitrary fixed axis z. Then build a frame x, y, z such that its origin coincides with the centre-of-mass of the distribution and rotates with the body such that the inertia of the body does not change with respect to such a frame. Let the z-axis be aligned with the axis of maximum inertia (here coinciding with the spin axis). The orientation of the x and y axis is not important for the definition of the rotating frame and it will be specified, whenever necessary, for each mass distribution considered. This reference frame is termed the *rotating frame*. Uniform rotation is assumed, and precession or nutation are neglected. This hypothesis is justified by the fact that,

under energy dissipation, uniform spin about the axis of maximum inertia is the minimum energy rotation state. The majority of asteroids are found to be in such a rotational state [121]. Also, assume that the centre-of-mass is not accelerating. Hence, the effects due to the heliocentric motion of the asteroid are neglected.

The effective potential U at the point $\mathbf{r} = (x, y, z)$ is then defined as

$$U(x,y,z) = V(x,y,z) - \frac{1}{2}\omega^2(x^2+y^2) \tag{2.1}$$

where $V < 0$ is the gravitational potential due to the mass distribution considered and $-1/2\omega^2(x^2+y^2)$ is the contribution due to the centrifugal-induced potential. The sign of the potential is defined using the classical convention that the opposite of its gradient $-\nabla U$ returns the effective acceleration of a point mass due to gravity and centrifugal-induced force. Let $\tilde{\mathbf{r}}$ be the position of an infinitesimal mass element dm of the mass distribution $\mathscr{M}$. Then, the most general form of the gravitational potential at the position $\mathbf{r}$ due to a mass distribution $\mathscr{M}$ is:

$$V(\mathbf{r}) = -G \iiint_{\mathscr{M}} \frac{dm}{|\mathbf{r}-\tilde{\mathbf{r}}|} \tag{2.2}$$

where $G = 6.67 \times 10^{-11}\,\mathrm{m^3\,kg^{-1}\,s^{-2}}$ is the gravitational constant. In this thesis it is assumed that the mass distribution is characterized by a constant and homogeneous density ρ, such that $dm = \rho dV$, where dV is an infinitesimal element of volume of the mass distribution. Under this condition, Eq.(2.2) can be rewritten as:

$$V(\mathbf{r}) = -G\rho \iiint_{\mathscr{V}} \frac{dV}{|\mathbf{r}-\tilde{\mathbf{r}}|} \tag{2.3}$$

where $\mathscr{V}$ is the total volume of the distribution.

In absence of additional external forces, the dynamics of a point mass in the rotating frame are then described by:

$$\ddot{\mathbf{r}} = -2\boldsymbol{\omega} \times \frac{d\mathbf{r}}{dt} - \frac{d\boldsymbol{\omega}}{dt} \times \mathbf{r} - \nabla U \tag{2.4}$$

The first term on the right-hand side is the Coriolis acceleration, the second term represents the Euler acceleration caused by a change in the angular velocity vector and the third term is the gradient of the effective potential. In this thesis, the variation of the asteroid angular velocity magnitude due to operation of the orbital siphon will be considered, however, it will be shown that $d\boldsymbol{\omega}/dt \approx 0$ and the Euler acceleration is always several order of magnitudes smaller than the other terms. Therefore, the Euler acceleration is neglected. Projecting Eq. (2.4) onto the x, y, z directions and considering the definition of the effective potential (Eq. (2.1)), Eq. (2.4) can

be written as

$$\begin{cases} \ddot{x} - 2\omega\dot{y} &= -\dfrac{\partial U}{\partial x} \\ \ddot{y} + 2\omega\dot{x} &= -\dfrac{\partial U}{\partial y} \\ \ddot{z} &= -\dfrac{\partial U}{\partial z} \end{cases} \tag{2.5}$$

Equations (2.5) can also be expressed in state form:

$$\dot{\mathbf{x}} = \mathbf{F}(\mathbf{x}) \tag{2.6}$$

where $\mathbf{x}$ is the state vector

$$\mathbf{x} = (x, y, z, \dot{x}, \dot{y}, \dot{z}) \tag{2.7}$$

and

$$\mathbf{F} = \begin{Bmatrix} \dot{x} \\ \dot{y} \\ \dot{z} \\ 2\omega\dot{y} - U_x \\ -2\omega\dot{x} - U_y \\ -U_z \end{Bmatrix} \tag{2.8}$$

where the compact notation $U_x = \partial U/\partial x$, $U_y = \partial U/\partial y$, $U_z = \partial U/\partial z$ has been used.

2.2 Mass distributions

This section includes the closed-form solution of the gravitational potential, its gradient and Hessian stemming from the three mass distribution used in this thesis: spherical, ellipsoidal and polyhedral mass distribution. For generality, the potential for points *inside* and *outside* the asteroid is provided in all cases.

2.2.1 Spherical mass distribution

A sphere is the simplest shape to model for an asteroid. Let R be the radius of the sphere. In this case, Eq. (2.3) simplifies to:

$$V = \begin{cases} -\dfrac{GM}{|\mathbf{r}|}, & |\mathbf{r}| > R \\ -\dfrac{GM}{2R^3}(3R^2 - |\mathbf{r}|^2), & |\mathbf{r}| \leq R \end{cases} \tag{2.9}$$

where the two cases are associated with a point inside and outside the asteroid and $M = \rho 4/3\pi R^3$ is the mass of the asteroid. The constant factor $3R^3$ in the second case is added to ensure continuity of the potential at the asteroid surface $|\mathbf{r}| = R$. The gravitational potential for points

inside the asteroid is calculated using Newton's shell theorem [92]. The gradient ∇V and the Hessian $\mathbf{H}_V$ of the gravitational potential are therefore:

$$\nabla V = \begin{cases} \dfrac{\mu}{|\mathbf{r}|^3}(x,y,z), & |\mathbf{r}| > R \\ \dfrac{GM}{R^3}(x,y,z), & |\mathbf{r}| \leq R \end{cases} \tag{2.10}$$

$$\mathbf{H}_V = \begin{cases} \dfrac{GM}{|\mathbf{r}|^5}\begin{pmatrix} -2x^2+y^2+z^2 & 3xy & 3xz \\ 3xy & -2y^2+x^2+z^2 & 3yz \\ 3xz & 3yz & -2z^2+x^2+y^2 \end{pmatrix}, & |\mathbf{r}| > R \\ \dfrac{GM}{R^3}\begin{pmatrix} 1 & 0 & 0 \\ 0 & 1 & 0 \\ 0 & 0 & 1 \end{pmatrix}, & |\mathbf{r}| \leq R \end{cases} \tag{2.11}$$

The gradient and Hessian of the gravitational potential will be used later to address the stability of equilibrium points associated with the effective potential. The case of a spherical mass distribution with a central internal cavity with radius $0 < b < R$ is also considered in this thesis. The gravitational potential for points outside and inside the cavity can be calculated again using Newton's shell theorem (note that the total mass of the asteroid in this case is $4/3\pi\rho(R^3 - b^3)$). The gravitational potential and its gradient in this case are:

$$V = \begin{cases} -\dfrac{GM}{|\mathbf{r}|}\left[1 - \left(\dfrac{b}{R}\right)^3\right], & |\mathbf{r}| > R \\ -\dfrac{GM}{2R^3}\left[\dfrac{2b^3}{|\mathbf{r}|} + |\mathbf{r}|^2 + R^2 - 4\dfrac{b^3}{R}\right], & b \leq |\mathbf{r}| \leq R \\ -\dfrac{GM}{2R^3}\left(3b^2 + R^2 - 4\dfrac{b^3}{R}\right), & 0 \leq |\mathbf{r}| < b \end{cases} \tag{2.12}$$

$$\nabla V = \begin{cases} \dfrac{GM}{|\mathbf{r}|^3}\left[1 - \left(\dfrac{b}{R}\right)^3\right]\mathbf{r}, & |\mathbf{r}| > R \\ \dfrac{GM}{R^3}\left[1 - \left(\dfrac{b}{|\mathbf{r}|}\right)^3\right]\mathbf{r}, & b \leq |\mathbf{r}| \leq R \\ 0, & 0 \leq |\mathbf{r}| < b \end{cases} \tag{2.13}$$

Again, the constant factors in the potential are included to ensure continuity of V at $|\mathbf{r}| = R$ and $|\mathbf{r}| = b$. Note that the gradient of the gravitational potential inside the cavity is zero. Therefore, the net gravitational force acting on a point mass inside the spherical cavity is zero.

2.2.2 Ellipsoidal mass distribution

Modelling the asteroid as a triaxial ellipsoid allows the main effects of the body's irregularities to be studied. Let α, β, γ be the semi-major axes of a constant-density ellipsoid centred at the

origin, such that $\alpha > \beta > \gamma$ and with the x-axis along the largest dimension, the y-axis along the intermediate dimension β and the z-axis along the shortest dimension γ.

From MacMillan [76], the gravitational potential for points outside the asteroid can be written as:

$$V = \frac{3}{4}GM\int_{\kappa}^{\infty}\left(\frac{x^2}{\alpha^2+s}+\frac{y^2}{\beta^2+s}+\frac{z^2}{\gamma^2+s}-1\right)\frac{ds}{\Delta(s)} \tag{2.14}$$

where

$$\Delta(s) = \sqrt{(\alpha^2+s)^2+(\beta^2+s)^2+(\gamma^2+s^2)} \tag{2.15}$$

The parameter $\kappa > 0$, which is a function of (x,y,z), satisfies:

$$\left(1-\frac{x^2}{\alpha^2+\kappa}-\frac{y^2}{\beta^2+\kappa}-\frac{z^2}{\gamma^2+\kappa}\right) = 0 \tag{2.16}$$

Equation 2.16 defines an ellipsoid passing through the point (x,y,z) which is confocal to the body's ellipsoid and it has a unique positive root whenever $\phi(x,y,z,0) > 0$. (i.e., the point lies outside the ellipsoid, as in the present case). For points on or below the surface $\kappa = 0$:

$$V = \frac{3}{4}GM\int_{0}^{\infty}\left(\frac{x^2}{\alpha^2+s}+\frac{y^2}{\beta^2+s}+\frac{z^2}{\gamma^2+s}-1\right)\frac{ds}{\Delta(s)} \tag{2.17}$$

The interested reader is referred to Appendix A for more details on the derivation of Eqs. (2.14) and (2.17).[1] The partial derivative of the potential can then be computed by applying Leibniz's rule

$$V_x = -\frac{3GMx}{2}\int_{\kappa}^{\infty}\frac{ds}{(\alpha^2+s)\Delta(s)} \tag{2.18a}$$

$$V_y = -\frac{3GMy}{2}\int_{\kappa}^{\infty}\frac{ds}{(\beta^2+s)\Delta(s)} \tag{2.18b}$$

$$V_z = -\frac{3GMz}{2}\int_{\kappa}^{\infty}\frac{ds}{(\gamma^2+s)\Delta(s)} \tag{2.18c}$$

[1]Note that MacMillan uses the convention that the gradient of the effective potential (and not its opposite) gives the net acceleration at the point mass due to gravity and centrifugal-induced force. Therefore the potential given by MacMillan has the opposite sign to of that reported in Eq. (2.14) and (2.17). The same holds for the polyhedral gravitational potential given by Eq. (2.20).

Similarly, the components of the Hessian matrix are:

$$V_{xx} = -\frac{3GM}{2}\int_{\kappa}^{\infty}\frac{ds}{(\alpha^2+s)\Delta(s)} \tag{2.19a}$$

$$V_{yy} = -\frac{3GM}{2}\int_{\kappa}^{\infty}\frac{ds}{(\beta^2+s)\Delta(s)} \tag{2.19b}$$

$$V_{zz} = -\frac{3GM}{2}\int_{\kappa}^{\infty}\frac{ds}{(\gamma^2+s)\Delta(s)} \tag{2.19c}$$

$$V_{xy} = 0 \tag{2.19d}$$

$$V_{xz} = 0 \tag{2.19e}$$

$$V_{yz} = 0 \tag{2.19f}$$

Equations (2.14), (2.17), (2.18) can be expressed in terms of Carlson elliptic integrals [22] for faster numerical computation (see Appendix C). The components of the Hessian are required to assess the stability of equilibrium points, to be discussed later.

2.2.3 Polyhedron

Modelling the asteroid as a polyhedron provides a more accurate description of the asteroid gravitational potential as it permits the resolution of small scale elements such as craters, overhangs or voids.

The polyhedron is defined by the coordinates of its vertexes and the connection topology, describing how the vertexes are connected with respect to each other. Figure 2.1 shows the polyhedron models of four asteroids: 101955 Bennu, 1620 Geographos, 6489 Golevka and 216 Kleopatra.[2] Werner and Scheeres [155] showed how the gravitational potential around a constant density polyhedron can be reduced to a summation over its edges and faces by applying the divergence theorem to Eq. (2.3). For a constant-density polyhedron made of triangular faces, define the following notation (this is taken from Werner and Scheeres [155]):

- For each edge, $\mathbf{s}_e$ is a vector from the field point $\mathbf{r}$ to an arbitrary point on the edge.
- For each face, $\mathbf{s}_f$ is a vector from the field point $\mathbf{r}$ to an arbitrary point on the face.
- $\hat{\mathbf{n}}_f$ is the normal of the face, directed outward from the body.
- For each edge e, $\hat{\mathbf{n}}_e^f$ is the unit vector normal to the edge and to the corresponding face normal $\hat{\mathbf{n}}_f$. Note that one edge always corresponds to exactly two faces f and f' and in general $\hat{\mathbf{n}}_e^f$ and $\hat{\mathbf{n}}_e^{f'}$ are different.
- For each face, $\hat{\mathbf{r}}_i^f$, for $i = 1,2,3$, is the vector from the origin to the corresponding vertex of the face (face vertexes are ordered counter-clockwise with respect to the face normal).

[2] All the shape models are taken from *www.3d-asteroids.space* (Last access: 22/10/2020) and are based on radar observations [37, 93, 125] of the four asteroids.

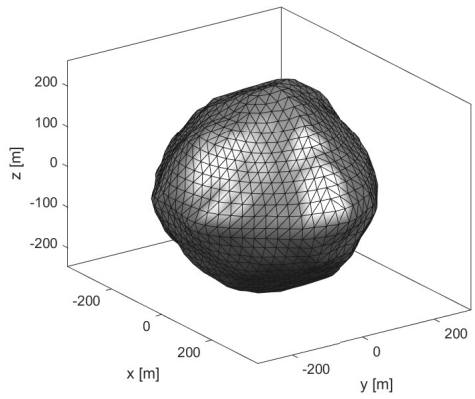

(a) 101955 Bennu.

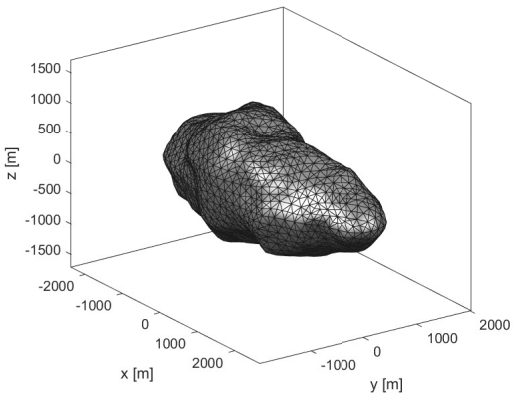

(b) 1620 Geographos.

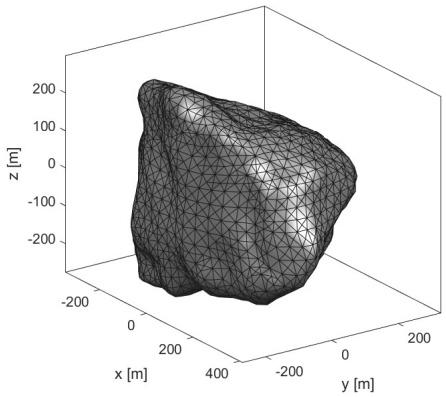

(c) 6489 Golevka.

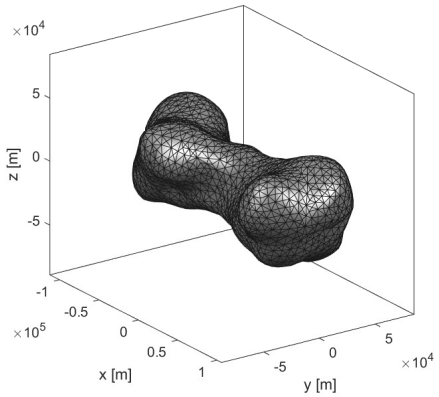

(d) 216 Kleopatra.

FIGURE 2.1: Polyhedral models of the asteroids 101955 Bennu, 1620 Geographos, 6489 Golevka and 216 Kleopatra (see footnote 2 on page 25).

- For each edge, $\hat{\mathbf{r}}_i^e$, for $i = 1,2$, is the vector from the origin to the corresponding vertex of the edge.
- For each edge e_e is the length of the edge.

The gravitational potential, its gradient and the Hessian are then defined as [155]:

$$V = -\frac{G\rho}{2}\left(\sum_{e\in\text{edges}} L_e \mathbf{s}_e \cdot \mathbf{E}_e \mathbf{s}_e - \sum_{f\in\text{faces}} \gamma_f \mathbf{s}_f \cdot \mathbf{F}_f \mathbf{s}_f\right) \tag{2.20}$$

$$\nabla V = G\rho\left(\sum_{e\in\text{edges}} L_e \mathbf{E}_e \mathbf{s}_e - \sum_{f\in\text{faces}} \gamma_f \mathbf{F}_f \mathbf{s}_f\right) \tag{2.21}$$

$$\mathbf{H}_V = -G\rho\left(\sum_{e\in\text{edges}} L_e \mathbf{E}_e - \sum_{f\in\text{faces}} \gamma_f \mathbf{F}_f\right) \tag{2.22}$$

where the quantities $\mathbf{E}_e$, $\mathbf{F}_f$, L_e and γ_f are defined as:

$$\mathbf{E}_e = \hat{\mathbf{n}}_f \hat{\mathbf{n}}_e^f + \hat{\mathbf{n}}_{f'} \hat{\mathbf{n}}_e^{f'} \tag{2.23}$$

$$\mathbf{F}_f = \hat{\mathbf{n}}_f \hat{\mathbf{n}}_f \tag{2.24}$$

$$L_e = \ln \frac{r_1^e + r_2^e + e_e}{r_1^e + r_2^e - e_e} \tag{2.25}$$

$$\gamma_f = 2\tan^{-1} \frac{\mathbf{r}_1^f \cdot (\mathbf{r}_2^f \times \mathbf{r}_3^f)}{r_1^f r_2^f r_3^f + r_1^f \mathbf{r}_2^f \cdot \mathbf{r}_3^f + r_2^f \mathbf{r}_3^f \cdot \mathbf{r}_1^f + r_3^f \mathbf{r}_1^f \cdot \mathbf{r}_2^f} \tag{2.26}$$

where the symbols $\cdot$ and $\times$ denote the scalar and vector product respectively. See Appendix B for some insights into the derivation of Eq. (2.20).

2.3 Integral of motion

Multiplying Eqs. (2.5) by $\dot{x}$, $\dot{y}$ and $\dot{z}$ respectively and summing all the terms yields:

$$\dot{x}\ddot{x} + \dot{y}\ddot{y} + \dot{z}\ddot{z} = -U_x\dot{x} - U_y\dot{y} - U_z\dot{z} \tag{2.27}$$

Noting that:

$$\dot{x}\ddot{x} + \dot{y}\ddot{y} + \dot{z}\ddot{z} = \frac{d}{dt}\left(\frac{|\mathbf{r}|^2}{2}\right) \tag{2.28}$$

and

$$-U_x\dot{x} - U_y\dot{y} - U_z\dot{z} = -\nabla U \cdot \frac{d\mathbf{r}}{dt} = -\frac{dU}{dt} \tag{2.29}$$

Eq. (2.27) can then be written as

$$\frac{d}{dt}\left(\frac{|\mathbf{r}|^2}{2}\right) = -\frac{dU}{dt} \tag{2.30}$$

and, integrating with respect to time, the following integral of motion is obtained:

$$C = \frac{1}{2}v^2 + U \tag{2.31}$$

where $v = \sqrt{\mathbf{r}\cdot\mathbf{r}}$ is the magnitude of the velocity of a point mass. The constant C is often referred to as the *Jacobi constant* and Eq. (2.31) states that mechanical energy is conserved. Equation (2.31) can be used as an aid to study the dynamics of a point mass in the rotating frame. In fact, for a given value of C (which is defined from the initial conditions of the point mass), the quantity $C-U$ has to be larger or equal to zero, otherwise the term v^2 would be negative. The regions where $C-U<0$ are therefore areas where motion is forbidden and the equation $C-U=0$ defines three-dimensional surfaces that separate regions where motion is forbidden from regions where motion is allowed. According to Eq. (2.31), a point mass standing on an equipotential surface $U=C$ would necessarily have zero velocity: for this reason, the equipotential surfaces are also called *zero-velocity surfaces* (ZVSs).

For example, Fig. 2.2 shows the morphology of the ZVSs for the asteroid 6489 Golevka, modelled as a polyhedron, calculated for different values of the Jacobi constant. For lower energy levels (Fig. 2.2a), the ZVSs partition the space into two regions of allowed motion, namely an inner region, close to the mass distribution, and an outer region, far from the mass distribution. Therefore, if an object is placed inside such inner region, it can never escape the asteroid, since the ZVSs are trapping the object inside the inner region. Conversely, an object starting its motion in the external region will never impact the asteroid. For higher energy levels, these regions are connected, and motion from the inner region to the outer region (or viceversa) is allowed. Note that far from the mass distribution, $V\to 0$ and therefore $C\approx -\frac{1}{2}\omega^2|\mathbf{r}|^2$. Hence the ZVSs approach cylinders of radius $\sqrt{2|C|/\omega^2}$.

The intersection of the ZVSs with a plane are called *zero velocity curves* (ZVCs). As ZVSs are often transverse to the xy plane and the equilibrium points (to be introduced later) are in the xy plane (or have $z\approx 0$ for the polyhedron model) it is useful to consider the restriction of ZVSs to planes. Figure 2.3 shows the ZVCs in the xy plane for the polyhedral models of the asteroids in Fig. 2.1, for a range of Jacobi constant C (physical properties of the asteroids are listed in Table 2.1). Figure 2.4 shows the ZVCs for the same asteroids modelled as ellipsoidal mass distributions. The ellipsoid axes are selected such that, the volume of the ellipsoid is the same as the polyhedron volume[3] constraining the ratios β/α, γ/α, selected from the literature (Table 2.1). It is apparent that, in proximity of the asteroid surface, the polyhedral models permit to capture with more accuracy the irregularities of the gravitational field due to asteroid shape.

[3]Using the divergence theorem it can be shown that the volume of the polyhedron is equal to

$$\frac{1}{3}\left|\sum_{f\in\text{faces}}(\mathbf{r}_f\cdot\hat{\mathbf{n}}_f)A_f\right| \tag{2.32}$$

being A_f the area of the face.

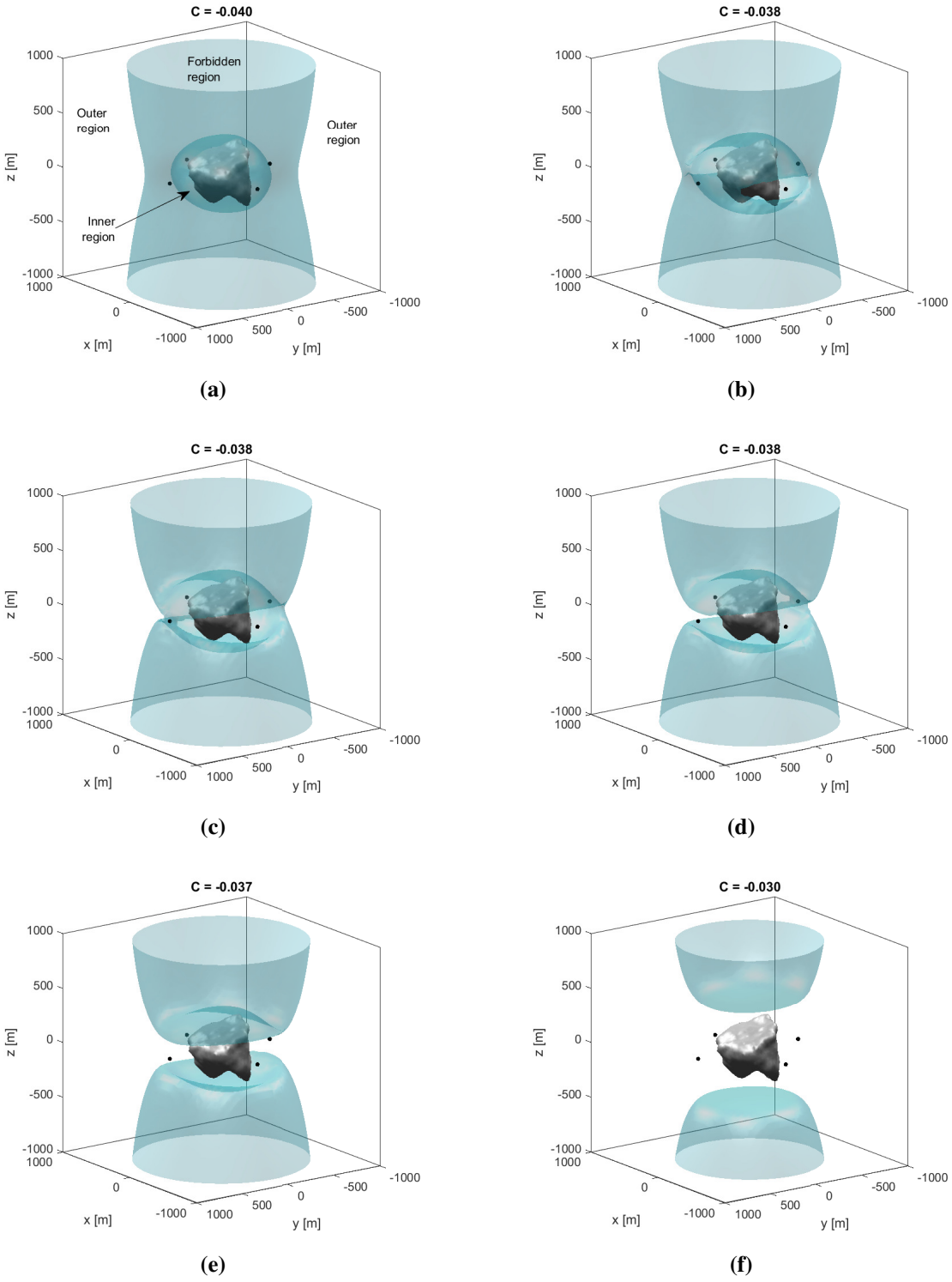

FIGURE 2.2: Zero velocity surfaces associated with the effective potential of the asteroid 6489 Golevka, for a range of Jacobi constants.

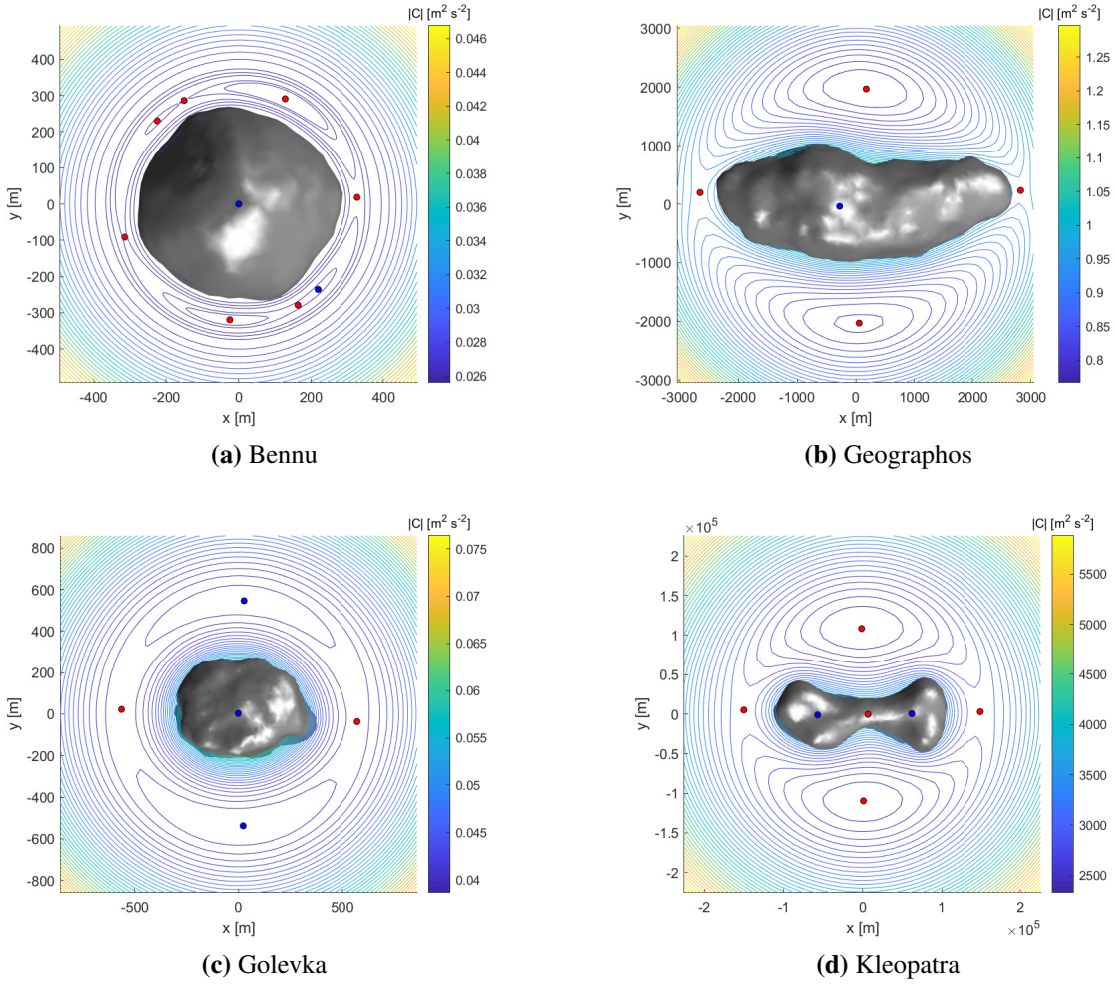

(a) Bennu **(b)** Geographos

(c) Golevka **(d)** Kleopatra

FIGURE 2.3: Zero velocity curves in the $z = 0$ plane for the polyhedral models of four asteroids listed in Table 2.1. Also shown as blue/red dots are the stable/unstable equilibria.

TABLE 2.1: Physical properties of some asteroids. The radius of the equivalent sphere is calculated such that the volume of the ellipsoid is the same as the polyhedron volume.

Asteroid	Density [kg/m^3]	Rotation period [h]	Eq. sphere radius [m]	Ellipsoid model extent		Polyhedron details [vertexes x faces]
Bennu [119]	1260	4.29	246	$\beta/\alpha = 0.95$ $\gamma/\alpha = 0.89$	[119]	1348 x 2692
Geographos [99]	2000	5.22	2.56×10^3	$\beta/\alpha = 0.4$ $\gamma/\alpha = 0.4$	[56]	2048 x 4092
Golevka [27, 90]	2700	6.02	265	$\beta/\alpha = 0.74$ $\gamma/\alpha = 0.74$	[90]	2048 x 4092
Kleopatra [23, 98]	4270	5.39	122×10^3	$\beta/\alpha = 0.34$ $\gamma/\alpha = 0.03$	[125]	2048 x 4092

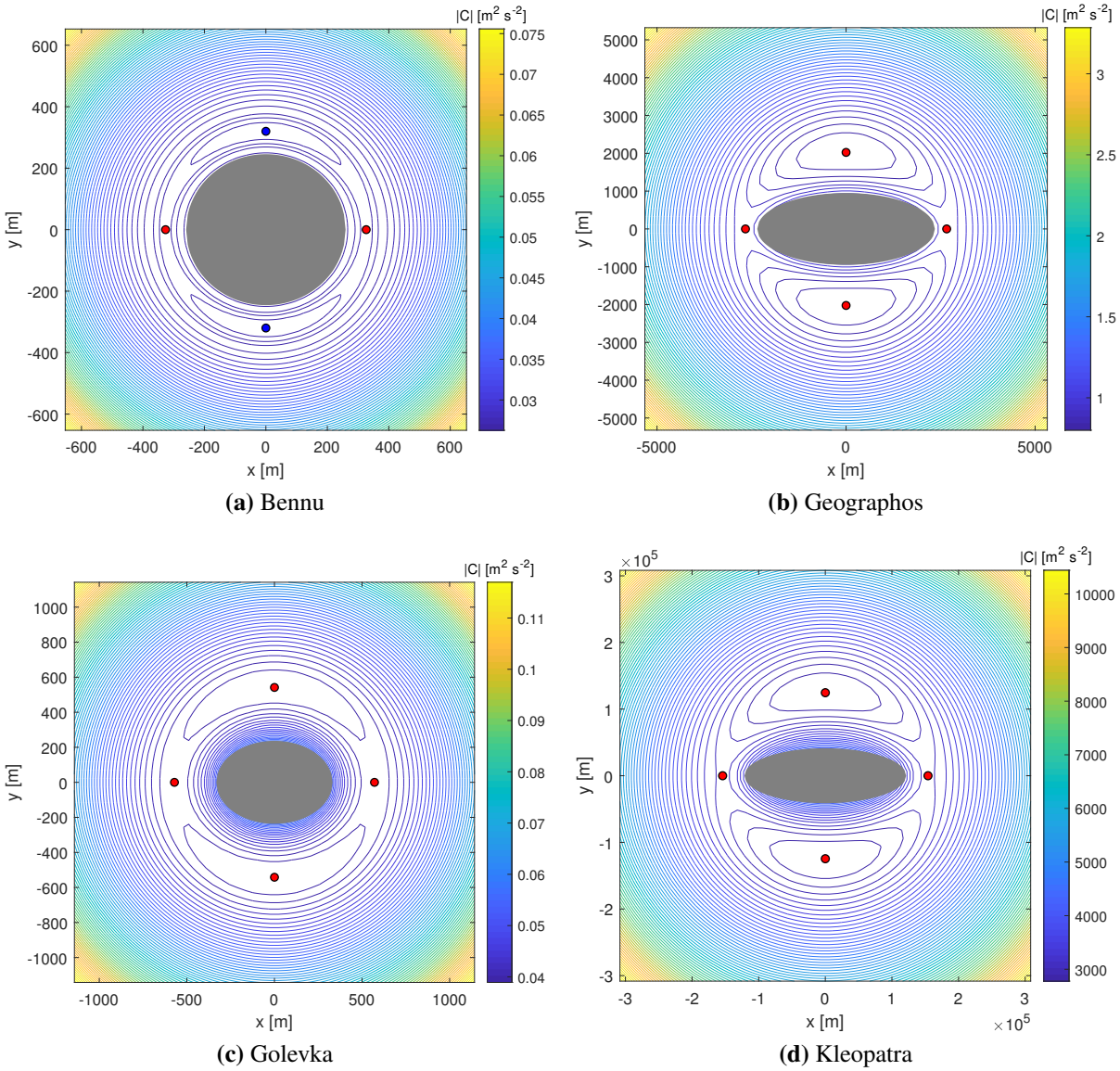

(a) Bennu **(b)** Geographos

(c) Golevka **(d)** Kleopatra

FIGURE 2.4: Zero velocity curves in the $\mathbf{z} = \mathbf{0}$ plane for the ellipsoidal models of four asteroids listed in Table 2.1. Also shown as blue/red dots are the stable/unstable equilibria.

Far from the asteroid, the morphology of the ZVCs is similar in the two cases.

2.4 Equilibrium points and their stability

The term *equilibrium point* (EP) is used to indicate the zeros of the gradient of the effective potential U in the rotating frame. The definition can be formally extended to the six-dimensional state-space: a state $\mathbf{x}_{\text{eq}} = (x, y, z, \dot{x}, \dot{y}, \dot{z})$ is an EP if $\mathbf{F}(\mathbf{x}_{\text{eq}}) = 0$ or, equivalently, if $\dot{x} = \dot{y} = \dot{z} = 0$ and

$$\nabla U(x, y, z) = (0, 0, 0) \tag{2.33}$$

As a consequence, the total force acting on a point mass at an EP is zero and therefore a point mass placed at an EP remains fixed with respect to the asteroid, therefore describing a circular synchronous orbit with respect to an inertial reference frame.

For a spherical mass distribution, substituting Eq. (2.10) into Eq. (2.33) gives:

$$\begin{cases} -\omega^2(x, y, 0) + \dfrac{GM}{|\mathbf{r}|^3}(x, y, z) = (0, 0, 0), & |\mathbf{r}| > R \\ -\omega^2(x, y, 0) + \dfrac{GM}{R^3}(x, y, z) = (0, 0, 0), & |\mathbf{r}| < R \end{cases} \tag{2.34}$$

which yields an equilibrium point at the origin $(x, y, z) = (0, 0, 0)$ and a locus of equilibria characterised by the equation

$$x^2 + y^2 = \left(\frac{GM}{\omega^2}\right)^{2/3}, \quad z = 0 \tag{2.35}$$

which is a circumference in the xy plane centred at the origin and with radius $(GM/\omega^2)^{1/3}$.

The same procedure can be used to identify the EPs associated to an ellipsoidal mass distribution. Substituting Eq. (2.18) into Eq. (2.33) yields:

$$\begin{cases} x\left[\omega^2 - \dfrac{3GM}{2}\displaystyle\int_\kappa^\infty \frac{ds}{(\alpha^2 + s)\Delta(s)}\right] = 0 & \text{(2.36a)} \\ y\left[\omega^2 - \dfrac{3GM}{2}\displaystyle\int_\kappa^\infty \frac{ds}{(\beta^2 + s)\Delta(s)}\right] = 0 & \text{(2.36b)} \\ -\dfrac{3GMz}{2}\displaystyle\int_\kappa^\infty \frac{ds}{(\gamma^2 + s)\Delta(s)} = 0 & \text{(2.36c)} \end{cases}$$

From the last condition (2.36c) it is apparent that, as for a spherical mass distribution, the EPs are all lying in the plane $z = 0$. Again, one trivial solution to Eqs. (2.36) is the origin, $(x, y, z) = (0, 0, 0)$. Four additional solutions can be found, namely two EPs on the x-axis and two on the y-axis, both pairs being symmetrical with respect to the origin. For reasons related to the topology of the phase space in their neighbourhood, the EPs on the x-axis are called *saddle* equilibrium points (SEPs), whereas, the EPs on the y-axis are called *centre* equilibrium points (CEPs), with evident implications on their stability [47]. The exterior EPs for the ellipsoidal mass distribution

of the four asteroids listed in Table 2.1 are shown in Fig. 2.4 as dots (the colour is associated to their stability properties, to be addressed later).

The localization of the EPs for polyhedral mass distributions is more complicated due to the complexity of the gravity gradient expression (Eq. (2.10)) which depends on the number of vertices and faces of the polyhedron. In general, more than four exterior EPs can exist in this case. The four equilibria found with the ellipsoid model can be used as an initial guess to find the EPs in the polyhedron model. Additional EP can be found using the systematic procedure described in Ref. [132].

Table 2.2 shows the location of the EPs for the asteroids Bennu, Geographos, Golevka and Bennu, using the spherical, ellipsoidal and polyhedral mass distribution. For the ellipsoid model, the distances between the EPs and the asteroid centre-of-mass are indicated. Note that nine equilibria (eight external and one internal) exist for the asteroid Bennu and, in general, more than one equilibrium may exist in the interior of the asteroid (for example the asteroid Kleopatra has three internal equilibria).

2.4.1 Stability of the equilibrium points

The stability at the EPs can be studied by linearising the equations of motion (2.6) in the vicinity of the equilibria. Let $\delta\mathbf{x} = (\delta x, \delta y, \delta z, \delta\dot{x}, \delta\dot{y}, \delta\dot{z})$ be a small displacement from the equilibrium $\mathbf{x}_{\text{eq}}$ such that

$$\mathbf{x} = \mathbf{x}_{\text{eq}} + \delta\mathbf{x} \tag{2.37}$$

Since $|\delta\mathbf{x}|$ is small, the effective potential U can be linearised, such that:

$$U \approx U_{\text{eq}} + U_x\delta x + U_y\delta y + U_z\delta z + \text{h.o.t.} \tag{2.38}$$

where U_{eq} is the value of the potential at the equilibrium point and h.o.t. are higher order terms. Substituting Eqs. (2.37) and (2.38) into Eq. (2.5), remembering that $\nabla(U) = (0,0,0)$ at the EPs and further simplifying yields:

$$\delta\dot{\mathbf{x}} = A\mathbf{x} \tag{2.39}$$

with

$$A = \begin{pmatrix} 0 & 0 & 0 & 1 & 0 & 0 \\ 0 & 0 & 0 & 0 & 1 & 0 \\ 0 & 0 & 0 & 0 & 0 & 1 \\ -U_{xx} & -U_{xy} & -U_{xz} & 0 & 2\omega & 0 \\ -U_{yx} & -U_{yy} & -U_{yz} & -2\omega & 0 & 0 \\ -U_{zx} & -U_{zy} & -U_{zz} & 0 & 0 & 0 \end{pmatrix} \tag{2.40}$$

TABLE 2.2: Location of the equilibria for the asteroids Bennu, Geographos, Golevka and Kleopatra, using the spherical, ellipsoidal and polyhedral mass distribution. For the spherical and ellipsoidal mass distribution, the location of the EP is expressed as a distance from the asteroid centre. The tags (U) and (S) indicate unstable and stable equilibria respectively for the polyhedron model.

	Sphere	Ellipsoid	Polyhedron				
					x	y	z
			EP_1	(U)	327.71 m	18.68 m	-3.22 m
			EP_2	(U)	-150.45 m	286.54 m	-7.94 m
		SEP	EP_3	(U)	-314.22 m	-91.22 m	-2.29 m
		326.41 m	EP_4	(U)	-3.66 m	-320.13 m	-0.07 m
Bennu	315 m		EP_5	(U)	128.78 m	290.97 m	-2.47 m
		CEP	EP_6	(U)	-224.70 m	230.45 m	-7.29 m
		319.93 m	EP_7	(S)	219.67 m	-235.16 m	-2.83 m
			EP_8	(U)	161.92 m	-279.77 m	-1.98 m
			EP_9	(S)	0.2 m	0.1 m	0.1 m
		SEP	EP_1	(U)	2819.5 m	232.1 m	-14.4 m
		2661.1m	EP_2	(U)	180.4 m	1965.7 m	10.6 m
Geographos	2.19km		EP_3	(U)	-2651.7 m	195.8 m	-0.3 m
		CEP	EP_4	(U)	58.9 m	-2025.8 m	-17.1 m
		2023.8 m	EP_5	(S)	-274.0 m	-38.2 m	-19.3 m
		SEP	EP_1	(U)	571.4 m	-36.2 m	-6.2 m
		571.0 m	EP_2	(S)	6.2 m	547.2 m	-0.2 m
Golevka	551.1m		EP_3	(U)	-564.1 m	22.7 m	-3.0 m
		CEP	EP_4	(S)	15.2 m	-537.8 m	-1.1 m
		541.7 m	EP_5	(S)	-2.3 m	3.3 m	2.1 m
			EP_1	(U)	149054.0 m	2954.6 m	237.7 m
		SEP	EP_2	(U)	-1330.2 m	108351.4 m	-893.5 m
		154.1 km	EP_3	(U)	-150207.6 m	5131.9 m	-1332.9 m
Kleopatra	124.9km		EP_4	(U)	1005.2 m	-109666.6 m	-53.4 m
		CEP	EP_5	(U)	6726.1 m	-251.7 m	-889.5 m
		124.6 km	EP_6	(S)	62073.5 m	525.5 m	1499.5 m
			EP_7	(S)	-56939.7 m	-1160.2 m	-593.5 m

The stability at the EP can therefore be inferred from the roots of the characteristic polynomials of A, i.e., the roots of the polynomial:

$$\det(A - \lambda \mathbf{1}) = 0 \tag{2.41}$$

being $\mathbf{1}$ the 6×6 identity matrix. Equation (2.41) can then be expanded as:

$$\begin{aligned} &\lambda^6 + (U_{xx} + U_{yy} + U_{zz} + 4\omega^2)\lambda^4 \\ &+ (U_{xx}U_{yy} + U_{yy}U_{zz} + U_{zz}U_{xx} - U_{xy}^2 - U_{yz}^2 - U_{xz}^2 + 4\omega^2 U_{zz})\lambda^2 \\ &+ (U_{xx}U_{yy}U_{zz} + 2U_{xy}U_{yz}U_{xz} - U_{xx}U_{yz}^2 - U_{yy}U_{xz}^2 - U_{zz}U_{xy}^2) = 0 \end{aligned} \tag{2.42}$$

The EP is called *linearly stable* (or simply *stable*) if all the eigenvalues of the matrix A are different and in the form $\pm i\beta_j$, with $\beta_j \in \mathbb{R}, \quad \beta_j > 0, \quad i = 1,2,3$. The EP is said *unstable* if there is at least one eigenvalue with positive real part. If an EP is stable, the linearised motion of a point mass in proximity of the EP follows a quasi-periodic orbit [59]. Furthermore, initial condition can be selected to force periodic or quasi-periodic motion around the EPs [142]. Conversely, if a point is unstable, depending on the initial conditions of a point mass in the vicinity of the EP, the resulting trajectories might exponentially depart from the EP. For a more general and comprehensive classification of the equilibria, the dynamics about EPs and invariant manifolds, the interested reader is referred to Ref. [59].

Stability of the EPs of a spherical asteroid. In this case, analysis of stability in this case is straightforward, since Eq. (2.39) admit a closed-form solution. For example, taking the EP $(x,y,z) = ((\mu/\omega^2)^{1/3}, 0, 0)$ (the analysis for the other EPs is analogous for symmetry) Eq. (2.39) becomes:

$$\begin{cases} \delta\ddot{x} &= 3\omega^2\delta x + 2\omega\delta\dot{y} \\ \delta\ddot{y} &= -2\omega\delta\dot{x} \\ \delta\ddot{z} &= -\omega^2\delta z \end{cases} \tag{2.43}$$

Which admits the closed-form solution [29]:

$$\begin{cases} \delta x(t) = (4 - 3\cos\omega t)\delta x_0 + \dfrac{\sin\omega t}{\omega}\delta\dot{x}_0 + \dfrac{2}{\omega}(1 - \cos\omega t)\delta\dot{y}_0 & \text{(2.44a)} \\ \delta y(t) = 6(\sin\omega t - \omega t)\delta x_0 + \delta y_0 - \dfrac{2}{\omega}(1 - \cos\omega t)\delta\dot{x}_0 + \dfrac{4\sin\omega t - 3\omega t}{\omega}\delta\dot{y}_o & \text{(2.44b)} \\ \delta z(t) = \delta z_0 \cos\omega t + \dfrac{\delta\dot{z}_0}{\omega}\sin\omega t & \text{(2.44c)} \end{cases}$$

where $(\delta x_0, \delta y_0, \delta z_0)$ and $(\delta\dot{x}_0, \delta\dot{y}_0\delta\dot{z})$ are the initial positions and velocity. The term $-3t\delta\dot{y}_0$ on the right-hand side of Eq. (2.44b) indicates a long-term drift in the y direction, if a small perturbation $\delta\dot{y}_0$ is applied. Therefore, equilibria at synchronous orbit are not stable.

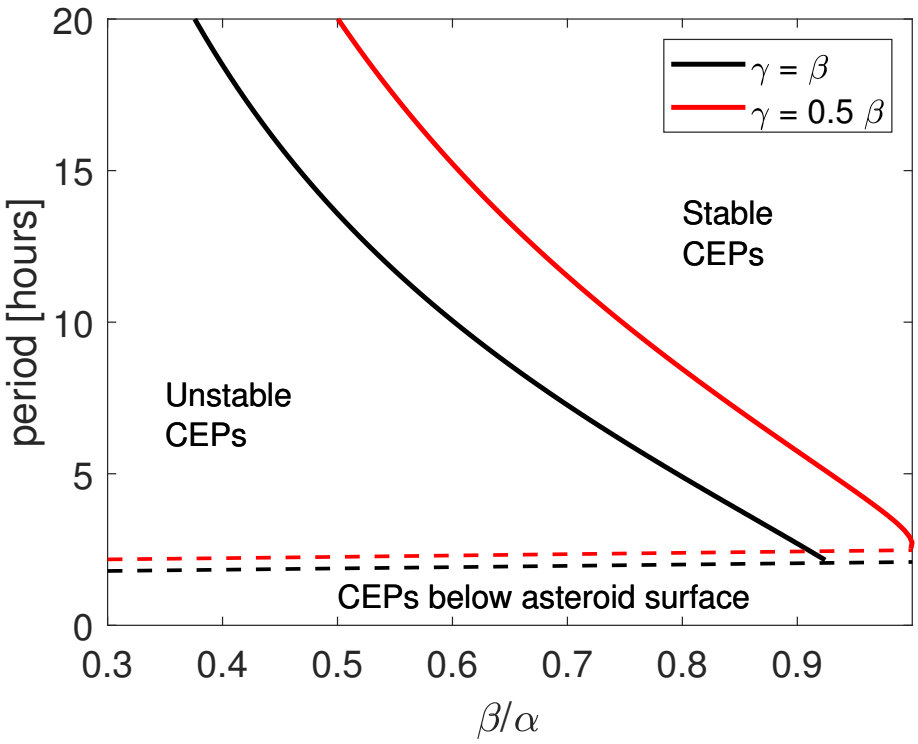

FIGURE 2.5: Regions of stability of the centre equilibria, for $\gamma = \beta$ and $\gamma = \beta/2$, as a function of β and the asteroid period. The dotted lines mark the region where centre points fall below the surface of the asteroid.

Using a similar analysis it can be shown that the EP at the centre of the asteroid is stable.

Stability of the EPs of an ellipsoidal asteroid. Substituting the second derivatives of the effective potential (where the gravitational component of the second derivatives is given by Eqs. (2.19)) into Eq. (2.40) and calculating the eigenvalues at the four EPs, it can be shown that the SEPs are always unstable. Conversely, CEPs stability depends on the asteroid semi-major axes and its angular velocity ω. Figure 2.5 shows the region of stability of the CEPs as a function of β/α and the asteroid period (in dimensional units, assuming an asteroid density $\rho = 2500\,\mathrm{kg\,m^{-3}}$), assuming $\gamma = \beta$ (black line) and $\gamma = \beta/2$ (red line) . For a given set of shape parameters, the CEPs are unstable beneath the associated curve. The two dotted lines represent the case where the CEPs fall below the asteroid surface (the dotted black line refers to the case $\gamma = \beta$, whereas the dotted red line refers to $\gamma = \beta/2$). It is apparent that fast-rotators are generally characterized by unstable CEPs. For $\gamma = \beta$, CEPs are below the surface for periods between 1.75 h and 2.3 h in the range of β shown in the figure. The reader is referred to Ref. [120] for a thorough analysis on stability of EPs of an ellipsoidal asteroid. Stable and unstable EPs for the ellipsoidal models of the asteroids in Table 2.1 are represented in blue and red respectively in Fig. 2.4.

Stability of EPs of a polyhedron. In general, contrary to the spherical and ellipsoidal model, the non-diagonal components of the Hessian of the effective potential can be non-zero and the stability properties of the EPs can change with respect to the ellipsoidal asteroid model. EPs are marked in blue/red in Fig. 2.3 when they are stable/unstable. Also, stability of equilibria is indicated for each EP in Table 2.2.

Chapter 3

Analytical mechanics of asteroid disassembly using the orbital siphon

3.1 Introduction

This chapter introduces the analytical mechanics of an orbital siphon anchored to a rotating spherical asteroid. The fundamental siphon parameters that will be used throughout the thesis are thoroughly defined here.

The orbital siphon is modelled as a chain of tether-connected payloads sliding without friction on a rigid rod, and arranged vertically from the asteroid equator. In parallel to such discrete formulation of the siphon, a continuous mass distribution model is also introduced. Conservation of angular momentum is used to study the variation of the angular velocity of the asteroid during siphon operation and then identify the maximum quantity of mass that can be extracted from the asteroid as a function of the initial asteroid period, using different extraction strategies (fixed and variable siphon length). Other key parameters, such as the siphon radial velocity and the timescale for mass extraction are defined. Eventually, some examples related to candidate asteroids are provided using dimensional variables.

3.2 System description

The model consists of a spherical asteroid with radius R, mass M rotating as a rigid body with angular velocity ω. A total of $n \geq 2$ payload masses (PMs) can slide frictionless along a rigid truss fixed at a point along the equator of the asteroid, as shown in Fig. 3.1 to generically indicate material mined from the asteroid. The truss supports the transversal Coriolis force due to the radial motion of the chain. Each PM is connected to the neighbouring masses by a (massless) tether with length l and infinite stiffness. The total length of the chain is therefore $L = (n-1)l$. The following assumptions are made:

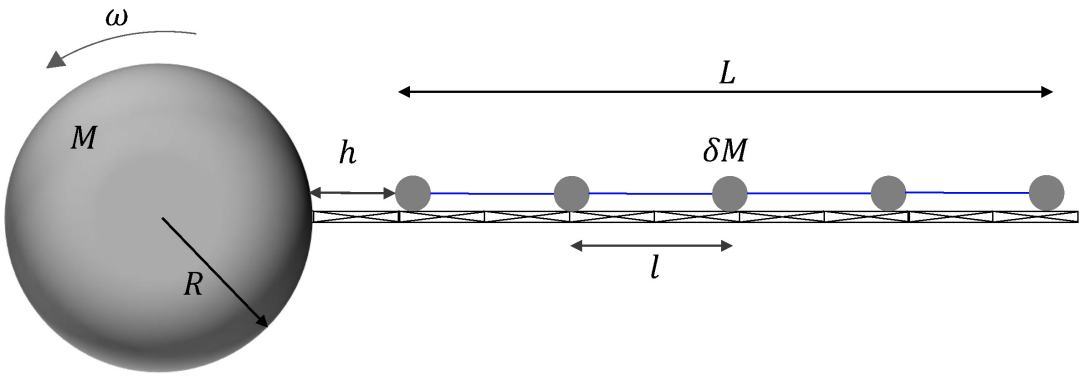

FIGURE 3.1: Model for the chain of masses. The masses of the chain can slide without friction on a rigid rod anchored to the asteroid equator. Consecutive masses are connected via infinitely rigid tethers with length l.

1. Each PM is considered a point-like mass δM, such that $\delta M/M << 1$.
2. The gravitational interaction between PMs is neglected. The sole gravitational interaction is between each PM and the asteroid.
3. The density ρ of the asteroid is constant and uniform.
4. The effects of the asteroid's orbit on the dynamics are neglected.
5. The truss is infinitely rigid, i.e., its deformations and interactions with the chain are neglected.
6. No external forces are acting on the asteroid and chain.
7. The centre of mass of the coupled system of the asteroid and chain is assumed to be coincident with the centre of mass of the asteroid.

As a consequence of these assumptions, the system has only one degree of freedom, i.e., the altitude h of the first PM. It is also assumed that mining units are uniformly removing material from the asteroid and transporting it at the siphon base such that, in the long term, the asteroid retains a spherical shape. However, the practical aspects related to mining operation (e.g., number of mining rovers, mass rate of transported material, energy required for drilling) are not taken into account here. The radius and mass of the asteroid will therefore change during mining operation. From this point, the subscript "0" appended to the, R, M represents the state of that variable at the beginning of siphon operation.

3.2.1 Forces on the siphon

Within the asteroid rotating frame, each PM is subjected to gravitational and centrifugal-induced forces, as well as the internal tensions along the tether. It is assumed that the i-th tether connects

TABLE 3.1: Scale factors for non-dimensional variables. Dimensional variables are obtained by multiplying the non-dimensional value by the scale factor listed in the table.

Scale factors		
Primary units	Distance	R_0
	Mass	M_0
	Time	$\omega_{\text{crit}}^{-1}$
Secondary units	Angular velocity	ω_{crit}
	Velocity	$\omega_{\text{crit}} R_0$
	Force	$M_0 \omega_{\text{crit}}^2 R_0$
	Energy	$\omega_{\text{crit}}^2 R_0^2$
	Linear density	M_0/R_0

the i-th and the $(i+1)$-th PM. Note that the transversal Coriolis force does not interfere with the radial motion of the chain if friction is neglected. The overall force on the i-th PM is the sum of the gravitational and centripetal force and the tether tensions. From Eq. (2.1):

$$f_i = -\delta M \nabla U_i + \tau_i - \tau_{i-1} \tag{3.1}$$

where U_i is the effective potential at the i-th PM and τ_i is the tension on the i-th tether connecting the i-th and the $(i+1)$-th PM. Therefore:

$$f_i = -G\frac{M\delta M}{(R+h+(i-1)l)^2} + \delta M \omega^2 (R+h+(i-1)l) + \tau_i - \tau_{i-1}, \quad i = 1,\ldots,n \tag{3.2}$$

where h is the altitude of the first payload mass. Equation (3.2) can be rewritten in non-dimensional form by scaling masses, radii and angular velocity by M_0, R_0 and $\sqrt{4/3\pi\rho G}$ respectively, such that:

$$\bar{f}_i = \left(-\frac{\bar{R}^3}{\left(\bar{R}+\bar{h}+(i-1)\bar{l}\right)^2} + \bar{\omega}^2 \left(\bar{R}+\bar{h}+(i-1)\bar{l}\right) + \bar{\tau}_i - \bar{\tau}_{i-1} \right) \delta\bar{M} \tag{3.3}$$

The upper bar indicates a non-dimensional variable. The angular velocity scale factor

$$\omega_{\text{crit}} = \sqrt{\frac{4}{3}\pi\rho G} \tag{3.4}$$

is here termed the *critical angular velocity* of the asteroid. When $\omega = \omega_{\text{crit}}$ the gravitational force on a particle δM at the equator of the asteroid is equal (in absolute value) to the centripetal force. Under the current assumption of a spherical asteroid, this parameter only depends on the asteroid density. For example, taking a density $\rho = 2000\,\text{kg}\,\text{m}^{-3}$ results in a critical rotation period $2\pi/\omega_{\text{crit}} \approx 2.3\,\text{h}$. If the asteroid is rotating with $\omega > \omega_{\text{crit}}$ then material at the asteroid equator can be lifted to orbit or to escape, unless some form of cohesion is preventing particles from being displaced or the asteroid is a monolithic body [117]. In this chapter, asteroids spinning

below the critical angular velocities are considered, i.e., $\bar{\omega} \in [0,1]$.

Table 3.1 shows all the relevant scale factors used in this and subsequent chapters. Note that all the scale factors listed as *secondary units* can be consistently derived from the *primary unit* scale factors. Unless explicitly indicated in the text, any variable with the upper bar is scaled with the scale factors listed in Table 3.1[1].

The overall force on the whole chain is then:

$$\bar{f} = \sum_{i=1}^{n} \bar{f}_i \tag{3.5}$$

Performing the summation, the internal tensions τ_i vanish and the net resultant force on the chain of masses is given by

$$\bar{f} = \frac{\delta \bar{M} \bar{R}^3}{\bar{l}^2} \left[\Psi\left(\frac{\bar{R} + n\bar{l} + \bar{h}}{\bar{l}} \right) - \Psi\left(\frac{\bar{R} + \bar{h}}{\bar{l}} \right) \right] + \bar{\omega}^2 n \delta \bar{M} \left(\bar{R} - \frac{\bar{l}}{2} + \bar{h} + \frac{n\bar{l}}{2} \right) \tag{3.6}$$

where $\Psi(\zeta)$ is the polygamma function of order 1, defined in series as [1]

$$\Psi(\zeta) = \sum_{i=0}^{\infty} (\zeta + i)^{-2}. \tag{3.7}$$

The product $n\bar{l}$ appearing in Eq. (3.6) is related to the normalized length of the chain $\bar{L} = L/R$. In fact:

$$n\bar{l} = n\frac{l}{R_0} = \frac{(n-1)l}{R_0} + \frac{l}{R_0} = \bar{L} + \bar{l}. \tag{3.8}$$

It can be shown that $df/dh > 0$ for every $l > 0$, n and $\bar{\omega} \in [0,1]$. Hence the overall force increases with an increase of the altitude of the first mass h. The motion of the chain is described by

$$n\delta M \frac{d^2}{dt^2} h = \sum_{i=1}^{n} f_i. \tag{3.9}$$

Using Eqs. (3.3), (3.4) and (3.6), Eq. (3.9) can be written in non-dimensional form as

$$n\ddot{\bar{h}} = \bar{f} \tag{3.10}$$

where $\ddot{\bar{h}}$ represents the non-dimensional acceleration of the first PM, such that:

$$\ddot{\bar{h}} = \frac{1}{{\omega_{\text{crit}}}^2} \frac{d^2}{dt^2} h \tag{3.11}$$

[1]Note that, for consistency with the rest of the thesis, a different set of scaling factors is used in this Chapter with respect to Ref. [149].

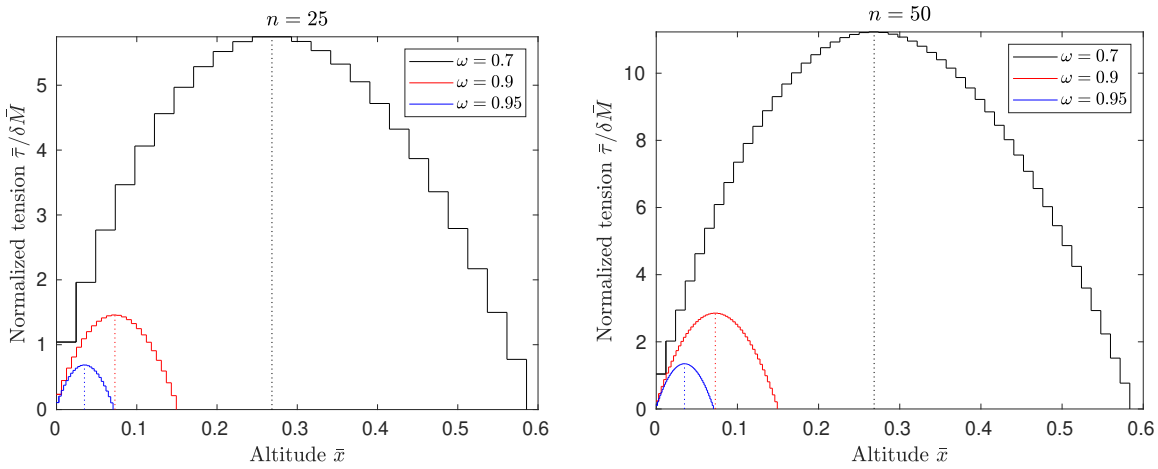

FIGURE 3.2: Normalized tension along the tethers for $n = 25$ (a) and $n = 50$ (b) at the equilibrium ($f = 0$). The dotted lines represent the synchronous orbit altitude for the given $\bar{\omega}$.

Similarly, $\dot{\bar{h}}$ is defined as

$$\dot{\bar{h}} = \frac{1}{\omega_{\text{crit}}} \frac{d}{dt} h \tag{3.12}$$

For a given h, if $f = 0$ the chain will be in equilibrium.

The normalised tensions $\bar{\tau}_i$ can be calculated solving the system of equations (3.3) once the chain acceleration $\ddot{h}$ is known from Eq. (3.9) (clearly, if the chain is in equilibrium then $\ddot{h} = 0$). Figure 3.2 shows the normalized tension along the tethers at equilibrium ($f = 0$) with $h = 0$ for three values of $\bar{\omega}$ and $n = 25$ (3.2a), $n = 50$ (3.2b), with respect to the normalized altitude h. Note that the chain length L varies for the angular velocities chosen, according to Eq. (3.6) with $f = 0$ and Eq. (3.8). As for the space elevator cable [102], the maximum tension is reached for the tether crossing the synchronous orbit altitude x_{sync}, which can be expressed as a function of ω from the definition of synchronous orbit altitude, with the condition

$$\frac{2\pi}{\sqrt{GM}}(R + x_{sync})^{3/2} = \frac{2\pi}{\omega} \tag{3.13}$$

and using the definition of ω_{crit} (Eq. (3.4)), to obtain:

$$\bar{x}_{sync} = \frac{x_{sync}}{R} = \bar{\omega}^{-2/3} - 1. \tag{3.14}$$

The non-dimensional synchronous orbit altitude x_{sync} is indicated with a dotted line in Fig. 3.2 for each ω considered. For a given ω the maximum tension becomes larger as the number of PMs is increased while, for a given n, smaller tensions are found as ω approaches the critical angular velocity.

For any $q > 0$ the function Ψ has the following property:

$$\lim_{\zeta \to +\infty} \zeta \Psi(q\zeta) = \frac{1}{q}. \tag{3.15}$$

Equation (3.15) can then be used to rearrange Eq. (3.6) when the chain length L is fixed and the number of PMs becomes large. In this case $n \to \infty$ with $l \to 0$ and, from Eq. (3.8), it can be shown that

$$n\bar{l} \approx \bar{L} \tag{3.16}$$

Upon simplification, Eq. (3.6) becomes

$$\bar{f}^* = -\frac{n\bar{R}^2}{\bar{R}+\bar{L}} + \bar{\omega}^2 n \left(\bar{R} + \frac{\bar{L}}{2}\right). \tag{3.17}$$

Then, it follows from Eq. (3.17) that the normalized chain length L_{eq} that guarantees equilibrium of the chain ($f^* = 0$) depends only on $\bar{\omega}$ and $\bar{R}$. Solving Eq. (3.17) for $f^* = 0$ with respect to $\bar{L}$ and considering the positive solution yields:

$$\bar{L}_{\text{eq}} = \frac{1}{2}\bar{R}\left(\sqrt{\frac{8}{\bar{\omega}^2} + 1} - 3\right). \tag{3.18}$$

If Eq. (3.18) is specialized in the case of the Earth ($\bar{\omega} \approx 0.058$) with $\bar{R} = 1$ then the equilibrium length is the same as the limit found by Pearson for a continuous hanging tower, i.e., 144 201.96 km [102]. Clearly, L_{eq} decreases as the angular velocity of the asteroid approaches the critical angular velocity (eventually it vanishes for $\bar{\omega} = 1$), while it tends to infinity as $\bar{\omega}$ tends to zero.

Figure 3.3 shows the relative error between Eq. (3.17) and Eq. (3.6) to evaluate the chain length $\bar{L}$ at equilibrium, as a function of n and a range of $\bar{\omega}$, for $\bar{R} = 1$. The solution to $\bar{f} = 0$ clearly approaches $\bar{L}_{eq}$ as n becomes larger. The relative error is below 3% for $\bar{\omega} > 0.5$ and $n \geq 50$: under such conditions Eq. (3.18) can be regarded as a good approximation to the solution of $f = 0$. Moreover, the equilibrium length calculated with Eq. (3.6) is always larger than L_{eq}, i.e., for a given $\bar{\omega}$, the equilibrium length of a chain with finite n is always larger than the equilibrium length of a chain with $n \to \infty$. Therefore, if $f^* = 0$ for a given $\bar{\omega}$ and L, then $f > 0$ for any n. However, it should be noted that other parameters not taken into account here, such as friction between payloads, may change the plot in Fig. 3.3.

If $f > 0$ (or $f^* > 0$ for large n) then an orbital siphon effect can be envisaged, where a new payload is attached to the chain and simultaneously the top one is removed. To assess this scenario, conservation principles are applied to model the dynamics. In particular, conservation of angular momentum (Sec. 3.2.3) allows the variation of the angular velocity of the asteroid and chain to be investigated as a consequence of mass extraction, while conservation of linear

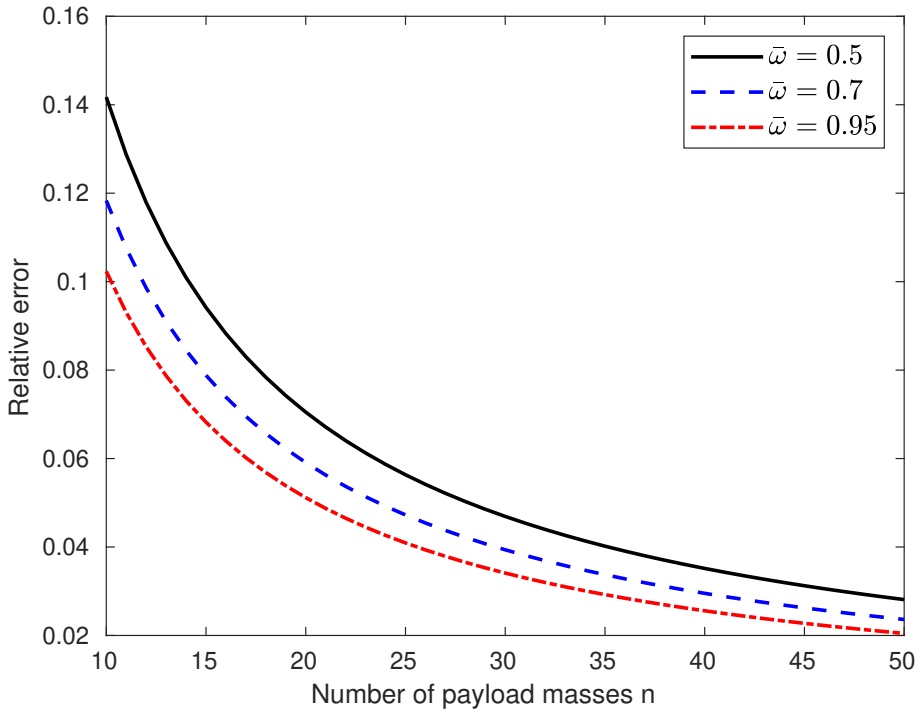

FIGURE 3.3: Relative error when using Eq. (3.17) in place of Eq. (3.6) to find the equilibrium length of the chain.

momentum together with the kinetic energy theorem (Sec. 3.2.4) allows the evolution of the chain velocity to be investigated. Conservation of mass is applied to model the mass decrease of the asteroid. Note that the actual mining techniques used to extract mass from the asteroid are beyond the scope of this thesis.

3.2.2 Siphon modelled as continuous mass distribution

For analysis to be performed later in this chapter and in the thesis it is useful to redefine the force equation (3.6) when the siphon is approximated with a continuous mass distribution with linear density μ. Given a chain with n PMs with mass δM, a continuum approximation can be found by setting $\mu = n\delta M/L$. In this case, the sums appearing in Eq. (3.5) are substituted with the integral:

$$f_{\text{cont}} = \int_0^L \left[\omega^2(R+x) - \frac{GM}{(R+x)^2}\right] \mu dx \tag{3.19}$$

Solving the integral (3.19) and converting to non-dimensional variables using the scale factors listed in Table 3.1 yields:

$$\bar{f}_{\text{cont}} = \bar{L}\bar{\mu}\left[-\frac{\bar{R}^2}{\bar{R}+\bar{L}} + \bar{\omega}^2\left(\bar{R}+\frac{\bar{L}}{2}\right)\right] \tag{3.20}$$

The non-dimensional siphon linear density $\bar{\mu}$ can be interpreted as the ratio between the mass of a siphon with length $L = R_0$ (i.e., a siphon with length equal to the initial asteroid radius) and

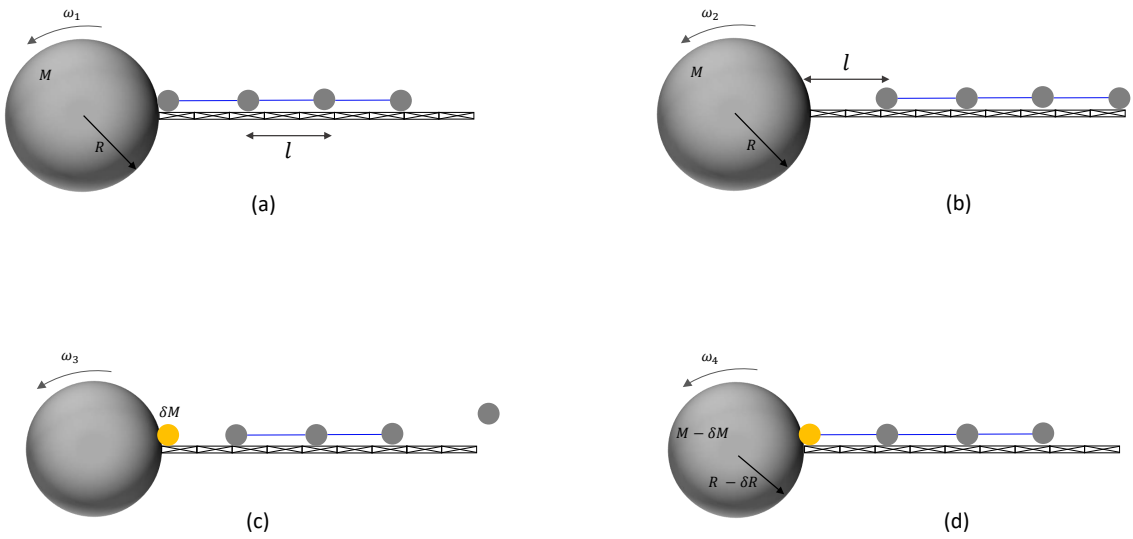

FIGURE 3.4: Four-step sequence to model the extraction of a payload mass. In this case a chain with $n = 4$ is represented.

the mass of the asteroid M_0. As expected the siphon length satisfying $f_{\text{cont}} = 0$ is exactly the equilibrium length L_{eq} given by Eq. (3.18), calculated for a discrete mass distribution with $n \to \infty$. However, note that a siphon modelled as a continuous mass distribution is not conceptually the same as a discrete siphon with $n \to \infty$: in fact, in the former case the mass of the siphon is finite, in the latter case it diverges to infinity if the PM is fixed.

The siphon linear density μ is also related to the cross section A of the siphon, with larger μ being associated to larger cross sections. In particular, the total mass of the siphon μL can be expressed as a function of the siphon cross section as:

$$\mu L = AL \tag{3.21}$$

thus:

$$A = \frac{\mu}{\rho} \tag{3.22}$$

Then, $\sqrt{A}$ provides the width and depth of the siphon, modelled as a continuous mass distribution, assuming a square cross section.

3.2.3 Conservation of angular momentum

The extraction of a PM from the asteroid and the subsequent release of the top PM from the chain is modelled through a four-step sequence (see Fig. 3.4):

1. Initially the bottom PM is on the surface, $h = 0$ (Fig. 3.4a) and, in general, $\dot{h} \geq 0$. If $f > 0$ the chain will lift.

2. The chain has lifted by $h = l$ (Fig. 3.4b).

3. The top PM is released and a new mass δM is positioned at the surface of the asteroid. Consequently, the asteroid mass decreases by δM to guarantee conservation of mass (Fig. 3.4c).

4. The bottom PM is connected to the chain (Fig. 3.4d) so that the chain is in the same geometrical configuration as step 1, with $h = 0$.

This sequence is then repeated, with the chain constantly operating with $h \in [0, l]$. A set of steps from 1 to 4 defines an iteration. Let R_j, M_j, $I_{A,j}$ and ω_j be the radius, mass, inertia and angular velocity of the asteroid at the j-th step ($j = 1, \ldots, 4$) of the k-th iteration (to avoid confusion in notation, the reference to the k-th iteration is omitted at this stage). Similarly, $I_{C,j}$, h_j and $\dot{h}_j$ are the inertia and position and velocity of the chain. It follows that:

$$I_{A,j} = \frac{2}{5} M_i R_i^2, \qquad j = 1,2,3,4 \tag{3.23a}$$

$$I_{C,j} = \delta M \sum_{i=1}^{a_j} (R_j + h_i + (i-1)l)^2, \qquad j = 1,2,3,4 \tag{3.23b}$$

where

$$a_1 = n, \quad a_2 = n, \quad a_3 = n-1, \quad a_4 = n \tag{3.24}$$

and

$$h_1 = 0, \quad h_2 = l, \quad h_3 = l, \quad h_4 = 0. \tag{3.25}$$

The mass of the asteroid changes at step 3. As conservation of mass holds, it is assumed that the sphere loses its outer shell of mass δM and thickness δR to form the new PM which is then positioned on the equator of the asteroid (although, in practice, the change in shape of the asteroid due to mass extraction would depend on the process used to gather mass at the base of the siphon). Hence:

$$\begin{aligned} &M_1 = M, \quad M_2 = M, \quad M_3 = M - \delta M, \quad M_4 = M - \delta M, \\ &R_1 = R, \quad R_2 = R, \quad R_3 = R - \delta R, \quad R_4 = R - \delta R. \end{aligned} \tag{3.26}$$

Note that $M = 4/3\pi R^3 \rho$ and, by differentiation, $\delta M = 4\pi R^2 \rho \, \delta R$. Therefore:

$$\frac{\delta R}{R} = \frac{1}{3} \frac{\delta M}{M}. \tag{3.27}$$

As no external torques are acting on the asteroid and chain, conservation of angular momen-

tum holds at each step. Therefore:

$$(I_{A,j}+I_{C,j})\bar{\omega}_j = (I_{A,j+1}+I_{C,j+1})\bar{\omega}_{j+1}, \qquad j=1,2,3. \tag{3.28}$$

Substituting Eqs. (3.23) and (3.27) into Eq. (3.28) and simplifying yields:

$$\frac{\delta\bar{\omega}_{12}}{\bar{\omega}_1} = 5\left(n\bar{l}+\frac{1}{2}(n\bar{l})^2\right)\frac{\delta M}{M} + \text{h.o.t.} \tag{3.29a}$$

$$\frac{\delta\bar{\omega}_{23}}{\bar{\omega}_2} = \frac{5}{6}\frac{\delta M}{M} + \text{h.o.t.} \tag{3.29b}$$

$$\frac{\delta\bar{\omega}_{34}}{\bar{\omega}_3} = 0 \tag{3.29c}$$

where $\delta\bar{\omega}_{12} = \bar{\omega}_2 - \bar{\omega}_1$, $\delta\bar{\omega}_{23} = \bar{\omega}_3 - \bar{\omega}_2$, $\delta\bar{\omega}_{34} = \bar{\omega}_4 - \bar{\omega}_3$ and the higher order terms (h.o.t.) are neglected. Therefore:

$$\frac{\delta\bar{\omega}_{23}}{\bar{\omega}_2} = \frac{\delta\bar{\omega}_{23}}{\bar{\omega}_1 - \delta\bar{\omega}_{12}} = \frac{\delta\bar{\omega}_{23}}{\bar{\omega}_1}\left(1+\frac{\delta\bar{\omega}_{12}}{\bar{\omega}_1}\right) + \text{h.o.t.} = \frac{\delta\bar{\omega}_{23}}{\bar{\omega}_1} + \text{h.o.t..} \tag{3.30}$$

Equivalently, it can be shown that

$$\frac{\delta\bar{\omega}_{34}}{\bar{\omega}_3} = \frac{\delta\bar{\omega}_{34}}{\bar{\omega}_1} + \text{h.o.t.} \tag{3.31}$$

Hence, by neglecting again the higher order terms, Eqs. (3.29) can be summed to find the overall angular velocity variation $\delta\bar{\omega} = \delta\bar{\omega}_{12} + \delta\bar{\omega}_{23} + \delta\bar{\omega}_{34}$ between step 1 and 4. Using the approximation for large n given by Eq. (3.16) finally yields:

$$\frac{\delta\bar{\omega}}{\bar{\omega}} = 5\left(\frac{1}{6}+\bar{L}+\frac{1}{2}\bar{L}^2\right)\frac{\delta M}{M}, \tag{3.32}$$

where the subscript 1 has been removed from $\bar{\omega}$ for clarity. Equation (3.32) dictates that the overall variation of angular velocity from step 1 to 4 is proportional to the ratio $\delta M/M$ through a coefficient depending only on the siphon length $\bar{L}$.

3.2.4 Chain radial velocity

The radial velocity of the chain is described by the variable $\dot{h}$. If $f > 0$ (Eq. (3.6)) the chain will rise between step 1 and 2. The work per unit mass $W(h)$ done by the force f to raise the chain from 0 to $h \in [0,l]$ can be written as:

$$W(h) = \int_0^h \frac{f}{n\delta M}dh \tag{3.33}$$

where the denominator is the total mass of the siphon. From the work-energy theorem:

$$W(h) = \frac{\dot{h}^2}{2} - \frac{\dot{h}_1^2}{2}. \tag{3.34}$$

where $\dot{h}_1$ is the velocity of the chain at step 1 of the sequence described in Sec. 3.2.3, i.e., for $\dot{h} = 0$. Hence, the velocity of the chain as a function of the position h can be written as

$$\dot{h} = \sqrt{\dot{h}_1^2 + 2W(h)}. \tag{3.35}$$

In particular, at step 2, $h = h_2 = l$. In this case $W(l)$ can be evaluated analytically:

$$W(l) = \frac{l}{2}\left[\omega^2(ln + 2R) - 2\frac{GM}{(ln+R)R}\right]. \tag{3.36}$$

Then, equation (3.35) simply becomes:

$$\dot{h}_2 = \sqrt{\dot{h}_1^2 + 2W(l)}. \tag{3.37}$$

At step 3 the top PM is released from the chain. In the inertial frame there are no external forces acting on the asteroid and chain (assumption 6), hence conservation of linear momentum holds. Conserving linear momentum between step 2 and 3 yields (see Appendix E [2])

$$\dot{h}_3 = \dot{h}_2. \tag{3.38}$$

Therefore the release of the top mass does not alter the radial velocity of the chain.

At step 4 the bottom PM, which is initially at rest, is connected to the asteroid. Again, applying conservation of linear momentum between steps 3 and 4 yields:

$$\dot{h}_4 = \frac{n-1}{n}\dot{h}_3. \tag{3.39}$$

The sequence is then repeated from step one, with a new $\dot{h}_1$ equal to the last PM velocity $\dot{h}_4$.

Now, let $\dot{h}_3^k$ be the value of the radial release velocity $\dot{h_3}$ at the k-th iteration. Then, it follows from Eqs. (3.37), (3.38) and (3.39) that

$$\dot{h}_3^k = \sqrt{\left(\frac{n-1}{n}\right)^2 \left(\dot{h_3}^{k-1}\right)^2 + 2W(l)} \tag{3.40}$$

It can be shown that the recursive sequence $\left\{\dot{h_3}^k\right\}$ is bound and monotonic and hence converges.

[2] Note that the derivation presented in Appendix E is for a bucket conveyor chain with ascending and descending line, as the one modelled in Chapter 4. However, as shown, the final result also holds for the simplified model used in this chapter.

Let v_l be the limit of the sequence. Its value can be found noting that $v_l = \lim_{k\to\infty} \dot{h}_3^k = \lim_{k\to\infty} \dot{h}_3^{k-1}$. Then $v_l = \sqrt{\left(\frac{n-1}{n}\right)^2 v_l^2 + 2W(l)}$, hence

$$v_l = \sqrt{\frac{2W(l)}{1-\left(\frac{n-1}{n}\right)^2}} \tag{3.41}$$

which represents the normalized radial release velocity of the chain at steady state. The velocity v_l depends on the length of the chain and the normalized angular velocity of the asteroid. Clearly, ω will change during the transient due to mass extraction (Eq. (3.32)) but, as the steady state is approached within a few iterations, this variation can reasonably be neglected. Equation (3.41) can be rewritten in non-dimensional form as:

$$\bar{v}_l = \sqrt{\frac{\bar{L}n(\bar{L}+\bar{R})(\bar{L}+2\bar{R})\bar{\omega}^2 - 2\bar{R}^2}{(\bar{L}+\bar{R})(2n-1)}} \tag{3.42}$$

Note that the value of v_l is finite. Hence, even though the chain is subjected to a non-zero force, its velocity does not diverge. In fact, although the chain does accelerate between step 1 and 2, its velocity then decreases at step 4, as a new PM is attached to the chain, in order to conserve linear momentum. As the tethers are assumed to be rigid, the change in velocity is instantaneous.

Note that $v_l > 0$ for $W(l) > 0$. By analysis of Eq. (3.36) it is straightforward to show that $W(l) > 0$ if $L > L_{\text{eq}}$. It has been noted in Sec. 3.2 that if $f = 0$ then $L > L_{\text{eq}}$. Therefore, even if the force on the chain is initially zero at the first iteration, any arbitrary small perturbation such that $\dot{h}_1 > 0$ will initialise the lifting process, and the release velocity at steady state will be positive as dictated by Eq. (3.41).

It is interesting to evaluate Eq. (3.41) when the number of masses on the chain becomes large. This can be done calculating the limit of Eq. (3.41) for $n \to \infty$. In non-dimensional form:

$$\bar{v}_l^* = \lim_{n\to\infty} \bar{v}_l = \sqrt{-\frac{\bar{L}\bar{R}^2}{\bar{R}+\bar{L}} + \frac{1}{2}\bar{L}(\bar{L}+2\bar{R})\bar{\omega}^2}. \tag{3.43}$$

When using Eq. (3.43) as an approximation of Eq. (3.42) for the radial velocity of a PM at release, the relative error depends on n:

$$\left|\frac{v_l - v_l^*}{v_l}\right| = 1 - \sqrt{1 - \frac{1}{2n}}. \tag{3.44}$$

This error is lower than 1% for $n > 25$. Therefore, for large n Eq. (3.43) is an accurate approximation of the radial release velocity (3.41).

3.2.5 Radial velocity of a siphon modelled as continuous mass distribution

In this section the equivalent form of the the radial velocity equation in the continuous domain is found and the results are compared with Eqs. (3.42), (3.43) for the discrete domain. The procedure is similar to that described in the previous section. In particular, let $dv_{12} = v_2 - v_1$, $dv_{23} = v_3 - v_2$, $dv_{34} = v_4 - v_3$ be the change in siphon velocity from step (1) to (2), (2) to (3) and (3) to (4) respectively, where the steps are the same as those described in Sec. 3.2.3. Then, the overall change in velocity dv_{14} from step (1) to (4) will be the sum:

$$dv_{14} = dv_{12} + dv_{23} + dv_{34} \tag{3.45}$$

In the following, the values of dv_{12}, dv_{23} and dv_{34} are found by invoking the work-energy theorem and the conservation of linear momentum.

- From step (1) to step (2). The work per unit mass dW done by the gravitational and centrifugal-induced forces on the siphon to raise it by the amount dh is by definition:

$$dW = \frac{f_{\text{cont}}}{\mu L} dh \tag{3.46}$$

  where the first factor is the external force acting on the siphon calculated in the continuous domain (Eq. (3.19)) divided by the mass of the siphon μL. From the work-energy theorem:

$$dW = \frac{(v_1 + dv_{12})^2}{2} - \frac{v_1^2}{2} \tag{3.47}$$

  By neglecting higher order terms and further simplifying, Eq. (3.47) can be written as:

$$dW = v_1 dv_{12} \tag{3.48}$$

  Then, equating Eq. (3.46) and (3.48) yields:

$$dv_{12} = \frac{f_{\text{cont}}}{\mu L} \frac{dh}{v} \tag{3.49}$$

- From step (2) to step (3). As in the discrete siphon case, the release of the top siphon mass does not change the instantaneous siphon velocity. Therefore:

$$dv_{23} = 0 \tag{3.50}$$

  Hence, $v_3 = v_2 = v_1 + dv_{12}$.

- From step (3) to step (4). As in the discrete siphon case, the connection of the mass dm is modelled as an instantaneous inelastic contact. Applying conservation of linear

momentum between step (3) and (4) yields:

$$\mu(L-dx)v_3 = \mu L v_4 \tag{3.51}$$

Then, substituting $v_3 = v_1 + dv_{12}$, dv_{34} can be written as:

$$dv_{34} = \frac{dh}{L}v_1 \tag{3.52}$$

where the substitution $v_b = v_a + dv_{ab}$ is used and the higher order terms are neglected.

Substituting Eq. (3.49) and (3.52) into (3.45) yields:

$$dv_{14} = \frac{f_{\text{cont}}}{\mu L}\frac{dh}{v_1} - \frac{dh}{L}v_1 \tag{3.53}$$

Dividing both sides by the infinitesimal time dt required to raise the siphon by dh and further simplifying yields

$$\frac{dv}{dt} + \frac{v^2}{L} = \frac{f_{\text{cont}}}{\mu L} \tag{3.54}$$

where the subscripts have been removed. Equation (3.54) is the differential equation governing the radial velocity of a siphon modelled as a continuous mass distribution. Note the damping term proportional to the square of the siphon velocity. As a new mass element dm is added to the chain it must be accelerated to speed v. However, the rate at which new masses are being added scales as v, hence it can be shown that there is an apparent drag term which is quadratic in v.

Taking a siphon starting from $v(0) = 0$, and assuming a quasi-static variation of f_{cont} (this hypothesis will be justified later), Eq. (3.54) admits the close-form solution:

$$v(t) = \sqrt{\frac{f_{\text{cont}}}{\mu}}\tanh\left(\sqrt{\frac{f_{\text{cont}}}{\mu}}\frac{t}{L}\right) \tag{3.55}$$

Using the non-dimensional scale factors in Table 3.1, Equation (3.55) can be written in non-dimensional form as:

$$\bar{v} = \sqrt{\frac{\bar{f}_{\text{cont}}}{\bar{\mu}}}\tanh\left(\frac{\bar{t}}{\bar{L}/\sqrt{\bar{f}_{\text{cont}}/\bar{\mu}}}\right) \tag{3.56}$$

Substituting Eq.(3.20) into Eq. (3.56) then yields:

$$\bar{v} = \sqrt{\frac{1}{2}\bar{L}(\bar{L}+2\bar{R})\bar{\omega}^2 - \frac{\bar{L}\bar{R}^2}{\bar{L}+\bar{R}}}\tanh\left(\bar{t}\sqrt{\frac{1}{2\bar{L}}(\bar{L}+2\bar{R})\bar{\omega}^2 - \frac{\bar{R}^2}{(\bar{L}+\bar{R})\bar{L}}}\right) \tag{3.57}$$

Therefore, the siphon asymptomatically approaches the steady state radial velocity $\sqrt{f_{\text{cont}}/\bar{\mu}}$. This was also clear from Eq. (3.54), setting $dv/dt = 0$. Note that the asymptotic value $\bar{f}_{\text{cont}}/\bar{\mu}$

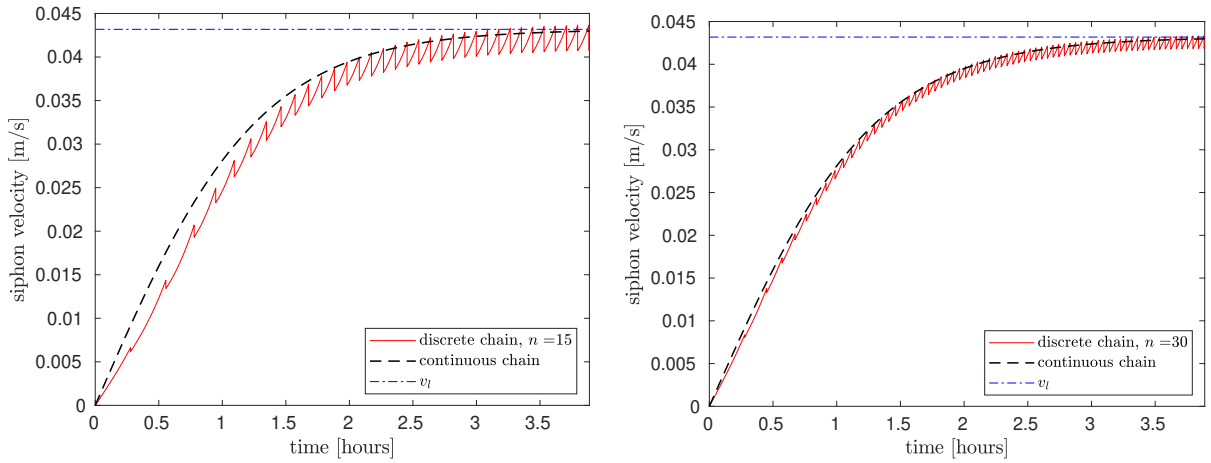

FIGURE 3.5: Siphon radial velocity as a function of time calculated using the siphon discrete mass distribution model (red, continuous line, Eqs. (3.37), (3.38), (3.39)), the continuous mass distribution model (black dotted line Eq. (3.57)), and the discrete model with $n \to \infty$ (blue dash-dotted line, Eq. (3.43)).

exactly matches the value given by Eq. (3.43), for the limit of a discrete chain when $n \to \infty$. The transient behavior depends on the factor $\bar{L}/\sqrt{\bar{F}/\bar{\mu}}$ which represents the time required to reach 0.76% of the steady state velocity. For example, taking an asteroid with $\bar{\omega} = 0.85$, $\bar{R} = 1$, $\bar{L} = 1$, the siphon reaches 76% of its asymptotic velocity after $\bar{t} = 1.3$ and 99% of its asymptotic velocity after $\bar{t} = 2.64$ corresponding to $t = 0.5$ h and $t = 1.3$ h respectively, for an asteroid with density $\rho = 2\,\mathrm{g\,cm^{-3}}$. If the transient phase is neglected, the siphon radial velocity can be therefore approximated by:

$$\bar{v} \approx \sqrt{\frac{\bar{f}_{\mathrm{cont}}}{\bar{\mu}}} \tag{3.58}$$

Note that the ratio $\bar{f}_{\mathrm{cont}}/\bar{\mu}$ does not depend on the siphon linear density (see Eq. (3.20)).

Figure 3.5 compares the radial velocity of the siphon modelled as a continuous mass distribution (Eq. (3.55)) with the discrete siphon model, for $n = 15$ (a) and $n = 30$ (b). In both cases the siphon is considered initially at rest and results are displayed in dimensional units, considering the physical parameters of the asteroid Bennu (Table 2.1) and a 200-metre siphon, at the beginning of siphon operation ($\bar{R} = 1$). Also displayed in blue is the asymptotic solution of the discrete chain model for $n \to \infty$ (Eq. (3.43)). It is apparent that the continuous solution provides a good approximation of the discrete chain behaviour, especially for larger n (Fig. 3.5b)

Figure 3.6 compares the velocities given by Eqs. (3.54), (3.57) and (3.58) for a continuous mass distribution when the variation of f_{cont} due to material extraction is taken into account. Again, a 200-metre long siphon anchored at Bennu is considered. As expected, Eq. (3.57) accurately matches the numerical solution to the differential equation (3.54), confirming the validity of the hypothesis on quasi-static variation of f_{cont}. Analogous results are obtained by

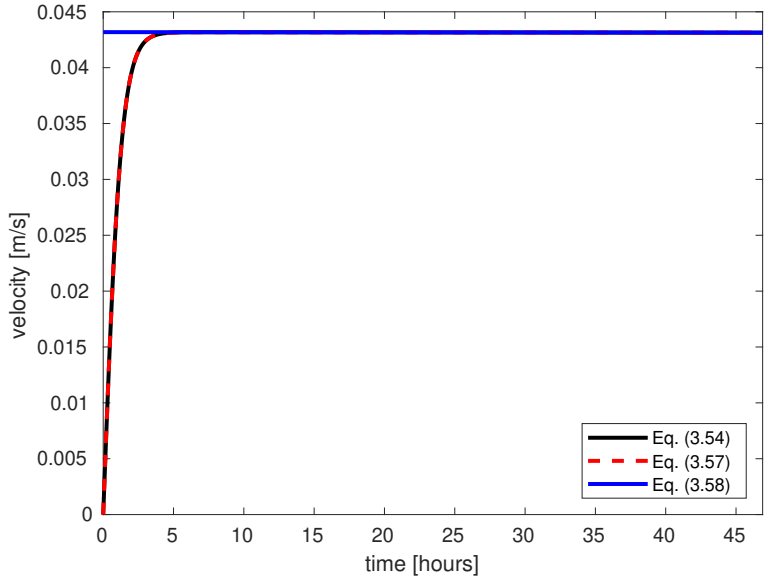

FIGURE 3.6: Comparison between Eqs. (3.54), (3.57) and (3.58) for a siphon modelled as a continuous mass distribution when the variation of f_{cont} due to material extraction is taken into account.

changing the siphon length and the asteroid angular velocity. Moreover, the siphon reaches its steady state condition in a timeframe of a few hours and the value of the velocity given by the three equations coincides at steady state. As it will be shown, typical timescales for long-term mass extraction are on the order of years. This confirms that, for long-term mass extraction, Eq. (3.58) can be regarded as a good approximation to the differential equation (3.54).

3.2.6 Energy

The kinetic and potential energy of the asteroid and chain at each step are given by:

$$K_j = \frac{1}{2}\left(I_{A,j} + I_{C,j}\right)\omega_j^2 + \frac{1}{2}a_j \delta M v_j^2 \quad j = 1,\ldots,4 \tag{3.59a}$$

$$P_j = -\frac{3}{5}G\frac{M_j^2}{R_j} - \sum_{i=1}^{a_j} G\frac{M\delta M}{R_i + x_i} \quad j = 1,\ldots,4 \tag{3.59b}$$

where the summation indexes a_j are the same as in Eqs. (3.24). The first term in K_j is due to the rotational kinetic energy of the asteroid and chain, while the second term is due to the velocity of the chain in the radial direction. The first term of the potential P_j represents the self gravitational potential of the asteroid, while the second term is the gravitational potential of the chain (note that, as the PMs are considered point-like masses, their self potential is neglected).

By substituting Eqs.(3.23), (3.24), (3.26), (3.28) and (3.37) into Eqs. (3.59) it can be verified that $K_1 + P_1 = K_2 + P_2$, i.e., mechanical energy between steps 1 and 2 is conserved at every

iteration. Conversely, it can be shown that

$$(K_3 - K_2) + (P_3 - P_2) = E_A + E_{\delta M} \tag{3.60}$$

where

$$E_A = -\frac{1}{6}\delta M R^2 \omega_1^2, \tag{3.61}$$

$$E_{\delta M} = -\frac{1}{2}\delta M \left(\omega_3^2 (R+L)^2 + \dot{h}_3^2\right) + G\frac{M\delta M}{R+L}. \tag{3.62}$$

E_A is the change in kinetic energy due to material rearrangement in the asteroid as each PM is formed (step 3 in Fig. 3.4): material in the vicinity of the rotation axis (with low moment of inertia) is moved towards the equator (by means of ideal conservative forces), thus decreasing the kinetic energy of the system while conserving the total angular momentum. Conversely, $E_{\delta M}$ is the mechanical energy of the top mass of the chain when released, which is then lost from the system asteroid and chain. The energy per unit mass $\mathscr{E} = E_{\delta M}/\delta M$ of the released material can be then be written as (see Table 3.1 for non-dimensional scale factors):

$$\bar{\mathscr{E}} = \frac{1}{2}\bar{\omega}^2 \left[(\bar{R}+\bar{L})^2 + \dot{\bar{h}}_3^2\right] - \frac{\bar{R}^3}{\bar{R}+\bar{L}}. \tag{3.63}$$

In the case of a siphon operating at steady state, with the assumption of $n \to \infty$, $\dot{\bar{h}}_3$ can be replaced by v_l^* (Eq. (3.43)). Upon using this substitution, Eq. (3.63) takes the form

$$\bar{\mathscr{E}} = -\frac{\bar{R}^3}{\bar{R}+\bar{L}} + \frac{1}{2}\bar{\omega}^2 \left(-\frac{\bar{L}\bar{R}}{\bar{L}+\bar{R}} + (\bar{R}+\bar{L}) + \frac{1}{2}\bar{L}(\bar{L}+2\bar{R})\bar{\omega}^2\right) \tag{3.64}$$

The sign of $\bar{\mathscr{E}}$ gives immediate information about the motion of the PMs upon release: if $\bar{\mathscr{E}} < 0$ the motion is bound, whereas for $\bar{\mathscr{E}} \geq 0$ material is ejected to escape. Note that, if $\bar{\mathscr{E}} \geq 0$, the normalized energy is linked to the hyperbolic escape speed $\bar{v}_\infty$ of the released PMs through

$$\frac{\bar{v}_\infty}{\bar{v}_{\text{esc}}} = \sqrt{\bar{\mathscr{E}}} \tag{3.65}$$

where $\bar{v}_{\text{esc}}$ is the escape velocity at the surface of the asteroid.

Eventually, by substituting Eqs.(3.23), (3.26), (3.28) and (3.39) into Eqs. (3.59) it can be shown that mechanical energy is conserved between steps 3 and 4.

3.2.7 Timescale for mass extraction

In this section, the time required to extract a given amount of mass from the asteroid is calculated using the continuous mass distribution approach. Let dm be the infinitesimal mass released from the top of the siphon in the time dt. Then, dm is related to dt via the siphon velocity and linear

density:

$$dm = \mu v dt \tag{3.66}$$

To guarantee conservation of mass, if an element dm is released from the siphon, the asteroid mass must decrease by the same amount. The infinitesimal mass of the outer shell of the asteroid is:

$$dm = 4\rho\pi R^2 dR \tag{3.67}$$

Equating Eqs. (3.67) and (3.66) and solving for dt yields:

$$dt = \frac{4\rho\pi R^2 dR}{\mu v} \tag{3.68}$$

Dividing both sides by the timescale factor $\omega_{\text{crit}}^{-1}$ and noting that $d\bar{m} = \bar{R}^2 d\bar{R}$ yields:

$$d\bar{t} = \frac{d\bar{m}}{\bar{\mu}\bar{v}} \tag{3.69}$$

The differential equation (3.69) describes the time required to extract the mass $d\bar{m}$ from the asteroid. Equation (3.69) can be integrated to find the total time $\bar{t}$ required to release to escape the mass $\bar{m}_f$:

$$\bar{t} = \int_0^{\bar{m}_f} \frac{d\bar{m}}{\bar{\mu}\bar{v}} \tag{3.70}$$

If the siphon linear density is constant during siphon operation (in the discrete siphon scenario, this is equivalent to a constant payload mass) the term $\bar{\mu}$ can be taken out from the integral. Neglecting the siphon radial velocity transient phase, $\bar{v} = \sqrt{\bar{f}_{\text{cont}}/\bar{\mu}}$ (Eq. (3.56)). Then, using conservation of angular momentum, the integrand of Eq. (3.70) can be written as a function of $\bar{m}$, the initial angular velocity of the asteroid $\bar{\omega}_0$ and the siphon length $\bar{L}$. The resulting integral does not admit closed-form solution, therefore numerical integration must be used to evaluate an approximated solution.

The ratio

$$\dot{m}_{\text{avg}} = \frac{m_f}{t} \tag{3.71}$$

represents the average rate at which mass is released from the siphon. This parameter is an indicator of the required feed rate at which mining rovers have to transfer material to the siphon, in order to release the mass m_f in the time t.

3.3 Siphon operation

Two conditions must be satisfied to guarantee proper operation of the orbital siphon: *(a)* there must be an overall centripetal-induced pull on the chain of masses and *(b)* if a PM is inserted into an orbit around the asteroid ($\mathscr{E} < 0$) then it must not impact the asteroid later in its motion.

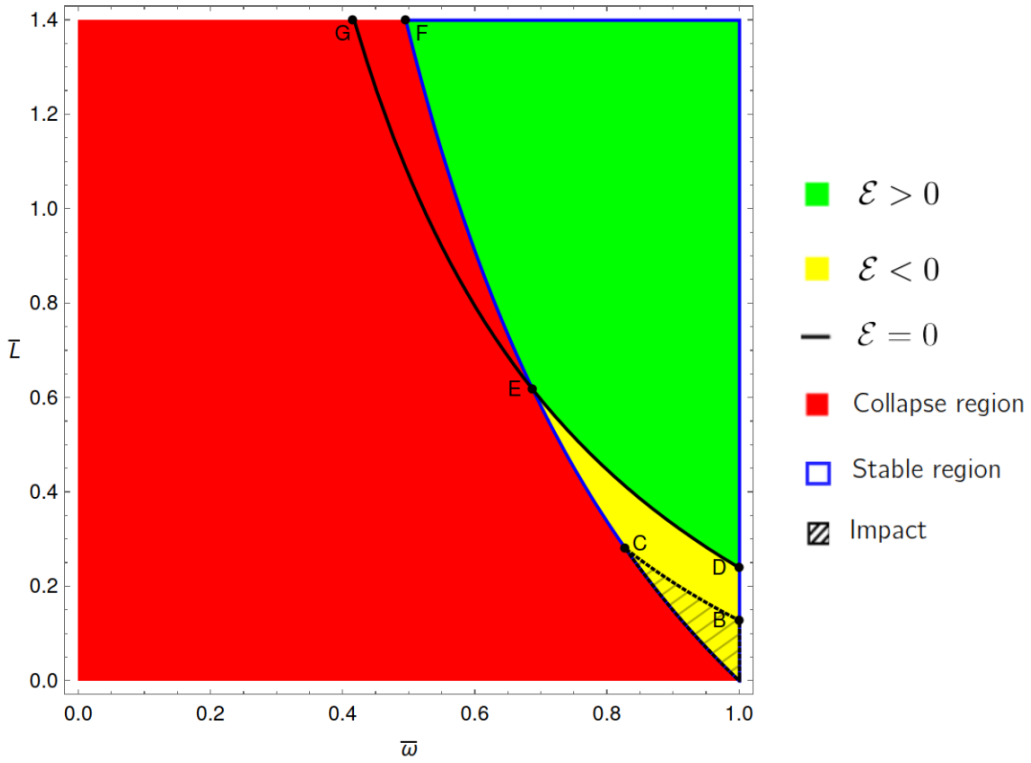

FIGURE 3.7: Regions of allowed and forbidden motion as a function of the asteroid normalized angular velocity $\bar{\omega}$ and the normalized chain length $\bar{L}$.

Assuming that n is large, condition *(a)* is satisfied if

$$f^* > 0, \tag{3.72}$$

where f^* is given by Eq. (3.17). If the first condition *(a)* is satisfied, then material will be inserted either into bound motion around the asteroid or into an escape trajectory, depending on the sign of the normalized energy per unit mass $\bar{\mathscr{E}}$, as given by Eq. (3.64). It can be shown that, when $\bar{\mathscr{E}} < 0$, condition *(b)* is verified if (see Appendix D)

$$\bar{r}_p = -\frac{\bar{R}}{2\bar{\mathscr{E}}}\sqrt{1+2\bar{\mathscr{E}}\bar{\omega}^2(1+\bar{L})^4} > 1, \tag{3.73}$$

where $\bar{r}_p$ represents the periapsis altitude of the the orbit. It is also assumed that, if material is released into orbit, it is collected by an orbiting platform before performing one period of rotation around the asteroid, to avoid a collision with the chain. Then, Eqs. (3.72), (3.73) and (3.64) comprehensively describe the behaviour of the orbital siphon as a function of $\bar{\omega}$, L and $\bar{R}$ (Eq. (3.72) also depends on the number n of PMs but this is irrelevant when only the sign of f^* is considered). These three conditions partition the ω-L plane into regions of allowed and forbidden motion, as represented in Fig. 3.7 for $\bar{R} = 1$, i.e., at the beginning of siphon operation. The plot does not change significantly for smaller values of $\bar{R}$. The range of $\bar{L}$ along the vertical axis has been limited between $\bar{L} = 0$ and $\bar{L} = 1.4$ as relevant information about the behaviour of

the system is contained within this region. However, in principle, there is not any upper bound on this parameter.

Any configuration falling within the red region (*collapse region*) is associated with a collapsing chain, i.e., a chain with length smaller than its equilibrium length. Complementary to the collapse region is the region with the blue boundary (*stable region*) and it is associated with chains longer than their equilibrium length. The separatrix between the two regions is the curve AF (*equilibrium curve*): if $\bar{L} \in$ AF then $\bar{L} = \bar{L}_{\text{eq}}$.

The stable region is then partitioned into two sections. The green region encompasses all configurations releasing PM onto hyperbolic orbits ($\mathscr{E} > 0$). Conversely, material is released into bound motion around the asteroid ($\mathscr{E} < 0$) for a chain within the yellow region. The boundary between these two regions is represented by the curve ED, which is associated with parabolic motion $\mathscr{E} = 0$. Note that this curve partially intersects the collapse region (curve EG): therefore, for $\bar{\omega} < \bar{\omega}_E$ material can be released exclusively into hyperbolic orbits. PMs can be placed into bound motion around the asteroid when the body rotates with $\bar{\omega} \in [\bar{\omega}_E, 1]$ (yellow region). The coordinates of the point E can be found at the intersection of two curves $\mathscr{E} = 0$ and $f^* = 0$:

$$\bar{\omega}_E = \sqrt{2\left(\sqrt{5}-2\right)} \approx 0.687, \tag{3.74}$$

$$\bar{L}_E = \frac{1}{2}\left(\sqrt{9+4\sqrt{5}}-3\right) \approx 0.618. \tag{3.75}$$

A chain working at point E would release material at escape velocity and, at the same time, be in its equilibrium configuration.

The condition for impact avoidance (Eq. (3.73)) further restricts the domain of allowed configurations. Any configuration within the impact region (represented with black diagonal lines) identifies a siphon releasing material into bound motion that will eventually impact the asteroid ($\bar{r}_p < 1$). Therefore, the domain of the bound motion region is actually reduced to the region $CBDE$. Thus, the impact region sets a lower bound for the chain length which cannot be less than $\bar{L}_B$ (see Table 3.2 for a summary of the relevant coordinates of Fig. 3.7).

It can be shown that the region $CBDE$ represents approximately 28% of the bound motion region. Therefore, almost one third of the possible configurations allowed for bound motion must be excluded due to the constraint of impact avoidance. Note that the semi-major axis of the orbit of the released material will increase while the asteroid loses mass [49]. Hence, material released in the $CBDE$ region will remain bound without impacting the asteroid.

Given the above constraints, two possible strategies can be envisaged for siphon operation within the allowed region, i.e., a constant-length chain or a variable-length chain. In both cases, the total amount of extractable mass as a function of the initial angular velocity ω_0 can be found by rearranging Eq. (3.32) as

$$\frac{1}{5\left(\frac{1}{6}+\bar{L}+\frac{1}{2}\bar{L}^2\right)}\frac{\delta\omega}{\omega} = \frac{\delta M}{M} \tag{3.76}$$

and integrating from ω_0 to $\omega < \omega_0$ and from M_0 to M, which yields

$$\xi_m = \frac{M_0 - M}{M_0} = 1 - e^{\mathscr{I}} \tag{3.77}$$

with

$$\mathscr{I} = \int_{\bar{\omega}_0}^{\bar{\omega}} \frac{1}{5\omega' \left(\frac{1}{6} + \bar{L} + \frac{1}{2}\bar{L}^2\right)} d\omega' \tag{3.78}$$

The parameter ξ_m is defined as the *extracted mass ratio*. Ideally, a complete disassembly of the asteroid corresponds to $\xi_m = 1$ and, by analysis of Eq. (3.77), this requires $\mathscr{I} \to -\infty$.

It is possible to find an upper bound for ξ_m when the orbital siphon is releasing material with $\bar{\mathscr{E}} \geq 0$, using simple energy balance considerations. In fact, for an asteroid spinning at $\omega = 1$, its rotational kinetic energy $K = \frac{1}{2}\left(\frac{2}{5}MR^2\right)(GM/R) = \frac{1}{5}GM^2/R$ is exactly one third of its gravitational binding energy $P_{\text{binding}} = \frac{3}{5}GM^2/R^3$. Assuming that this kinetic energy is entirely used to remove subsequent layers of the asteroid to escape, material can be extracted from the asteroid until the radius $R_{\min} < R$ is reached, such that:

$$\int_{R_{\min}}^{R} -G\frac{M\delta M}{R} = -\frac{1}{5}G\frac{M^2}{R^3}. \tag{3.79}$$

By solving Eq. (3.79), $R_{\min} = \sqrt[5]{2/3}R$ which corresponds to

$$\xi_m = 1 - (2/3)^{3/5} \approx 21.6\%. \tag{3.80}$$

Although the siphon can work at different energy levels, Eq. (3.80) represents a useful indicator of the maximum theoretical quantity of material which can be released to escape.

In the following sections, the extracted mass ratio is studied for different scenarios: $\bar{L} = const$ (Sec. 3.4), $\bar{\mathscr{E}} = const$ (Sec. 3.5.1) and $\bar{f} = const$ (Sec. 3.5.2). The symbol ξ_m is used to indicate the maximum ξ_m when $\bar{\omega}$ is on the curve *BCF* in Fig. 3.7.

Undoubtedly, a constant-length chain represents the best choice when considering practical implementation (for example, through conveyor systems). However, as shown in the next section, the best performance in terms of extracted mass is obtained for siphons with variable-length chains (within the simplifying assumptions underpinning this model). Then, the optimal choice will be a trade-off between maximizing the extracted mass or increasing the complexity of the system.

3.4 Constant-length siphon

If the non-dimensional chain length $\bar{L}$ is constant during the extraction sequence (*iso-length* extraction), the integral $\mathscr{I}$ from Eq. (3.78) can be trivially solved analytically and the extracted

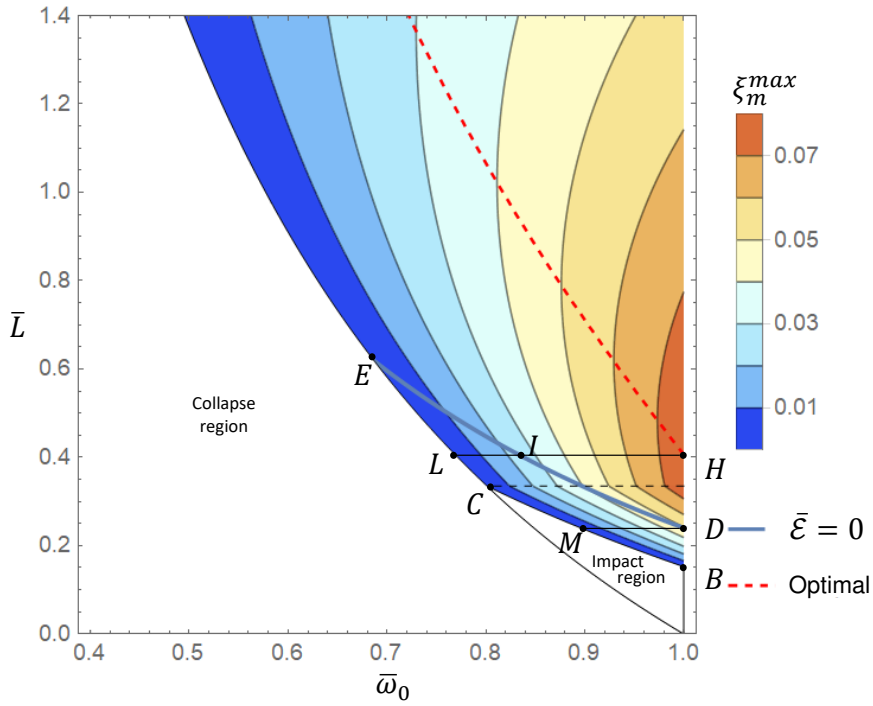

FIGURE 3.8: Contour of the maximum extracted mass ratio $\xi_m^{\max}$ as a function of the initial normalized angular velocity $\bar{\omega}_0$ and the normalized chain length $\bar{L}$ for a constant-length siphon (Eq. (3.82)).

mass ratio becomes

$$\xi_m = 1 - \left(\frac{\omega}{\omega_0}\right)^{1/\gamma} \tag{3.81}$$

with $\gamma = 5(1/6 + \bar{L} + \bar{L}^2/2)$. For a given $\bar{L}$, Eq. (3.81) indicates the amount of extracted mass when the asteroid has decreased its angular velocity from $\bar{\omega}_0$ to $\bar{\omega}$. It has been noted from Fig. 3.7 that the final angular velocity $\bar{\omega}$ cannot be arbitrarily small: when the curve *BCF* is reached the siphon can no longer work (unless the chain length is allowed to increase, but this case is studied in the next section). Solving Eq. (3.81) for $\bar{\omega}$, substituting into Eqs. (3.17) (if $\bar{L} \geq \bar{L}_C$) and (3.73) (if $\bar{L} < \bar{L}_C$) and setting for $f^* = 0$ and $\bar{r}_p = 1$ respectively yields:

$$\begin{cases} \dfrac{(1-\xi_m^{\max})^{2/3}}{(1-\xi_m^{\max})^{1/3} + \bar{L}} + \omega_0^2 (1-\xi_m^{\max})^{2\gamma} \left((1-\xi_m^{\max})^{1/3} + \dfrac{\bar{L}}{2} \right) = 0, & \bar{L} \geq \bar{L}_C \quad (3.82a) \\ 1 + \dfrac{(1-\xi_m^{\max})^{1/3}}{2} \bar{\mathcal{E}}^{-1} \left[1 + 2\bar{\mathcal{E}} \bar{\omega}_0^2 (1-\xi_m^{\max})^{2\gamma} (1+\bar{L})^4 \right]^{1/2} = 0, & \bar{L} < \bar{L}_C \quad (3.82b) \end{cases}$$

Solving Eqs. (3.82) for $\xi_m^{\max}$ returns the maximum mass fraction that can be extracted from an asteroid with initial angular velocity ω_0, using a siphon with constant length $\bar{L}$. Figure 3.8 shows a contour of $\xi_m^{\max}$ as a function of $\bar{\omega}_0$ and $\bar{L}$. The maximum extractable mass ratio is approximately 0.077 and corresponds to $\bar{L} = \bar{L}_H \approx 0.405$ for an asteroid initially spinning at $\bar{\omega}_0 = 1$. Thus, for an asteroid initially spinning at its critical angular velocity, up to 7.7% of its

TABLE 3.2: Coordinates of relevant points in Figs. 3.7 and 3.8.

	A	B	C	D	E	H	I	L	M
$\bar{\omega}$	1	1	0.827	1	0.687	1	0.834	0.768	0.896
$\bar{L}$	0	0.128	0.281	0.240	0.618	0.405	0.405	0.405	0.293

mass can be lifted from the asteroid using the siphon effect In this case, material is released with $\bar{\mathscr{E}} > 0$, until $\bar{\omega} < \bar{\omega}_I$, where material is released into bound motion around the asteroid. The red dashed line indicates the optimal $\bar{L}$ which maximizes ξ_m as a function of $\bar{\omega}_0$. Note that for $\bar{\omega}_0 < 0.82$ the optimal chain length must be larger than the radius of the asteroid.

To perform the entire extraction into bound orbits, $\bar{\omega}_0$ must be within $\bar{\omega}_M$ and 1. In this case, the optimal chain length varies between $\bar{L}_B$ and $\bar{L}_D$ with extracted mass ratios up to 5%.

Note that $\xi_m^{\max} < 0.08$, hence the non-dimensional asteroid radius $\bar{R} > (1-0.08)^3 \approx 0.97$. Therefore, it is reasonable to assume $\bar{R} \approx 1$ in all the equations used in this and previous sections. In particular, Eq. (3.82a) admits the closed-form solution:

$$\xi_m^{\max} = 1 - \left[\frac{1}{\bar{\omega}_0^2} \frac{1}{(1+\bar{L})(1+\bar{L}/2)} \right]^{\frac{1}{2\gamma}} \tag{3.83}$$

which can be used to quickly estimate the extractable mass as a function of the initial asteroid angular velocity $\bar{\omega}_0$ and the siphon length $\bar{L}$.

3.5 Variable-length siphon

In this section the effects of a chain with variable length are investigated. In theory, $\bar{L}$ can be changed following any path with decreasing $\bar{\omega}$ in the allowed region of Fig. 3.7. In particular, in Sec. 3.5.1 $\bar{L}$ is varied by keeping the release energy $\bar{\mathscr{E}}$ constant (*iso-energy*), while in Sec. 3.5.2 by keeping the force f^* constant (*iso-force*) and equal to zero (i.e., the siphon is working along the equilibrium curve).

The choice of these paths is motivated by the following reasons. By analysis of the iso-energy curves it is possible to understand the maximum ξ_m with the minimum energy necessary to escape ($\bar{\mathscr{E}} = 0$) and compare it with other energy regimes. Conversely, the iso-force curve at equilibrium offers insight into the maximum amount of extractable material by keeping the chain length at the minimum allowed. In the latter case, then, the variation of angular velocity at each step of the sequence described in Sec. 3.3 is minimized (Eq. (3.29)).

3.5.1 Iso-energy siphon operation

In this scenario $\bar{L}$ and $\bar{\omega}$ vary according to Eq. (3.64) with $\mathscr{E} = const$. The domain of possible iso-energy curves is restricted between $\bar{\mathscr{E}} \approx -0.219$ and $\bar{\mathscr{E}} = 1$ (Fig. 3.9). When $\bar{\mathscr{E}} > 1$ the

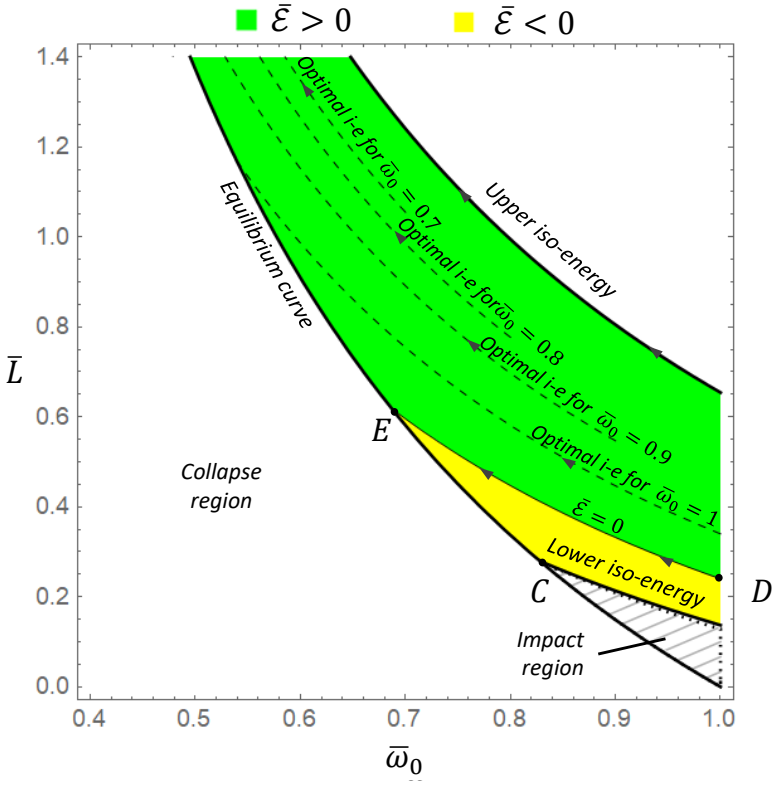

FIGURE 3.9: Domain for the iso-energy curves in the $\bar{\omega}$-$\bar{L}$ plane. The dashed lines represents the optimal iso-energy obtained for four different $\bar{\omega}_0$.

iso-energy curves never cross the equilibrium curve, thus leading to a degenerate case of an infinitely increasing chain (for $\bar{\mathscr{E}} = 1$, the two curves ideally intersect at $\bar{\omega} = 0$, where $\bar{L} \to \infty$). Conversely, when $\bar{\mathscr{E}} < -0.219$ the iso-energy curve would cross the impact region. The lower iso-energy curve passes through the point C (the iso-energy curve through B has lower energy and would therefore cross the impact region).

The extracted mass ratio can be found by solving Eq. (3.64) for $\bar{L}$ and then substituting into Eq. (3.78). Equation (3.78) is then integrated from $\bar{\omega}_0$ to $\bar{\omega} < \bar{\omega}_0$ where the iso-energy curve crosses the equilibrium curve. Figure 3.10a shows a plot of $\xi_m^{\max}$ as a function of $\bar{\mathscr{E}}$ within the energy domain for some values of the initial angular velocity $\bar{\omega}_0$. The maximum $\xi_m^{\max}$ is obtained for $\bar{\omega}_0 = 1$, $\bar{\mathscr{E}} = 0.224$ and is approximately 11%. For any other initial velocity $\bar{\omega}_0 < 1$ the energy of the optimal iso-energy curve is larger and $\xi_m^{\max}$ decreases. For $\bar{\omega}_0 = 0.7$ the maximum extractable mass is less than half the maximum found for $\bar{\omega}_0 = 1$. In any case, optimal iso-energy extraction requires $\bar{\mathscr{E}} > 0$, therefore material is released on a hyperbolic trajectory with a hyperbolic excess speed which is at least half the escape velocity at the surface (Eq. (3.65)) [3]. It is also apparent from Fig. 3.9 that $\bar{\omega}$ decreases significantly from the beginning to the end of the iso-energy curve.

For a given energy, the normalized length of the chain varies between a minimum (when

[3]Note that as material is extracted the escape velocity at the surface varies. However the ratio between the hyperbolic excess velocity of the released PM and the escape velocity remains constant, as dictated by Eq. (3.65)

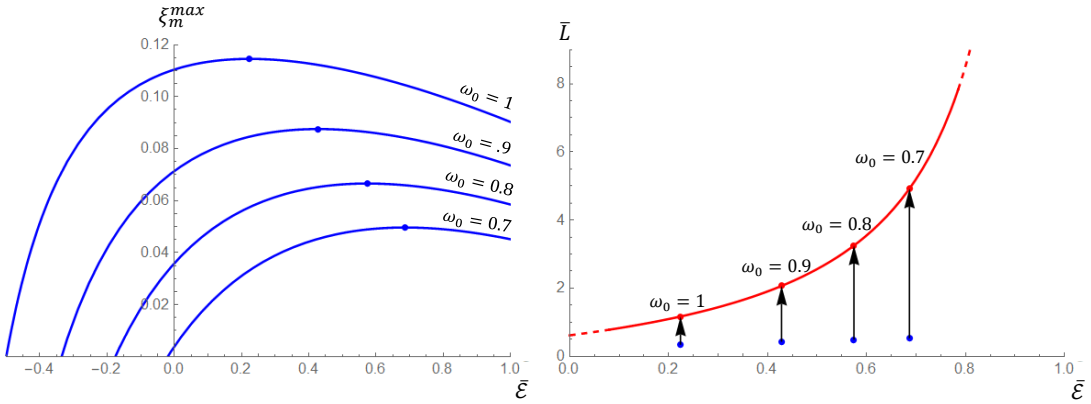

FIGURE 3.10: (a) Extractable mass as function of $\bar{\mathscr{E}}$ for different $\bar{\omega}_0$. (b) Variation of $\bar{L}$ on four optimal iso-energy curves corresponding to different $\bar{\omega}_0$.

$\xi_m = 0$) and a maximum (when $\xi_m = \xi_m^{\max}$), as represented in Fig. 3.10b for different $\bar{\omega}_0$. For $\bar{\omega}_0 = 1$, the final chain length is comparable with the radius of the asteroid, however for lower $\bar{\omega}_0$ the final length becomes much larger (approximately five times the radius of the asteroid for $\bar{\omega}_0 = 0.7$). On the contrary for negative energies, $\bar{L} < 1$.

For a given $\bar{\omega}_0$, the iso-energy with $\bar{\mathscr{E}} = 0$ provides extractable ratios comparable with the optimal case only for $\bar{\omega}_0$ close to 1 (Fig. 3.10a). Eventually, when $\bar{\omega} < \bar{\omega}_E$ extraction in bound orbits is not allowed.

3.5.2 Iso-force siphon operation

In this section the case with $f^* = 0$ is analysed, which is the best-case scenario to maximize the amount of extractable mass. In fact, it is apparent from analysis of Eq. (3.77) that ξ_m is maximum when $\mathscr{I}$ (Eq. (3.78)) is minimum (note that $\mathscr{I} < 0$, since $\bar{\omega} < \bar{\omega}_0$ and the integrand is always positive for any $\bar{L} > 0$). Given $\bar{\omega}_0$ and $\bar{\omega}$, the integral $\mathscr{I}$ is minimized when $\bar{L}$ is minimum, i.e., when $f^* = 0$. In this case, although the siphon is initially in equilibrium for $h = 0$, an infinitesimal perturbation can initialize the siphon effect, since the equilibrium is unstable. Again, it is assumed that $n \to \infty$: in this case $\bar{L}$ varies along the equilibrium curve in Fig. 3.7. Note that, the section AC of the equilibrium curve is also the boundary of the impact region: for a chain operating in such conditions, material would be released into an orbit with periapsis equal to the radius of the asteroid. For this reason, AC is excluded from the domain of this analysis, meaning that $\bar{\omega}_0 \leq \bar{\omega}_C$. However, if $\bar{\omega}_0 \in [\bar{\omega}_C, 1]$, the point C can be approached through the lower iso-energy curve (Fig. 3.9).

The extracted mass ratio in this scenario is evaluated by substituting Eq. (3.18) into Eq. (3.77), where the integral $\mathscr{I}$ is evaluated from $\bar{\omega}_0 \leq \bar{\omega}_C$ to $\bar{\omega} < \bar{\omega}_0$. The maximum ξ_m is evidently found when the initial angular velocity is the maximum allowed in the domain just defined, i.e., $\bar{\omega}_0 = \bar{\omega}_C$.

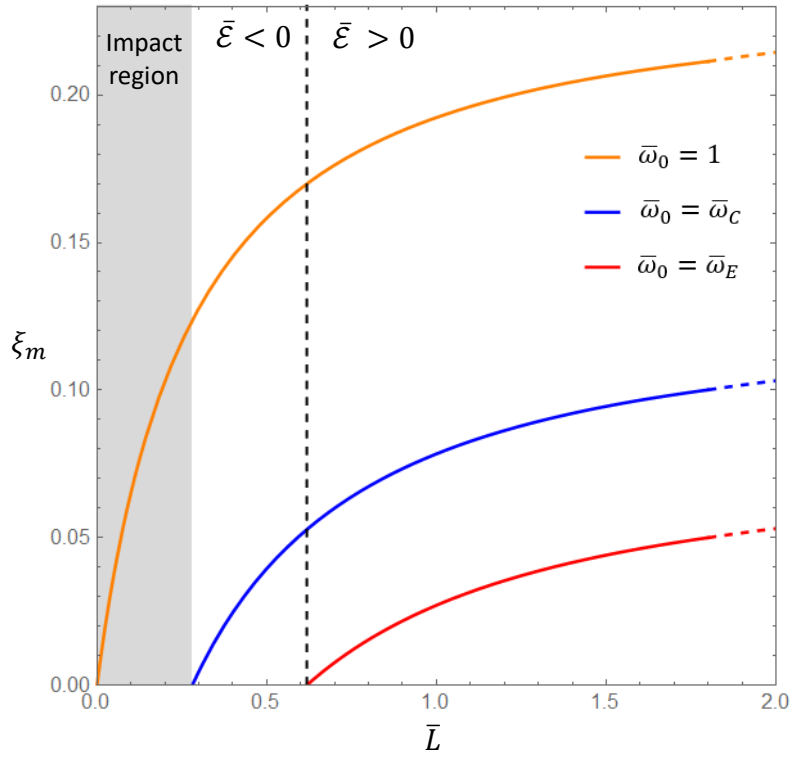

FIGURE 3.11: Extractable mass for three iso-force curves (at $f^* = 0$) as a function of $\bar{L}$. The dashed black line marks the transition between negative and positive release energy $\bar{\mathscr{E}}$.

The blue curve in Fig. 3.11 represents the evolution of $\xi_m^{\max}$ as a function of $\bar{L}$, assuming that $\bar{\omega}_0 = \bar{\omega}_C$ (and, accordingly, $\bar{L} = \bar{L}_C$). The theoretical maximum extractable mass is reached when the chain is infinitely long and is approximately 12% of the asteroid initial mass. However, when the chain has reached twice the radius of the asteroid, the extracted mass ratio has already reached 85% of the theoretical maximum. The process releases PMs into bound orbits between $\bar{L}_C < \bar{L} < \bar{L}_E$ and into a hyperbolic trajectory for $\bar{L} > \bar{L}_E$. It is apparent from Fig. 3.11 that almost half of the extractable material is released into a bound orbit. Clearly, if $\bar{\omega}_0 < \bar{\omega}_C$ then $\bar{L}_0 > \bar{L}_C$ and ξ_m will be lower than 12%. For comparison, the red curve on Fig. 3.11 shows the evolution of ξ_m from $\bar{\omega}_0 = \bar{\omega}_E$.

It is interesting to evaluate $\xi_m^{\max}$ taking into account the section *AC* of the equilibrium curve, as a measure of the maximum disassembly capabilities of the orbital siphon. In this case, a body rotating with $\bar{\omega}_0 = 1$ is considered and the equilibrium curve is followed from point *A* (see orange curve in Fig. 3.11). Then, Eq. (3.77) has an analytical solution for this scenario:

$$\xi_m^{\text{MAX}} = \lim_{\bar{\omega}\to 0^+} \xi_m^{\max} = 1 - \exp\left[\frac{3}{20}\left(\log 48 + \sqrt{6}\log(5-2\sqrt{6})\right)\right] \approx 0.23. \tag{3.84}$$

This value is almost twice the maximum extractable mass found for $\bar{\omega}_0 = \bar{\omega}_C$. It is apparent from Fig. 3.11 that more than half of this material would be extracted inside the impact region, using chains with maximum length up to $\bar{L}_C \approx 0.281$. Hence, the impact avoidance constraint

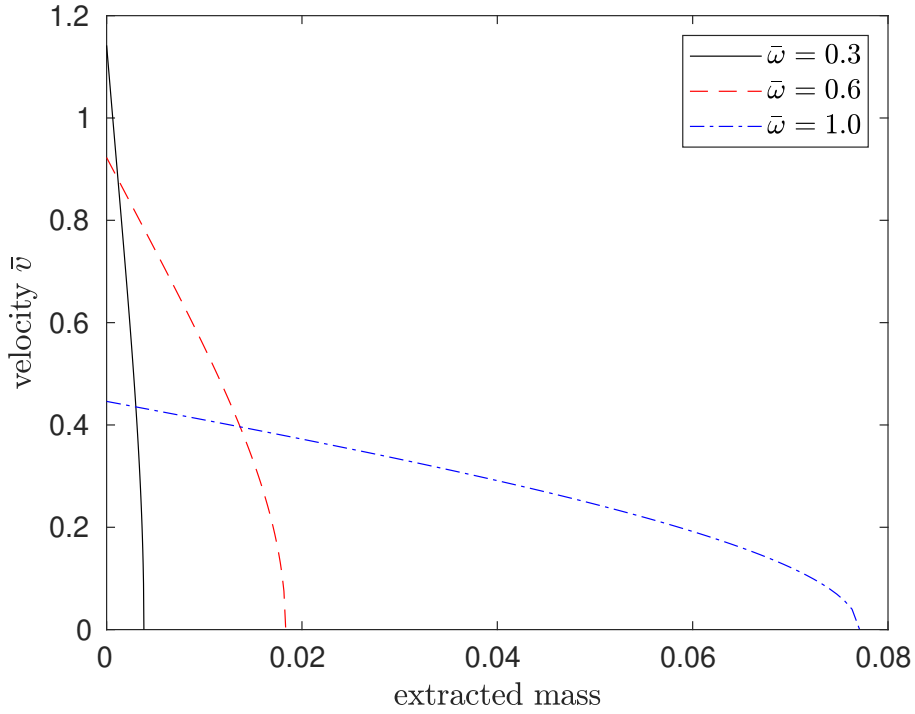

FIGURE 3.12: Siphon non-dimensional radial velocity $\bar{v}$ as a function of the extracted mass, for a range of initial angular velocities $\bar{\omega}_0$.

excludes a valuable region which would enable large mass extraction with $\bar{\mathscr{E}} < 0$. However, it is easy to show that a chain with a braking mechanism at the base, which reduces to zero the radial velocity of a PM at release, would move the impact region inside the collapse region, thus increasing the overall range of allowed configurations. In this case, not only the orbital siphon works in the range $\bar{\omega} = 1$ and $\bar{\omega} = \bar{\omega}_C$ but also braking may be used in principle to generate power.

Although not directly comparable, it is interesting to observe that ξ_m^{MAX} in Eq. (3.84) is close to the theoretical 21.5% specified in Eq. (3.80), found from basic energy balance considerations. In this case, ξ_m is slightly larger as part of the extraction is performed with $\bar{\mathscr{E}} < 0$, thus releasing material into bound orbit and not to escape. In both cases, however, ξ_m is always below one quarter of the initial mass.

3.6 Mass flow rate, timescale and discussion

Figure 3.12 shows the non-dimensional siphon velocity as a function of the extracted mass, for a range of initial angular velocities $\bar{\omega}_0$. The velocity represented is that given by Eq. (3.43) and a constant length siphon is considered, with the length chosen to maximize the extractable mass. (Sec. 3.4). The velocity is maximum at the beginning of the siphon operation and then progressively decreases as more mass is extracted. Note that, towards the end of the siphon operation the velocity drops to zero, as the siphon approaches its equilibrium condition. For

reference, a non-dimensional velocity $\bar{v} = 1$ corresponds to approximately $v = 7.5\,\mathrm{cm\,s^{-1}}$ for an asteroid with density $\rho = 2000\,\mathrm{kg\,m^{-3}}$ and radius $R_0 = 100\,\mathrm{m}$; the velocity scales with the asteroid radius R_0. Figure 3.13a shows, in dimensional units, the maximum extractable mass $\xi_m^{\max}$ (coloured contour) and the average mass rate $\dot{m}_{\mathrm{avg}}$ required to extract $\xi_m^{\max}$ (black curves) as a function of the asteroid radius and the asteroid period, taking an asteroid density $\rho = 2000\,\mathrm{kg\,m^{-3}}$. The average mass rate is calculated assuming an operational time of 10 years. The black dots represent candidate near-Earth asteroids[4] with radii between 50 and 500 m and rotational periods between 2.33 and 10 h (the lower end of the period corresponds to the critical angular velocity for an asteroid with density $\rho = 2000\,\mathrm{kg\,m^{-3}}$). As expected, a larger mass can be extracted from fast rotators and larger asteroids. However, a larger asteroid also implies larger average mass flow rates, on the order of tens of kilograms per second. Figure 3.13b shows the siphon width $\sqrt{A}$ (see Sec. 3.2.2) and the siphon length as a function of the asteroid radius and the asteroid period. The siphon width varies between 10 and 50 cm, whereas the siphon length varies between 100 and 3000 m, for the selected range of asteroid radius and period. Table 3.3 shows the extractable mass and required siphon length for some candidate asteroids with radii in a range between 246 m and 858 m. The extractable mass is in the range between 10^8 and 10^{11} kg, showing that in principle a large amount of mass can be lifted from asteroids using the orbital siphon.

The mass rate $\dot{m}_{\mathrm{avg}}$ is an important design parameter and clearly depends upon the technology of the mining units transferring material from the surface of the asteroid to the siphon and the physical properties of the asteroid. The mass rates $\dot{m}_{\mathrm{avg}}$ represented in Fig. 3.13a appear quite large when compared to mining rates suggested in the literature (e.g., Ref. [126] suggests mining rates between 300 and 1000 kg/day). However it must be noted that these large mining rates are associated with a *complete* siphon operation, with extracted mass between 10^7 and 10^{11} kg in a time frame of 10 years, for the selected range of asteroid radius and period. Reference [143] suggests a total mined mass during a single trip to an asteroid on the order of 5×10^5 kg, at least two order of magnitude less than the maximum extractable mass for an asteroid with radius in the range $50 \sim 500$ m.

Figure 3.14 shows how the extraction time t changes as a function of the extracted mass, for a range of siphon linear densities μ and the associated average mass rate $\dot{m}_{\mathrm{avg}}$ required. The radius and rotational period of the asteroid Bennu (see Table 3.3) are here chosen. The extraction time required varies almost linearly with respect to the extracted mass (note that a logarithmic scale is used on both axes), suggesting that for a given siphon linear density μ the average mass flow rate is independent of the extracted mass. For example, with an average mass rate of $1.26 \times 10^{-2}\,\mathrm{kg\,s^{-1}}$, 5×10^5 kg of asteroid material can be lifted in 1.24 years, or with an average mass flow rate of 1.26×10^{-1}, 5×10^5 kg of asteroid material can be lifted in just 46 days. Those mining rates are much smaller than that shown in Fig. 3.13a for *complete* siphon

[4]Data taken from https://ssd.jpl.nasa.gov, accessed on 23rd July 2020

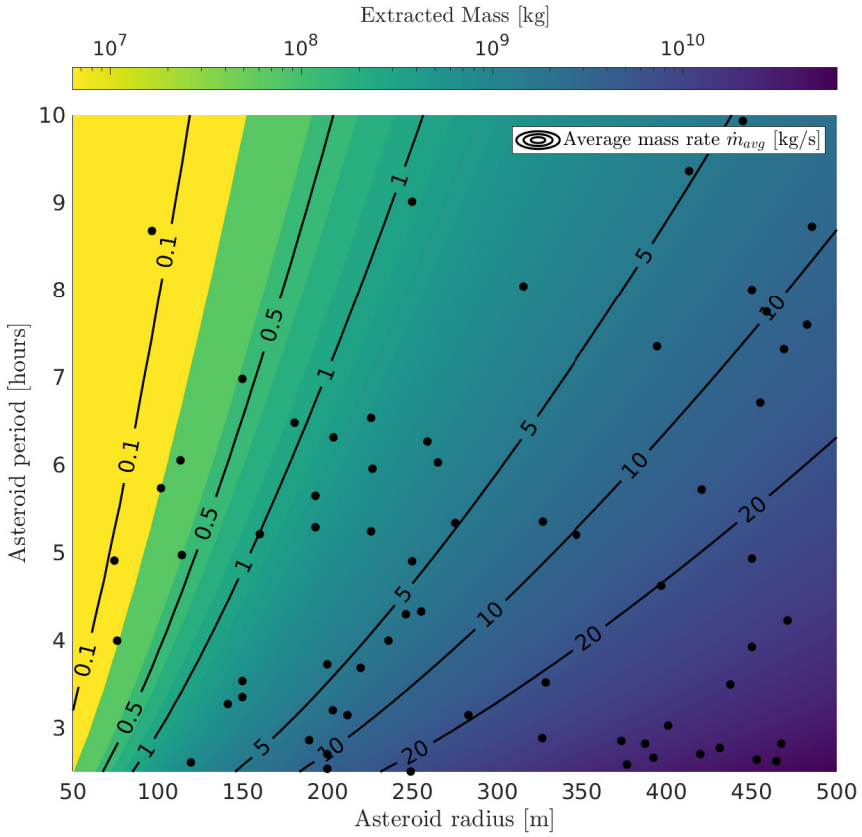

(a)

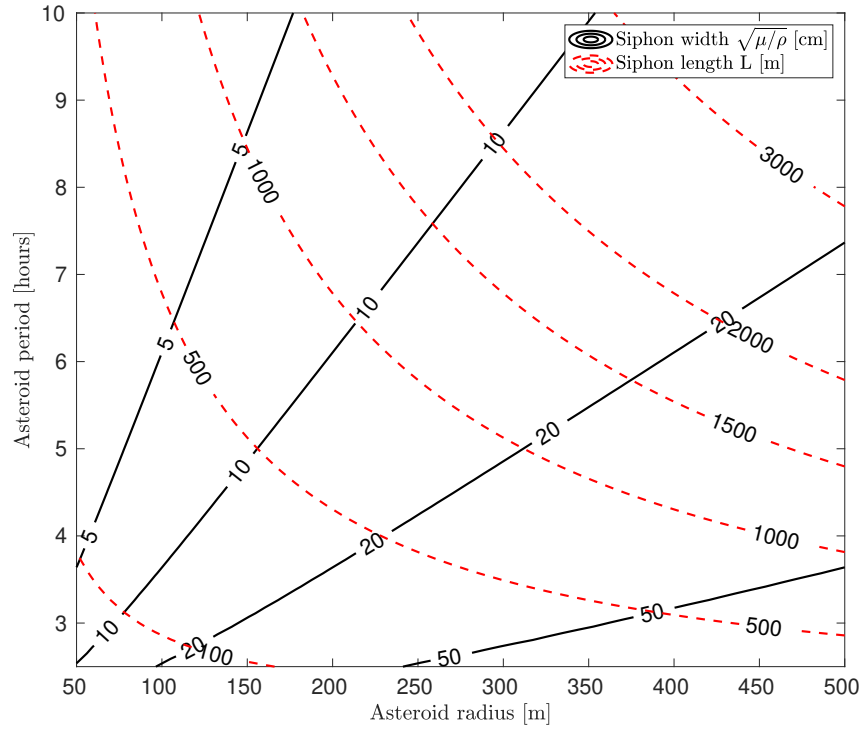

(b)

FIGURE 3.13: (a) Maximum extractable mass and average mass rate as a function of the asteroid radius and the asteroid period. (b) Siphon width and siphon length as a function of the asteroid radius and period. In both cases an asteroid density $\rho = 2000\,\mathrm{kg\,m^{-3}}$ is assumed.

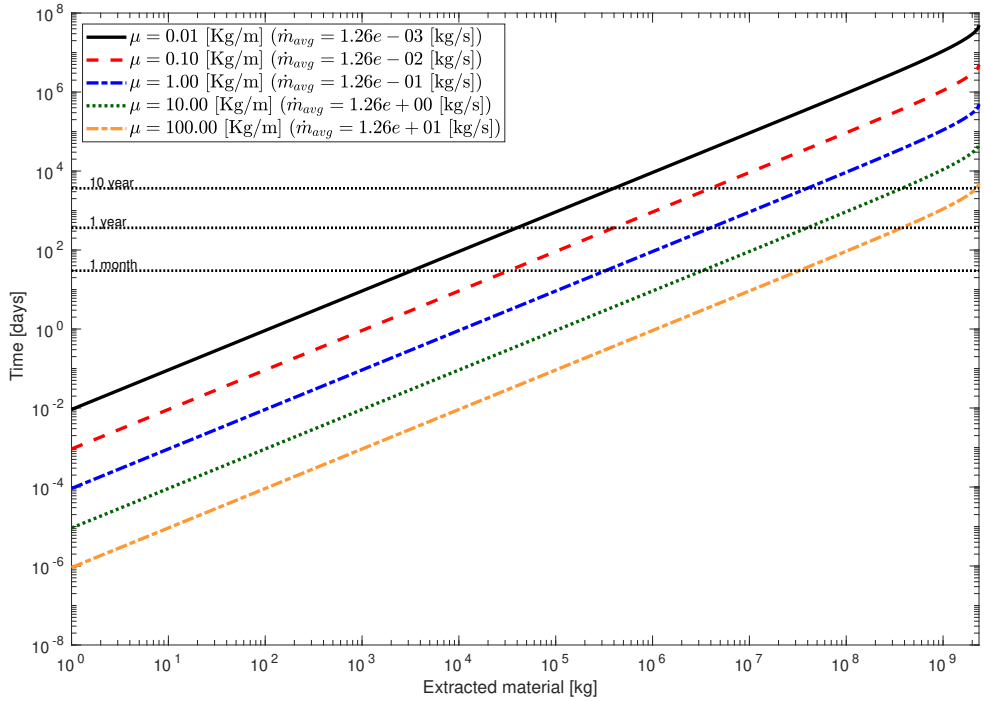

FIGURE 3.14: Extraction time as a function of the extracted mass, for a range of siphon linear density μ.

operation, and are closer to the mining rates suggested by Ref. [126].

However, when compared to lifting material using standard propulsion systems, the orbital siphon concept becomes effective for a large quantity of mined mass to be lifted from the surface. As an example, assuming the entire extractable mass ΔM of the first asteroid in Table 3.3 is sent to escape, a propellant mass $m_{\text{prop}} = \Delta M \frac{M_f}{1-M_f} = 8.7 \times 10^7\,\text{kg}$ is required, where the propellant mass fraction is $M_f = 1 - e^{(-v_{\text{esc}}/v_{\text{exhaust}})}$ and v_{esc}, v_{exhaust} are the escape velocity and effective exhaust velocity respectively (in this case it is assumed $v_{\text{exhaust}} = 4.2\,\text{km}\,\text{s}^{-1}$, as in Ref. [35]). Then, the siphon becomes more efficient than the propulsion system when its mass m_{siphon} is less than m_{prop} and, although an estimate of the siphon mass has not been provided here, it is reasonable to assume $m_{\text{siphon}} << m_{\text{prop}}$.

It should be emphasized that the energy required to transport material from different regions of the asteroid to the siphon base has not been considered here. Although this problem requires detailed additional investigation, the energy requirements could be minimized if multiple orbital siphons are envisaged, distributed along the equatorial region of the asteroid.

3.7 A speculative thought experiment: the fluid orbital siphon

Longsdon [74] envisioned an orbital siphon concept for fluids as a thought experiment, where a pipe is used instead of a chain of masses, to raise sea water above synchronous Earth orbit. Speculatively, he has shown that the water flux may drive turbines to generate power. Again of

TABLE 3.3: Extractable mass and siphon length for some candidate asteroids (see footnote 4 on page 65). The extracted mass is calculated assuming an asteroid density $\rho = 2000\,\mathrm{kg\,m^{-3}}$.

Asteroid	Radius [m]	Period [h]	$\bar{\omega}$	Extr. mass [kg]	Siphon length [m]
164121 (2003 YT1)	858	2.34	1.00	4.03×10^{11}	357
185851 (2000 DP107)	432	2.78	0.99	3.63×10^{10}	184
2102 Tantalus (1975 YA)	824	2.38	0.98	3.36×10^{11}	384
7822 (1991 CS)	801	2.39	0.98	3.06×10^{11}	378
66251 (1999 GJ2)	611	2.46	0.95	1.23×10^{11}	341
387733 (2003 GS)	172	2.47	0.95	2.72×10^{9}	97
334673 (2003 AL18)	285	2.48	0.94	1.21×10^{10}	166
7025 (1993 QA)	249	2.51	0.93	7.83×10^{9}	152
99907 (1989 VA)	700	2.51	0.93	1.72×10^{11}	433
303174 (2004 FH11)	752	2.52	0.93	2.11×10^{11}	473
162000 (1990 OS)	200	2.54	0.92	3.90×10^{9}	129
154029 (2002 CY46)	560	2.55	0.91	8.36×10^{10}	372
7482 (1994 PC1)	526	2.60	0.90	6.57×10^{10}	377
137062 (1998 WM)	632	2.58	0.90	1.17×10^{11}	439
138127 (2000 EE14)	377	2.59	0.90	2.46×10^{10}	264
141432 (2002 CQ11)	120	2.60	0.90	7.66×10^{8}	86
35107 (1991 VH)	464	2.62	0.89	4.40×10^{10}	345
162483 (2000 PJ5)	453	2.64	0.88	4.00×10^{10}	346
263976 (2009 KD5)	392	2.66	0.88	2.53×10^{10}	309
88188 (2000 XH44)	686	2.69	0.87	1.31×10^{11}	560
3671 Dionysus (1984 KD)	750	2.71	0.86	1.69×10^{11}	625
5797 Bivoj (1980 AA)	200	2.71	0.86	3.20×10^{9}	167
209924 (2005 WS55)	930	2.73	0.86	3.15×10^{11}	797
(2002 BM26)	420	2.70	0.86	2.98×10^{10}	348
7889 (1994 LX)	840	2.74	0.85	2.28×10^{11}	733
66391 Moshup (1999 KW4)	658	2.76	0.84	1.07×10^{11}	592
5381 Sekhmet (1991 JY)	468	2.82	0.83	3.62×10^{10}	450
85628 (1998 KV2)	388	2.82	0.83	2.06×10^{10}	373
274138 (2008 FU6)	374	2.85	0.82	1.79×10^{10}	371
388838 (2008 EZ5)	189	2.86	0.82	2.31×10^{9}	189
(2013 WT44)	326	2.88	0.81	1.16×10^{10}	336
9856 (1991 EE)	500	3.04	0.77	3.59×10^{10}	600
86819 (2000 GK137)	401	3.02	0.77	1.89×10^{10}	472
162463 (2000 JH5)	524	3.02	0.77	4.21×10^{10}	617
1862 Apollo (1932 HA)	750	3.06	0.76	1.19×10^{11}	916
86829 (2000 GR146)	912	3.10	0.75	2.07×10^{11}	1147
140158 (2001 SX169)	283	3.14	0.74	5.98×10^{9}	369
207945 (1991 JW)	212	3.15	0.74	2.48×10^{9}	277
345705 (2006 VB14)	203	3.20	0.73	2.10×10^{9}	278
68350 (2001 MK3)	897	3.27	0.71	1.71×10^{11}	1292
152564 (1992 HF)	141	3.28	0.71	6.63×10^{8}	204
2340 Hathor (1976 UA)	150	3.35	0.70	7.53×10^{8}	228
101955 Bennu (1999 RQ36)	246	4.30	0.69	2.00×10^{9}	386

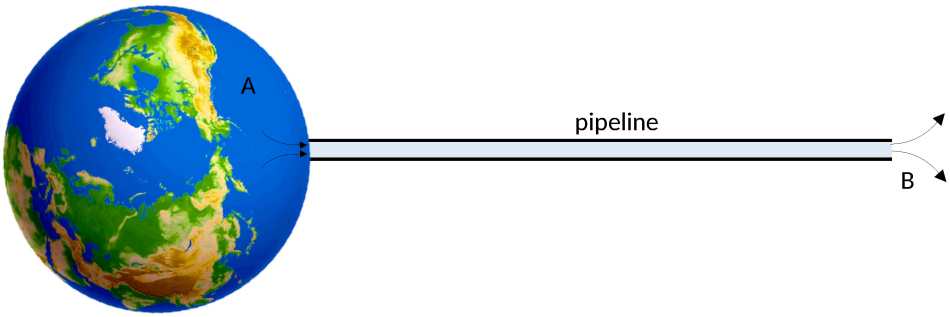

FIGURE 3.15: A fluid orbital siphon anchored to Earth.

course speculatively, such a structure could also be used to offset the sea level rise due to melting glaciers and ice sheets. A preliminary assessment of the scale of such infrastructure is provided in this section and an application in the context of asteroid resource exploitation is discussed.

Assume a pipe with diameter d_{pipe} stands vertically from a point on Earth equator to orbit as represented in Fig. 3.15. Let A be a point on Earth at sea level far from the pipe inlet and B be a point on the outlet. Assuming the pipe is filled with water and that the resulting flow is steady and isoentropic (any turbulence or heat radiation is neglected), then the Bernoulli principle applies. The sum of all forms of energy on a streamline is then conserved, in particular:

$$\frac{v^2}{2} + \frac{p}{\rho_W} + U = const \tag{3.85}$$

where v is the velocity at a point on the streamline, p is the pressure, ρ_W is the water density (here assumed equal to $1000\,\mathrm{kg\,m^{-3}}$) and U is the effective potential (defined by Eq. (2.1)), including the effect of gravity and centrifugal-induced force due to the Earth's rotation. Assuming a spherical Earth model:

$$U = -\frac{1}{2}\left(\frac{2\pi}{T_E}\right)^2 r^2 - \frac{GM_E}{r} \tag{3.86}$$

where $T_E = 24\,\mathrm{h}$, $GM_E = 3.986 \times 10^{14}\,\mathrm{m^3\,s^{-2}}$ are the Earth's rotation period and gravitational parameter respectively and r is the distance between a point on the streamline and the center of the Earth. Note that a generalized version of the Bernoulli principle has been used, to include the effects of the conservative gravitational field and centrifugal force [9]. Since A is far from the pipe inlet, it can be assumed that the velocity of the water at this point is zero. Then, specifying Eq. (3.85) between points A and B and solving for v_B yields:

$$v_B = \sqrt{2GM_E\left(\frac{1}{r_B} - \frac{1}{r_A}\right) + \frac{1}{2}\left(\frac{2\pi}{T_E}\right)^2 (r_B^2 - r_A^2) + \frac{p_A}{\rho_W}} \tag{3.87}$$

where $p_A = 101\,325\,\mathrm{Pa}$ is atmospheric pressure, $p_B = 0$ and $r_A = R_E = 6378\,\mathrm{km}$ is the Earth's radius. If the pipe has constant cross section, for conservation of mass the water velocity is

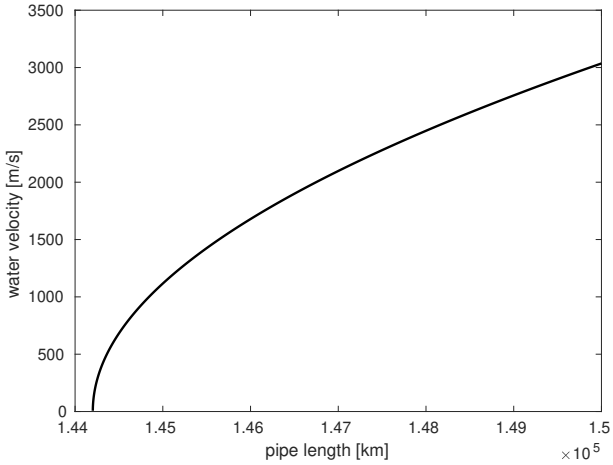

FIGURE 3.16: Velocity of the water as a function of the pipe length.

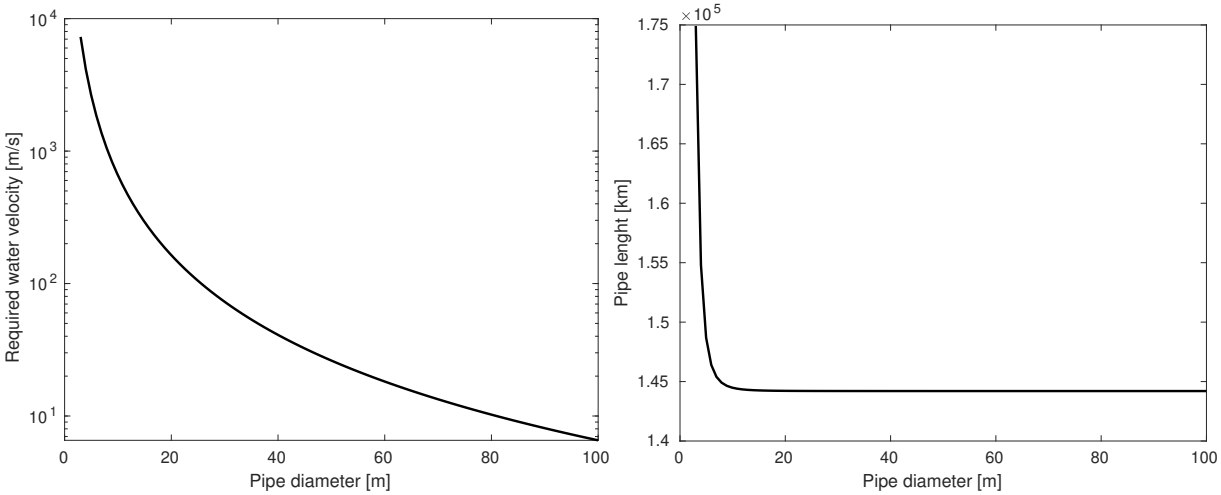

FIGURE 3.17: (a) Required water velocity inside the pipe to counteract a sea level rise of 3.3 mm/year, as a function of the pipe diameter. (b) Required pipe length to achieve such velocities, as a function of the pipe diameter.

the same throughout the pipe. Therefore, $v_B = v_{\text{water}}$ is the velocity of the water at any point inside the pipe. To guarantee positive velocity, the term under square root must be positive. The minimum pipe length L_{eq} (the same symbol as the siphon equilibrium length is used for analogy) to guarantee positive water velocity is $L_{eq} = 1\,442\,018.29\,\text{km}$. This value is approximately 130 m smaller than the equilibrium length of a terrestrial space elevator or, equivalently, an orbital siphon modelled as a continuous mass distribution (Eq. (3.18)). The small difference is due to atmospheric pressure. Figure 3.16 shows the velocity of the water inside the pipe as a function of the pipe length. For lengths above L_{eq}, the water velocity rapidly increases.

In order to estimate the required pipe cross-section and water velocity to compensate for sea level rise, assume for simplicity that the Earth is entirely covered by water. Let m_{water} be the mass of water resulting from melting of a given amount of ice and ΔR the resulting sea level

rise. Let R_0 be the original sea level before the ice melting, measured with respect to the Earth's center. For simplicity assume $R_0 \approx R_E$. Then:

$$m_{\text{water}} = \rho_W \frac{4}{3}\pi \left(R_E^3 - (R_E - \Delta R)^3\right) \tag{3.88}$$

Assuming $\Delta R << R_E$, Eq. (3.88) can be approximated as

$$m_{\text{water}} = 4\rho_W \pi R_E^2 \Delta R \tag{3.89}$$

Now, the flow rate of melting ice in unit time Δt is:

$$\begin{aligned} \dot{m}_{\text{water}} &= \frac{m_{\text{water}}}{\Delta t} \\ &= 4\pi R_E^2 \rho \dot{R}_{\text{sea level}} \end{aligned} \tag{3.90}$$

The factor $\dot{R}_{\text{sea level}} = \Delta R/\Delta t$ is the sea level rise per unit time. According to NASA, sea level is rising at a rate of 3.3 mm per year.[5] The mass flow rate $\dot{m}_{\text{pipe}}$ of water exiting from the pipe is:

$$m_{\text{pipe}} = S v_{\text{water}} \rho_W \tag{3.91}$$

where $S = \pi d_{\text{pipe}}^2/4$ is the cross section of the pipe. Setting $\dot{m}_{\text{water}} = \dot{m}_{\text{pipe}}$ with $\dot{R}_{\text{sea level}} = 3.3$ mm/year, the allowed combinations of pipe cross-sections and required velocities to compensate for sea level rise can be found as:

$$S v_{\text{water}} = 4\pi R_E^2 \dot{R}_{\text{sea level}} \tag{3.92}$$

which is independent of the water density. Figure 3.17a shows the required water velocity as a function of the pipe diameter. For a pipe diameter in the range between 1 and 100 m, the required water velocity changes by four orders of magnitude, in the range between 10 and 10^4 m/s. Figure 3.17b shows the length of the siphon needed to achieve such velocity. It is interesting to note that for pipe diameters larger than approximately 20 m the required siphon length is independent of the pipe cross section and equal to 144 203 km.

Figure 3.18 shows the variation of the pressure inside the pipe as a function of the altitude for a pipe with length 144 203 km. The maximum pressure is reached at geosynchronous altitude and it is approximately 5×10^{10} Pa. For reference, the strength σ_{pipe} required by a pipe with diameter d_{pipe} and thickness δ to withstand the pressure p can be found using Barlow's formula [69]:

$$\sigma_{\text{pipe}} = \frac{p d_{\text{pipe}}}{2\delta} \tag{3.93}$$

A 20-metre diameter pipe, with thickness of 1 m would require a strength of 50 GPa. The

[5] `https://climate.nasa.gov/vital-signs/sea-level/` Accessed on 22 November 2020

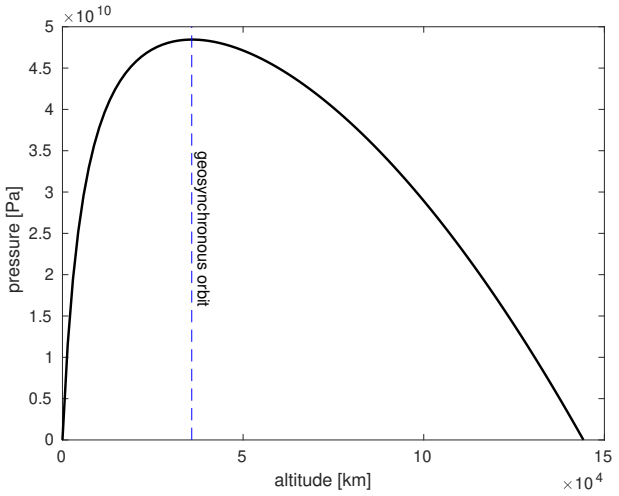

FIGURE 3.18: Pressure of the water flowing inside the pipe, as a function of the altitude. A pipe with length 144203 km is assumed.

strength of a carbon steel tube, commonly used for process piping, is three orders of magnitude smaller, approximately 0.4 GPa [130], suggesting that stronger materials are required. Carbon nanotubes, proposed for the construction of space elevator, have a strength of approximately 1.3 GPa [38]. In analogy with the space elevator design [102], the material strength requirements may be reduced using a tapered pipe. In this case, carbon nanotubes may be a suitable choice for the pipe material, although further analysis is required. Additionally, other phenomena not considered in this simple analysis should be included in future studies to verify the actual feasibility of such a concept, such as cavitation, phase change, heat transfer, compressibility, supersonic flow and anchoring.

3.7.1 Application to asteroids

It is instructive to analyse the same problem applied in the context of asteroid resource exploitation. In this case the magnitude of the gravitational and centrifugal-induced forces involved is much smaller than those for terrestrial applications, and therefore the required pipe length and material strength are significantly reduced. Such a liquid orbital siphon could be used to transfer liquids or propellant from the surface of the asteroid to a fuel depot or collecting spacecraft docked at the upper end of the pipe. For example, taking the asteroid Bennu (details in Table 3.3), Fig. 3.19a shows the achievable mass flow rates of water that can be transferred from the asteroid surface, as a function of the pipe diameter and its length, using the method outlined in the previous section. The smaller length on the vertical axis is the minimum length required to initialise a positive mass flow rate of fluid to orbit, in this case approximately 154 m. It is also assumed that the water is not initially pressurised ($p_A = 0$). Mass flow rates on the order of tens of kilograms per second can be achieved with pipe diameters in a range between 0.1 m and 1 m and siphon lengths below 230 m.

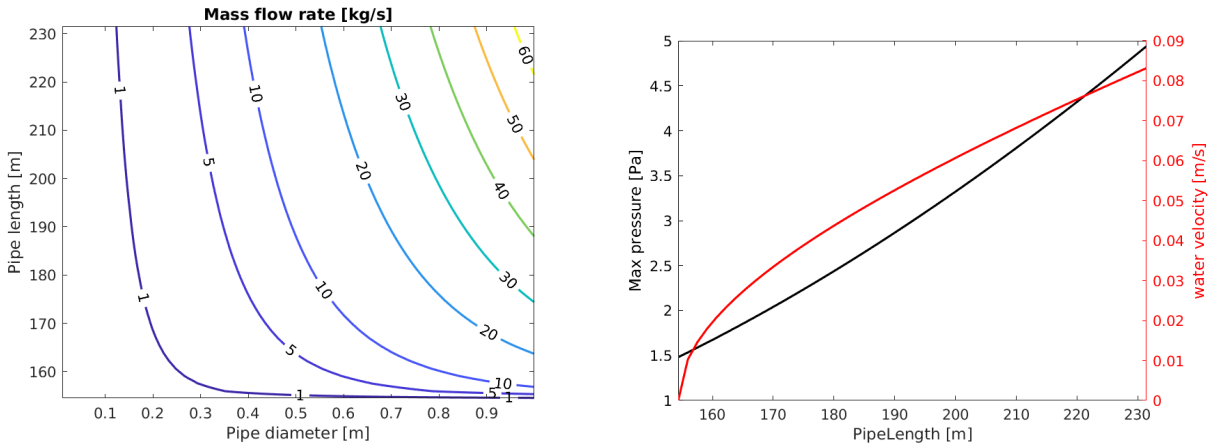

(a) **(b)**

FIGURE 3.19: (a) Mass flow rate of water that can be lifted through a liquid siphon anchored at Bennu, as a function of the pipe diameter and the pipe length. (b) Maximum pressure and water velocity on the pipe as a function of the pipe length.

Figure 3.19b shows the maximum water pressure (achieved at synchronous orbit) and velocity as a function of the pipe length. As expected, the required pressure is several orders of magnitude smaller than that required for terrestrial applications, suggesting that application of this concept to asteroids is more feasible. The velocity of the water is on the order of cm/s, similar to the radial velocity of a discrete siphon (Sec. 3.6). Assuming Bennu contains approximately 8% water mass fraction (this is an estimate for C-class hydrated asteroids [113]), a 220-metre long pipe with a 0.9-metre diameter could raise processed water from the surface of Bennu for approximately four years (the asteroid angular velocity variation due to siphon operation has been neglected here for simplicity) at a rate of approximately $50\,\mathrm{kg\,s^{-1}}$ (Fig. 3.19a), with maximum pipe pressure on the order of 4 Pa (Fig. 3.19b). This suggests that conventional pipe material may be used for asteroid applications.

Despite the significant simplifications used in this preliminary study, it is reasonable to conclude that liquid siphons may be a viable solution for transportation of fluid resources from the asteroid surface, and therefore this analysis offers scope for further future investigation. However, further work such as thermal analysis would be required to ensure that the liquid does not solidify during transfer. On the other side, it must be verified that the liquid pressure is large enough to avoid vaporisation.

Chapter 4

Orbital siphon rotational dynamics and material transfer to equilibrium points

4.1 Introduction

This chapter discusses the effects of the siphon equatorial oscillations due to the Coriolis forces acting on the chain. Also, a collecting spacecraft connected at the top of the siphon is envisaged to collect material resources lifted by the siphon. The asteroid is modelled as a rotating tri-axial ellipsoid and the effects of the asteroid shape on the siphon dynamics are studied, by changing the semi-major axes of the ellipsoid. Moreover, different anchor longitudes are considered. Eventually, a method is proposed to exploit the equatorial Coriolis-induced oscillations of the siphon to transfer payload masses from the collecting spacecraft to the stable equilibrium points associated with the effective potential of the ellipsoidal asteroid, where a catcher would collect the material.

4.2 Asteroid model

An asteroid of mass M is modelled as a triaxial ellipsoid with semi-major axes $\alpha \geq \beta \geq \gamma$ and constant density ρ, rotating with constant angular velocity ω about the axis with largest inertia. A co-rotating reference frame is defined such that the x-axis lies along the largest dimension α, the y-axis lies along the intermediate dimension β and the z-axis lies along the smallest dimension γ, parallel to the angular velocity vector. The asteroid gravitational parameter GM is then defined as

$$GM = \frac{4}{3}\pi G\rho\alpha\beta\gamma \tag{4.1}$$

Similar to chapter 3, a set of non-dimensional variables is used, indicated with an upper-bar symbol. Distances are here scaled by the largest semimajor axis α (such that $\bar{\alpha} = 1$) and the

time is scaled by $\omega_{\text{crit}}^{-1}$, where

$$\omega_{\text{crit}} = \sqrt{\frac{GM}{\alpha^3}} \tag{4.2}$$

The parameter ω_{crit} is defined in analogy with Eq. (3.4). It is effectively the square root of the ratio between the centripetal acceleration and the gravitational acceleration acting on a particle at the longest end of the ellipsoid, assuming that the entire mass of the asteroid is concentrated at the origin. The mass scaling factor is chosen here as the mass on a payload of the siphon, which will be defined later in Sec. 4.3.

The effective potential given by Eq. (2.1) combines the effects of the centrifugal-induced potential and the gravitational acceleration for a rotating ellipsoid. In non dimensional-units, the effective potential can be written as:

$$\bar{U} = \frac{1}{2}\bar{\omega}^2(\bar{x}^2 + \bar{y}^2 + \bar{z}^2) + \bar{V} \tag{4.3}$$

being $\bar{V}$ the non-dimensional gravitational potential:

$$\bar{V} = \frac{3}{4}\int_{\kappa}^{\infty}\left(1 - \frac{\bar{x}^2}{1+s} - \frac{\bar{y}^2}{\bar{\beta}^2+s} - \frac{\bar{z}^2}{\bar{\gamma}^2+s}\right)\frac{ds}{\sqrt{(1+s)^2 + (\bar{\beta}^2+s)^2 + (\bar{\gamma}^2+s^2)}} \tag{4.4}$$

Note that, by using non-dimensional coordinates, the effective potential $\bar{U}$ at any point at the asteroid is completely defined by the three parameters $\bar{\beta}$, $\bar{\gamma}$ and $\bar{\omega}$.

4.3 Orbital Siphon model

Here, the orbital siphon is arranged as a chain of $2n$ masses, divided in a lifting-side (LS) and a descending-side (DS), each one with n masses, as represented in Fig. 4.1. The former contains bucket masses m_b filled with payload masses m_p to be lifted, whereas the latter contains the empty buckets m_b going back to the asteroid for refilling. Each bucket is connected to its two neighbours with a tether, and two pulleys at the two endpoints (at the anchoring point and at the top of the chain) connect the LS with the DS. The bucket chain slides without friction on a rigid rod with length L, which allows rotation on the equatorial plane with respect to the fixed anchor point A. At the top of the rigid rod a collecting spacecraft (CS), here modelled as point mass M_{cs}, collects the payloads released by the LS. Note that the CS mass M_{cs} increases over time, as more payloads are released.

It is assumed that all the payloads have constant mass m_p. Therefore, an element on the LS will have a mass $m_{ls} = m_b + m_p$ whereas an element on the DS has mass $m_{ds} = m_b$. Moreover, it is assumed that the mass of the asteroid remains constant, implying that the removed mass is small.

Some additional assumptions are made.

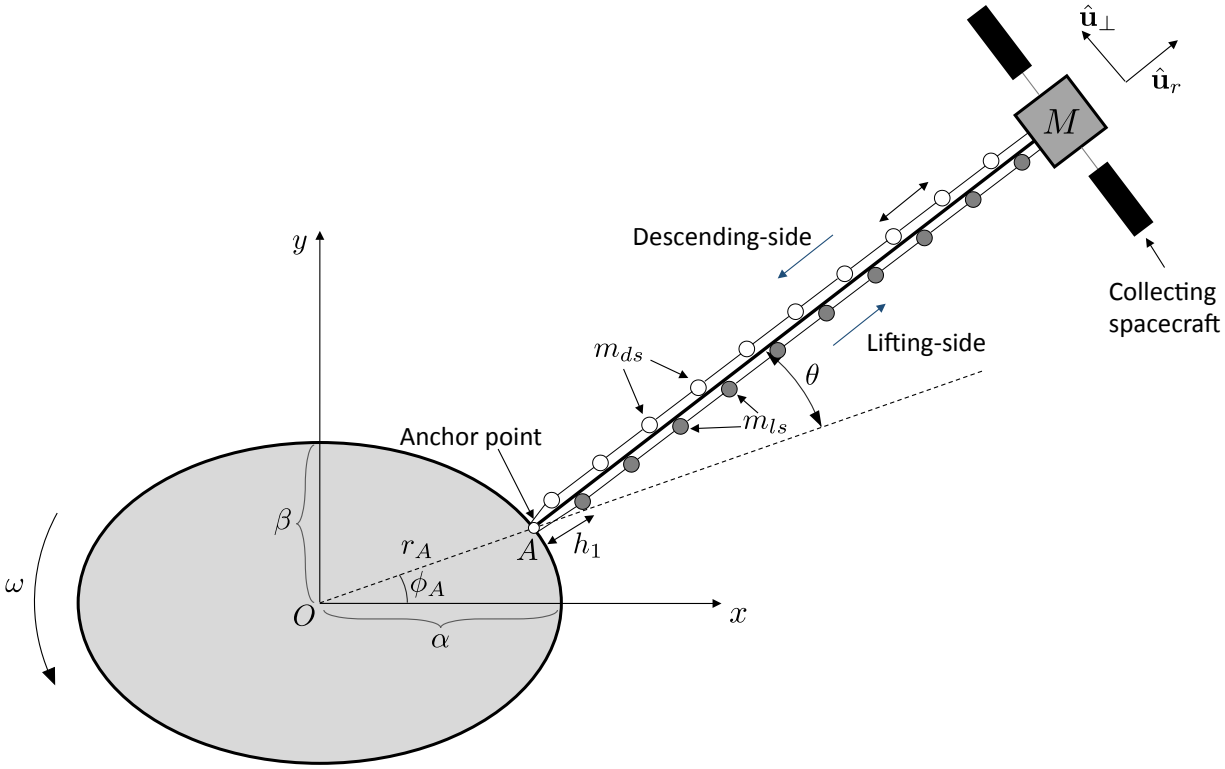

FIGURE 4.1: Orbital siphon model. Rotations are measured positive in the counter-clockwise direction.

1. Any friction due to the bucket-pulley interaction is neglected.
2. Other external perturbations (e.g., third-body perturbation, solar radiation pressure) are not considered.
3. The dynamics is restricted to motion in the equatorial plane $x-y$.
4. The tethers connecting consecutive buckets are assumed massless and infinitely rigid, with constant length l.

As a consequence of the last assumption, the entire LS and DS are effectively treated as rigid bodies sliding on a rod and the overall dynamics of the siphon can be described via two generalised coordinates: the rotation of the siphon θ and the distance h of the first bucket mass of the LS from the anchor point. All rotations are assumed positive when measured from the x-axis in the counter-clockwise direction.

4.3.1 Siphon radial force

The coordinates of the i-th mass ($1 \leq i \leq 2n$) on the chain can now be written as

$$x_i = r_A \cos\phi_A + h_i \cos(\phi_A + \theta) \tag{4.5a}$$

$$y_i = r_A \sin\phi_A + h_i \sin(\phi_A + \theta) \tag{4.5b}$$

where θ is the angle between the chain radial unit vector $\hat{\mathbf{u}}_r$ and the line OA (see Fig. 4.1) while r_A and ϕ_A are the polar coordinates of the anchor point, related by the ellipse equation written with respect to its centre:

$$r_A = \frac{\beta}{\sqrt{1-\left[1-\left(\frac{\beta}{\alpha}\right)^2\right]\cos^2(\phi_A)}}. \tag{4.6}$$

The parameter h_i is the distance between the i-th bucket and the anchor point A, which can be written as a function of h_1, such that

$$h_i = \begin{cases} h_1 + (i-1)l, & 1 \leq i \leq n \\ L - (h_1 + (i-1)l), & n+1 \leq i \leq 2n \end{cases} \tag{4.7}$$

where the first and second case corresponds to payload masses (PMs) on the LS and DS respectively. The force f_i acting on the i-th element of the chain in the radial direction $\hat{\mathbf{u}}_r$ is given by

$$f_i = \begin{cases} m_{ls}(\nabla U(h_i)\cdot\hat{\mathbf{u}}_r + h_i\dot{\theta}^2 + 2\omega\dot{\theta}h_i), & 1 \leq i \leq n \\ -m_{ds}(\nabla U(h_i)\cdot\hat{\mathbf{u}}_r + h_i\dot{\theta}^2 + 2\omega\dot{\theta}h_i), & n+1 \leq i \leq 2n \end{cases} \tag{4.8}$$

The internal tension forces are not explicitly listed here as they will vanish in a summation to be performed later.

The first term of Eq. (4.8) ($\nabla U(h_i)\cdot\hat{\mathbf{u}}_r$) is the force associated to the gradient of the effective potential U. The second ($h_i\dot{\theta}^2$) and third ($2\omega\dot{\theta}h_i$) terms are due to the chain dynamics and are non-zero if the chain is rotating with $\dot{\theta} \neq 0$. In particular, the term $h\dot{\theta}^2$ is the centrifugal-induced acceleration due to the rotation of the siphon with angular velocity $\dot{\theta}$, while the last term is the Coriolis acceleration in the direction $\hat{\mathbf{u}}_r$, associated with the velocity $\dot{\theta}h$ in the $\hat{\mathbf{u}}_\perp$ direction. Note that the contribution of the terms involving the chain angular velocity $\dot{\theta}$ is negative for $-2\omega < \dot{\theta} < 0$, $\forall\ i \leq 1 \leq n$. Therefore, if the chain is rotating in the clockwise direction with angular velocities up to two times the angular velocity of the asteroid, then the chain rotation induces a net radial force contribution opposite to $\hat{\mathbf{u}}_r$. The unit vectors $\hat{\mathbf{u}}_r$ and $\hat{\mathbf{u}}_\perp$ can be written as a function of the anchor longitude and the chain angle as:

$$\hat{\mathbf{u}}_r = \begin{Bmatrix} \cos(\phi_A+\theta) \\ \sin(\phi_A+\theta) \end{Bmatrix} \tag{4.9a}$$

$$\hat{\mathbf{u}}_\perp = \begin{Bmatrix} -\sin(\phi_A+\theta) \\ \cos(\phi_A+\theta) \end{Bmatrix} \tag{4.9b}$$

Then, the overall radial force acting on the chain can be written in non-dimensional form as

$$\begin{aligned}\bar{f} = &\sum_{i=1}^{n}\left[\left(\nabla\bar{U}(\bar{h}_i)\cdot\hat{\mathbf{u}}_r + \bar{h}_i\dot{\bar{\theta}}^2 + 2\bar{\omega}\dot{\bar{\theta}}\dot{\bar{h}}_i\right)\right] + \\ &-\sum_{i=n+1}^{2n}\left[D\left(\nabla\bar{U}(\bar{h}_i)\cdot\hat{\mathbf{u}}_r + \bar{h}_i\dot{\bar{\theta}}^2 + 2\bar{\omega}\dot{\bar{\theta}}\dot{\bar{h}}_i\right)\right].\end{aligned} \tag{4.10}$$

where the ratio between m_{ds} and m_{ls} has been defined with the symbol D due to its significance in later analysis:

$$D = \frac{m_{ds}}{m_{ls}} = \frac{1}{1+\frac{m_p}{m_b}} \tag{4.11}$$

Note that D can be written as a function of the ratio between the payload mass and the bucket mass and $D \in [0,1]$. When the siphon is loaded with small payload masses $m_p \to 0$ then $D \to 1$ (see Eq. (4.11)) and the contribution of the DS on the radial force is maximum, whereas if the mass of the payload is much larger than the mass of the bucket then $D \to 0$ and the DS effect on f becomes negligible. In particular, if $D = 1$ and the LS and DS are aligned (this occurs when $h_1 = l/2$) then the radial force is zero, regardless of the other parameters. Note that in the siphon model studied in this chapter the CS does not influence the radial force.

4.3.2 Siphon torque

While material is moving towards the CS, Coriolis forces due to the motion of the LS (DS) will induce a clockwise (counter-clockwise) torque. The torque T_i due to the i-th element of the chain with respect to the anchor point can be written as

$$T_i = \begin{cases} m_{ls}\left[\nabla U(h_i)\cdot\hat{\mathbf{u}}_\perp - 2(\omega+\dot{\theta})\dot{h}_1\right]h_i, & 1 \le i \le n \\ m_{ds}\left[\nabla U(h_i)\cdot\hat{\mathbf{u}}_\perp + 2(\omega+\dot{\theta})\dot{h}_1\right]h_i, & n+1 \le i \le 2n \end{cases} \tag{4.12}$$

The first term $\nabla U(h_i)\cdot\hat{\mathbf{u}}_\perp$ is the contribution due to the gradient of the effective potential U in the transversal direction $\hat{\mathbf{u}}_\perp$. The second part $2(\omega+\dot{\theta})\dot{h}$ is the contribution due to the Coriolis force in the direction $\hat{\mathbf{u}}_\perp$ due to the motion of the chain (note that this contribution is opposite between LS and DS, since the buckets are travelling in opposite directions in the two cases).

Similarly, the torque generated by the CS with respect to the anchor point is

$$T_{\mathrm{cs}} = M_{cs}L\nabla U(L)\cdot\hat{\mathbf{u}}_\perp \tag{4.13}$$

where $\nabla U(L)$ is the gradient of the effective potential at the location of the CS. Then, the overall torque T of the system chain and CS is the sum $T_{cs} + \sum_{i=1}^{2n} T_i$ and can be expressed in non-

dimensional form as:

$$\begin{aligned}\bar{T} = \bar{M}_{cs}\bar{L}\nabla\bar{U}(\bar{L})\cdot\hat{\mathbf{u}}_{\perp} + \sum_{i=1}^{n}\left[\nabla\bar{U}(h_i)\cdot\hat{\mathbf{u}}_{\perp} - 2(\bar{\omega}+\dot{\bar{\theta}})\dot{\bar{h}}_1\right]\bar{h}_i + \\ + D\sum_{i=n+1}^{2n}\left[\nabla\bar{U}(\bar{h}_i)\cdot\hat{\mathbf{u}}_{\perp} + 2(\bar{\omega}+\dot{\bar{\theta}})\dot{\bar{h}}_1\right]\bar{h}_i\end{aligned} \tag{4.14}$$

Note that if $\dot{\bar{\theta}} > -\bar{\omega}$, the Coriolis torque (proportional to $(\bar{\omega}+\dot{\bar{\theta}})$ on Eq.(4.14)) is always negative (i.e., inducing a clockwise rotation, opposite to the asteroid rotation). The limiting case $\dot{\bar{\theta}} = -\bar{\omega}$ corresponds to the scenario where the angular velocity of the siphon has the same magnitude as the angular velocity of the asteroid however with opposite direction: in this case, the global Coriolis torque vanishes.

4.3.3 Siphon dynamics

The overall siphon dynamics are then described by the combination of the translational chain motion h_1 and the rotation θ and can be written in non-dimensional form as:

$$n(1+D)\ddot{\bar{h}}_1 = \bar{f} \tag{4.15a}$$

$$\left[\sum_{i=1}^{2n}\bar{m}_i\bar{h}_i^2 + \bar{M}_{cs}\bar{L}^2\right]\ddot{\bar{\theta}} = \bar{T} \tag{4.15b}$$

where $\bar{f}$ and $\bar{T}$ are the radial force and torque on the siphon, given by Eqs. (4.10) and (4.14) respectively. Note that the two equations of motion are coupled, where $\bar{f}$ is a function of θ and $\dot{\bar{\theta}}$, and $\bar{T}$ a function of $\bar{h}_1$ and $\dot{\bar{h}}_1$. From now on, when the context is clear, the subscript 1 will be omitted from the generalized coordinate h_1.

Equations (4.15) are non-autonomous, non-linear and non-homogeneous differential equations and do not admit a closed-form solution. They can be numerically integrated from an initial state $\left\{h(t_0), \dot{h}(t_0), \theta(t_0), \dot{\theta}(t_0)\right\}$ and an initial CS mass $M_{cs,0}$. Let $\left\{h(t_1), \dot{h}(t_1), \theta(t_1), \dot{\theta}(t_1)\right\}$ be the state when $h = l$, i.e., when the top payload has reached the CS and a new empty bucket from the DS has reached the anchor point. As in Chapter 3 it is assumed that the payload to be added to the chain has zero velocity within the rotating frame. By modelling this event as an inelastic collision, the new velocity of the chain $\dot{h}$ after a new payload is added is given by $\dot{h}(t_1)(n-1)/n$ (see Appendix E). Then, the new state after this event will be

$$\left\{0, \frac{n-1}{n}\dot{h}(t_1), \theta(t_1), \dot{\theta}(t_1)\right\} \tag{4.16}$$

A new integration can then be performed with the updated velocity and CS mass $M_{cs}(t_1) = M_{cs}(t_0) + m_p$, and the process is iteratively repeated. Note that the translational degree of freedom h is bounded between 0 and l. As a compact notation, the subscript 0 will be used in the

following sections to indicate a variable at the beginning of the simulation.

4.3.4 Siphon rotational damping

The siphon rotational dynamics, Eq. (4.15b), can be rearranged as:

$$I\ddot{\bar{\theta}} + c\dot{\bar{\theta}} + k(\theta) = -c \tag{4.17}$$

where

$$I = \sum_{i=1}^{2n} \bar{m}_i \bar{h}_i^2 + \bar{M}_{cs}\bar{L}^2 \tag{4.18}$$

$$c = 2\bar{h}_1 \left(\sum_{i=1}^{n} \bar{h}_i - \sum_{i=n+1}^{2n} D\bar{h}_i \right) \tag{4.19}$$

$$k = \bar{T} + \sum_{i=1}^{n} \left(\nabla\bar{U}(\bar{h}_i) \cdot \hat{\mathbf{u}}_\perp - 2\bar{\omega}\dot{\bar{h}}_1 \right) \bar{h}_i + \tag{4.20}$$

$$+ \sum_{i=n+1}^{2n} D \left(\nabla\bar{U}(\bar{h}_i) \cdot \hat{\mathbf{u}}_\perp + \bar{\omega}\dot{\bar{h}}_1 \right) \bar{h}_i$$

The first and third terms on the left-hand side of Eq. (4.17) represent the inertia and the stiffness of the siphon respectively, and they linearly increase with the CS mass M_{cs}. The second term, c does not depend on the CS mass but on the current chain mass distribution and the chain velocity $\dot{\theta}$. Since $0 \leq D < 1$ by definition (Eq. (4.11)), the term within square brackets in Eq. (4.19) is always positive, for any choice of n and L. Then, the sign of c depends on the sign of the siphon radial velocity, which is positive if the orbital siphon effect is generated (i.e., $f > 0$, Eq. (4.10)). Therefore, the term c can be thought of as a damping term, responsible for attenuation of the siphon oscillation and it is due to the Coriolis forces associated with the rotation of the chain. This behaviour is typical of frictionless pendulums with a moving mass (see, for example, Ref. [131]). Note that the term c also appears at the right-hand-side of Eq. (4.17). Since $c > 0$, the term $-c$ effectively represents a torque in the clockwise direction, which induces the chain to rotate opposite to the direction of the asteroid rotation. Therefore, the motion of the chain has a double effect on the system: (1) it attenuates the amplitude of the siphon oscillation and (2) forces the siphon to rotate clockwise.

As more mass is delivered to the CS and $M_{cs} \gg 0$, the term c (not depending on M_{cs}) becomes negligible with respect to I and k, therefore it is expected that the damping is gradually reduced over time. Although a formal stability analysis of the system is not performed here, such qualitative comments will be helpful for interpretation of the numerical simulation results presented in Sec. 4.5.

4.4 Approximations for a continuous chain

In the following sections a set of parameters are defined, where the LS and DS are approximated with continuous mass distributions with linear densities $\mu_{ls} = nm_{ls}/L$ and $\mu_{ds} = nm_{ds}/L$. In this scenario, the parameter D can also be written as the ratio between the two densities μ_{ds}/μ_{ls}. It will be shown that such approximations can be exploited to quickly analyse the effects of the asteroid shape on the siphon dynamics.

4.4.1 Siphon equilibrium length

In analogy with Eq. (3.18), the siphon equilibrium length is defined as the length L_{eq} such that the overall radial force f is zero when the siphon orientation is fixed ($\dot{\theta} = 0$) for continuous mass distributions along the LS and DS. In such a scenario the radial force given by Eq. (4.10) can be written as the integral

$$f_{\text{cont}} = (\mu_{ls} - \mu_{ds}) \int_0^L \nabla U \cdot \hat{\mathbf{u}}_r d\chi \tag{4.21}$$

where the discrete variable h_i is replaced with χ, which varies continuously in the range $[0, L]$ and represents the distance of a generic point on the (continuous) chain with respect to the anchor point. Then, L_{eq} can be found by solving $f_{\text{cont}} = 0$, i.e.,

$$\int_0^{L_{\text{eq}}} \nabla U(\chi) \cdot \hat{\mathbf{u}}_r d\chi = 0. \tag{4.22}$$

When $L = L_{\text{eq}}$ the gravitational and centrifugal-induced forces acting on the DS and LS balance, removing any orbital siphon effect. In general, Eq. (4.22) does not admit a closed-form solution, due to the integrals in ∇U, related to the gravitational component of the effective potential. However, if $\bar{\beta} = \bar{\gamma} = 1$, and $\theta = 0$ then Eq. (4.22) simplifies to Eq. (3.18) found in Chapter 3 for an orbital siphon anchored to a spherical asteroid. As in Chapter 3 it can be shown that if $L > L_{\text{eq}}$ then $f > 0$ for any $n \geq 2$ (with $h_1 > l/2$). Therefore, to guarantee the siphon effect, it is necessary to ensure that $L > L_{\text{eq}}$ for the angle θ (or the range of angles) at which the siphon is operating.

Figure 4.2 shows L_{eq} for $\phi_A \in [0, 2\pi]$ considering an asteroid rotational period of 5 h, assuming $\theta = 0, \forall \phi_A$ and $\bar{\beta} = \bar{\gamma} = 0.5$ (Fig. 4.2a), $\bar{\beta} = \bar{\gamma} = 0.9$ (Fig. 4.2b). If the top of the siphon is contained within the shaded region then $f < 0$ and the siphon effect cannot be generated. Note that the shaded region contains the EPs and the minimum length in the region $\phi_A \approx \pi/2$ is larger than that for $\phi_A \approx 0$ when the asteroid is more prolate.

Figures 4.3a and 4.3b show the equilibrium length L_{eq} as a function of the asteroid period for anchoring longitude $\phi_A = 0$ (a), $\phi_A = \pi/2$ (b) and a range of $\bar{\beta}$ assuming $\bar{\gamma} = \bar{\beta}$ and the chain normal to the surface ($\theta = 0$) in both cases. As expected, the equilibrium length increases (al-

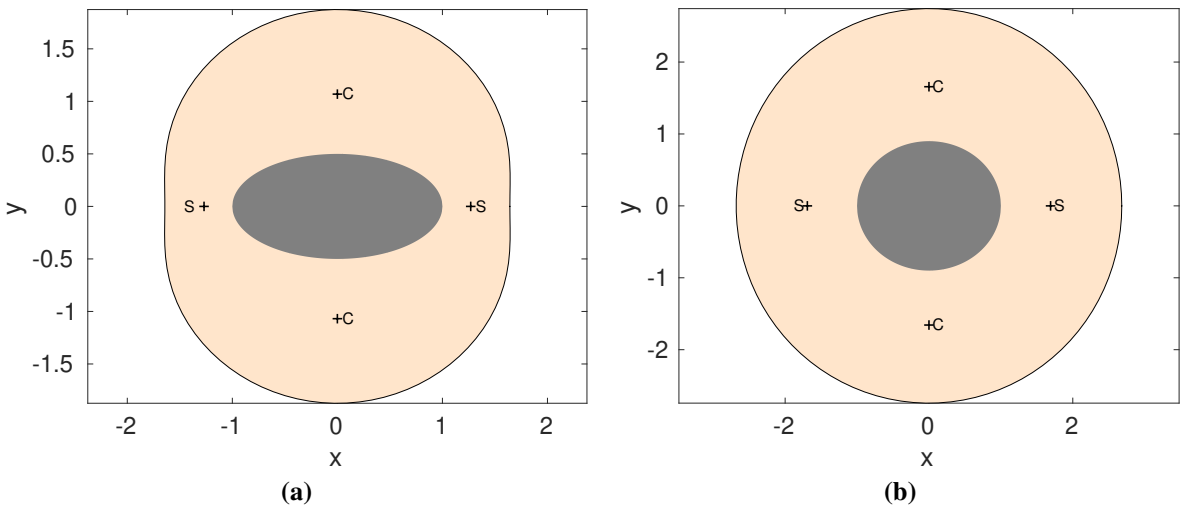

FIGURE 4.2: Representation of L_{eq} assuming $\theta = 0$ (thicker line) for an asteroid with period 5 h and $\bar{\beta} = \bar{\gamma} = 0.5$ (a), $\bar{\beta} = \bar{\gamma} = 0.9$ (b). To guarantee the orbital siphon effect the chain length must extend beyond the shaded region. Center (C) and Saddle (S) equilibrium points are also represented.

most linearly) with the asteroid rotational period. In fact, larger rotational periods will decrease the effect of the centrifugal-induced acceleration in the effective potential, thus increasing the altitude of the EPs and requiring longer chains for equilibrium. When the chain is anchored at $\phi_A = \pi/2$ the equilibrium length becomes longer, as shown in Fig. 4.2 (the difference with respect to the case $\phi_A = 0$ is more evident for more prolate ellipsoids). It can be shown that when $\bar{\gamma} < \bar{\beta}$ the equilibrium length decreases for a given period.

Figures 4.3c and 4.3d show the equilibrium length as a function of the chain angle θ for anchoring longitude $\phi_A = 0$ (left), $\phi_A = \pi/2$ (right) and a range of β assuming again $\gamma = \beta$. It is apparent that when $\theta \neq 0$ the equilibrium length increases (the plot is the same for $\theta \in [0, -\pi/2]$ due to symmetries and the case with $\phi_A = \pi$ and $\phi_A = 3\pi/2$ would be equivalent to $\phi_A = 0$ and $\phi_A = \pi/2$ respectively). Larger (smaller) asteroid densities will also increase (reduce) the magnitude of the gravitational acceleration thus increasing (reducing) the equilibrium length.

4.4.2 Siphon steady state velocity

The siphon steady state velocity v_{ss} is defined as the velocity of the chain when the time $t \to \infty$ for a given fixed θ, using a continuous mass distribution for the chain. From Eq. (3.41):

$$v_{ss} = \sqrt{\frac{2W}{1 - \left(\frac{n-1}{n}\right)^2}} \tag{4.23}$$

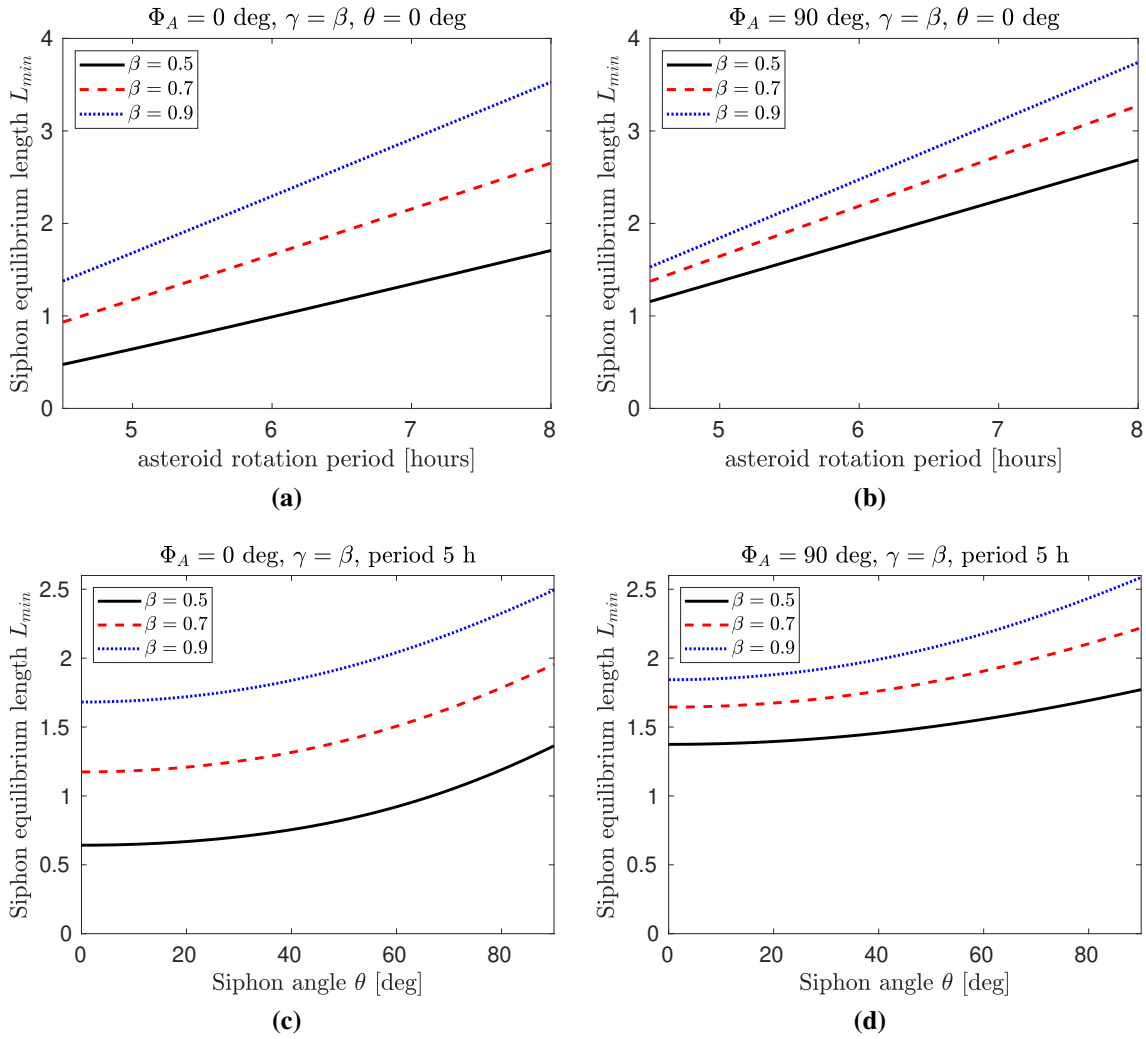

FIGURE 4.3: (a), (b): Equilibrium length L_{eq} as a function of the asteroid period for anchoring longitude $\phi_A = 0$ (a) and $\phi_A = \pi/2$ (b) assuming $\theta = 0$ in both cases. (c), (d): Equilibrium length as a function of the chain angle θ for anchoring longitude $\phi_A = 0$ (c) and $\phi_A = \pi/2$ (d) assuming $\theta = 0$ and a rotation period of 5 h.

where W is the work per unit mass done by the gravitational and centrifugal-induced forces to pull the chain up by the distance between two consecutive payload masses l:

$$W = \int_0^l a \, dl \tag{4.24}$$

where a is the acceleration of the chain. For a continuous mass distribution $n \to \infty$, $l \to L/n \to 0$ and the work per unit mass becomes

$$W = a\frac{L}{n} \tag{4.25}$$

where the acceleration can be written as

$$a = \frac{f_{\text{cont}}}{(1+D)L} \tag{4.26}$$

with f_{cont} given by Eq. (4.21). Note that the denominator of Eq. (4.26) is the overall mass of the siphon under the continuous mass distribution approximation, comprising the LS and DS. Substituting Eq. (4.25) into Eq.(4.23) and calculating the limit for $n \to \infty$, the steady state velocity can be written in non-dimensional form as:

$$\bar{v}_{ss} = \sqrt{\frac{1-D}{1+D}\left(\int_0^L \nabla\bar{U}(\bar{\chi})\cdot\hat{\mathbf{u}}_r d\bar{\chi}\right)} \tag{4.27}$$

When $D = 1$ (i.e., the LS is unloaded) it can be seen that $v_{\text{ss}} = 0$. Similarly, if the chain length is equal to the equilibrium length then, by Eq. (4.22) $\int_0^L \nabla U(\chi)\cdot\hat{\mathbf{u}}_r d\chi = 0$ and again $v_{\text{ss}} = 0$. Conversely, when the ratio $m_p/m_b \gg 1$ ($D \to 0$) the chain velocity is maximum, for a given asteroid, chain length, anchor longitude and angle θ. The terms including $\dot{\theta}$ do not appear in Eq. (4.27) as the steady state velocity is defined for fixed θ. Note that the same result given by Eq. (4.27) could have been obtained using Eq. (3.58), with $\mu_{ls} + \mu_{ds}$ in the denominator to take into account the combined mass of the LS and the DS.

It is instructive to simplify Eq. (4.27) in case of a spherical asteroid ($\bar{\beta} = \bar{\gamma} = 1$), which admits the closed-form solution

$$\bar{v}_{ss}^{sphere} = \sqrt{\frac{1-D}{1+D}\left[\frac{1}{2}\bar{\omega}^2(\bar{r}_L^2 - 1) - \frac{\bar{r}_L - 1}{\bar{r}_L}\right]} \tag{4.28}$$

where $\bar{r}_L = \sqrt{1+\bar{L}^2+2\bar{L}\cos\theta}$ is the distance between the CS and the center of the asteroid. Setting $D = 0$ and taking the chain normal to the asteroid surface ($\theta = 0$), Eq. (4.28) reduces to Eq. (3.43).

TABLE 4.1: Baseline simulation parameters. All units are non-dimensional. The selected siphon length corresponds to $1.5L_{\text{eq}}$. The parameter ω corresponds to an asteroid with density $\rho = 2500\,\text{kg}\,\text{m}^{-3}$ with rotation period of 5 h.

Asteroid	Angular velocity	ω	0.84
	Extent	β	0.5
		γ	0.5
Siphon	Length	L	0.96
	Initial CS mass	$M_{cs,0}$	100
	Number of payloads	$2n$	70
	Initial state	$\{h_0, \dot{h}_0, \theta_0, \dot{\theta}_0\}$	$\{0,0,0,0\}$
	DS to LS mass ratio	D	0
	Anchor longitude	ϕ_A	0

4.4.3 Siphon equilibrium angle

This parameter is defined as the angle θ_{eq} such that the overall torque T with respect to the anchor point is zero, when the chain is approximated with a continuous mass distribution and $\dot{h} = v_{ss}$. As it will be shown in Sec. 4.5, θ_{eq} is an indicator of the average oscillation θ of the siphon. From Eq. (4.14), substituting the sums with integrals, θ_{eq} can be found as the solution of

$$\frac{\bar{L}^2}{2}(D-1)\bar{v}_{ss}(\theta_{\text{eq}}) + \bar{L}^2 M^*_{cs} \nabla\bar{U}(\bar{L}) \cdot \hat{\mathbf{u}}_\perp + (1+D)\int_0^{\bar{L}} \nabla\bar{U}(\bar{\chi}) \cdot \hat{\mathbf{u}}_\perp \bar{\chi} d\bar{\chi} = 0 \tag{4.29}$$

where $\bar{v}_{ss}(\theta_{\text{eq}})$ is the steady state velocity calculated at the equilibrium angle. Here M^*_{cs} is the mass of the CS scaled with respect to the total mass on the LS of the siphon.

4.5 Results

In this section the orbital siphon dynamics (Eqs. (4.15)) are integrated for a given choice of asteroid and siphon parameters. Unless explicitly specified in the text, the baseline simulation parameters are listed in Table 4.1. Whenever the context is clear the upper-bar notation is removed from non-dimensional variables.

Figure 4.4 shows the angle θ (Fig. 4.4a), siphon angular velocity $\dot{\theta}$ (Fig. 4.4b), chain velocity $\dot{h}$ (Fig. 4.4c) and CS mass M_{cs} (Fig. 4.4d) as a function of time for two different initial states: $\{h_0, \dot{h}_0, \theta_0, \dot{\theta}_0\} = \{0,0,0,0\}$ (case A) and $\{h_0, \dot{h}_0, \theta_0, \dot{\theta}_0\} = \{0, v_{ss}, \theta_{\text{eq}}, 0\}$ (case B). In case A, the siphon is initially aligned with the local vertical and is at rest. In case B, the siphon is initialized at its equilibrium angle θ_{eq} for the initial CS mass $M_{cs,0}$, and its initial velocity $\dot{h}_0$ is the steady state velocity at θ_{eq}. Figures 4.4a and 4.4c also show the equilibrium angle θ_{eq} (blue, dashed line) for the current CS mass at time t and the steady state velocity v_{ss} respectively. Some relevant information can be inferred:

1. The siphon exhibits a damped oscillatory behaviour. In both cases, the siphon angle θ

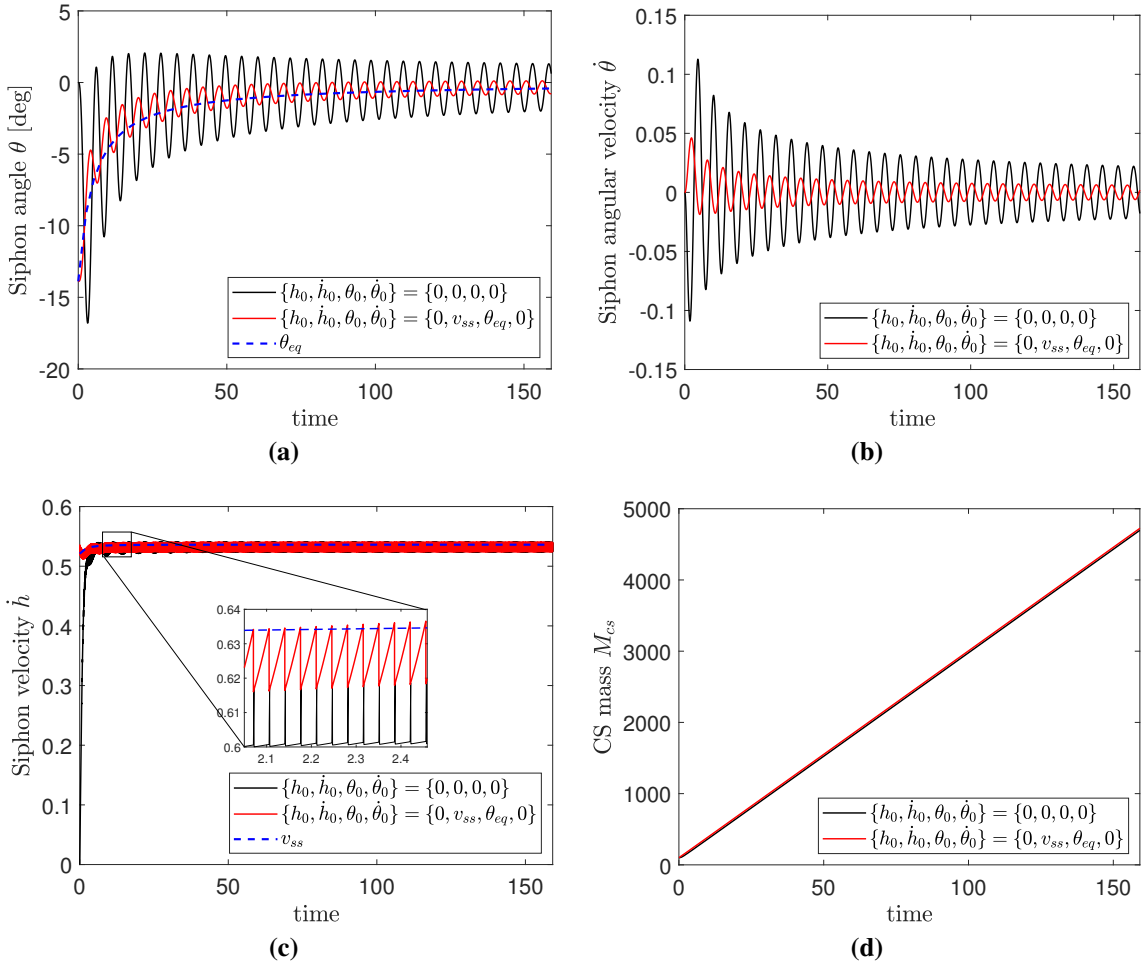

FIGURE 4.4: Siphon angle θ (a), non-dimensional siphon angular velocity $\dot{\theta}$ (b), non-dimensional chain velocity $\dot{h}$ (c) and non-dimensional CS mass M_{cs}, (d), as a function of time. The blue dotted curve in Figs. 4.4a and 4.4c represent the instantaneous equilibrium angle (Eq. 4.29) and the steady state velocity (Eq. (4.27)) respectively. The time is in non-dimensional units, with scale factor $\omega_{\text{crit}}^{-1}$.

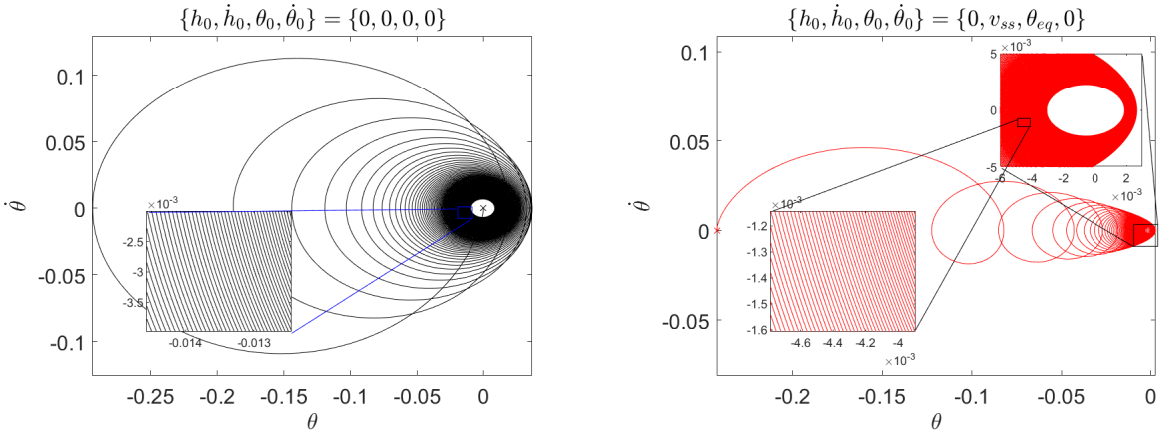

FIGURE 4.5: Siphon trajectories in the phase space $(\theta, \dot{\theta})$ for a 33-day simulation, for different initial conditions, $\{h_0, \dot{h}_0, \theta_0, \dot{\theta}_0\} = \{0, 0, 0, 0\}$ (a) and $\{h_0, \dot{h}_0, \theta_0, \dot{\theta}_0\} = \{0, v_{ss}, \theta_{\text{eq}}, 0\}$ (b). The insets are close-up views near $(\theta, \dot{\theta}) \approx (0, 0)$.

oscillates about the equilibrium angle θ_{eq}, and $\theta_{eq} \to 0$, as $t \to \infty$. The amplitude of the oscillations is smaller if the siphon is initialised at the equilibrium angle (case B).

2. The period of the oscillations is comparable with the asteroid period.

3. The chain velocity changes at two different frequencies (see Fig. 4.4c): a lower frequency is associated with the variation of the siphon angle θ (which regulates the magnitude of the net radial force on the chain) while the higher frequency is due to the bucket refilling. Note that at each bucket refilling, the chain velocity changes according to Eq. (4.16). In the long term, the chain velocity does not diverge but oscillates about an average value which is well approximated by v_{ss}.

4. The CS mass varies almost linearly over time and it is slightly larger in case B due to the larger velocity of the chain at the beginning of the simulation.

As anticipated in Sec. 4.3.4, the damping effect is progressively reduced as the mass of the CS increases and the siphon exhibits stable oscillations about θ_{eq}. Figure 4.5 shows the results of a longer simulation (33 days) in the phase space $(\theta, \dot{\theta})$ for case A (4.5a) and B (4.5b). The initial state at $t = 0$ is marked with a cross. As expected, the equilibrium of the system gradually shifts towards $(\theta, \dot{\theta}) = (0, 0)$ and the damping effect is progressively reduced over time.

Figure 4.6 shows the siphon angle (a) and velocity (b) if material is released at the top of the siphon, rather than being collected at the CS. In this case, the CS mass remains constant and therefore the CS torque does not increase with M_{cs} as in the previous case. Again, the siphon oscillates about the equilibrium angle with period comparable to the asteroid period, however, in this case the equilibrium angle θ_{eq} does not decrease to 0 as $t \to \infty$. The initial amplitude of the oscillation is significantly reduced when the siphon is initialized at the equilibrium angle

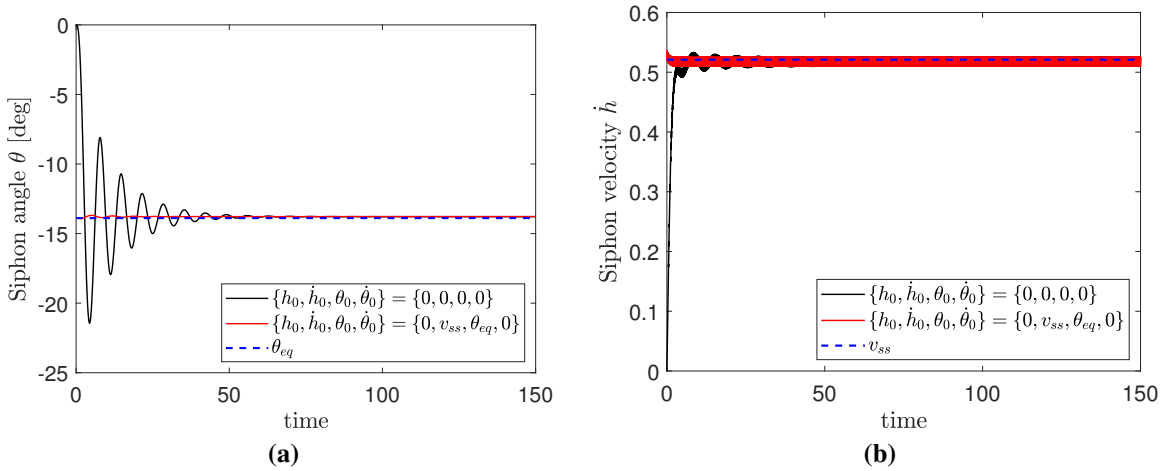

FIGURE 4.6: Siphon angle θ (a) and chain velocity $\dot{h}$ (b) as a function of time assuming material is not collected at the CS but released to escape.

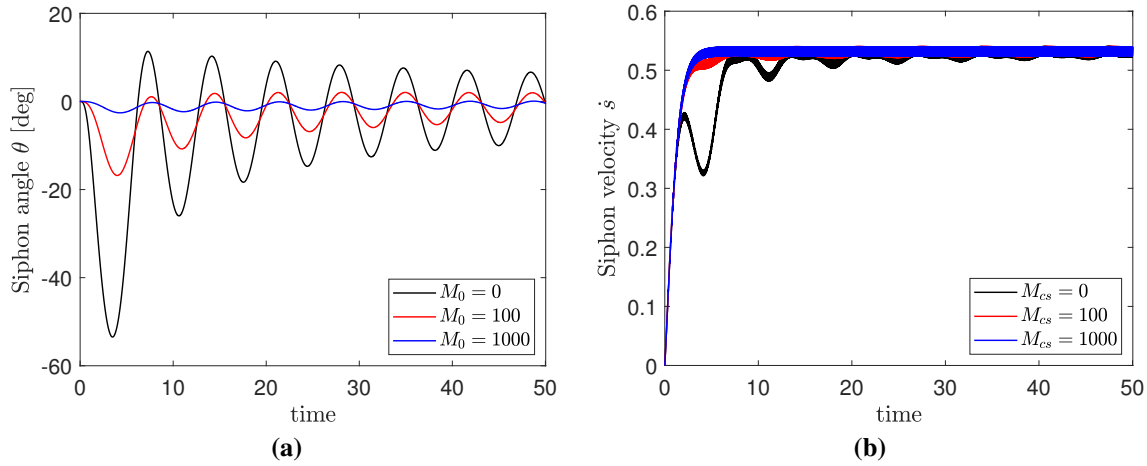

FIGURE 4.7: Siphon angle θ (a) and chain velocity $\dot{h}$ (b) as a function of time for different CS mass at $t = 0$, $M_{cs,0} = 0$, $M_{cs,0} = 100$, $M_{cs,0} = 1000$.

$\theta = \theta_{eq}$. In the long term, the chain angle θ reaches the asymptotic value $\theta_{eq} < 0$. The steady state velocity is slightly smaller than the case represented in Fig. 4.4c: in fact, the siphon force is smaller if the chain is not aligned with the local vertical, and therefore v_l is reduced (Eq. (3.58)).

Figure 4.7 shows the siphon angle and chain velocity as a function of time for variable initial CS masses $M_{cs,0}$. The initial CS mass influences the amplitude of the oscillations, in particular, the initial overshoot. As the initial CS mass increases, the Coriolis torque becomes negligible with respect to the centrifugal-induced torque caused by the CS, thus reducing the magnitude of θ.

Figure 4.8 shows the siphon angle and chain velocity as a function of time for variable mass ratios D. The mass ratio D mainly affects the chain velocity. As D increases, the ratio between the mass of the payloads and the mass of the buckets decreases as dictated by Eq. (4.11), thus reducing the radial force on the chain (Eq. (4.10)), eventually reducing its velocity. As a

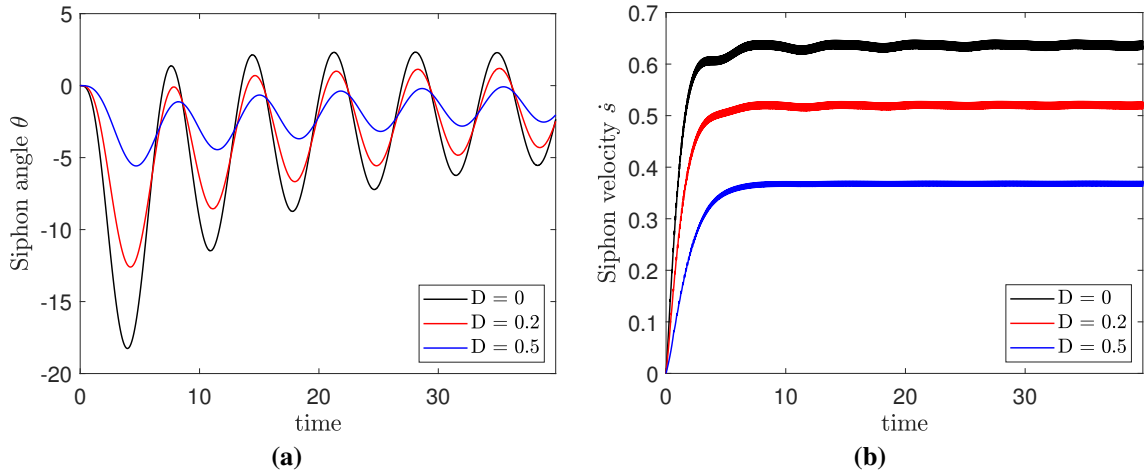

FIGURE 4.8: Siphon angle θ (a) and chain velocity $\dot{h}$ (b) as a function of time for $D = 0$, $D = 0.2$ and $D = 0.5$.

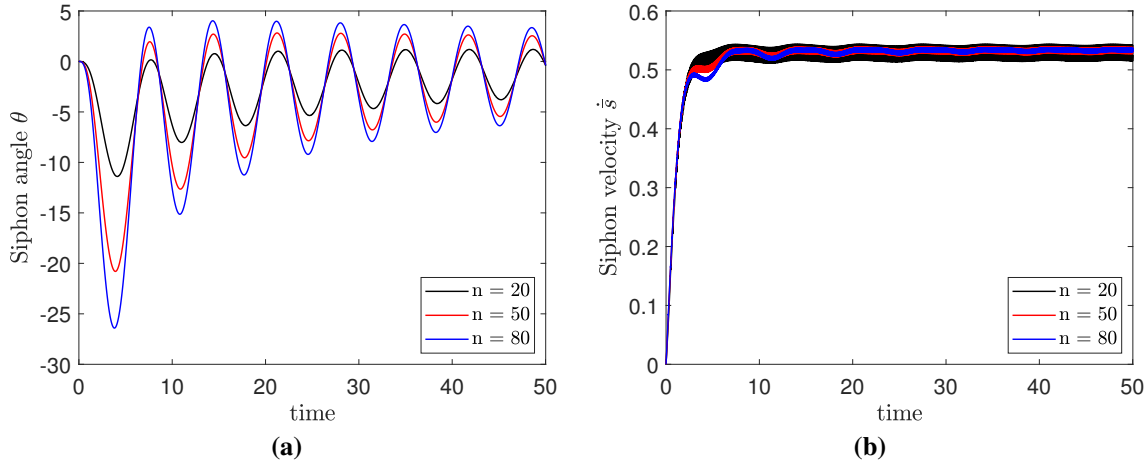

FIGURE 4.9: Siphon angle θ (a) and chain velocity $\dot{h}$ (b) as a function of time for $n = 20$, $n = 50$ and $n = 80$.

consequence, also the steady state velocity decreases, as predicted by Eq. (4.27).

Figure 4.9 shows the siphon angle and chain velocity as a function of time for $n = 20$, $n = 50$ and $n = 80$. The number of payloads affects the magnitude of the Coriolis torque on the chain: more payloads on the chain will lead to larger oscillations. The chain velocity is almost unaffected even though as n increases the variation of $\dot{h}$ between consecutive bucket-refilling events slightly decreases (Fig. 4.9b): in fact, by increasing n with a fixed chain length, the distance l between consecutive buckets decreases and therefore the frequency of payload refilling increases.

Figure 4.10 shows the siphon angle and chain velocity as a function of time for the two siphon lengths $L = 1.2L_{\text{eq}}$ and $L = 1.7L_{\text{eq}}$. A larger chain length will cause a larger radial velocity. Note that, although the oscillations have slight different phases, the period of the oscillations does not vary significantly between the two cases.

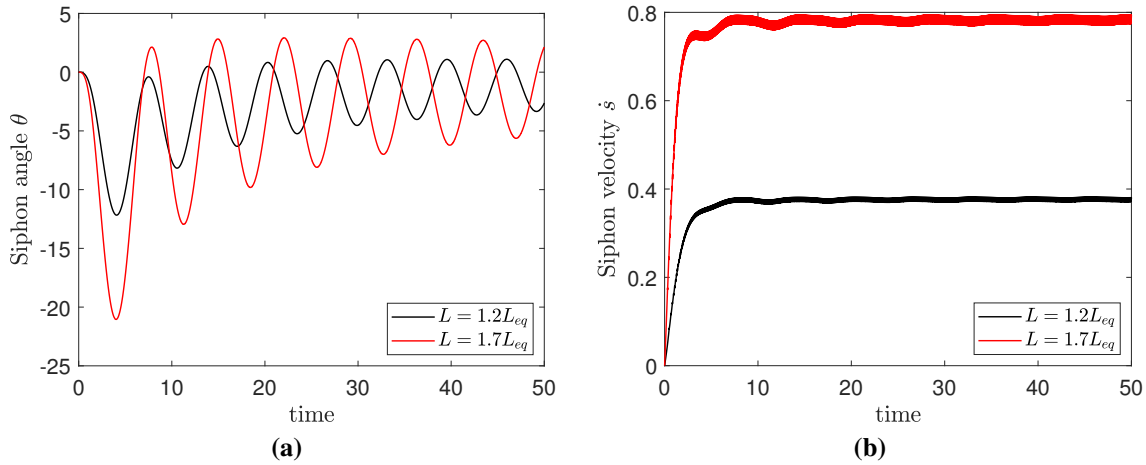

FIGURE 4.10: Siphon angle θ (a) and chain velocity $\dot{h}$ (b) as a function of time for $L = 1.2L_{\text{eq}}$ and $L = 1.7L_{\text{eq}}$.

It has been noted that the parameters θ_{eq} and v_{ss} are good approximations of the siphon angle and the chain velocity at steady state. Moreover, the CS mass varies almost linearly with time. Therefore, it is instructive to investigate how the equilibrium angle and chain velocity vary as a function of the CS mass M_{cs}, by varying other parameters such as the asteroid shape and the anchor longitude. Figure 4.11 illustrates the variation of θ_{eq} and v_{ss} as a function of the CS mass for a range of chain lengths L and anchor longitudes ($\phi_A = 0$, $\phi_A = \pi/4$, $\phi_A = \pi/2$), taking an asteroid with $\beta = \gamma = 0.3$ and other parameters as indicated in Table 4.1. Figure 4.12, shows the same parameters, with $\beta = \gamma = 0.8$. The siphon length is here chosen as a function of the minimum siphon length L_{eq}, calculated for $\theta = 0$ ($1.1L_{\text{eq}}$ (black curve), $1.5L_{\text{eq}}$ (dashed red curve) and $2.5L_{\text{eq}}$ (dotted blue curve)). To guarantee impact avoidance with the surface of the asteroid, the equilibrium angle θ_{eq} cannot exceed the threshold angle θ_{lim}, which depends on the anchor location and β. The parameter θ_{lim} is defined as the angle between OA and the tangent to the anchor point in the equatorial plane, in the direction shown in Fig. 4.13 (the complementary angle to θ_{lim} is not considered, since the siphon will rotate clockwise due to the Coriolis torque). For a siphon anchored at the longest or shortest equatorial end, $\theta_{\text{lim}} = -\pi/2$ independent of β, whereas for $\phi_A = \pi/4$, $\theta_{\text{lim}} \approx -50\,\text{deg}$ when $\beta = 0.3$ and $\theta_{\text{lim}} \approx -70\,\text{deg}$ when $\beta = 0.8$. In all the cases represented, the equilibrium angle decreases as the CS mass increases and v_{ss} is constant when the ratio M^*_{cs} between the CS mass and the LS of the siphon is larger than 10^2. In particular, for $\phi_A = 0$ or $\phi_A = \pi/2$, $\theta_{\text{eq}} \to 0$ as the CS mass increases, and this holds for any $L > L_{\text{eq}}$ and does not depend on the asteroid shape. Note that at these anchor locations, the direction $\theta = 0$ corresponds to the local vertical. Conversely, the effect of the asteroid shape influences θ_{eq} for intermediate anchor locations: the equilibrium angle for large values of the CS mass decreases for prolate bodies and this effect is enhanced if the siphon length is close to the equilibrium length (see Figs. 4.11c and 4.12d). The equilibrium angle is not defined for some small values of M^*_{cs}. In these cases, the siphon might exceed θ_{lim} during the initial overshoot and

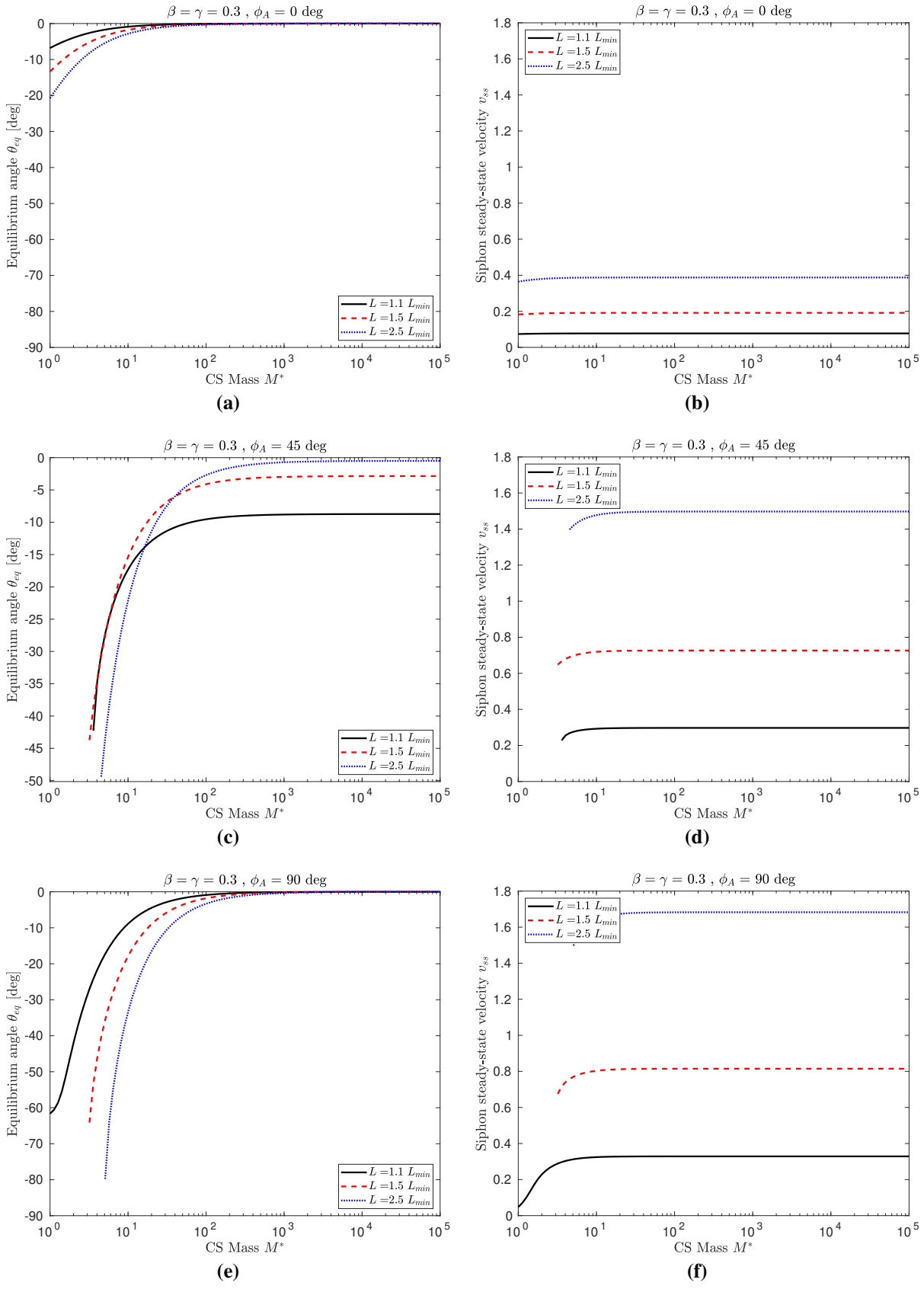

FIGURE 4.11: Equilibrium angle θ_{eq} as a function of the CS mass M^*_{cs}, for a range of anchor longitudes and $\beta = \gamma = 0.3$.

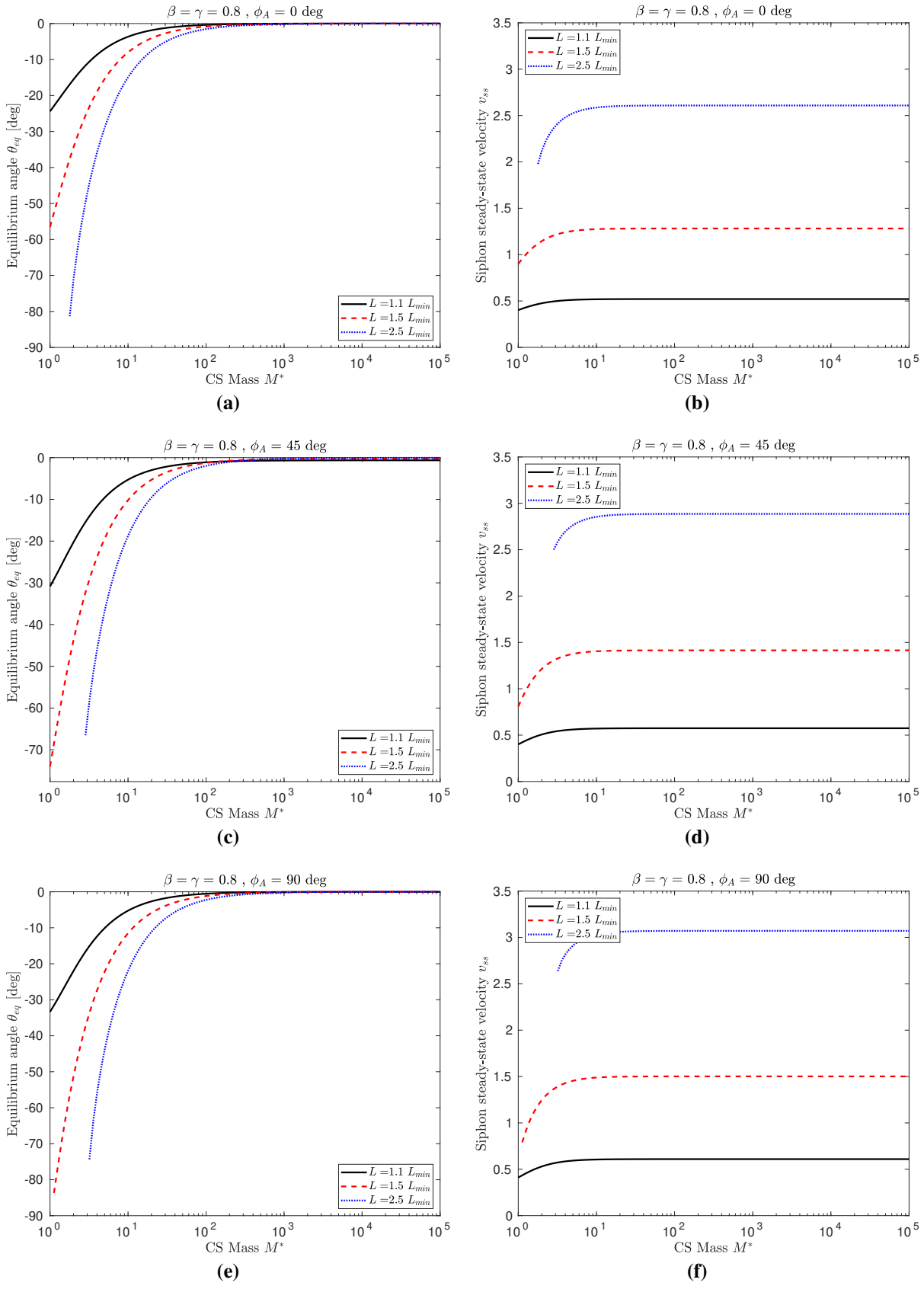

FIGURE 4.12: Equilibrium angle θ_{eq} as a function of the CS mass M^*_{cs}, for a range of anchor longitudes and $\beta = \gamma = 0.8$.

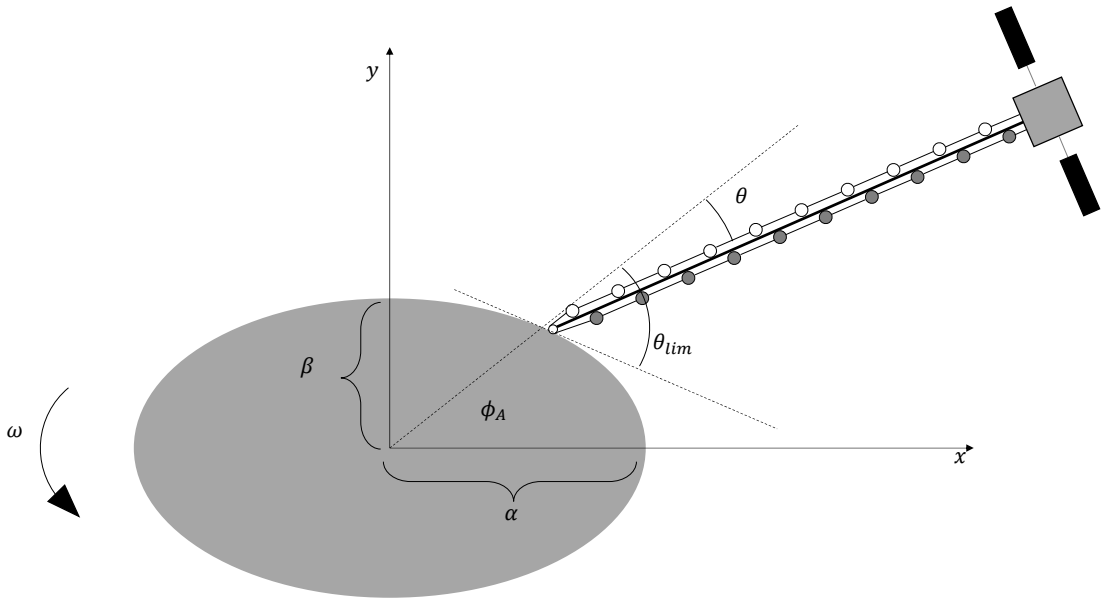

FIGURE 4.13: Maximum siphon angle θ_{lim}.

impact onto the asteroid surface. For longer chains, a larger initial CS mass is required to ensure $|\theta_{\text{eq}}| \leq |\theta_{\text{lim}}|$. Therefore, for a given initial CS mass the siphon cannot be arbitrarily long: it is possible to define an upper bound on the siphon length that guarantees impact avoidance with the surface. Note that a lower bound also exists, to ensure that $L > L_{\text{eq}}$.

In summary, the following remarks can be made:

- An orbital siphon effect is generated if the mass on the LS is larger than the mass of the DS (i.e., when $D < 1$): the buckets on the LS are therefore pulled towards the CS while buckets on the DS cycle back to the anchor for refilling.

- The minimum siphon length required to generate the siphon effect depends on the anchor location. Smaller chains can be used when the siphon is anchored at the longest equatorial end.

- The orbital siphon effect introduces torques with respect to the anchor point, inducing damped oscillation of the chain. In the long term the equilibrium angle approaches the local vertical (for chains anchored at the longest or shortest equatorial end).

- As for a non-rotating siphon (Chapter 3), the radial velocity of the chain does not diverge, although a positive force is always acting on the LS. This is due to conservation of linear momentum during the bucket refilling process.

- The behaviour of the discrete chain can be approximated by a continuous mass distribution. This allows an estimation of the equilibrium angle and the chain radial velocity as a function of the CS mass and asteroid shape. The equilibrium angle approaches a constant value when the mass of the CS is large. In particular, if the siphon is anchored at

the longest or smallest equatorial end, the siphon tends to align with the local vertical. However, if material is released to orbit or escape rather than being collected to the CS, the equilibrium angle is negative, although the oscillation are still damped.

- Similarly to the results obtained in Chapter 3, by increasing the siphon length, the radial velocity of the chain increases and therefore the rate of payload material released to the CS also increases. As expected, larger chain velocities are achieved when the ratio $D \to 0$, i.e., when the mass of the buckets becomes negligible with respect to the mass of the payloads. In dimensional units, for siphon lengths comparable with the asteroid largest semi-major axis, the chain velocity is on the order of centimetres per second. For example, taking the asteroid Bennu (details in Table 2.1), a siphon with length $L = 0.6\alpha$ has a radial velocity of approximately $2.5\,\mathrm{cm\,s^{-1}}$.

4.6 Transfers to equilibrium points

It has been shown that as the siphon delivers material to the CS it will eventually reach a condition of stable oscillation and the velocity of the chain does not diverge. Due to the requirement $L > L_{\mathrm{eq}}$ a released mass cannot intersect either the asteroid or any EP, and will eventually escape from the asteroid. This is a useful scenario if the material has to be sent to a higher energy orbit or to escape.

The existence of equilibrium points, however, offers scope for further analysis. It has been shown in Sec. 2.4 that if the period of the asteroid is above a critical value depending on its shape, the CEPs are stable. Under such conditions, these points could be used in principle as gravitational depots for material. Taking advantage of these equilibria may therefore be useful in a large-scale mining scenario. For example, CEPs might host an orbiting catcher, receiving material from the siphon, for temporary storage or further processing.

Transfer of material to EPs may also be beneficial if the mined asteroid is a rubble pile with low cohesive strength [117], thus reducing the anchor force required to hold the orbital siphon to the asteroid surface. A conservative estimate of the required anchor force, assuming the CS mass M_{cs} is much larger than the mass of the siphon, is $M_{cs}\omega^2(\alpha + L)$, i.e., the centrifugal-induced force acting on the CS, for anchoring at the longest equatorial end ($\phi_A = 0$) and $\theta = 0$. For example, for a siphon with length $L = L_{\mathrm{eq}}$ anchored at the asteroid Bennu (Table 2.1), the anchor force (in Newtons) scales as $10^{-6}M_{cs}$. Achievable anchor forces on rubble piles are on the order of 10 N for cohesion levels of 10 Pa [87]. In a large-scale mining scenario, where the processed mass is larger than 10^3 tonnes, the required force to keep this mass at the CS would be on the order of 10^2 N, hence one order of magnitude larger then the value suggested in Ref. [87].

A possible mechanism to deliver material to the CEPs is by employing a mass driver from the surface. Although the energy requirements are expected to be very small (due to the low-gravity on a typical near-Earth asteroid) it will be shown that the orbital siphon mechanism can

offer in principle a more energy efficient way to deliver payloads to the CEPs.

As an example, the analysis proposed in the following sections is referred to the asteroid Bennu (Table 2.1) which has stable CEPs under the triaxial ellipsoid model.

4.6.1 Material transfer from the surface to a stable CEP

The minimum amount of energy required to send material to any location around an asteroid from a given position at the surface can be derived analytically. In particular, let $\mathscr{E}_0$ be the total energy per unit mass at the initial location of the material and let $\mathscr{E}_c$ be the energy per unit mass at the CEPs (note that the two CEPs have the same energy due to symmetry in the ellipsoid model). If a change in velocity Δv is applied at the initial point then, in order to intersect the CEP, the energy of the transfer trajectory should satisfy

$$\mathscr{E}_0 + \frac{1}{2}\Delta v^2 \geq \mathscr{E}_c \tag{4.30}$$

If Eq. (4.30) is not satisfied, then the position of the CEPs would be inside the forbidden region associated with the zero velocity curve of the transfer trajectory. Using dimensional units applied to the asteroid Bennu, a transfer from the longest end of the ellipsoid to the CEP requires $\Delta v \geq 6.1\,\mathrm{cm\,s^{-1}}$, whereas a transfer from the shortest end to the CEP requires $\Delta v > 5.9\,\mathrm{cm\,s^{-1}}$. Let $\Delta v^{min}_{direct} = 5.9\,\mathrm{cm\,s^{-1}}$ be the minimum of these two values, which will be used in later analysis.

Figure 4.14 shows an example of such trajectory in the asteroid rotating frame, for several departure longitudes. The trajectories are obtained by solving a boundary value problem (with constraints on the initial and final position) and controlling the initial Δv at the departure on the surface. Here, Δv_1 represents the change in velocity required to insert the particle into the trajectory, whereas Δv_2 is the change in velocity required to stop the particle at the equilibrium point.

4.6.2 Exploiting siphon dynamics to transfer material to a stable CEP

The proposed strategy is now to exploit the siphon dynamics to induce oscillations to the chain in order to increase the energy of the CS and make the CEP accessible, using a swing-and-release technique.

A possible method to avoid the intrinsic damping observed in Sec. 4.5 is to stop the chain during the counter-clockwise rotation of the siphon, to avoid the Coriolis torque which would reduce the oscillation amplitude. In particular, for a siphon anchored at $\phi_A = 0$ with $\theta_0 = 0$:

1. While the LS delivers material to the CS, the Coriolis torque will induce a clockwise rotation ($\dot{\theta} < 0$).

2. When $\dot{\theta} = 0$ the chain is stopped, so $\dot{h} = 0$.

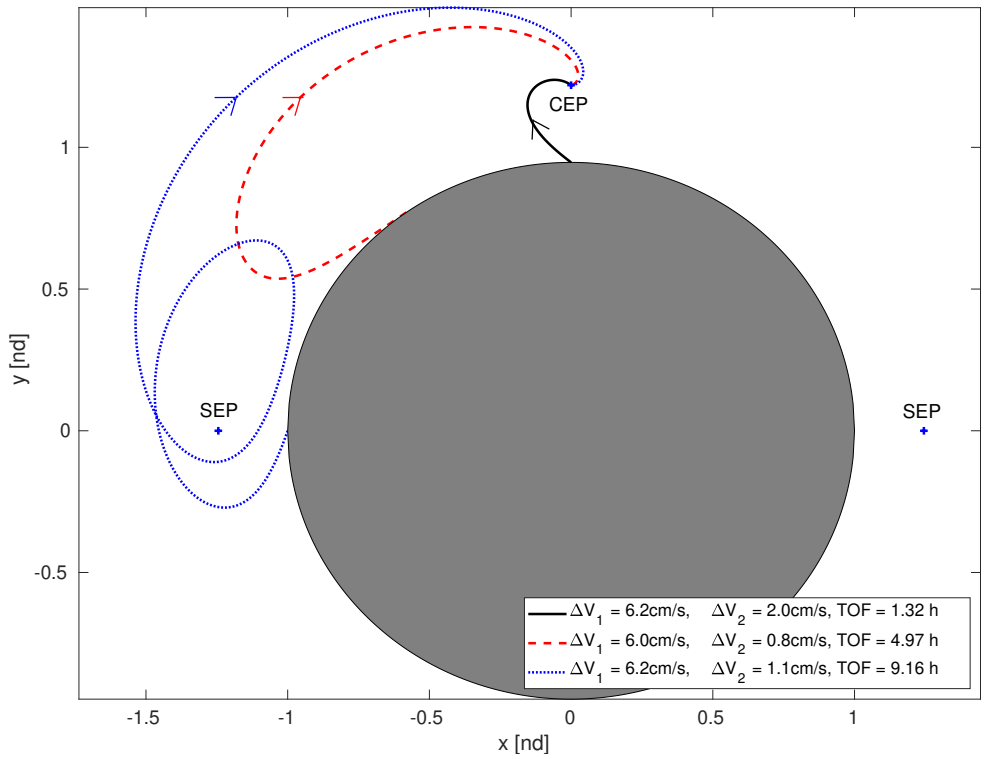

FIGURE 4.14: Example of low-Δv transfer trajectories with a range of time of flight (TOF) from the surface of the asteroid Bennu to one of the two CEPs.

3. As no Coriolis torque is now acting on the siphon (due to the braked chain), the siphon operates like a standard undamped pendulum, reaching $\dot{\theta} = 0$, without reducing the oscillation amplitude.

4. When $\dot{\theta} = 0$ the chain brake is now released an the process repeated.

The maximum velocity which can be reached by the CS depends on the maximum amplitude of the chain $\theta_{\max}$ and on the length of the chain L. The maximum amplitude $\theta_{\max}$ must guarantee $L > L_{\text{eq}}(\theta_{\max})$ where $L_{\text{eq}}(\theta_{\max})$ is the equilibrium length calculated at $\theta = \theta_{\max}$. In any case, $\theta_{\max} < \pi/2$ is necessary to avoid contact between the siphon and the asteroid surface. The length L is chosen such that, when $\theta = 0$, the CS velocity vector is tangent to a periodic orbit (PO) passing in close proximity to the CEPs. The PO is selected from the family displayed in Fig. 4.15a. These orbits are direct POs generated using standard differential correction algorithms. Suitable initial conditions were found via Ref. [120] and a continuation method was used to extend the family. Figure 4.15a shows some of the POs passing in close proximity to the CEPs. The orbits of this family are particularly interesting as they cross the x-axis with $\dot{y} = 0$, and therefore they match the velocity direction of the CS when $\theta = 0$. In particular, the trajectory represented in red, intersects both CEPs. This PO, with a period of 12.62 h, is selected as a candidate transfer trajectory which will deliver material from the CS to one of the two CEPs, where an orbiting catcher is envisaged to capture the transferred material. It can be shown, using the stability index method explained in Ref. [55], that this periodic orbit is stable. The

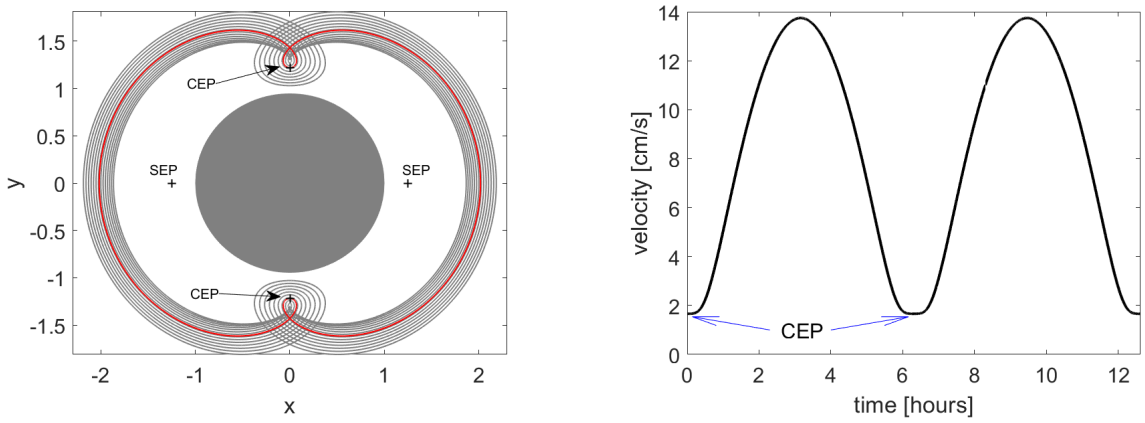

(a) (b)

FIGURE 4.15: (a): Family of periodic orbits around Bennu. The trajectory intersecting the two CEPs is marked in red. (b): Velocity of the periodic orbit intersecting the CEPs. Lower value of the velocity are reached at the intersection with the CEPs.

velocity of this PO as a function of time is represented in Fig. 4.15b using dimensional units. The maximum velocity $v_{po} = 13.8\,\mathrm{cm\,s^{-1}}$ is reached at the crossing with the x-axis, whereas the lowest velocity is reached at the intersection with the two CEPs. The selected PO crosses the x-axis at $\bar{x} = 2.02$ and therefore, with the siphon anchored at $\phi_A = 0$, the siphon length must be $\bar{L} = 2.02 - 1 = 1.02$, i.e., $L = 288\,\mathrm{m}$. The maximum angle $\theta_{\max}$ which guarantees $L > L_{eq}(\theta_{\max})$ is $\theta_{\max} = 80.3\,\mathrm{deg}$.

Figure 4.16 shows the chain angle (a), CS velocity magnitude (b) and CS mass (c) as a function of time, during the angular acceleration of the siphon using the sequence described above, assuming $n = 40$, $\bar{M}_{cs,0} = 50$ and $D = 0$. The braking phases are plotted with a red line. It takes approximately 175 h to reach the maximum amplitude $\theta_{\max}$ and the CS mass at this point is $\bar{M}_{cs,f} = 1937$. In such conditions, the maximum velocity reached by the CS at $\theta = 0$ is $v_{cs}^{max} = 12.2\,\mathrm{cm\,s^{-1}}$. Note that variations of the initial CS mass (that depends on the volume of material the CS can host, the mass of the processing units and other sub-systems) will clearly affect $\bar{M}_{cs,f}$ and the time required to reach $\theta_{\max}$. In particular, larger $M_{cs,0}$ will lead to a larger final mass and longer time to reach the maximum amplitude.

Once $\theta_{\max}$ is reached, two different methods are proposed to deliver material to one of the two stable CEPs. In the first scenario, the entire CS is released from the siphon and inserted into the PO intersecting the CEPs (Fig. 4.17a), whereas in the second scenario the CS remains attached to the chain and sub-units of payload material are inserted into the PO intersecting the CEPs (Fig. 4.17b).

Scenario 1 The entire CS is released from the siphon and inserted into the PO by applying a small $\Delta v = v_{po} - v_{cs}^{max} = 1.6\,\mathrm{cm\,s^{-1}}$. The CS will then release the material to a catcher located at one of the two CEPs while the siphon oscillation is reduced through a dissipation mechanism at

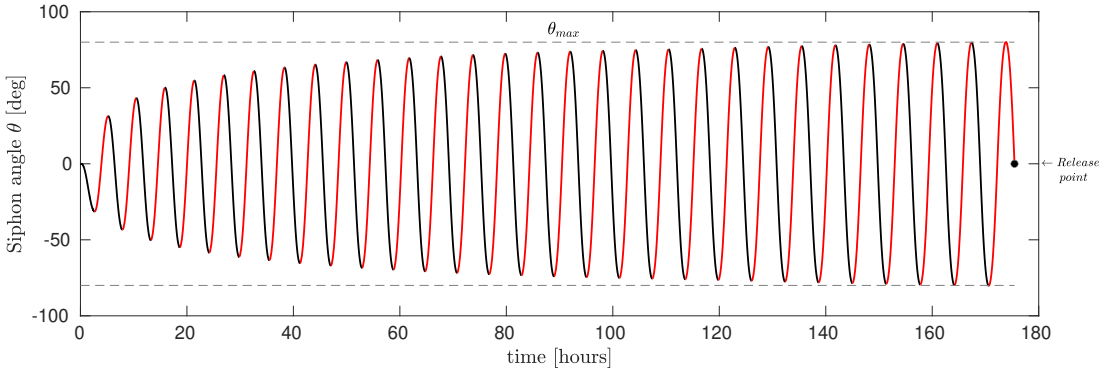

(a)

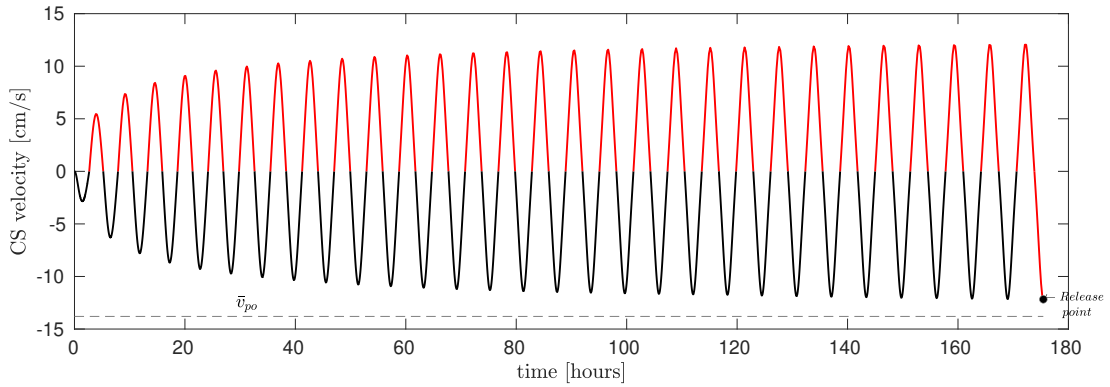

(b)

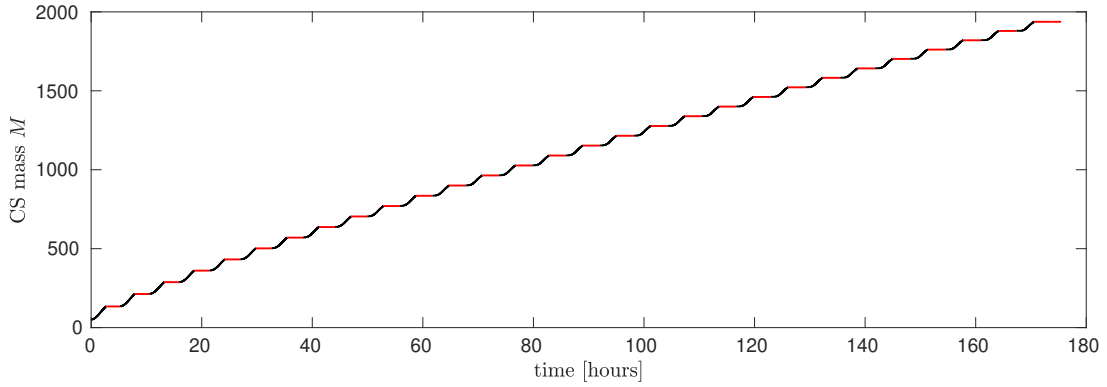

(c)

FIGURE 4.16: Chain angle (a), CS velocity (b) and CS mass (c) as a function of time during the acceleration process. The red lines represent the braking phases, when $\dot{h} = 0$.

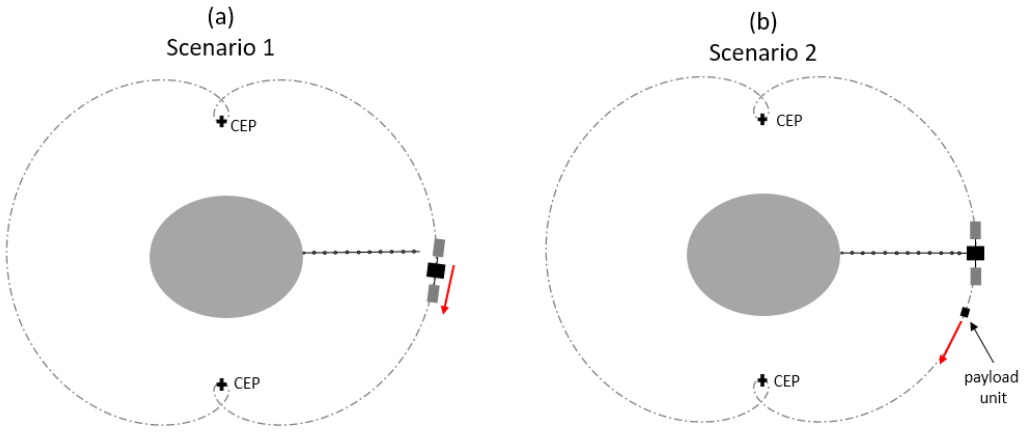

FIGURE 4.17: Two proposed release scenarios to transfer payload material from the siphon to the CEP. (a): the entire CS is released from the siphon once the maximum CS velocity v_{cs}^{max} is reached. (b): a payload unit is released from the CS, while the CS remains attached to the siphon.

the anchor. After one period of the PO, the CS will dock with the siphon, transferring its angular momentum and thus inducing a rotation on the siphon. Assuming a perfectly inelastic impact, the siphon angular velocity $\dot{\theta}$ after docking will be

$$\dot{\theta} = \frac{M_{cs,0} L v_{po}}{\sum_{i=1}^{2n} m_i s_i^2 + M_{cs,0} L^2} \tag{4.31}$$

The delivery of payloads to the CS then restarts, until M_f is reached again and the process continues. Note that, due to $\dot{\theta} \neq 0$ after the CS docking, the time to reach $\theta_{\max}$ will be shorter in this phase.

The overall outcome of this process is the periodic transfer of material from the asteroid surface to a CEP with $\Delta v < \Delta v_{direct}^{min}$.

Scenario 2 In this scenario, the material collected is organized into sub-units with mass δm, then accelerated by the CS through a spring system or a linear actuator to reach v_{po}. When a single unit δm is released, the siphon angular velocity decreases to conserve the overall angular momentum:

$$\left(\sum_{i=1}^{2n} m_i s_i^2 + M_{cs} L^2 \right) \dot{\theta}_1 = \left(\sum_{i=1}^{2n} m_i s_i^2 + (M_{cs} - \delta m) L^2 \right) \dot{\theta}_2 + L \delta M_{cs} v_{po} \tag{4.32}$$

where $\dot{\theta}_1$ and $\dot{\theta}_2$ are the siphon angular velocities before and after the Δv. If $\delta m << M_{cs}$ and the inertia of the chain is much smaller than the inertia of the CS (which is true at the end of the

acceleration process) then

$$\dot{\theta}_2 \approx \dot{\theta}_1 \left[1 - \frac{\delta m}{M_{cs}} \frac{\Delta v / L}{\dot{\theta}_1} \right]. \tag{4.33}$$

If the chain is stopped while the masses δm are inserted into the PO, the angular velocity of the chain would decrease at each unit release according to Eq. (4.33) (since the CS mass M_{cs} would decrease). This problem can be circumvented by continuously delivering mass to the CS (using the same sequence described at the beginning of this section) while releasing units δm after each period of oscillation of the siphon. Nonetheless, since it is not possible to tune δm such that the rate of incoming/outcoming mass to/from the CS is the same, part of the material delivered to the CS has to be sent to escape, in order to keep the CS mass constant.

Using Eq. (4.32) coupled with the siphon equations of motion (4.15) it can be shown that $\delta m = 1.65$ units of mass can be transferred to the CEP every 6.4 h at the cost of 56 units of mass released to escape in the same amount of time, while keeping $\Delta v < \Delta v^{min}_{direct}$.

The large ratio between the escape mass and the released mass in the second scenario makes such solution less viable than the first one. However, a combination between the two methods can be used. Whenever a large fraction of material has to be delivered to the CEPs for storing, the method described in *Scenario 1* is used. Conversely, if a large fraction of material has to be released to escape (e.g., waste) the double release sequence described in *Scenario 2* is used. Although both methods pose a number of undoubtedly challenging engineering issues that should be further discussed and the effects of additional perturbations (e.g., solar radiation pressure) should be included in the future models, this preliminary study has shown that the siphon dynamics can be leveraged to deliver resource payloads to the stable equilibrium points with a smaller Δv than direct transfer from the asteroid surface using mass drivers, which can be beneficial in a large-scale mining scenario.

4.6.3 Transfers to retrograde orbits

It was noted in Sect 2.4 that fast rotators are characterised by unstable CEPs. In this case, material transfer to CEPs would not be effective, since small perturbations, for example due to solar radiation pressure, will cause the material to migrate from the equilibrium point towards the asteroid or to escape. Moreover, when considering more complex asteroid shape models, the stability of the centres might be very sensitive to small variations in the asteroid gravity field and shape [122]. A different strategy for material transfer into orbit can be envisaged if CEPs are unstable, taking advantage of retrograde periodic orbits. Retrograde orbits rotate opposite to the asteroid (with respect to inertial space) and they are generally more stable than direct orbits or EPs [120].

In this case, the orbiting catcher would be placed on a stable retrograde orbit intersecting the CS when $\theta = 0$, and material is periodically transferred from the CS to the orbiting catcher, each time the catcher completes one revolution around the asteroid (or at multiples of the revolution

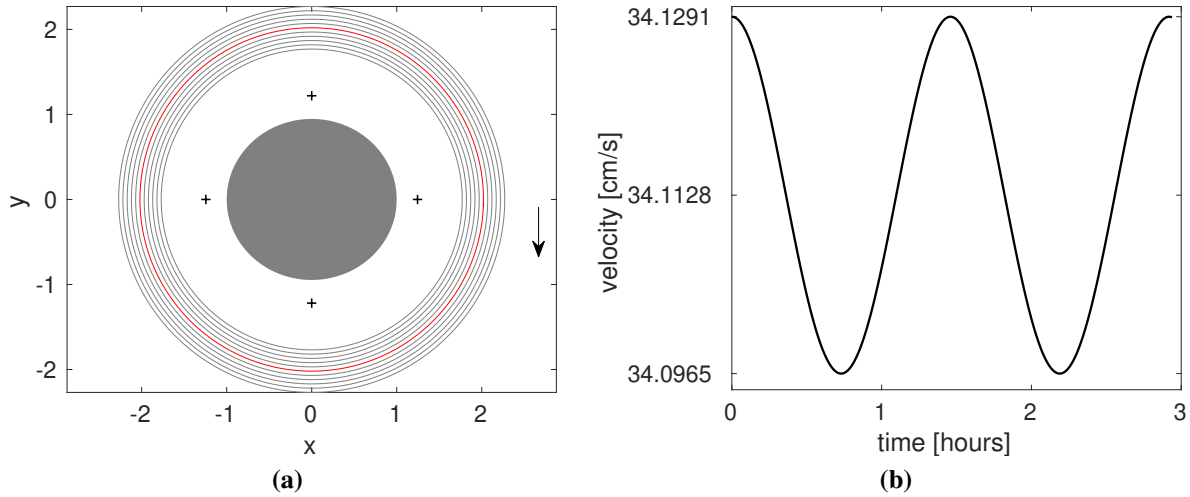

FIGURE 4.18: (a) Stable periodic retrograde orbits around Bennu. (b) Velocity profile for the periodic orbit displayed in red. The largest velocity is achieved at the intersection with the x axis.

period).

For simplicity, an example referred to retrograde orbits around Bennu is proposed here, however this method can be easily extended to other asteroids with unstable CEPs. Figure 4.18a shows a family of retrograde periodic orbits around Bennu. A lower bound on the minimum orbit altitude can be defined to ensure that a siphon with $L > L_{\text{eq}}$ can reach the orbit. In principle any stable orbit in the family above such minimum altitude can then be selected as the nominal catcher orbit, even though higher orbits will have a larger relative velocity with respect to the asteroid, thus increasing the required energy for transfer to the catcher. Take, for example, the red orbit in Fig. (4.18a) that intersects the x-axis at the same point as the direct orbit used in the previous section, for transfers to CEPs. Figure 4.18b shows the velocity of the red periodic orbit over one period. At the intersection with the x-axis, the velocity is approximately $34\,\text{cm}\,\text{s}^{-1}$, more than two times larger than the velocity of the direct orbit in Fig. 4.15a passing through the same point. However, using the same swing-and-release technique described in the previous section, an additional $\Delta v \approx 21\,\text{cm}\,\text{s}^{-1}$ is required to match with the velocity of the catcher at the intersection with the x-axis. In comparison, the minimum Δv for insertion into the same periodic orbit from the asteroid surface (calculated using Eq. (4.30)) is approximately $32\,\text{cm}\,\text{s}^{-1}$, suggesting that, even in this case, the siphon might reduce the overall Δv requirements in a large-scale mining scenario.

Chapter 5

Dynamics of a non-rigid orbital siphon anchored at a near-Earth asteroid

5.1 Introduction

This chapter studies an extension of the siphon model presented in Chapter 4. In particular, the siphon is modelled as a non-rigid chain of buckets, with consecutive buckets linked by spring-dashpot connections (rather than rigid tethers) without a support structure and the siphon dynamics is extended to three-dimensional space. It is shown that, even without a rigid support structure, the orbital siphon effect is still generated, and the dynamics is similar to that described in the previous chapter. Moreover, the gravity field of the asteroid is modelled using a potential closed-form solution for arbitrary constant density triangular-faced polyhedra, for two candidate near-Earth asteroids. As in the previous chapter, a spacecraft is connected to the top of the siphon, collecting the material released by the buckets and its effect is included in the dynamics. The siphon behaviour is studied with both a fixed and moving anchor. In the second case, the base of the siphon moves on the asteroid surface with constant velocity. This allows the mining location to be moved without interrupting the flow of material being delivered to the collecting spacecraft. Eventually, preliminary granular dynamics simulations are performed to investigate the behaviour of the material upon release to the collecting spacecraft. In particular, it is proposed to exploit the centrifugal-induced force at the collecting spacecraft as a driving force to sort asteroid material by grain size.

5.2 Dynamical model

In the scenario presented in this chapter the chain of masses is designed similar to a bucket conveyor (see Fig. 5.1), with consecutive buckets connected to neighbouring buckets via massless elastic tethers with axial Young modulus E, constant cross section S, viscosity coefficient C and unstrained length l. The siphon length L is defined here as half the unstrained length of the

chain loop, i.e., $L = nl/2$. Buckets on the lifting side (LS) are filled with payload masses m_p, i.e., raw material mined from the asteroid. The descending side (DS) of the siphon hosts empty buckets, returning to the asteroid surface for refilling, after having released their payload mass to the CS, which is physically connected to the siphon through a pulley. Another pulley at the anchor ensures continuous cycling of the buckets. It is assumed that the pulley size is much

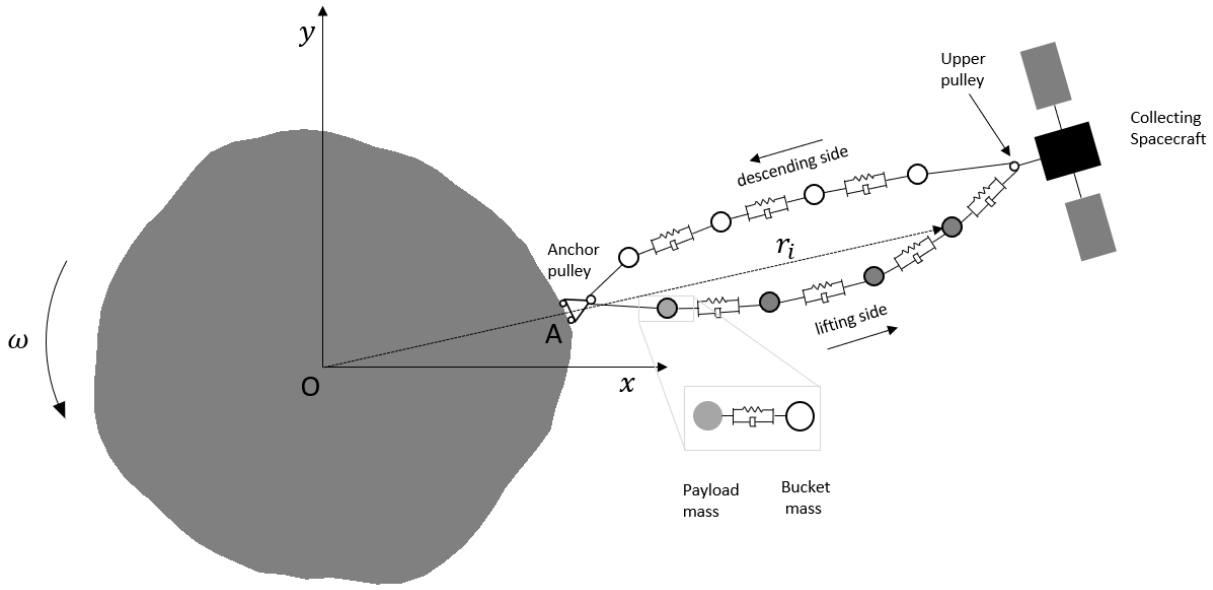

FIGURE 5.1: Dynamical model of an orbital siphon anchored to a rotating asteroid. For clarity the siphon is represented on the asteroid $x-y$ plane.

smaller than L and their mass is neglected in this model. This choice offers significant savings in computational time with respect to a finite-size pulley. In fact, a finite-size pulley would require modeling of the tether with intermediate nodes, separated by a distance smaller then the diameter of the pulley itself, thus considerably increasing the number of degrees of freedom of the system. Any friction between the tether and the pulley is neglected.

When a bucket reaches the anchor pulley, it is refilled with a new payload. In Chapters 3 and 4 this event was modelled as an inelastic impact, resulting in a discontinuous velocity change of the system (note that the "waiting" payload is at rest with respect to the siphon, in the asteroid reference frame). This choice may cause numerical instabilities in this model. Hence, the bucket refilling is modelled using a spring-dashpot connection between the bucket and the new payload. Then, the first bucket mass on the LS and the corresponding payload mass are considered as separate point masses, with position vectors $\mathbf{r}_1$ and $\mathbf{r}_{p1}$ respectively, connected via a spring with stiffness k and damping constant c. Once the bucket reaches a sufficient altitude, the payload is then attached to the bucket. Here, it is chosen to attach the payload to the bucket when another bucket reaches the anchor. For all the other buckets on the LS, the mass of the payloads is simply summed to that of the bucket, without considering two separate masses.

It is assumed that the size of the CS is small with respect to the distance between the anchor

and the CS centre-of-mass. For this reason, the CS is also modelled as a point mass, located in the same position as the upper pulley. Although this choice does not allow a model of the CS attitude, this approximation permits the effect of the CS mass variation (increasing over time, as more payload masses are released) to be included into the siphon dynamics.

Let xyz be the asteroid rotating frame centred on the asteroid centre-of-mass with the x, y and z axes corresponding to the principal axis of smallest, intermediate and largest inertia. Let $\mathbf{r}_i$ be the position vector from the origin to the i-th bucket of the chain. The equation of motion of the i-th bucket is then

$$\ddot{\mathbf{r}}_i + 2\boldsymbol{\omega} \times \dot{\mathbf{r}}_i + \boldsymbol{\omega} \times (\boldsymbol{\omega} \times \mathbf{r}_i) = \nabla V(\mathbf{r}_i) + \mathbf{f}^i_{tether}/m_i \tag{5.1}$$

where $\mathbf{f}^i_{tether}$ is the total force generated by the two tethers connected to the i-th bucket. In this chapter the asteroid is modelled as triangular-faced polyhedron and, therefore the gravitational potential in given by Eq. (2.20). The term m_i is the mass of the buckets, including the payload mass if the bucket is travelling on the LS. Note that the acceleration of the asteroid centre-of-mass due to the asteroid orbit is neglected in Eq. (5.1).

The potential V can be amended to include the centrifugal potential (Eq. (2.1)) such that the equations of motion reduce to

$$\ddot{\mathbf{r}}_i + 2\boldsymbol{\omega} \times \dot{\mathbf{r}}_i = \nabla U(\mathbf{r}_i) + \mathbf{f}^i_{tether}. \tag{5.2}$$

By extension, the equations of motion of the entire dynamical system, including the CS and the payload mass m_{p1} attached to the bucket closest to the anchor are

$$\begin{cases} \ddot{\mathbf{r}}_i + 2\boldsymbol{\omega} \times \dot{\mathbf{r}}_i = \nabla V(\mathbf{r}_i) + \mathbf{f}^i_{tether}/m_i & \text{(5.3a)} \\ \ddot{\mathbf{r}}_{cs} + 2\boldsymbol{\omega} \times \dot{\mathbf{r}}_{cs} = \nabla V(\mathbf{r}_{cs}) + \mathbf{f}^{cs}_{tether}/M_{cs} & \text{(5.3b)} \\ \ddot{\mathbf{r}}_{p1} + 2\boldsymbol{\omega} \times \dot{\mathbf{r}}_{p1} = \nabla V(\mathbf{r}_{p1}) + \mathbf{f}^{p1}/m_{p1} & \text{(5.3c)} \end{cases}$$

where $\mathbf{r}_{cs}$ is the position vector of the CS, $\mathbf{f}^{cs}_{tether}$ represents the tether forces acting on the CS, $\mathbf{f}^{p1}$ includes the contact forces used to model the interaction between the new payload mass attached to the chain and the first bucket mass on the LS. Note that for the bucket closest to the anchor pulley, $\mathbf{f}^i_{tether}$ includes the force $-\mathbf{f}^{p1}$ due to the interaction between the bucket and the payload.

Equations (5.3) can be reduced to a form suitable for numerical integration :

$$\dot{\mathbf{x}} = B\mathbf{x} \tag{5.4}$$

where $\mathbf{x} = \{\boldsymbol{u}, \dot{\boldsymbol{u}}\}$, and $\boldsymbol{u}$ is a vector containing the coordinates of the buckets, the CS and the first payload mass:

$$\mathbf{u} = \left\{x_1, y_1, z_1, \ldots, x_n, y_n, z_n, x_{cs}, y_{cs}, z_{cs}, x_{p1}, y_{p1}, z_{p1}\right\}^T \tag{5.5}$$

The matrix B contains time-dependent terms due to inertial forces, gravitational forces and tension forces. Equation (5.4) can be numerically integrated in a given time range for a given initial state $\mathbf{x}_0$. Integration is interrupted when a bucket reaches a pulley, to modify the direction of the velocity of the bucket intersecting the pulley. In particular, the following two cases are considered:

1. A bucket reaches the CS pulley. The payload mass m_p contained within the bucket is summed to the CS mass. The direction of the velocity of the bucket is then changed such that it is parallel to the vector connecting the CS with the first bucket on the DS closest to the CS. The velocity magnitude is not changed.

2. A bucket reaches the anchor pulley. Let i_0 be the index of this bucket. A payload mass m_p is connected to the i_0-th bucket via a spring-dashpot connection characterized by stiffness k and damping constant c. The direction of the velocity of the i_0-th bucket is then changed such that it is parallel to the vector connecting the anchor with the first bucket on the LS closest to the anchor. The velocity magnitude of the bucket is not changed. The spring-dashpot connection between the (i_0+1)-th bucket and the corresponding payload is removed, by fixing the payload to the bucket.

5.2.1 Tether tension forces

Let $\mathbf{q}_j$ be the relative displacement between the j-th and $(j+1)$-th mass of the chain, so that

$$\mathbf{q}_j = (x_{j+1} - x_j)\hat{\mathbf{i}} + (y_{j+1} - y_j)\hat{\mathbf{j}} + (z_{j+1} - z_j)\hat{\mathbf{k}}. \tag{5.6}$$

Here $\hat{\mathbf{i}}$, $\hat{\mathbf{j}}$ and $\hat{\mathbf{k}}$ are the unit vectors parallel to the x, y and z directions. Then, the tension forces $\mathbf{f}_j^s$ acting on the j-th mass are modelled according to Hooke's law, and therefore depend on the displacements $\mathbf{q}_j$ and $\mathbf{q}_{j-1}$:

$$\mathbf{f}_j^s = ES\varepsilon_j \frac{\mathbf{q}_j}{|\mathbf{q}_j|} - ES\varepsilon_{j-1} \frac{\mathbf{q}_{j-1}}{|\mathbf{q}_{j-1}|}. \tag{5.7}$$

Here, ε_j is the strain of the j-th tether, given by

$$\varepsilon_j = \begin{cases} \dfrac{(|\mathbf{q}_j| - l)}{l} & \text{if} \quad |\mathbf{q}_j| > l \\ 0 & \text{if} \quad |\mathbf{q}_j| \leq l \end{cases} \tag{5.8}$$

Note that the tether cannot support axial compression, thus the tension vanishes when the tether becomes slack.

If the j-th tether is in contact with one of the two pulleys, let $\mathbf{q}_j^a = \mathbf{r}_P - \mathbf{r}_j$ be the relative displacement between the j-th mass and the pulley, where $\mathbf{r}_P = \{x_P, y_P, z_P\}$ is the position vector

of the pulley and $\mathbf{q}_j^b = \mathbf{r}_{j+1} - \mathbf{r}_P$ is the relative displacement between the pulley and the $(j+1)$-th mass. It is assumed that the tension on the j-th tether is constant between the two sections $\mathbf{q}_j^a$ and $\mathbf{q}_j^b$. Note that this is an approximation, as the pulley normally alters the tensions on the tether if friction at the tether-pulley interface is considered. Therefore, the assumption of a constant tension of the tether intersecting the pulley node is equivalent to assuming that the tether is sliding over the pulley. In this case the strain along the tether is given by

$$\varepsilon_j = \frac{|\mathbf{q}_j^a| + |\mathbf{q}_j^b| - l}{l}. \tag{5.9}$$

5.2.2 Tether damping forces

It is assumed that the damping forces are proportional to the strain rate $\dot{\varepsilon}_j$. From Eq.(5.8) it can be shown that:

$$\dot{\varepsilon}_j = \begin{cases} \dfrac{\dot{\mathbf{q}}_j \cdot \mathbf{q}_j}{|\mathbf{q}_j| l} & \text{if} \quad |\mathbf{q}_j| > l \\ 0 & \text{if} \quad |\mathbf{q}_j| < l \end{cases} \tag{5.10}$$

where

$$\dot{\mathbf{q}}_j = (\dot{x}_{j+1} - \dot{x}_j)\hat{\mathbf{i}} + (\dot{y}_{j+1} - \dot{y}_j)\hat{\mathbf{j}} + (\dot{z}_{j+1} - \dot{z}_j)\hat{\mathbf{k}} \tag{5.11}$$

Then, the total damping force contribution to the motion of the j-th mass is given by

$$\mathbf{f}_j^d = C\dot{\varepsilon}_j \frac{\mathbf{q}_j}{|\mathbf{q}_j|} - C\dot{\varepsilon}_{j-1} \frac{\mathbf{q}_{j-1}}{|\mathbf{q}_{j-1}|} \tag{5.12}$$

If the j-th tether is in contact with one of the two pulleys, the strain rate $\dot{\varepsilon}_j$ is obtained by taking the time derivative of Eq. (5.9), under the assumption that the damping force remains constant over the tether crossing the pulley:

$$\dot{\varepsilon}_j = \frac{1}{l}\left[\frac{\mathbf{q}_j^a \cdot \dot{\mathbf{q}}_j^a}{\left|\mathbf{q}_j^a\right|} + \frac{\mathbf{q}_j^b \cdot \dot{\mathbf{q}}_j^b}{\left|\mathbf{q}_j^b\right|}\right] \tag{5.13}$$

Then, the total tether force acting on the j-th mass is given by

$$\mathbf{f}_{tether}^j = \mathbf{f}_j^s + \mathbf{f}_j^d \tag{5.14}$$

5.2.3 Tether forces on the collecting spacecraft

The dynamics of the CS is governed by Eq. (5.3b). Using the notation introduced above, the force $\mathbf{f}^{cs}_{tether}$ acting on the CS is written as

$$\mathbf{f}^{cs}_{tether} = (ES\varepsilon_j + C\dot{\varepsilon}_j)\frac{\mathbf{q}^b_j}{|\mathbf{q}^b_j|} - (ES\varepsilon_j + C\dot{\varepsilon}_j)\frac{\mathbf{q}^a_j}{|\mathbf{q}^a_j|} \tag{5.15}$$

where the index j in this case refers to the tether in contact with the pulley. Note that any other external force generated by the contact between the released material and the CS is neglected.

5.3 Case studies

Simulations are now performed considering the two near-Earth asteroids 101955 Bennu and 6489 Golevka. The physical properties and details of the polyhedral models used are given in Table 2.1. Figures 2.1a and 2.1c show the shape models of the two asteroids. Bennu has a spinning top-shape and a ridge along the equatorial region. Bennu is the 4-th most profitable known asteroid for mining purposes[1] within the near-Earth asteroid population. Golevka has a more irregular shape and hence it represents an interesting case study for the orbital siphon, to understand how the gravitational field influences the siphon dynamics.

It is assumed that both asteroids are principal axis rotators [90, 119], i.e., their angular velocity vector is aligned with their maximum moment of inertia axis (here the z axis) and therefore maintain a constant angular velocity in the absence of external torques. Precession and nutation are neglected as the majority of asteroids in a complex rotational state are characterized by a slow rotational rate [121] (unlike Bennu and Golevka) and therefore are not suitable for this application: a slow rotation rate would be associated with very large orbital siphon structures [149].

Figure 5.2 shows the magnitude of the effective acceleration $|\nabla U|$ on the surface of the two asteroids. For Bennu the effective acceleration is larger at the poles and lower at the equatorial region (this trend is typical for spheroidal asteroids). In fact, close to the poles, the centrifugal-induced acceleration is small and thus the gradient of the effective potential V is mainly influenced by the gravitational field. Moving away from the poles, the centrifugal-induced acceleration increases, thus competing with the gravitational acceleration and reducing $|\nabla U|$. The map of $|\nabla U|$ does not follow the same pattern on the surface of the asteroid Golevka, due to its more irregular shape. The acceleration is minimized in a region close to 90 deg longitude at the equator and is larger at the north pole. Although not directly represented here, the vector ∇U points inward across the surface of both asteroids.

The effective acceleration is related to the minimum length (called *equilibrium length* in

[1] According to *asterank.com* (Date accessed: 11/10/2019)

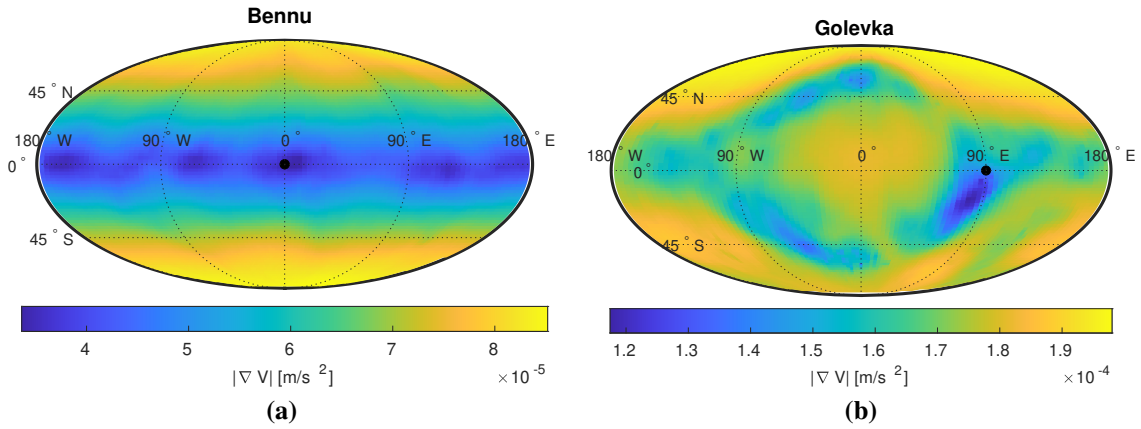

FIGURE 5.2: Effective acceleration $|\nabla V|$ at the surface of Bennu (a) and Golevka (b). A black circle indicates the selected anchor location for the two bodies.

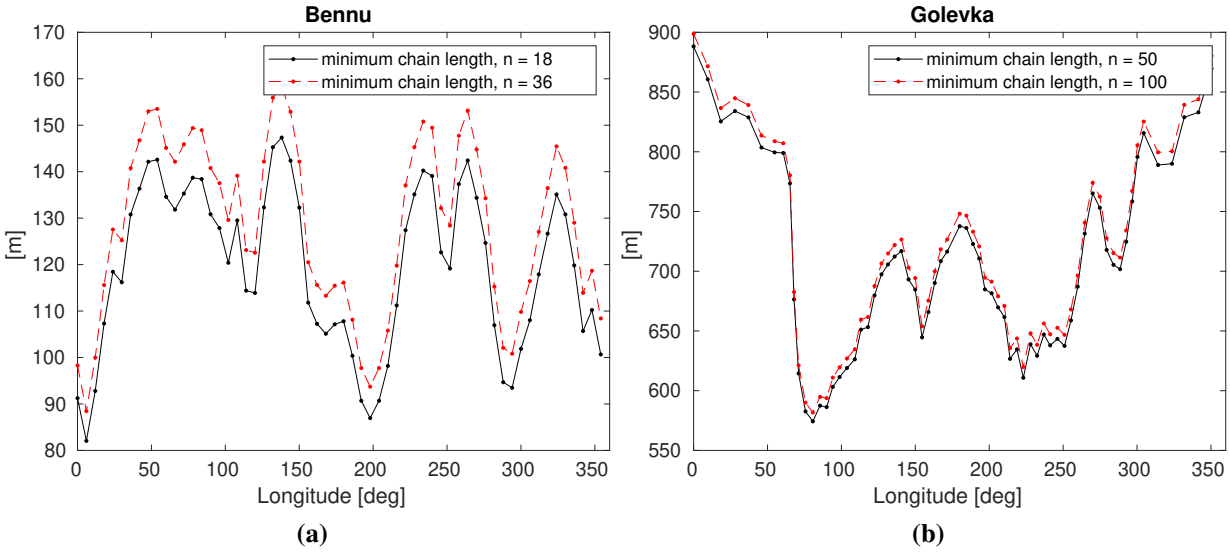

FIGURE 5.3: Equilibrium length of equatorial chains anchored on Bennu (a) and Golevka (b) as a function of the anchor longitude and the number of buckets.

analogy with the previous chapters) the siphon must have to guarantee the siphon effect. Figure 7.3 shows the equilibrium length for Bennu (5.3a) and Golevka (5.3b) for equatorial anchor positions, as a function of the anchor longitude and the number of payload masses. Here the equilibrium length is calculated assuming that the two sides of the chain are coincident and normal to the z-axis. Note that equatorial regions with smaller equilibrium lengths are also characterized by a smaller effective acceleration at the surface (see Fig. 5.2). The anchor longitude which minimizes the equilibrium length is approximately 6 deg for Bennu and 80 deg for Golevka. Larger siphon lengths are required for Golevka due to its larger density and rotation period (in fact, the effective acceleration for Golevka is on average one order of magnitude larger than Bennu). Note that the equilibrium length decreases with more buckets. This is consistent with results found in Chapter 3. It is important to emphasize that the equilibrium length will

change depending on the current chain configuration. Values shown in Fig. 5.3 are used as a reference for the selection of suitable chain lengths for the following case studies:

Scenario 1. Bennu: orbital siphon with a fixed anchor. The simulations are performed for three cases, varying the siphon length and/or payload mass

Case (a): $m_p = 34\,\text{kg}$, $L = 99\,\text{m}$.

Case (b): $m_p = 126\,\text{kg}$, $L = 99\,\text{m}$.

Case (c): $m_p = 34\,\text{kg}$, $L = 124\,\text{m}$.

Case (d): $m_p \in [17, 34]$ kg, $L = 124\,\text{m}$.

The number of buckets n is set to 35. The two different payload masses for cases (a), (b), (c) correspond to the mass of asteroid material which can be filled in a cubic bucket with size 30 cm or 46 cm. The bucket mass is calculated assuming the bucket is made of Aluminium 7075-T6 with a density of $\rho = 2810\,\text{kg}\,\text{m}^{-3}$ and each face has a thickness of 1 mm. This leads to $m_b = 1.5\,\text{kg}$ for the smaller bucket and $m_b = 3.5\,\text{kg}$ for the larger bucket. The orbital siphon is anchored at 0 deg longitude at the equator. In case (d), new PMs to be connected to the siphon have random masses between 17 and 34 kg (taking a uniform probability distribution). Note that both the siphon lengths used in this scenario are larger then the equilibrium length for this longitude, as shown in Fig. 5.3a. In all cases the initial mass of the CS is assumed to be 800 kg.

Scenario 2. Golevka: orbital siphon with a fixed anchor at 90 deg longitude at the equator. A 595 m chain with 105 payloads is used for the simulation. Again, note that such a length is larger than the equilibrium length shown in Fig. 5.3b for an equatorial siphon at the indicated longitude. A 30 cm side cube is used for this simulation, corresponding to a payload mass $m_p = 73\,\text{kg}$ (note that in this case more mass can be filled in the 30 cm bucket due to the larger density of Golevka). In this case two scenarios are studied, to analyze the effect of the CS mass at the beginning of the mass transfer process:

Case (a): $M_{cs}(t = 0) = 1600\,\text{kg}$,

Case (b): $M_{cs}(t = 0) = 2400\,\text{kg}$.

Scenario 3. Bennu: orbital siphon with moving base. The siphon base undergoes a constant velocity translation on the asteroid surface, for example to move to a new mining location without interrupting the flow of transported material. The initial base point is the same as Scenario 1 and two cases are here considered:

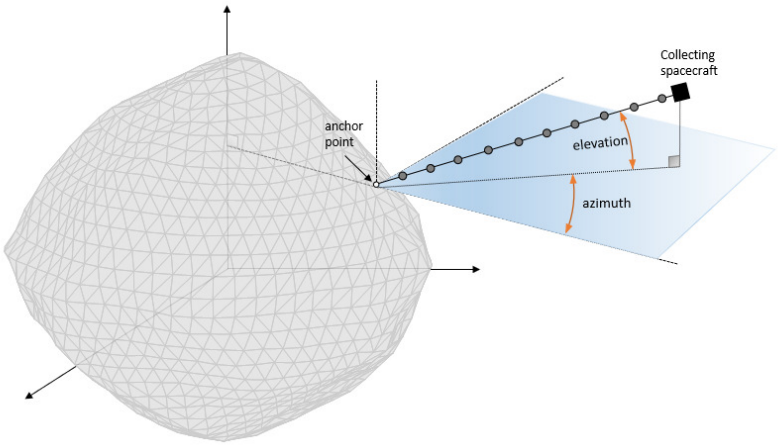

FIGURE 5.4: Definition of azimuth and elevation angles, used to define the orientation of the CS with respect to the anchor point. For illustration, the siphon is represented here as a straight line.

Case (a) Longitudinal motion of the anchor base, with siphon length 99 m. The anchor is moved by 60 m over the surface in the positive y direction, with constant anchor velocity $1 \times 10^{-3}\,\mathrm{m\,s^{-1}}$.

Case (b) Latitudinal motion of the anchor base, with siphon length 124 m. The anchor is moved by 30 m over the surface in the positive z direction, with constant anchor velocity $1 \times 10^{-3}\,\mathrm{m\,s^{-1}}$.

In both cases the payload mass is 34 kg and the initial mass of the CS is 800 kg.

The siphon is initialized by arranging the LS and DS buckets starting from the anchor point and following a straight line, parallel to the segment OA (Fig. 5.1), with the first bucket coincident with the anchor point. The siphon initial deployment and LS loading are not taken into account here: the LS buckets are already loaded with payloads at the beginning of the simulation. All the buckets are initialized with zero velocity. In each simulation, the tether stiffness and damping are $ES = 21\,100\,\mathrm{N}$, $C = 2500\,\mathrm{N\,s}$ (values taken from Ref. [164]), while $k = 300\,\mathrm{N/m}$ and $c = 200\,\mathrm{Ns/m}$.

The siphon orientation is measured with respect to the CS (in general the chain shape will deform in the three dimensional space), using the local azimuth and elevation defined as in Fig. 5.4. Note that the elevation is defined with respect to the the plane passing through the anchor point and normal to the spin axis (which corresponds to the equatorial plane in Scenarios 1, 2 and 3a).

In all simulations the asteroid mass is considered constant and the effects of long-term mass removal are not taken into account, since the removed mass fraction is small.

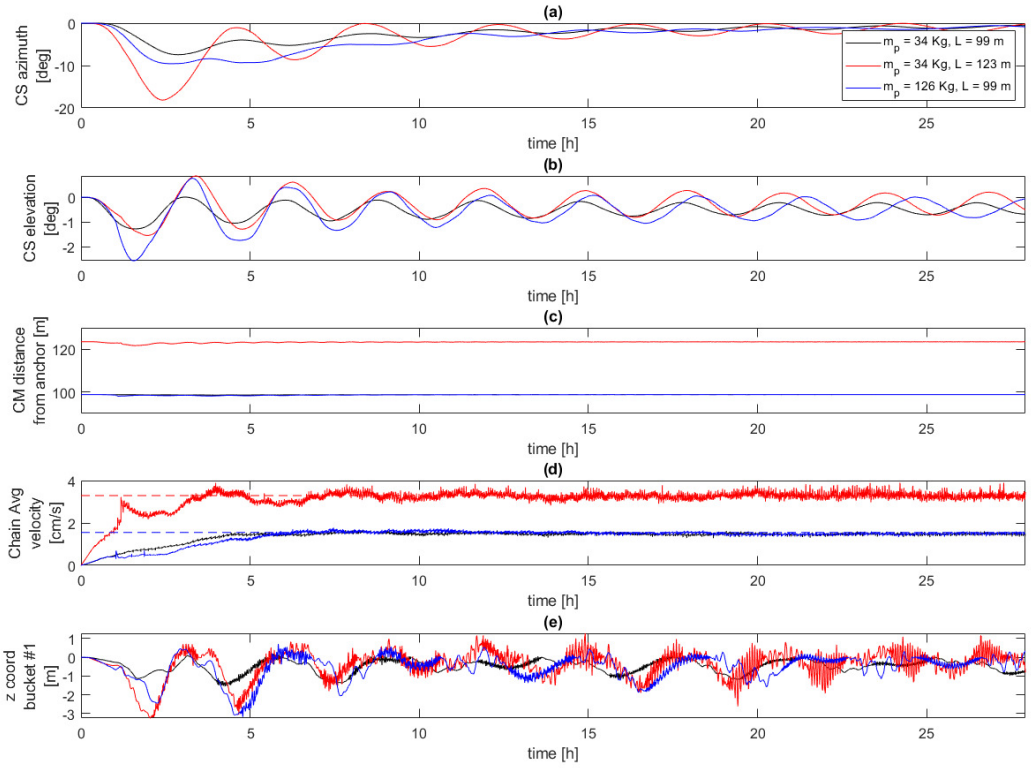

FIGURE 5.5: Scenario 1, cases (a), (b), (c): CS azimuth (a), CS elevation (b), CS distance from anchor (c), chain average velocity (d) and z-coordinate of bucket #1 (e) as a function of time.

5.4 Results

Scenario 1. Figure 5.5 shows the CS azimuth, CS elevation, CS distance from the anchor, average chain velocity (defined as $(1/n)\sum_{i=1}^{n}|\dot{\mathbf{r}}_i|$) and the z coordinate of bucket #1 for a 28 h simulation, for cases (a), (b) and (c). The Coriolis forces due to the chain motion initially causes a clockwise rotation of the chain (opposite to the asteroid rotation) and the amplitude of such oscillations is eventually reduced over time (Fig. 5.5a). A similar trend can be observed for the CS elevation (Fig. 5.5b). The variation of the CS elevation is due to the irregularities of the gravitational field, especially in close proximity to the asteroid, where buckets are deflected in the z direction (see also Fig. 5.5e) and the consequent oscillation is propagated to the other buckets of the chain and eventually to the CS.

The average chain speed (Fig. 5.5e) reaches a steady value after an initial transient. The radial deceleration is due to payload refilling and is similar to the effect described in Chapters 3, 4: when a new payload mass is added at the bottom of the siphon, this mass is accelerated by the bucket while the average chain speed decreases to conserve the linear momentum of the system. Hence, although the uppermost masses of the LS are generating a net radial force, the average chain speed does not diverge, due to the deceleration phase caused by bucket refilling. Such

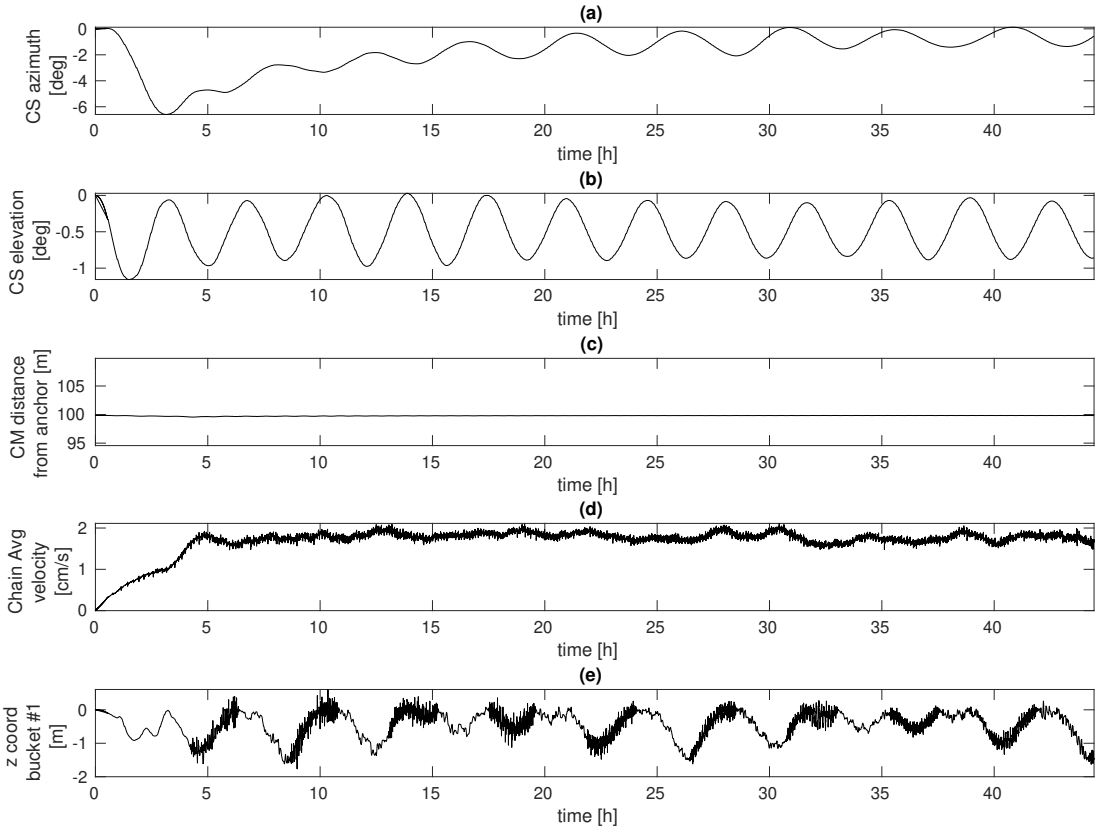

FIGURE 5.6: Scenario 1, case (d): CS azimuth (a), CS elevation (b), CS distance from anchor (c), chain average velocity (d) and z-coordinate of bucket #1 (e) as a function of time.

a braking effect introduces elastic forces on the siphon, which are propagated along the entire chain. The higher frequency variations on the average chain speed are a consequence of this effect. The dashed line in Fig. 5.5 represents the steady state speed predicted by the analytical model described in Chapter 3, using Eq. (3.43)[2]. This matches quite accurately the average chain speed after approximately 10 hours of simulation time in all cases.

Figure 5.6 shows the CS azimuth, CS elevation, CS distance from the anchor, average chain velocity and the z coordinate of bucket #1 as a function of time for Scenario 1, case (d). In this case, the average chain velocity at steady state does not oscillate with respect to a constant value as in cases (a), (b) and (c) in Scenario 1. This result is expected, since the siphon is loaded with random masses. Results for other parameters are similar to the previous cases.

Figure 5.7 is a view of the siphon from the positive z axis at the beginning of the fourth, fifth and sixth loop of the chain (the chain completes a *loop* when bucket #1 reaches the anchor after completing an entire ascent on the LS and descent on the DS) for Scenario 1, case (a). The siphon is transversally stretched, due to the opposite direction of the Coriolis forces on the two sides of the chain, which contributes to keeping the two sides separated. It has been verified that

[2]Here, the radius R and ω of the spherical asteroid (used in Eq. (3.43)) are chosen such that the gravitational acceleration and the centrifugal-induced acceleration are matching with that of the polyhedron model at the anchor point.

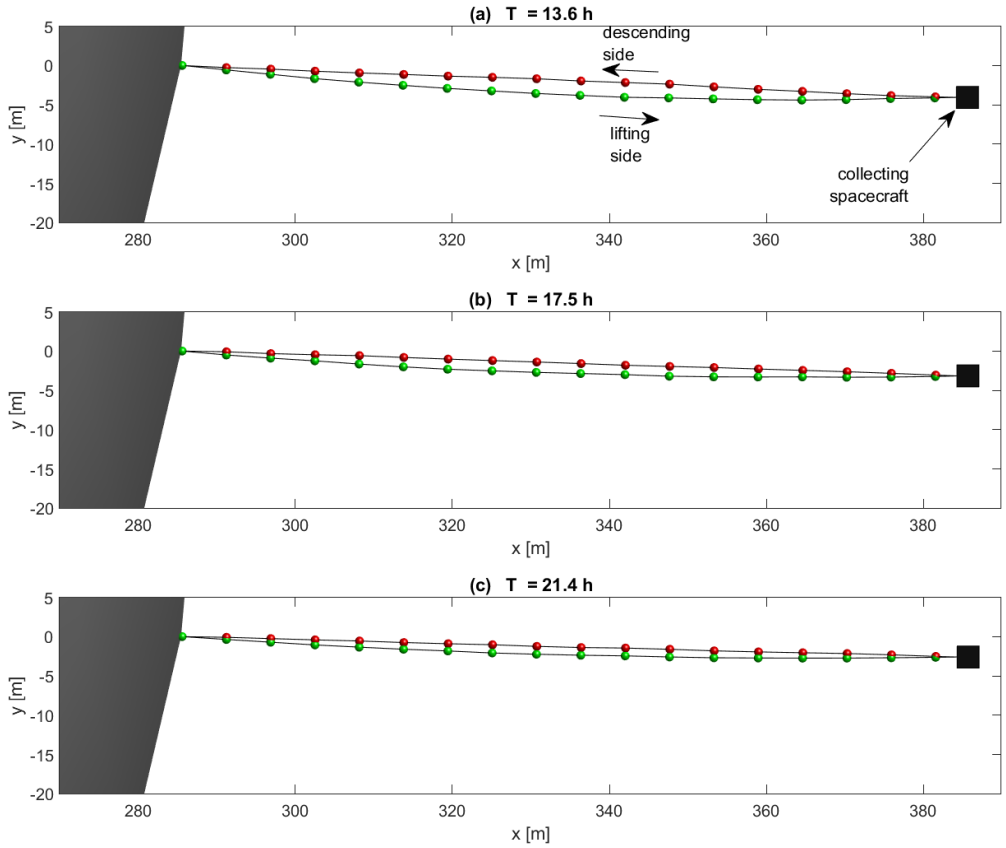

FIGURE 5.7: Scenario 1, case (a): orbital siphon as viewed from the positive z axis.

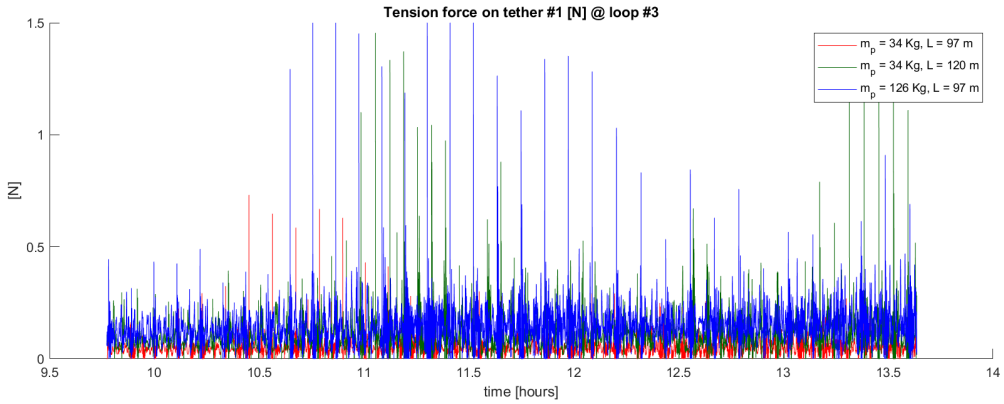

FIGURE 5.8: Tension force on the tether #1 during the third loop of the chain for Scenario 1, cases (a), (b) and (c).

buckets on opposite sides do not collide.

Figure 5.8 shows the tension force on the tether connecting bucket #1 with bucket #2 during the third loop of the chain for all three cases. Overall, the tension force is very small, less than 0.2 N on average and with peaks below 2 N for Scenarios 2 and 3. The peaks are associated with a new payload being attached to the bucket entering the LS: this can cause the tether to lose tension and become slack, even though the overall stability of the analysed scenarios is not compromised. The amplitude of the peaks depends on the current configuration of the chain. In general, the tension force on the tethers increases for larger chain length or payload mass.

Figure 5.9 shows the magnitude of the relative position between the new payload and the bucket after connection at the anchor, referred to Scenario (1), case (a). Connection of the first eight payloads at the beginning of the third cycle is displayed here as reference: the other cases exhibit equivalent characteristics. After an initial peak, corresponding to the payload being accelerated by the chain, oscillations are damped within a few seconds after the connection.

Scenario 2. Figure 5.10 shows the CS azimuth, CS elevation, CS distance from anchor, average anchor speed and the z coordinate of bucket #1 for a 50 h simulation, in the two cases considered.

Again, as in the previous scenario, the siphon rotates clockwise, opposite to the asteroid rotation, due to the Coriolis forces. After an initial transient, the CS azimuth is reduced and the chain tends to approach the local vertical (see also Fig. 5.11). It is interesting to observe that the variation of the CS elevation is rather small, although the asteroid shape is quite irregular. Therefore, it is plausible that the centrifugal-induced forces on the uppermost payloads are large enough to counteract the z component of the gravitational force on the lowermost masses. The difference between Scenario 2, case (a) and Scenario 2, case (b) is not significant. The CS elevation in case (b) is slightly smaller in amplitude, due to the larger centrifugal-induced force available at the CS.

Figure 5.11 is a view of the siphon from the positive z axis at different timesteps for Scenario

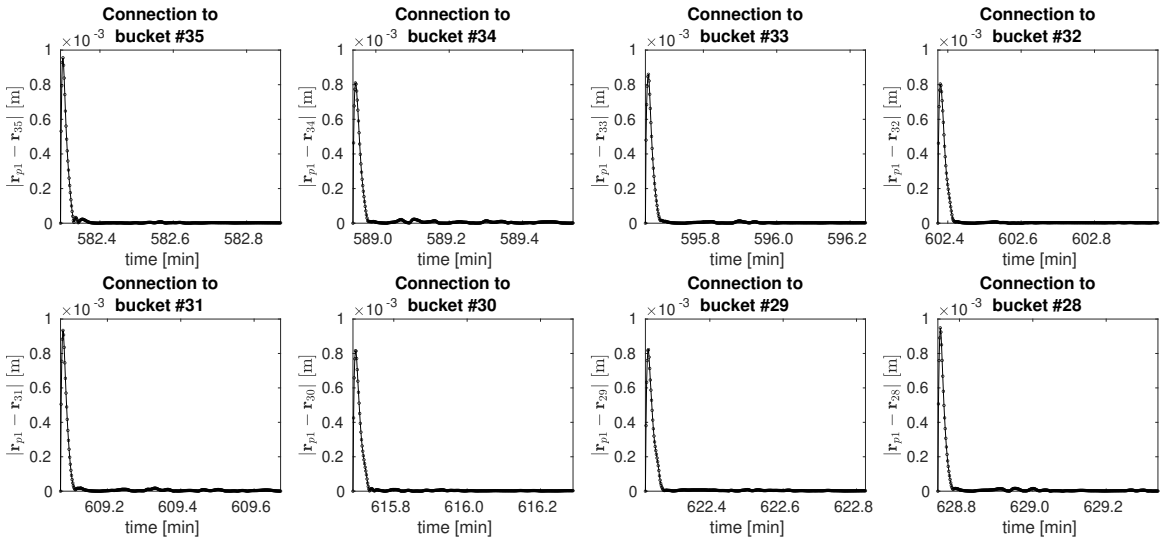

FIGURE 5.9: Relative position between new payload and bucket after connection. Connections of the first eight payloads at the beginning of the third cycle are shown.

2, case (a). The situation here is analogous to Fig. 5.7. In this case, the transversal stretching is larger at the beginning but is reduced over time. No collision between buckets on opposite sides was detected for these simulations.

Scenario 3 Figure 5.12 shows the CS azimuth, CS elevation, average anchor velocity and the z coordinate of bucket #1 for a 58 h simulation of Scenario 3, case (a) and Scenario 3, case (b). The dotted vertical lines mark the interval when the siphon base is moving.

For the longitudinal base motion, the siphon changes its orientation to follow the direction of the centrifugal-induced force, which is parallel to the vector *OA* (Fig. 5.1). The chain average velocity is larger during the base motion phase and then reduces once the base is fixed. The larger chain velocity is due to the additional centrifugal-induced force caused by the moving anchor. The amplitude of the CS azimuth is reduced over time once the siphon base is fixed.

When the anchor is moving towards the positive z axis a significant change is noted in the CS elevation: the chain bends slightly southward (see Fig. 5.12b and Fig. 5.14). This effect is caused by the misalignment between the gravitational force and the centrifugal-induced force when the anchor moves northwards: the centrifugal-induced force on each bucket will keep the siphon perpendicular to the spin axis whereas the gravitational force is (approximately) pointing towards the asteroid centre-of-mass, thus their sum has a net negative (positive if the siphon was moving southward) z component. This same effect has been noted in Ref. [153], where the static behaviour of a non-equatorial space elevator was analysed for Earth applications.

Figures 5.13 and 5.14 show the siphon at four different times during the simulation. Note from Fig. 5.13 that the siphon orientation adjusts during the anchor motion to follow the radial direction of the centrifugal-induced force. Moreover, for latitudinal motion, the bending effect is evident from Fig. 5.14. No collision was detected between buckets on opposite sides.

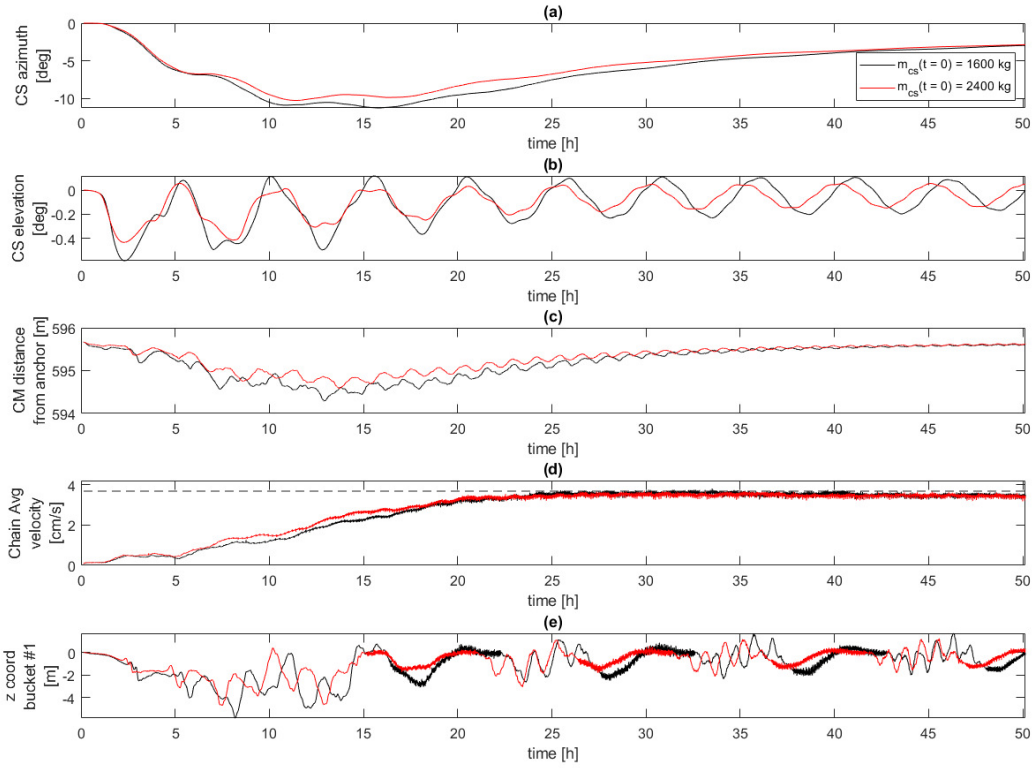

FIGURE 5.10: Scenario 2: CS azimuth (a), CS elevation (b), chain average velocity (c) and z-coordinate of bucket #1 (d) as a function of time.

It should be noted that the speed of the anchor is about one order of magnitude smaller with respect to the average chain speed in the cases simulated here. It is plausible that, for a larger anchor speed, the average chain speed will increase even further during the translation phase, possibly introducing instabilities and/or collision between buckets on opposite sides.

5.5 Discussion

Following the results, two key remarks can be made. First, stability of the orbital siphon is achieved when the siphon is anchored at an irregularly shaped asteroid. This result is consistent with Ref. [80] where oscillations of a tether attached to an irregularly shaped celestial body were studied, taking into account C_{20} and C_{22} in the spherical harmonic expansion of the gravitational potential. Secondly, the siphon effect can be generated using a self-supporting tether-structure, without the payloads sliding on a rigid rod or a support tether: such a siphon architecture reduces the scale of infrastructure mass with respect to a siphon with support structure. Moreover, the lifting side and descending side of the siphon do not interfere or touch in all the cases presented here, due to the opposite direction of the Coriolis forces on the two sides.

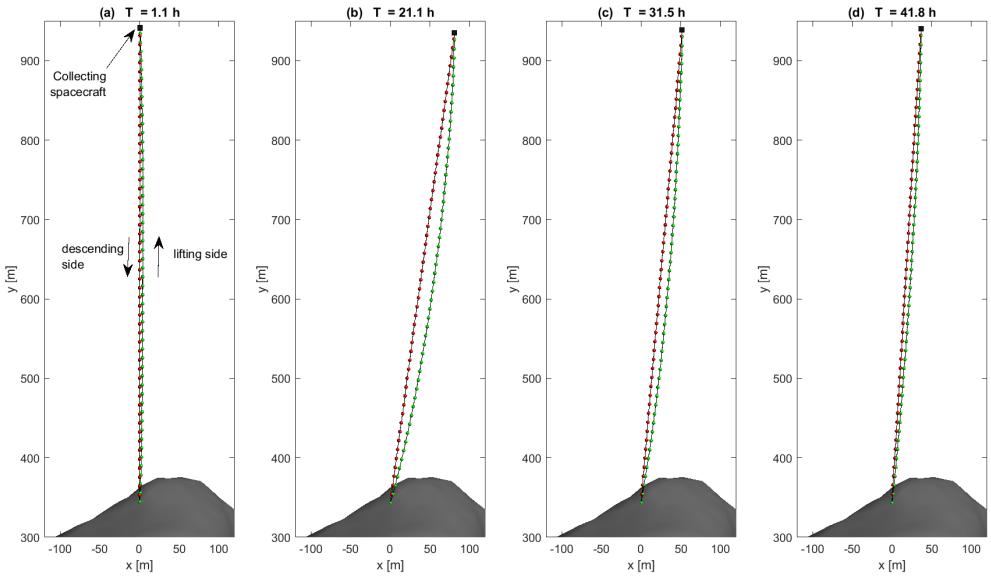

FIGURE 5.11: Scenario 2, Case (a): orbital siphon as viewed from the positive z axis.

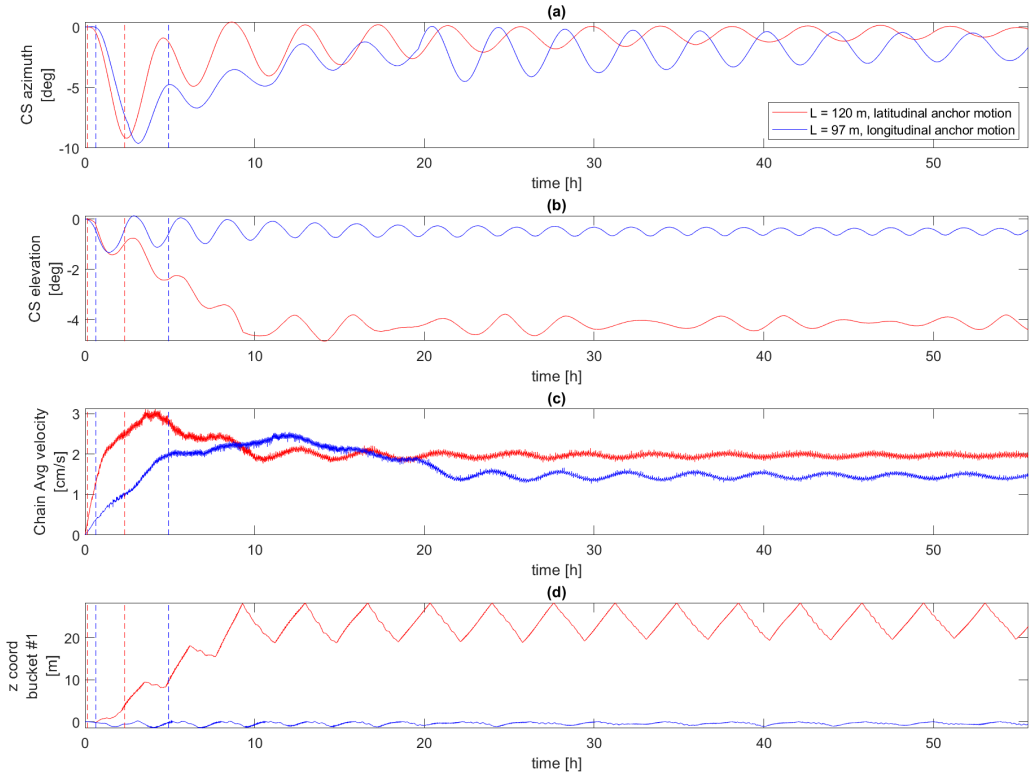

FIGURE 5.12: Scenario 3, case (a) (blue) and Scenario 3, case (b) (red): CS azimuth (a), CS elevation (b), chain average velocity (c) and z-coordinate of bucket #1 (d) as a function of time. The dotted vertical lines mark the interval when the siphon base is moving.

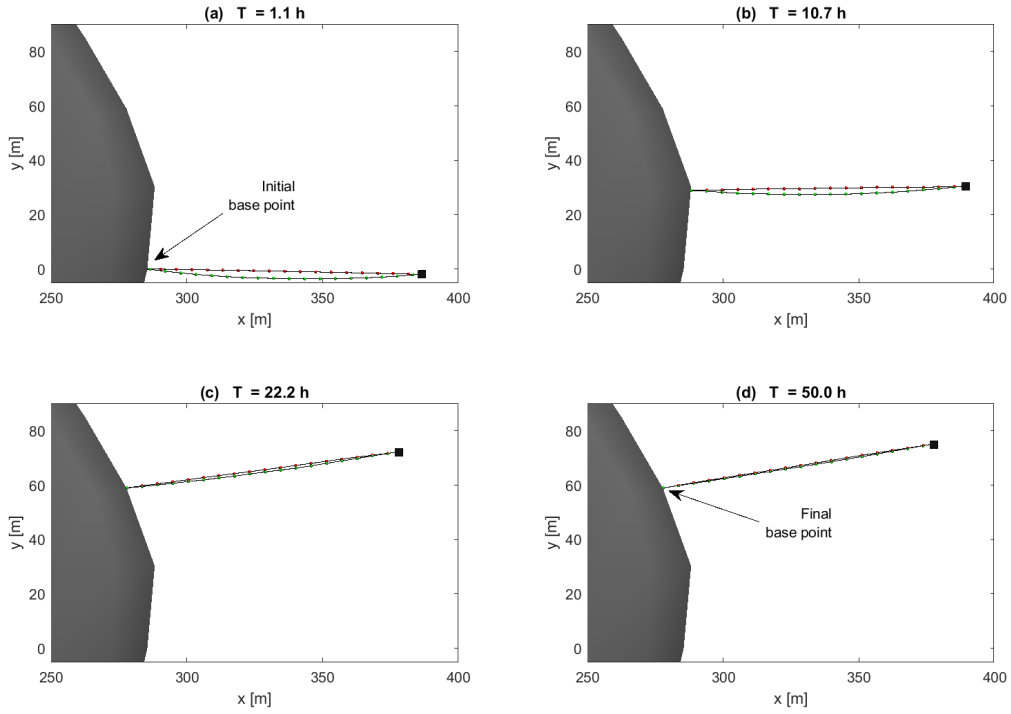

FIGURE 5.13: Scenario 3, case (a): orbital siphon as viewed from the positive z axis.

The siphon dynamics can be divided in two phases: a transition phase and a steady state phase. During the transition phase the chain accelerates and the siphon rotates with respect to the anchor point. A key aspect of this phase is the progressive reduction of the siphon azimuth (see Fig.5.4 for azimuth definition), with the chain gradually aligning with the local vertical. This effect was also observed in the model in Chapter 4 that studied the siphon rotation with payload masses constrained to slide along a rigid support. It is observed in Chapter 4 that the siphon oscillates about an axis, passing through the anchor, where the net torque produced by the inertial and external forces with respect to the anchor cancels out. Here, although the siphon is non-rigid, the dynamics appears similar. The Coriolis forces generate a net clockwise torque, shifting the equilibrium towards negative azimuth values. The equilibrium axis then asymptotically approaches the direction of zero azimuth as more mass is delivered to the CS and the torque produced by the centrifugal forces on the CS with respect to the anchor point counteracts the Coriolis torque. In the following steady-state phase the average chain speed reaches an asymptotic value (small oscillation are still observed here mainly due to undumped motion in the z direction). This steady state speed matches quite accurately the value predicted by Eq. (3.43), which was derived in Chapter 3 for a siphon with payloads sliding on a non-rotating structure and ranges from 2 to $4\,\mathrm{cm\,s^{-1}}$ for the scenarios presented here.

It is instructive to compare the CS azimuth with the chain angle defined with the model in Chapter 4. Figure 5.15 compares the CS azimuth (black line) with the chain angle θ (red dotted

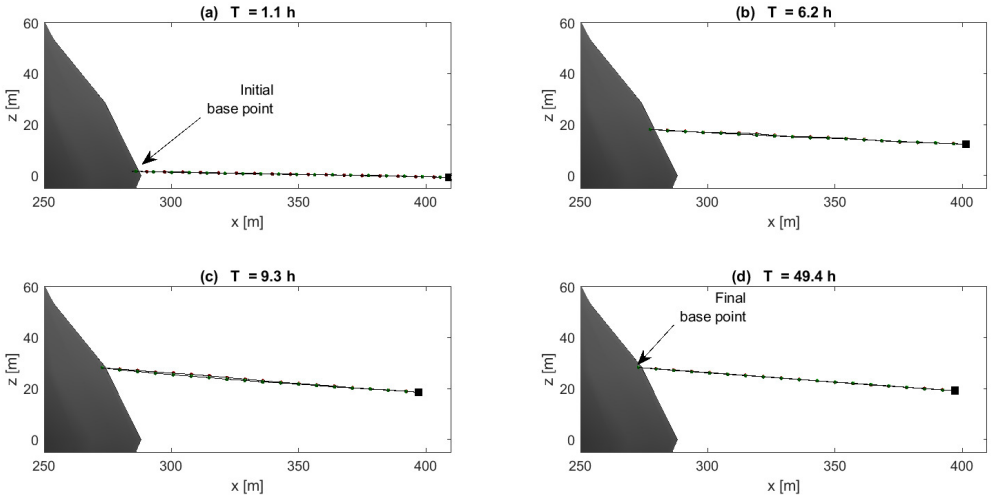

FIGURE 5.14: Scenario 3, case (b): orbital siphon as viewed from the negative y axis.

line) for cases (a), (b) and (c) in Scenario 1 (θ is calculated using the model presented in Chapter 4, approximating Bennu as a spherical asteroid with equivalent radius R and angular velocity ω calculated as stated in footnote 2). Also shown is the equilibrium angle θ_{eq} (blue dash-dotted line) as defined in Sec. 4.4.3. As noted, in both cases the amplitude of the oscillations is reduced over time and the chain tends to approach the local vertical although, for the self sustaining siphon model studied in this chapter, the damping effect is more pronounced. This may be due to the the energy dissipated by the tethers. In fact, the tethers connecting consecutive payloads were considered rigid in the model defined in Chapter 4, whereas they are modelled here as spring-dashpot connections. Also note that the frequency of the oscillations is similar in the two models.

Although seemingly small, the mass flow rate of material delivered to the CS, can be increased by using larger payload masses. For example, using a 34 kg payload mass on Bennu the average mass flow rate is 288 kg/hr (Scenario 1, case (a)), whereas for a 126 kg payload mass the mass flow rate raises to 1005 kg/hr (Scenario 1, case (b)). One of the major disadvantages of large payload masses is the larger bucket volume required to host the material (in relation to the asteroid material density), which increases the structural mass of the siphon and hence the costs to deliver the infrastructure to the asteroid. Other possible drawbacks of larger buckets are related to the bucket-cable attachment, and the sliding motion of the cable through the two pulleys in case of larger attachments. Further studies are required to investigate these engineering issues in detail.

As noted in previous chapters, by using longer siphons the average speed of the chain increases (compare case (a) and (b) in Scenario 1), as the chain will benefit from larger centrifugal-induced force on the uppermost masses, thus in principle increasing the mass flow rate. However, it has been observed that if the chain length increases after a certain threshold (which

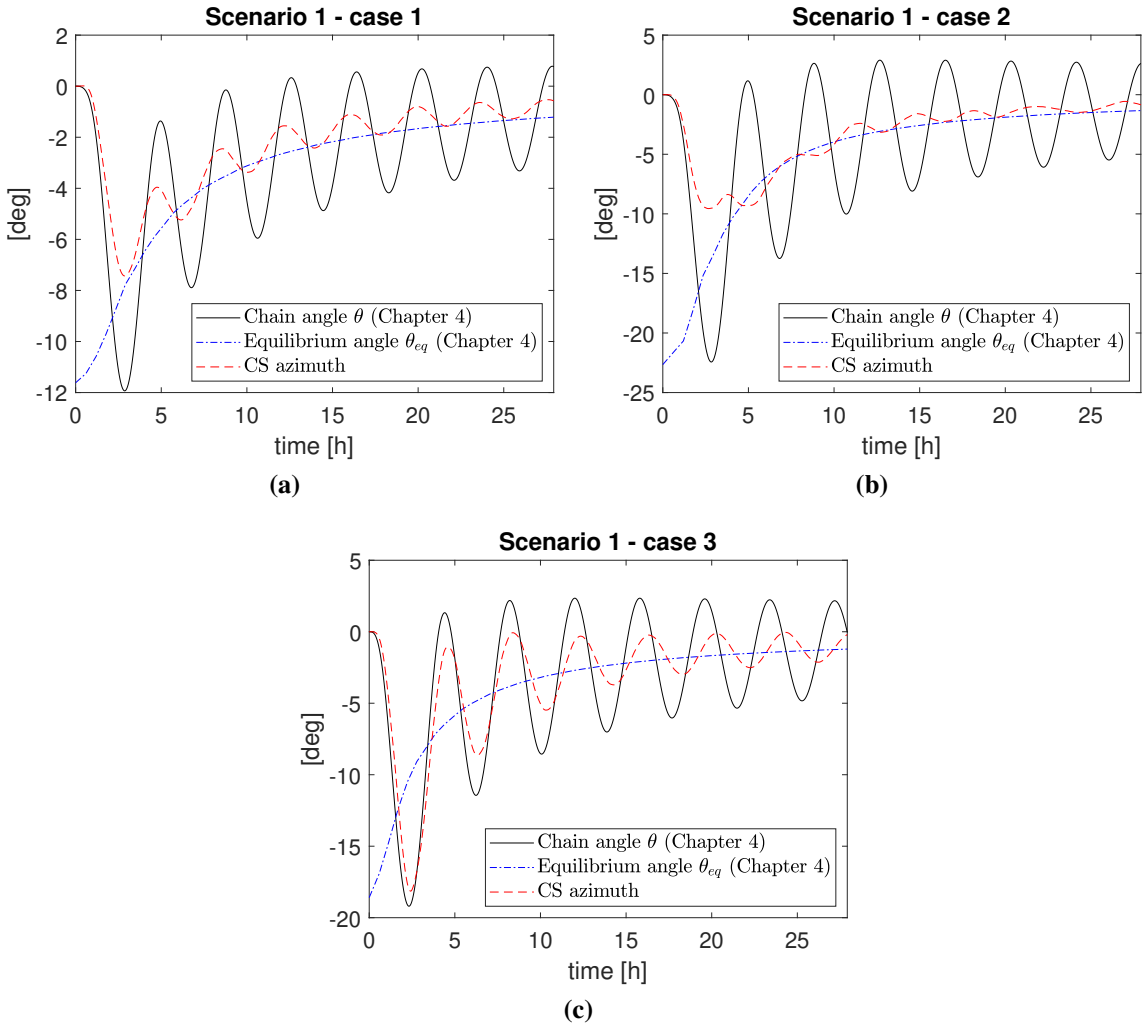

FIGURE 5.15: Comparison between the CS azimuth and the chain angle calculated with the model in Chapter 4.

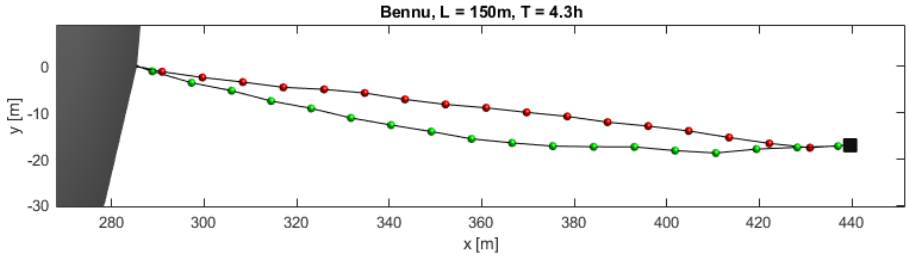

FIGURE 5.16: Interference between LS and DS for a siphon anchored at Bennu with length $L = 150\,\mathrm{m}$ and other parameters as in Scenario 1. Top view from the positive z axis.

depends on the asteroid, anchor location and tether properties) the two sides of the chain can interfere causing unwanted bucket collision. Figure 5.16 shows an example of a siphon with length $L = 150\,\mathrm{m}$ anchored at Bennu, with other parameters as in Scenario 1, case (a). The LS and DS are interfering in proximity of the CS. This problem may be circumvented by dissipating residual oscillation through dampers located in proximity to the anchor and the CS. However, a laterally constrained siphon (as considered for the models studied in Chapters 4 and 5) would not experience this issue, as any oscillation in a direction perpendicular to the structure would be damped by the structure itself, without propagating through the chain.

For the chain velocities considered here, the tension on the tethers is of the order of 1 N. The small magnitude of the tension force is a consequence of the small length-scale of the structure involved, when compared to similar concepts applied at larger scales such as the space elevator for terrestrial applications.

The required anchor forces have the same order of magnitude as the tether forces. According to recent work on anchor mechanisms for asteroid landing and mining operations, proposed anchoring devices can withstand much larger forces. For example, *area-of-effect softbots* [87] are soft-robotic spacecrafts with a large and flexible surface area to exploit the dynamical environment at rubble pile asteroids: a $1\,\mathrm{m}^2$ softbot can generate a 10 N net force to remain anchored to the asteroid surface [87]. Other recent research on asteroid landing [165] compares the behaviour of different anchor tips in different media, claiming anchor forces between 36 N and 178 N.

The dynamics of a siphon with a moving base was also investigated. In particular, the behaviour of a siphon undergoing small longitudinal and latitudinal anchor displacement on the surface of the asteroid Bennu has been analyzed. For a small base velocity ($1 \times 10^{-3}\,\mathrm{m\,s^{-1}}$) a siphon undergoing longitudinal motion tends to remain parallel to the radial direction defined by the centrifugal-induced force. Latitudinal surface motion causes a significant change of the CS elevation (Fig. 5.14), due to the misalignment between the gravitational force and the centrifugal-induced force. In both cases, the siphon has to be long enough to generate the orbital siphon effect at the desired final anchor location.

A siphon with a moving base may be a convenient solution to move the entire infrastructure

to a different mining location without interrupting the delivery of material to the CS. However, this scenario calls for several engineering challenges. Among them is the efficient locomotion of the base on the asteroid surface, which is clearly influenced by small-scale surface features, e.g., boulders or cavities. An interesting solution is the recent *grappler* concept proposed in Reference [26]. The key idea is to create a net-like mechanism by connecting multiple bi-stable array elements (called grapplers) that would grip variable asteroid terrain. In this case, the siphon base would move along an articulated structure defined by multiple grapplers adhering to the asteroid surface. The small siphon anchoring force requirements make the grapplers a viable solution to address the problem of a siphon with moving base.

The power requirements to perform locomotion manoeuvrers on the surface will depend in general on the projection of the anchor force on the anchor velocity direction, the magnitude of the anchor velocity and any friction involved. Neglecting friction, in principle an anchor force of 1 N in the direction of motion[3] requires a power of 1×10^{-3} W to move the siphon at a speed of $1 \times 10^{-3}\,\mathrm{m\,s^{-1}}$.

Another significant engineering challenge is the deployment of the orbital siphon system. A proposed deployment scenario (see Fig. 5.17) is to station the CS in proximity to an equilibrium point around the asteroid (a) and then deploy the tether to the surface (b). The tether is then anchored to the surface (c). To avoid deflection caused by inertial forces during the tether deployment, motion control is required in this phase, for example by using a propulsion system attached at the bottom of the tether. If a net-like structure is to be used to control the locomotion of the siphon base on the asteroid surface, this has to be landed in advance: the siphon anchoring device would then be attached to the grappler system. Once the anchor is fixed, the CS is raised to reach the desired siphon length. Buckets are attached to the tether by cycling the tether using external torque applied to the pulleys. In this phase, the siphon structure can be exploited to land mining equipment (e.g., mining rovers) onto the surface. The LS of the siphon is then filled with material. When all the LS buckets are filled with payloads, the orbital siphon effect is initialized and the anchor base is translated to the desired location (d).

5.6 Material release to the collecting spacecraft

In previous models, the CS and the payload units were modelled as a point mass. However, asteroid regolith is composed of particles with sizes in the millimetre to centimetre regime [48]. Also, several studies have shown that cohesive forces between grains might exist (mainly van der Waals forces) [117], which may influence the behaviour of the regolith under static or dynamic conditions. More detailed models are required to shed light on the dynamics of granular material during the release phase, to design an efficient release system and prevent material loss at the CS.

[3]Note that, in general, the component of the anchor force in the direction of anchor motion will be much smaller than the component normal to the asteroid surface.

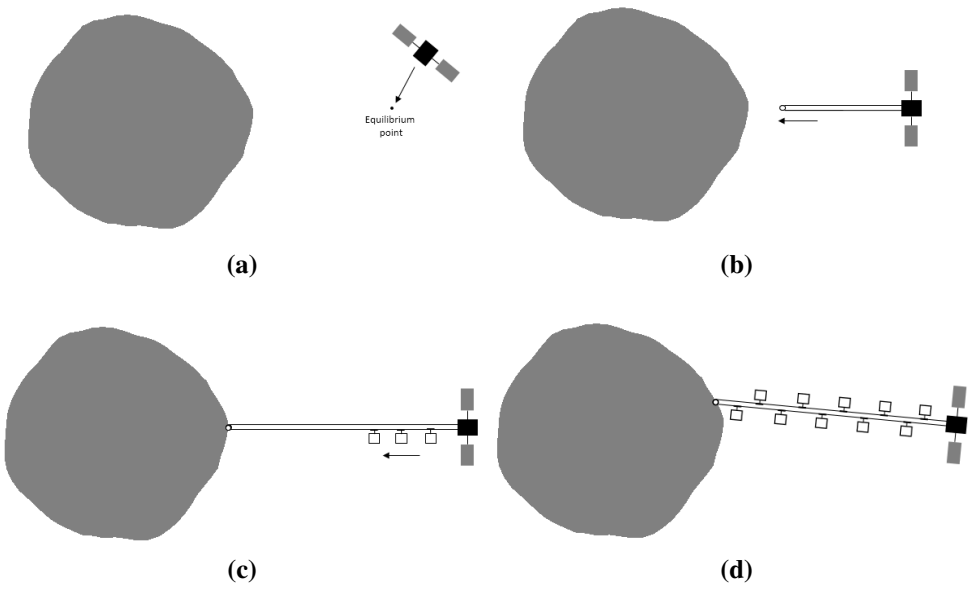

FIGURE 5.17: Concept of system deployment. (a) The CS approaches one of the asteroid equilibrium points. (b) The tether system is released. (c) Anchoring and bucket attachment (d) Buckets on the LS are filled with payload material.

Moreover, industrial-scale utilisation of asteroid resources will likely require regolith sorting by size. In terrestrial applications, sieving processes are based on gravity or electrostatic separation. Vibrating structures are often used to enhance the separation process of material by gravity. However most of the gravity-driven separation method are no longer applicable in microgravity, or will have a reduced performance.

Here, it is proposed to exploit the centrifugal-induced force at the CS as a driving force to convey particles to a collection unit and filter them by size. Figure 5.18 shows a high-level subdivision of the CS at the top of the siphon. A first section, here called *regolith collector* is needed to collect the material released by the buckets and convey material to the subsequent sections. The *sorting tower* is connected to the regolith collector and it is envisaged as a cylindrical structure used for material sorting: particles are accelerated by the centrifugal force due to the asteroid rotation and sieved according to their size. The final sections are dedicated to material processing and storage.

In the following some key aspects of the first two stages, i.e., regolith collector and sorting tower, are discussed showing preliminary results using Discrete Element Modelling (DEM) simulations for a few test cases. A DEM is a numerical method used to simulate the mechanics of a granular medium, modelled as a collection of finite-size particles (in this case, the asteroid regolith) interacting via collisions, subjected to an external force field (e.g., gravity) and constraints (e.g, fixed/moving walls). The method applies Newton's second law to simulate the behaviour of the particles under the external force field. Position, velocity and forces on the particles are calculated at every time-step using an explicit integration method [65]. When

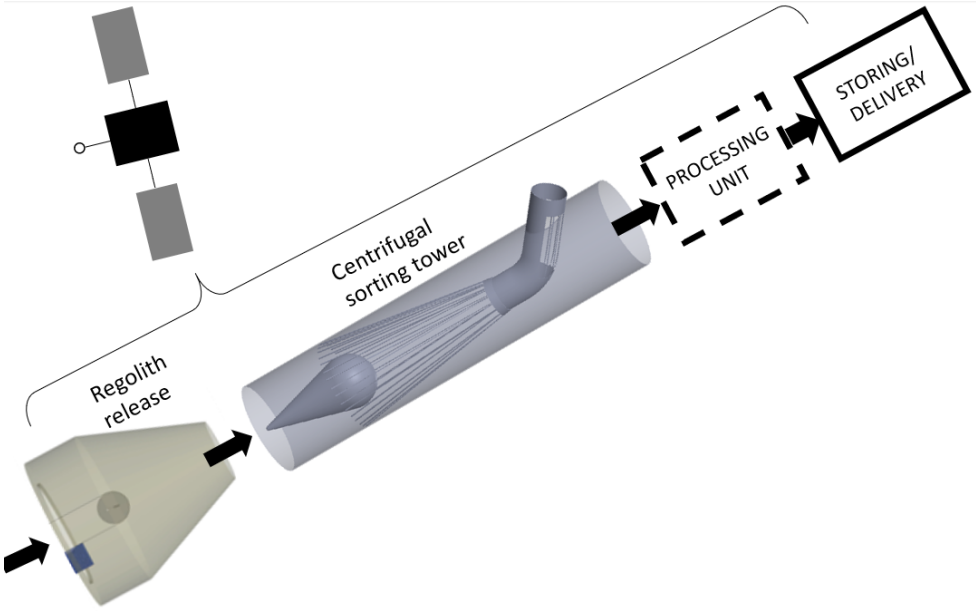

FIGURE 5.18: Collecting spacecraft preliminary architecture

particles are colliding, the contact dynamics are modelled using non-linear spring-dashpot models, taking into account the deformation area between two colliding spheres (or a sphere and a wall). Other methods exist where particles are treated as rigid spheres, without elastic deformation (these methods are called *hard-sphere* DEM [152], in opposition to the former, called *soft-sphere* DEM [33, 34]). In this section, soft-sphere DEM simulations are used to analyse the behaviour of particles upon release and filtering through the sorting tower. The open-source software LIGGGHTS is used to produce the simulations [65]. In order to define a granular agglomerate of particles the following physical properties are required by LIGGGHTS: the particle density, their shape (here spherical particles are only considered for simplicity) and size, the Young's modulus of the particle material, the Poisson's ratio, the coefficient of restitution and the coefficient of friction [65]. Additionally, LIGGGHTS permits modelling of cohesion between particles, in the form of a force f_{cohesion} applied to two colliding spheres, proportional to their contact area, such that:

$$f_{\text{cohesion}} = k_{\text{cohesion}} A_{\text{contact}} \tag{5.16}$$

The contact area A_{contact} for the cohesion model is the area of the circle corresponding to the intersection of the colliding spheres (see Ref. [107], Eq. (13)). The coefficient k_{cohesion} is called the *cohesion energy density* and is measured in $\mathrm{J/m^3}$.

Figure 5.19a shows the schematics of the particle collector used as a test case for a regolith release simulation. The collector is envisaged as an inverted conical hopper. The incoming siphon bucket releases material upon rotation from the upper pulley. The centrifugal-induced forces due to the asteroid rotation as well as the force induced by the bucket rotation on the

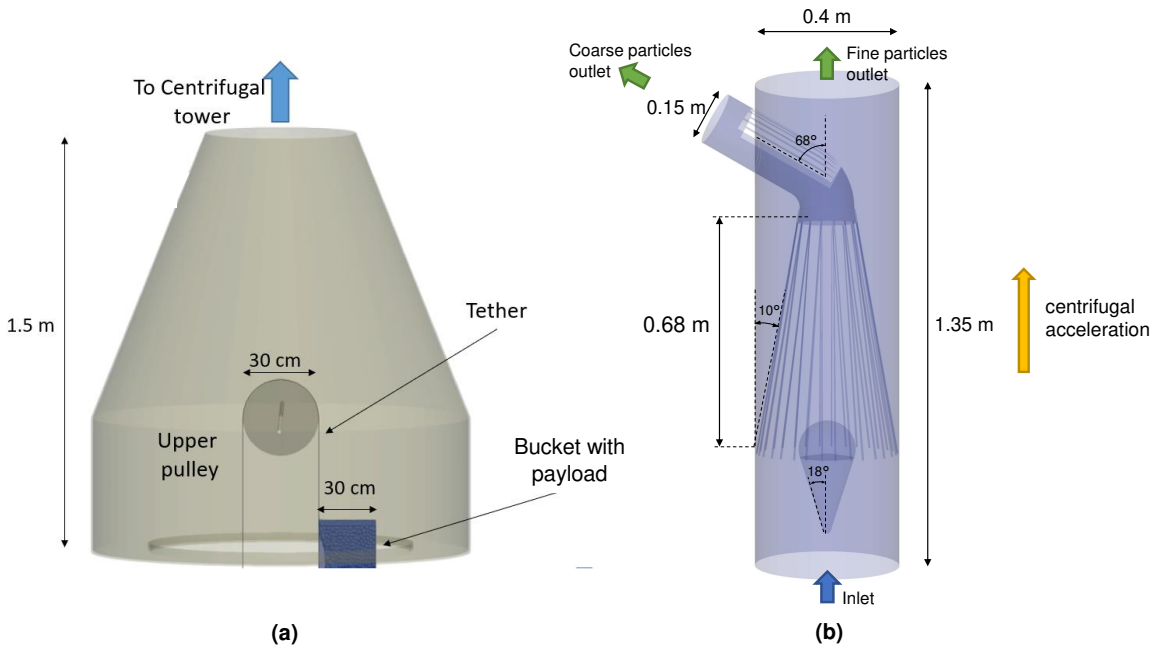

FIGURE 5.19: Regolith collector (a) and sorting tower (b). Not to scale.

TABLE 5.1: Physical parameters of the granular material used in all DEM simulations

Particle density	$2000\,\mathrm{kg\,m^{-3}}$
Young's modulus	$6\times10^{6}\,\mathrm{Pa}$
Poisson's ratio	0.25
Coefficient of restitution	0.1
Coefficient of friction	0.3

pulley will cause material migration towards the upper outlet of the collector. As in Scenario (1), case (a) (Sec. 5.3), a cubic 30 cm-side bucket is chosen and the velocity of the bucket is set to 2 cm/s, consistent with the steady-state radial velocity of a 99-metre long siphon anchored at Bennu. For simplicity, it is assumed here that the siphon elevation and azimuth angles are both zero. Under these conditions, the net acceleration acting at the CS altitude is $2.6\times10^{-5}\,\mathrm{m\,s^{-2}}$. The parameters used for the DEM simulation are listed in Table 5.1 and are based on Ref. [68] (the Young's modulus is reduced here for computational purposes).

Figure 5.20 shows six still frames of the material release sequence with $k_{\mathrm{cohesion}}=0$ and particles with 1 cm radius. It is apparent that most of the material migrates immediately towards the upper end of the hopper. A fraction of material remains inside the collector but slowly migrates towards the upper end due to the centrifugal-induced acceleration caused by the asteroid rotation. Figure 5.21 shows results for a simulation with a non-zero cohesion energy density ($k_{\mathrm{cohesion}}=25\times10^{3}\,\mathrm{J\,m^{-3}}$). In this case, particles tend to collect in small agglomerations and the release process appears to be more efficient: less particles are dispersed before exiting the outlet (this is clear when comparing Figs. 5.20e, 5.20f with 5.21e, 5.21f).

Figure 5.19b illustrates the geometry of the sorting tower. After exiting the regolith collec-

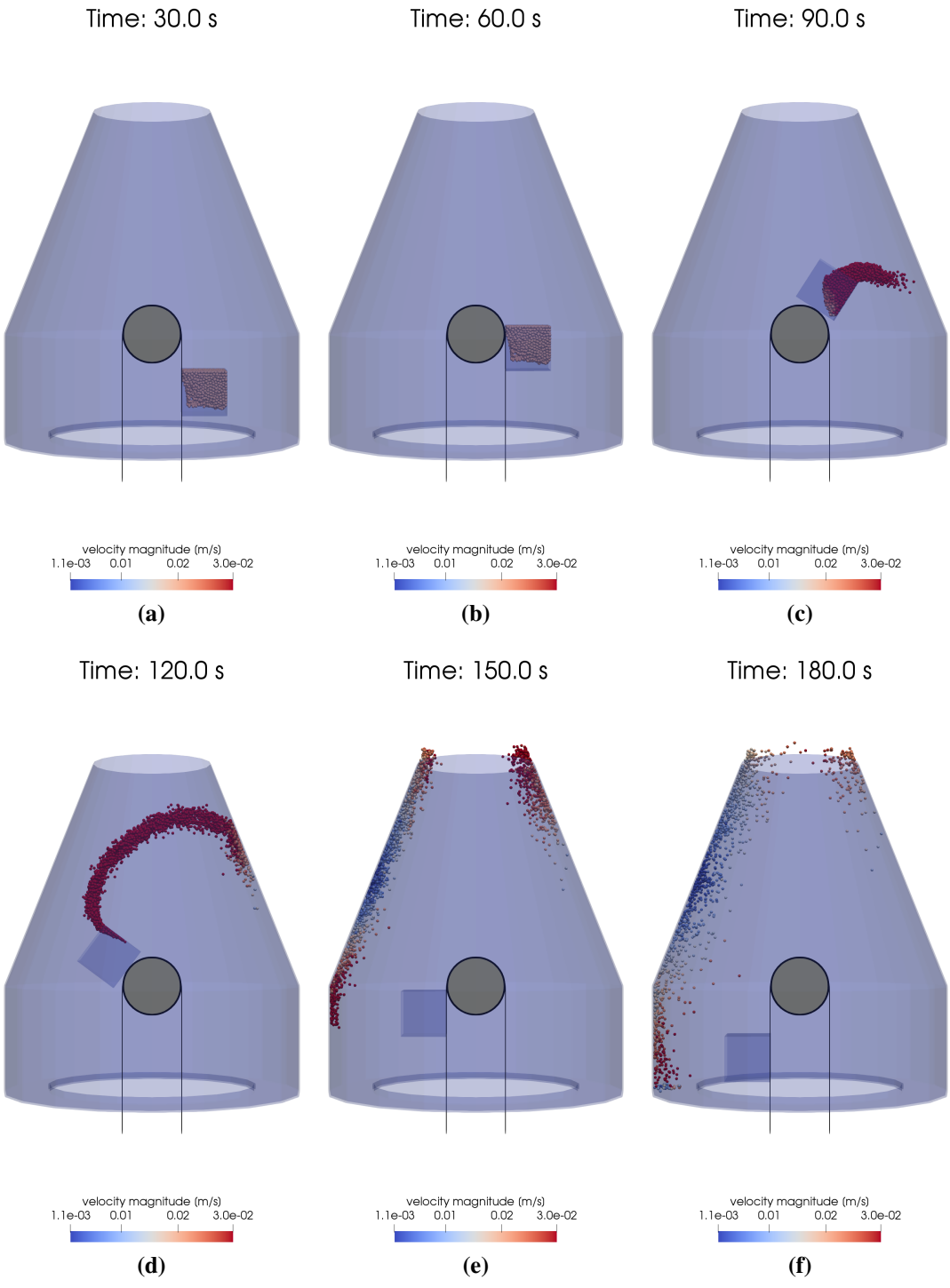

FIGURE 5.20: Particle release to regolith collector, with $k_{\text{cohesion}} = 0$.

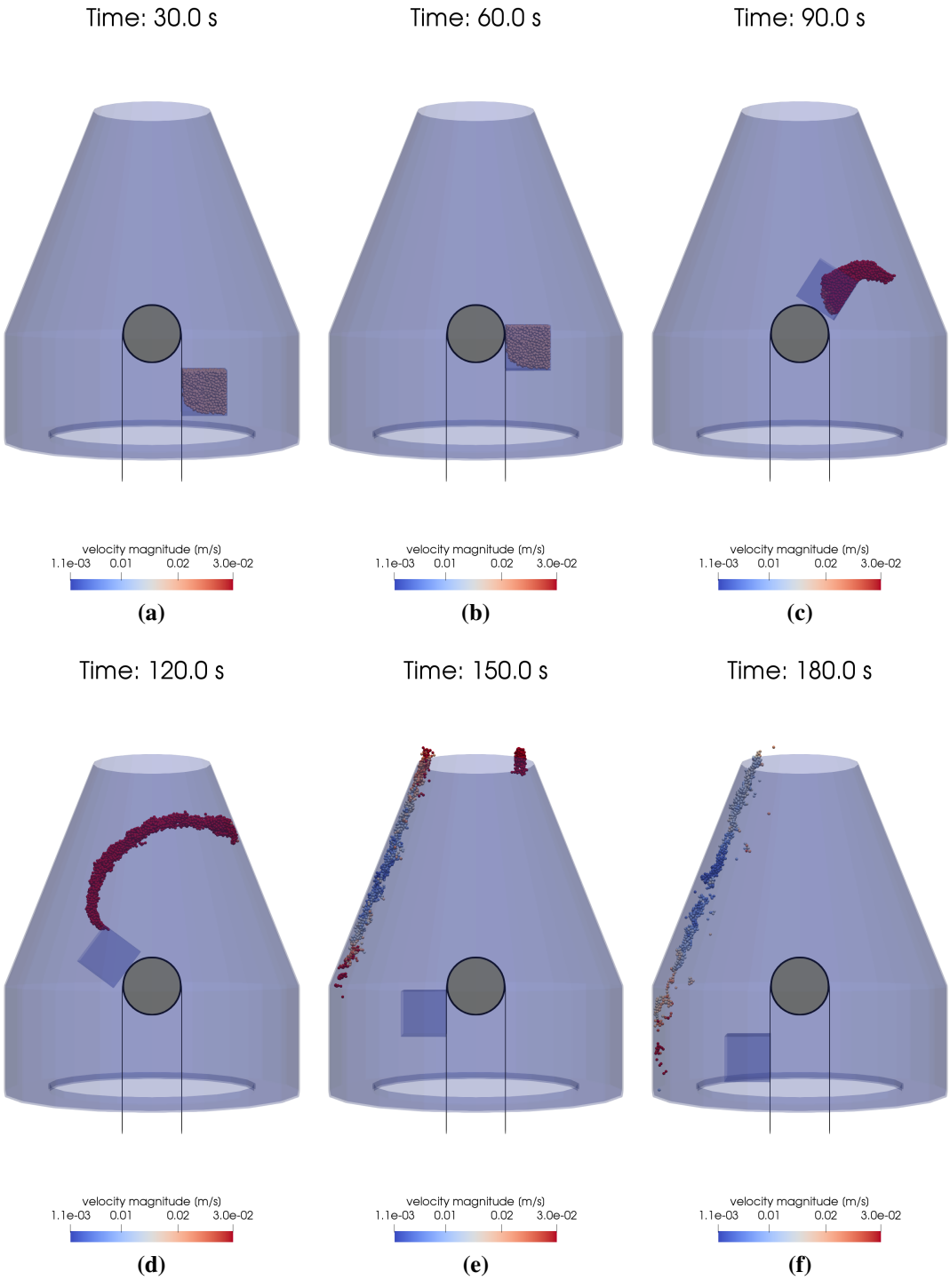

FIGURE 5.21: Particle release to regolith collector, with $k_{\text{cohesion}} = 25 \times 10^3\,\text{J}\,\text{m}^{-3}$.

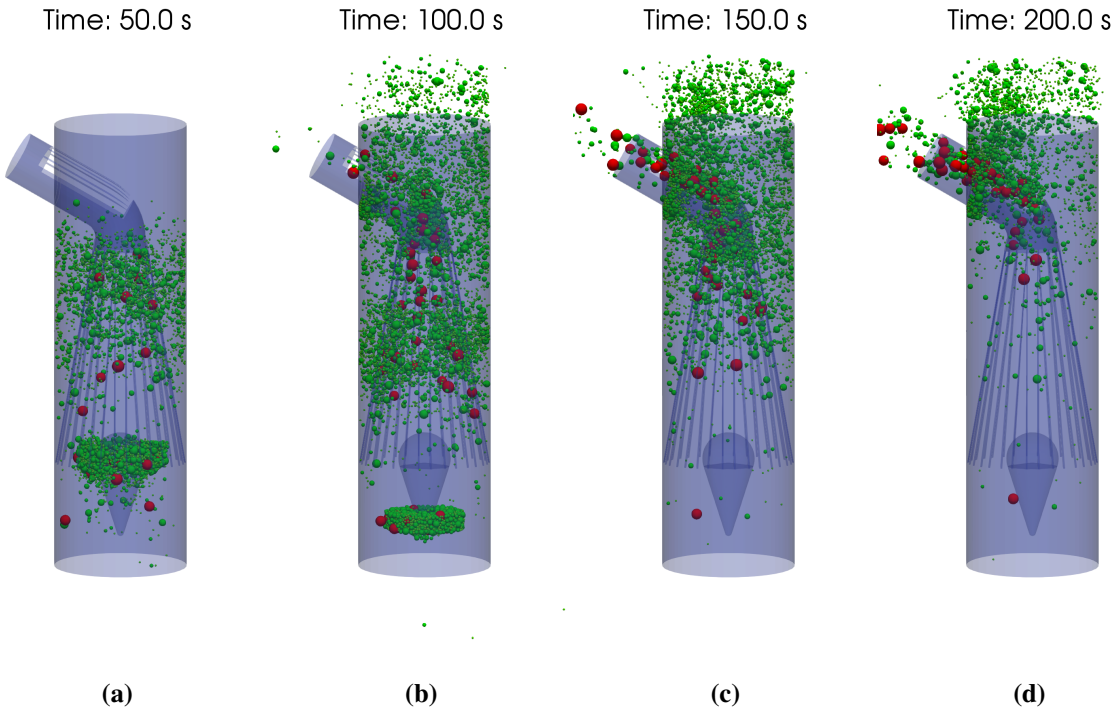

FIGURE 5.22: Sorting tower, with cohesionless particles. The filter allows screening of particles with radius smaller than 1.5 cm. Larger particles are represented in red.

tor, material enters the sorting tower through the inlet, indicated with a blue arrow. A spike then provides the incoming particles with a transversal velocity, such that finer grains can be sieved through the conical filter. Larger grains remain trapped inside the conical filter and exit through the coarse outlet. A second filter is envisaged at the end of the conical filter to allow any remaining fine grain trapped inside the cone to be removed. Figures 5.22 and 5.23 show four still frames of the release process for particles with $k_{\text{cohesion}} = 0$ and $k_{\text{cohesion}} = 10 \times 10^3\,\text{J m}^{-3}$ respectively and variable particle radii between 3.3 mm and 1.9 cm, assuming a d^{-3} size distribution, being d the diameter of the particles [115]. Larger particles are trapped inside the internal converging cone, while smaller particles are sieved and released to the top outlet. The filter allows filtering of particles with a radius below 1.5 cm (represented in green). Particles with a radius larger than 1.5 cm are represented in red. In these simulation, 2200 particles are released four times from the inlet, with 30 s delay between subsequent releases. The magnitude of the release velocity is again $2\,\text{cm s}^{-1}$. It is apparent that most fine particles are released through the upper outlet, although a small fraction of them remain trapped inside the filter and are later released through the coarse grain outlet. In the case with cohesion, a larger fraction of fine particles exit through the coarse grain outlet, thus reducing the overall performance of the sorting tower.

Figure 5.24 shows the efficiency of the sorting tower for the two cases discussed (continuous black line). The efficiency is defined here as the percentage of sorted fine particles: a 100% efficient scenario corresponds to all fine particles being released from the fine particle outlet. Also shown are the efficiencies in the case of longer siphons, producing a larger effective

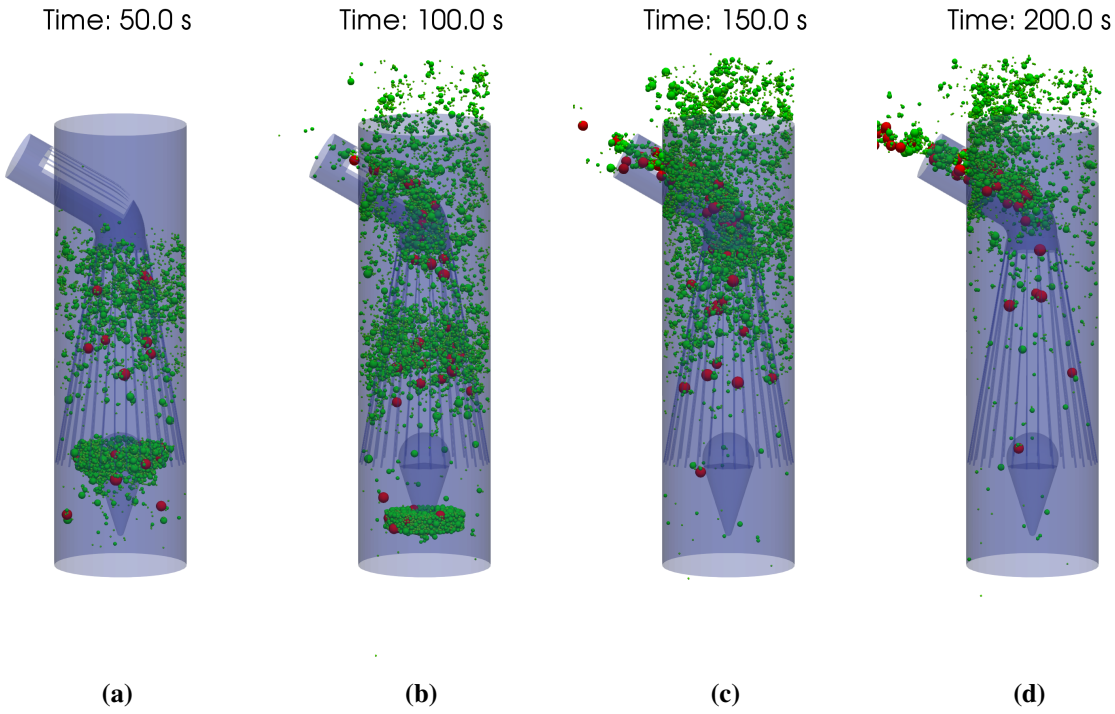

FIGURE 5.23: Sorting tower, with $k_{\text{cohesion}} = 10 \times 10^3\,\text{J}\,\text{m}^{-3}$. The filter allows screening of particles with radius smaller than 1.5 cm (represented in green). Larger particles are represented in red.

acceleration: the red dashed line and blue dot-dashed line correspond to a siphon with length 1.3 km and 15.5 km respectively (and corresponding effective accelerations of $2.6 \times 10^{-4}\,\text{m}\,\text{s}^{-2}$ and $2.6 \times 10^{-3}\,\text{m}\,\text{s}^{-2}$ respectively). No upper bound on the time is chosen, to allow all particles to exit through one of the two outlets. As expected, a larger effective acceleration associated with a longer siphon leads to faster and more efficient sorting. Efficiency is above 95% percent in all cases without cohesion. For the case with $k_{\text{cohesion}} = 10 \times 10^3\,\text{J}\,\text{m}^{-3}$ some finer grains remain attached to larger grains due to cohesive forces and exit through the coarse grain outlet, thus reducing the overall performance of the sorting tower. It can be observed that by further increasing k_{cohesion}, the efficiency is progressively reduced until eventually a macro-agglomeration of particles is generated inside the conical filter which prevents larger grains from exiting through the coarse outlet.

Although this preliminary analysis is far from a comprehensive description of the problem and only a few test cases have been considered, the broad conclusions that can be derived are the following:

- The centrifugal-induced acceleration at the CS may be exploited to sort regolith by size. This operation may be beneficial in large-scale mining scenarios.

- Longer siphons will benefit from larger centrifugal-induced accelerations at the sorting tower thus the efficiency and speed of the sorting process will increase. However, note that

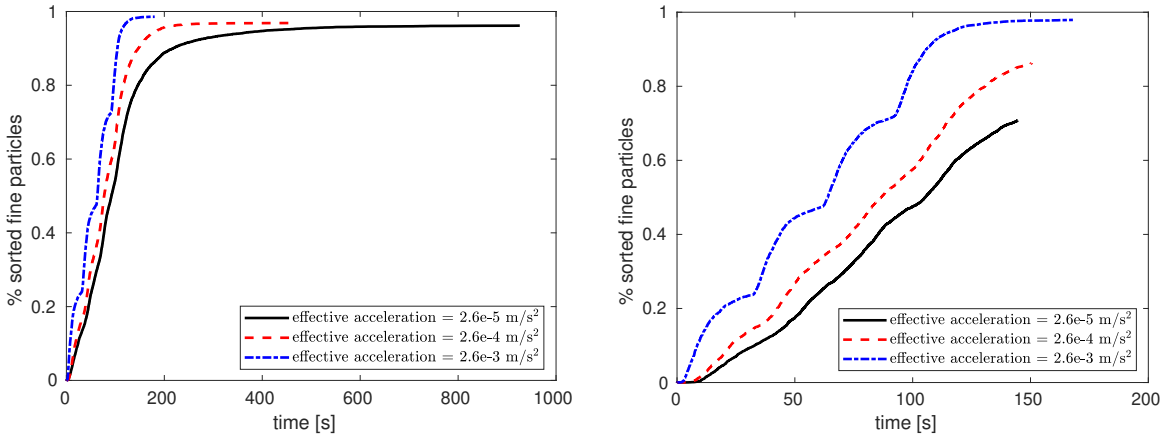

FIGURE 5.24: Percentage of released fine particles as a function of time for $k_{\text{cohesion}} = 0$ (a) and $k_{\text{cohesion}} = 10 \times 10^3$ J/m^3 (b) and a range of effective accelerations.

long conveyor-belt siphons may undergo collisions between the ascending and descending side (Sec. 5.5), thus compromising the whole siphon operation process.

- The efficiency of the sorting process is above 95% for the cohesionless cases analysed here.

- Cohesion between particles may facilitate the release of material at the regolith collector, however reducing the efficiency of the sorting process, since a fraction of the finer grains remain attached to larger grains without exiting the conical filter in the sorting tower.

Future work will require a more detailed parametrisation of the problem, where different geometrical configurations of the sorting tower are considered, to optimise the efficiency of the sorting process. Furthermore, different particle shapes should be used, for a more realistic characterisation of the regolith. It would also be of interest to consider multiple-stage sorting towers, with multiple levels of filters at different altitudes, to enable multiple separation of grains.

Chapter 6

Deflection of asteroids by leveraging rotational self-energy

6.1 Introduction

In this chapter it is proposed to use the orbital siphon effect to change the asteroid orbit. The key idea is to collect material lifted by the siphon and use it as a reaction mass to be released to change the asteroid velocity, thus reducing the impact hazard of a potentially hazardous asteroid. If material is raised to a sufficient altitude, its mechanical energy overcomes the threshold required for escape, therefore simple release of the collected mass without any additional energy input is sufficient to induce a change in the asteroid velocity. In particular, two different release strategies are considered and discussed: (*i*) single mass and (*ii*) multiple mass release. In the first case the largest possible quantity of reaction mass that can be collected using the siphon effect is released. In the second case, rather than releasing the reaction mass once, smaller quantities of mass are collected and released multiple times. For generality, the analysis is extended to asteroids spinning above their critical angular velocity. For this reason, since the collected mass may become significant in case (*i*), its gravitational effect on the siphon is taken into account, as well as the displacement of the system centre-of-mass.

6.2 Model

The system is composed of four main elements: the asteroid to be deflected (primary), the orbital siphon, the collected mass (secondary), and the support tether (Fig. 6.1). The asteroid is modelled as sphere with uniform density ρ, radius R, rotating with angular velocity ω, with the spin axis normal to the orbital plane. The secondary body is the material collected at the top of the siphon. It is assumed that the material is held together by a net-like or deformable structure which expands as material is collected. Detailed modelling of the secondary, including its shape, is outside the scope of this thesis; here, for simplicity, the secondary is treated as a sphere.

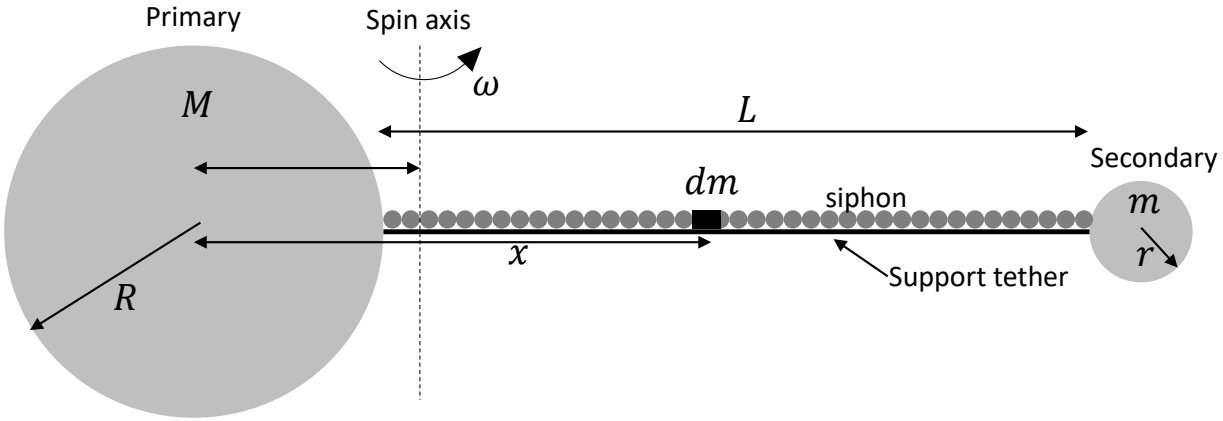

FIGURE 6.1: Orbital siphon model.

A support tether connects the secondary to the primary and provides the necessary tension to prevent the secondary from escaping. The support tether is anchored at a point on the equator of the asteroid and it is assumed to be massless and inextensible.

The orbital siphon is modelled as a continuous mass distribution with linear density μ and total length L. Contrary to Chapter 3, here the mass of the secondary is allowed to increase to non-negligible values, allowing the centre-of-mass to be displaced significantly. Moreover, the gravitational interaction between the secondary and the siphon is taken into account.

In general, the motion of the siphon will induce Coriolis forces, causing oscillations of the support tether in the equatorial plane. However, it has been shown in Chapter 4 that such oscillations are damped, and when the mass collected on the secondary is approximately two orders of magnitude larger than the mass of the siphon, the siphon is effectively aligned with the local vertical (Sec. 4.5). In this chapter, the collected mass on the secondary is much larger than the mass transported on the siphon and therefore the initial oscillation phase is neglected. Therefore, the support tether (and also the siphon) is assumed to remain normal to the asteroid surface at the anchor point.

6.2.1 Force on the siphon

Let $M = 4/3\pi\rho R^3$ and $m = 4/3\pi\rho r^3$ represent the primary and secondary mass at some time during siphon operation. Let dm be an infinitesimal element of mass of the siphon, x its distance from the primary and dx its length. Within an asteroid-fixed reference frame, the element dm is subjected to gravitational and centrifugal-induced forces. The gravitational force acting on dm can be written as:

$$df_g = G\left(\frac{m}{(H-x)^2} - \frac{M}{x^2}\right)\mu dx \tag{6.1}$$

where $H = R + L + r$ is the distance between primary and secondary centre-of-mass. Note that the first positive component is due to the attraction towards the secondary, which enhances the siphon effect. Likewise, the centrifugal-induced force acting on the same mass element can be

written as

$$df_c = \omega^2(x - x_b)\mu dx \tag{6.2}$$

where x_b is the distance between the centre-of-mass of the system and the center of the primary:

$$x_b = \frac{mH}{M+m} \tag{6.3}$$

From this point, the subscript "0" appended to a variable represents the state of that variable at the beginning of siphon operation. Hence, for example, R_0 and M_0 represent the initial radius and mass of the asteroid, respectively. The two forces can be written in non-dimensional form using the scale factors listed in Table 3.1 (note that all scale factors are here referred to the primary), such that:

$$d\bar{f}_g = \left(\frac{\bar{m}}{(\bar{H} - \bar{x})^2} - \frac{\bar{M}}{\bar{x}^2} \right) \bar{\mu} d\bar{x} \tag{6.4}$$

$$d\bar{f}_c = \bar{m}\bar{\omega}^2(\bar{x} - \bar{H})\bar{\mu} d\bar{x} \tag{6.5}$$

Contrary to previous chapters, here $\omega > \omega_{\text{crit}}$ is allowed for the sake of generality (the critical angular velocity ω_{crit} is given by Eq. (3.4)). Then, the total force acting on the siphon is given by the integral

$$\bar{f} = \int_{\bar{R}}^{\bar{R}+\bar{L}} (d\bar{f}_g + d\bar{f}_c) \tag{6.6}$$

Upon simplification, Eq. (6.6) can be written as:

$$\bar{f} = \bar{\mu} \left[\frac{\bar{L}(1-\bar{R}^3)^{2/3}}{\bar{L} + (1-\bar{R}^3)^{1/3}} - \frac{\bar{L}\bar{R}^2}{\bar{L}+\bar{R}} + \frac{1}{2}\bar{L}\left[\bar{L} + 2\bar{R} + 2(\bar{R}^3 - 1)(\bar{L} + \bar{R} + (1-\bar{R}^3)^{1/3}) \right] \bar{\omega}^2 \right] \tag{6.7}$$

Due to the continuous mass distribution, the siphon is effectively treated as a rigid body and the force $\bar{f}$ is applied at its centre-of-mass. Note that Eq. (6.7) can also be written as a function of the secondary mass by applying the substitution

$$\bar{R} = (1 - \bar{m})^{1/3} \tag{6.8}$$

Equation (6.8) follows from the conservation of mass $\bar{M} + \bar{m} = 1$. As in previous chapters, the force $\bar{f}$ must be positive to enable siphon operation, i.e., directed towards the secondary:

$$\bar{f} > 0 \tag{6.9}$$

The siphon length $\bar{L}_{\text{eq}}$ that leads to $\bar{f} = 0$ is the equilibrium length and corresponds to the minimum length to guarantee the siphon effect. Figure 6.2 shows the equilibrium length as a function of the asteroid angular velocity $\bar{\omega}_0$ and the secondary mass $\bar{m}$. The black curve,

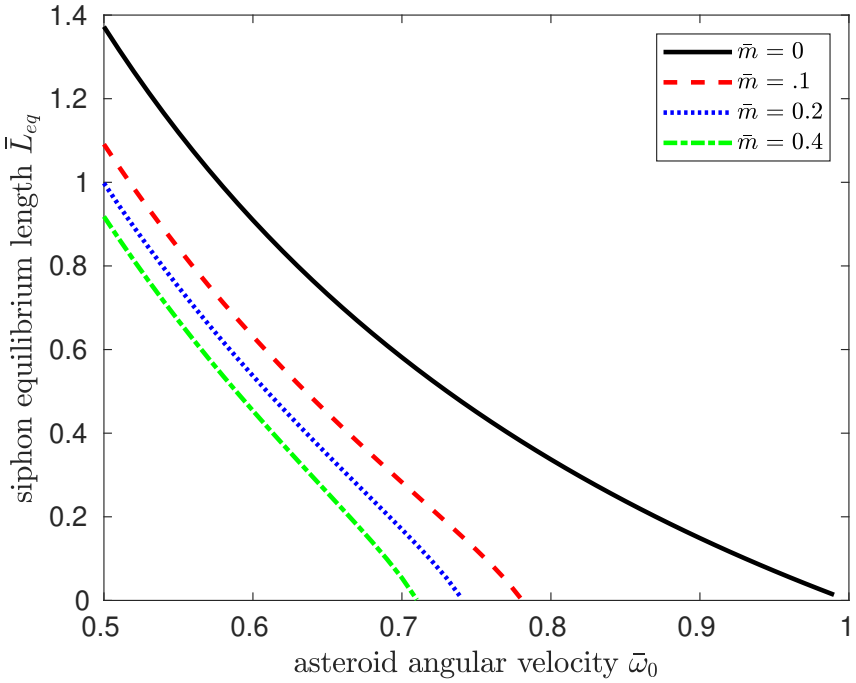

FIGURE 6.2: Siphon equilibrium length as a function of the angular velocity for a range of secondary masses.

corresponding to the case $\bar{m} = 0$ is the same equilibrium curve found in Chapter 3 for a siphon without a secondary mass. It is apparent from Fig. 6.2 that a larger secondary mass decreases the equilibrium length for a given angular velocity. Note that if $\bar{m} = 0.5$, the condition $\bar{f} = 0$ is verified for any $\bar{L}$. In fact, the condition $\bar{m} = 0.5$ implies that the system is symmetric with respect to its rotation axis.

6.2.2 Support tether tension

The tension on the support tether can be found by considering the equilibrium of the forces at one of its ends. It must be stressed that the support is modelled as a massless, inextensible tether and therefore its tension is constant over its length. The equilibrium of forces acting on the anchor point of the primary can be written as (the same result is obtained by considering the equilibrium on the attachment to the secondary):

$$M\omega^2 x_b - G\frac{Mm}{H^2} - \tau = 0 \tag{6.10}$$

where the tension force τ is considered positive when the tether is in tension. The first term appearing in Eq. (6.10) is the centrifugal-induced force due to the rotation of the primary with respect to the centre-of-mass of the system and the second term is the gravitational attraction between the primary and the secondary. Clearly, a larger angular velocity will increase the tension in the tether, whereas a larger gravitational attraction between the primary and the secondary will reduce it. Solving Eq. (6.10) for τ and dividing both sides by the force scale factor (see

Table 3.1), the resulting non-dimensional tension becomes:

$$\bar{\tau} = \bar{m}(1-\bar{m})\left(\bar{\omega}^2\bar{H} - \frac{1}{\bar{H}^2}\right) \tag{6.11}$$

The condition $\tau > 0$ must be verified to ensure the tether is always in tension. Such a requirement can be translated into a lower bound for the angular velocity:

$$\bar{\omega} > \sqrt{\frac{1}{\bar{H}^3}} \tag{6.12}$$

It will be shown that Eq. (6.12) is a necessary condition to enable insertion of the secondary mass to escape.

6.2.3 Conservation of angular momentum

If the inequalities (6.9) and (6.12) are satisfied, material is transferred from the primary to the secondary. Conservation of angular momentum can be invoked to evaluate the variation of the angular velocity of the system in response to the transfer of a given quantity of mass Δm from the primary to the secondary. Then, let the subscripts 1 and 2 refer to a variable *before* and *after* the transfer of material, respectively. Neglecting the mass of the siphon, the inertia of the system in the two states can be written as:

$$I_i = \frac{2}{5}(M_i R_i^2 + m_i r_i^2) + M_i x_{b,i}^2 + m_i(R_i + L + r_i - x_b)^2, \quad i = 1,2 \tag{6.13}$$

where

$$\begin{aligned} M_1 &= M; \quad M_2 = M - \Delta m; \\ m_1 &= m; \quad m_2 = m + \Delta m; \end{aligned} \tag{6.14}$$

Note that R_i and $x_{b,i}$ can be written as a function of Δm through Eqs.(6.3) and (6.8). Conservation of angular momentum therefore requires that

$$I_1\omega_1 = I_2\omega_2 \tag{6.15}$$

Setting $M = M_0$, it follows $\Delta m = m$ and Eq. (6.15) can be further simplified and written in non-dimensional form:

$$\frac{\bar{\omega}_2}{\bar{\omega}_1} = \frac{2}{5\left(\bar{m}(1-\bar{m})\left(\bar{L} + \bar{m}^{1/3} + (1-\bar{m})^{1/3}\right)^2 + \frac{2}{5}\left(\bar{m}^{5/3} + (1-\bar{m})^{5/3}\right)\right)} \tag{6.16}$$

Equation (6.16) describes the variation of the angular velocity of the system from the initial condition $\bar{M}_1 = 1$, $\bar{m}_2 = 0$ to the final condition $\bar{M}_2 = 1 - \bar{m}$, $\bar{m}_2 = \bar{m}$ as a function of the secondary mass. Note that, if the secondary mass is small ($m \to 0$), linearisation of Eq. (6.16)

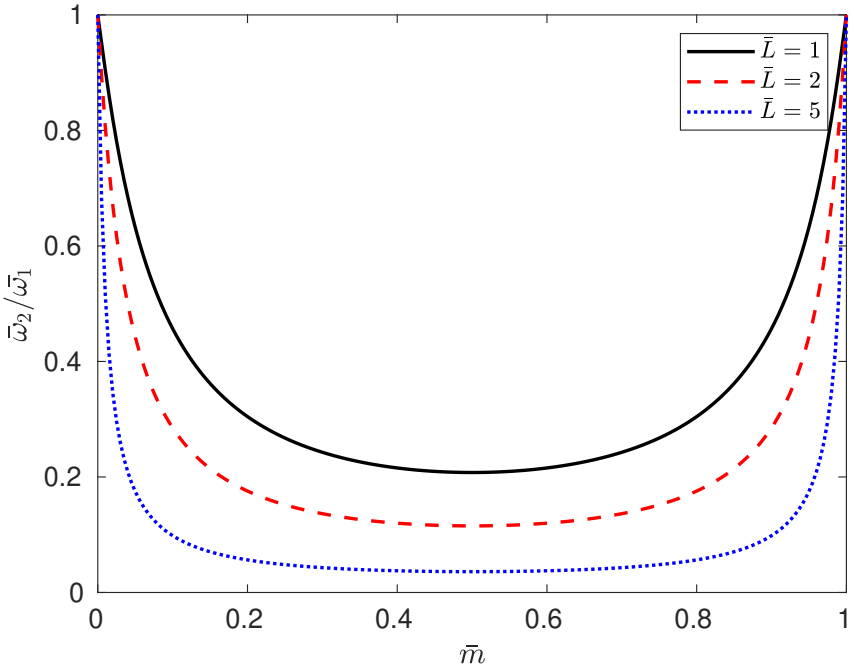

FIGURE 6.3: Angular velocity ratio $\bar{\omega}_1/\bar{\omega}_2$ as a function of the secondary mass for a range of siphon lengths $\bar{L}$.

reduces to the angular velocity ratio found in Chapter 3 for an orbital siphon releasing material to orbit.

Figure 6.3 shows the angular velocity ratio $\bar{\omega}_2/\bar{\omega}_1$ as a function of the secondary mass $\bar{m} \in [0,1]$ for a range of siphon lengths. As expected, the ratio strictly decreases for $\bar{m} \in [0,0.5]$. Clearly, the plot is symmetric with respect to $\bar{m} = 0.5$, i.e., if the secondary mass could be increased beyond $M_0/2$, the system would recover its initial angular velocity ω_0 when the entire asteroid mass is transferred to the secondary.

Substituting Eq. (6.16) into Eq. (6.7) with $\omega_2 = \omega$ and $\omega_1 = \omega_0$ allows the change of the siphon force as a function of the asteroid initial angular velocity ω_0, the siphon length L and the extracted mass $\bar{m}$ to be seen. As an example, Fig. 6.4 shows the variation of the non-dimensional siphon force (here divided by $\bar{\mu}$) as a function of the secondary mass for a range of initial angular velocities $\bar{\omega}_0$ and taking $\bar{L} = 0.5$. When the siphon force is zero, the system has reached its equilibrium, thus arresting the siphon effect (unless the siphon length is changed, however variable length siphons are not consider here). Clearly, larger initial angular velocities permits the collection of a larger mass on the secondary. It can be verified that, if ω_0 is large enough to reach $\bar{m} = 0.5$, then $F < 0$, for any $\bar{m} \in [0.5,1]$. Therefore, self sustaining mass flow from the primary to the secondary is not possible for $\bar{m} > 0.5$.

Siphon operation for a continuous mass distribution can be modelled by the three-step sequence shown in Fig. 6.5. If a net force $f > 0$ is acting on the siphon, it will accelerate in the direction of the secondary (from step (a) to step (b) in Fig.6.5). The radial velocity v of the chain for a siphon modelled as a continuous mass distribution is related to the radial force

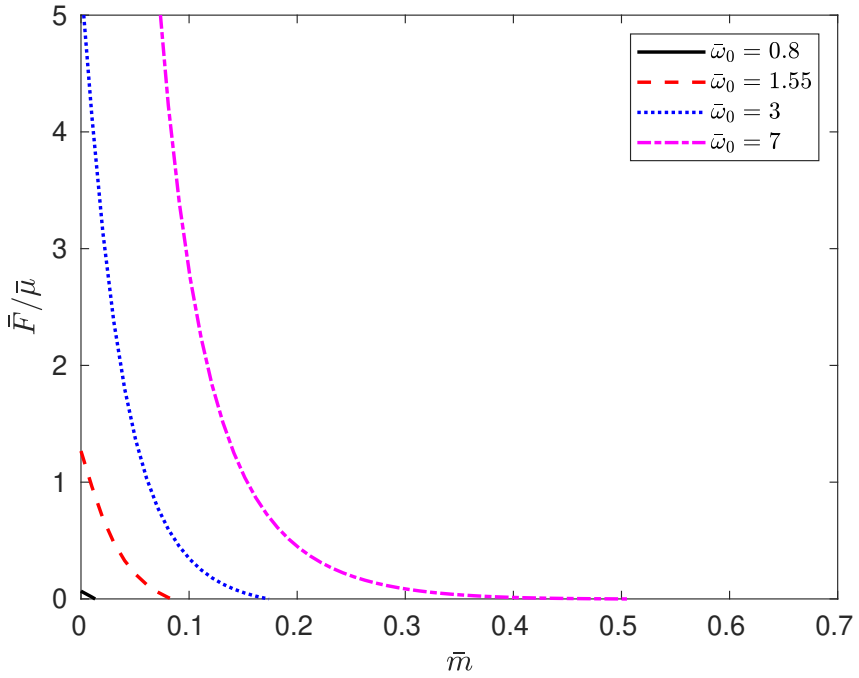

FIGURE 6.4: Siphon force as a function of the secondary mass, for a range of initial angular velocities, taking $\bar{L} = 0.5$.

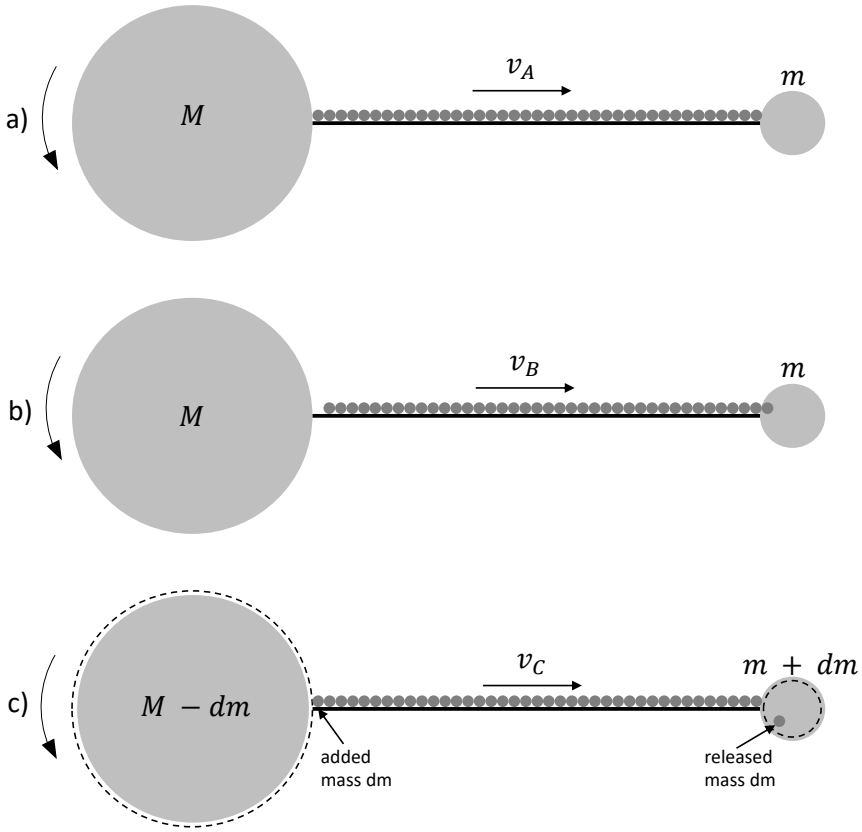

FIGURE 6.5: Siphon operation sequence

and the siphon linear density, via Eq. (3.58), with $\bar{f}_{\text{cont}}$ here given by Eq. (6.7). As in previous chapters, the initial transitory phase is neglected.

The manipulation time t_{man} required to collect the mass m_f on the secondary is related to the siphon radial velocity and linear density via Eq. (3.70).

6.3 Primary deflection

In this section the variation of the kinetic and potential energy of the system before and after detachment of the secondary from the support tether is considered, to study the fraction of rotational kinetic energy of the primary that can be converted into translational kinetic energy. Let E_0, E_-, E_+ and E_∞ represent the total energy of the system before the siphon operation starts (0), after collection of a mass m on the secondary ($-$), after release of mass m from the secondary ($+$) and, when the secondary has reached the sphere of influence of the primary after its release (∞).

The total energy of the system in the initial state 0 can be written as

$$E_0 = \frac{1}{2}\left(\frac{2}{5}M_0R_0^2\right)\omega_0^2 - \frac{3}{5}\frac{GM_0^2}{R_0} \tag{6.17}$$

where the first term is the total rotational kinetic energy of the primary while the second term is the gravitational self-energy of the primary. Upon delivery of mass m to the secondary, the total energy becomes (neglecting the mass of the siphon)

$$E_- = K_r^- + P_{self,p}^- + P_{self,s}^- + P_{mutual}^- \tag{6.18}$$

where K_r^- is the total rotational kinetic energy of the system (including primary and secondary), $P_{self,p}^-$ and $P_{self,s}^-$ are the gravitational self-energies of the primary and the secondary respectively whereas P_{mutual}^- is the mutual gravitational potential energy between two masses. The rotational kinetic energy can be written as:

$$K_r^- = \frac{1}{2}\left(\frac{2}{5}MR^2 + Mx_b^2 + \frac{2}{5}mr^2 + m(D-x_b)^2\right)(\omega^-)^2 \tag{6.19}$$

The angular velocity ω^- is obtained via conservation of angular momentum (Eq. (6.16)). The mutual gravitational potential P_{mutual}^- is:

$$P_{mutual}^- = -G\frac{Mm}{H} \tag{6.20}$$

It can be verified that $E_- - E_0 < 0$. In fact, part of the kinetic energy of material reaching the top of the siphon is lost due to the inelastic impact with the secondary.

Upon detachment of the secondary from the siphon, the primary and the secondary are re-

leased with velocity magnitudes Δv_p^+ and Δv_s^+, such that the total angular momentum before and after release is conserved:

$$\left(\frac{2}{5}MR^2 + Mx_b^2 + \frac{2}{5}mr^2 + m(D-x_b)^2\right)\omega^- = \frac{2}{5}MR^2\omega_p^+ + x_bM\Delta v_p^+ + \frac{2}{5}mr^2\omega_s^+ + (D-x_b)m\Delta v_s^+ \tag{6.21}$$

The angular momentum is evaluated with respect to the axis passing through the system center-of-mass and normal to the orbital plane. The variables ω_p^+ and ω_s^+ represent the angular velocity of the primary and the secondary after release. Eq. (6.21) is verified if

$$\omega_p^+ = \omega^- \tag{6.22a}$$

$$\omega_s^+ = \omega^- \tag{6.22b}$$

and

$$\Delta v_p^+ = \omega^- x_b \tag{6.23a}$$

$$\Delta v_s^+ = \omega^-(H-x_b) \tag{6.23b}$$

Equations (6.22a), (6.22b) dictate that the two bodies will spin about their respective center-of-mass with angular velocity ω^-, i.e., the same angular velocity about the system center-of-mass before release. The total energy of the system after release is then:

$$E_+ = K_{r,p}^+ + K_{r,s}^+ + K_{t,p}^+ + K_{t,s}^+ + P_{self,p}^+ + P_{self,s}^+ + P_{mutual}^+ \tag{6.24}$$

where

$$K_{r,p} = \frac{1}{2}\left(\frac{2}{5}MR^2\right)(\omega_p^+)^2, \quad K_{r,s} = \frac{1}{2}\left(\frac{2}{5}mr^2\right)(\omega_s^+)^2 \tag{6.25}$$

are the rotational kinetic energies of the primary and secondary after release respectively, and

$$K_{t,p} = \frac{1}{2}M(\Delta v_p^+)^2, \quad K_{t,s} = \frac{1}{2}m(\Delta v_s^+)^2 \tag{6.26}$$

are the corresponding translational kinetic energy. Substituting Eq. (6.22) and (6.23) into Eq. (6.24) yields $E_+ = E_-$, i.e., in absence of the energy losses during detachment, the total energy of the system is conserved.

Assuming two body dynamics after release, the total energy of the system is conserved. In particular, $E_\infty = E_+$. Since the rotational kinetic energies and self-energies of the two bodies play no role in the subsequent dynamical evolution of the system (their value is conserved and they cannot be further exchanged into other forms of energy within the system) let $E = E_+ - K_{r,p}^+ - K_{r,s}^+ - P_{self,p}^+ - P_{self,s}^+$ be the sum of translational kinetic energy and mutual potential upon release, which is conserved and regulates the subsequent orbital behaviour of the two bodies. In particular, if $E > 0$ primary and secondary will have enough energy to escape each other.

Conservation of the energy E from state $+$ to ∞ yields:

$$\frac{1}{2}M(\Delta v_p^+)^2+\frac{1}{2}m(\Delta v_s^+)^2-G\frac{Mm}{H}=\frac{1}{2}M(\Delta v_p^\infty)^2+\frac{1}{2}m(\Delta v_s^\infty)^2 \tag{6.27}$$

where Δv_p^∞ and Δv_s^∞ are the velocity magnitudes or the primary and the secondary with respect to the system center-of-mass when the two bodies are sufficiently far apart, i.e., at the the sphere of influence. The value Δv_p^∞ represents the effective change in velocity imparted to the primary due to the release of m, taking into account the gravitational interaction between the two bodies within the sphere of influence. In order to solve Eq. (6.27) for Δv_p^∞, conservation of linear momentum is invoked [1]:

$$\Delta v_s^+=\frac{M}{m}\Delta v_p^+ \tag{6.28}$$

Inserting Eq. (6.28), (6.23) and (6.3) into Eq. (6.27), after some algebraic manipulation, the magnitude of the primary hyperbolic escape velocity can be written in non-dimensional form as:

$$\Delta\bar{v}_p^\infty=\bar{m}\sqrt{(\bar{\omega}^+)^2\bar{H}^2-\frac{2}{\bar{H}}} \tag{6.29}$$

As expected, $\Delta\bar{v}_p^\infty$ is proportional to $\bar{m}$, suggesting that the collection of a larger secondary mass will increase the momentum exchange between the two bodies, thus contributing to a larger change in velocity of the primary. However, a larger $\bar{m}$ also implies a larger reduction of the asteroid angular velocity at release (Eq. (6.16)), thus reducing $\Delta\bar{v}_p^\infty$.

It is instructive to observe that the condition of secondary escape $E>0$ can also be expressed as a lower bound for the angular velocity at release:

$$\bar{\omega}>\sqrt{\frac{2}{\bar{H}^3}} \tag{6.30}$$

where the superscript $+$ has been removed from ω for simplicity. By comparing Eqs. (6.30) and (6.12), it is apparent that the condition of secondary escape $E>0$ is sufficient to guarantee positive tension of the support tether $\tau>0$.

Moreover, by comparing Eq. (6.29) with (6.23a), the primary hyperbolic excess velocity can be written as a function of its release velocity:

$$\Delta\bar{v}_p^\infty=(\Delta\bar{v}_p)^+\left(1-\frac{2}{\bar{H}^3\bar{\omega}^2}\right) \tag{6.31}$$

The factor $\frac{2}{\bar{H}^3\bar{\omega}^2}$ can be interpreted as a gravitational dragging coefficient, written as a function of the distance between the two bodies and the angular velocity of the system at release. When $\bar{H}^3\bar{\omega}^2=2$ $\Delta\bar{v}_p^\infty=0$, and the secondary is inserted in bound motion around the primary.

Figure 6.6 shows in green the region of secondary escape ($E>0$), as a function of $\bar{\omega}$ and

[1] It is emphasized that Eq. (6.28) is relating the *magnitudes* of the velocities. From a vectorial point of view $\Delta\mathbf{v}_s=-\frac{M}{m}\Delta\mathbf{v}_p$. Note that Eq. (6.28) clearly holds also for Eqs. (6.23)

$\bar{L}$, for $\bar{m} = 0$, $\bar{m} = 0.01$, $\bar{m} = 0.05$ and $\bar{m} = 0.12$. The orange region is associated with the secondary being inserted into a bound orbit about the primary with $E < 0$. The red region represents the combination of $\bar{\omega}$ and $\bar{L}$ leading to an inverted mass flow, from the secondary to the primary ($f < 0$, Eq. (6.7)). For larger $\bar{m}$ the $E < 0$ region gradually shrinks and for $\bar{m} > 0.12$ the secondary can only be released to escape. The black contour on the $E > 0$ regions represents the value of the gravitational dragging factor. The black dotted line indicates the condition for zero tension on the support tether ($\tau = 0$, Eq. (6.10)). The region with $f > 0$ is also characterized by a positive support tether tension $\tau > 0$.

In the following sections, the superscript ∞ is removed and the hyperbolic excess velocity of the primary is simply indicated indicated with $\Delta\bar{v}_p$.

6.3.1 Upper bound for $\Delta\bar{v}_p$

It is instructive to observe that the velocity change of the primary $\Delta\bar{v}_p$ admits a theoretical upper bound due to energy conservation. In fact, assuming that the entire rotational kinetic energy could be converted into translational kinetic energy:

$$\frac{1}{2}\left(\frac{2}{5}M_0R_0^2\right)\omega_0^2 = \frac{1}{2}M_0\Delta v_{\max}^2 \tag{6.32}$$

where $\Delta v_{\max}$ is the maximum Δv_p achievable under these conditions and again the term in brackets on the left hand side is the asteroid moment inertia. Then:

$$\Delta\bar{v}_{\max} = \sqrt{\frac{2}{5}}\bar{\omega}_0 \tag{6.33}$$

For example, an asteroid with density $\rho = 2000\,\mathrm{kg\,m^{-3}}$, radius $R_0 = 250\,\mathrm{m}$ and period 4 h admits a $\Delta v_{\max} = 0.069\,\mathrm{m\,s^{-1}}$. This theoretical upper bound will be compared with Δv_p to assess the practical performance of the orbital siphon for deflection.

6.3.2 Deflection distance

The Clohessy-Wiltshire (CW) equations [29] are used to assess the primary deflection achieved through release of the secondary mass. Here it is assumed that the initial heliocentric orbit of the primary is circular with zero inclination. The CW equations describe the motion of a point (in this case, the primary) with respect to a reference frame (in this case, the unperturbed position of the primary before any manipulation occurs). Let $X - Y$ be a reference frame centred on the unperturbed position with the X-axis parallel to the Sun-asteroid direction and the Y-axis in the direction of motion (Fig. 6.7). Let X_p, Y_p be the position of the primary in this frame and $\dot{X}_p, \dot{Y}_p$ its velocity. Analogous variables are defined for the secondary, with subscript s. Then, the CW

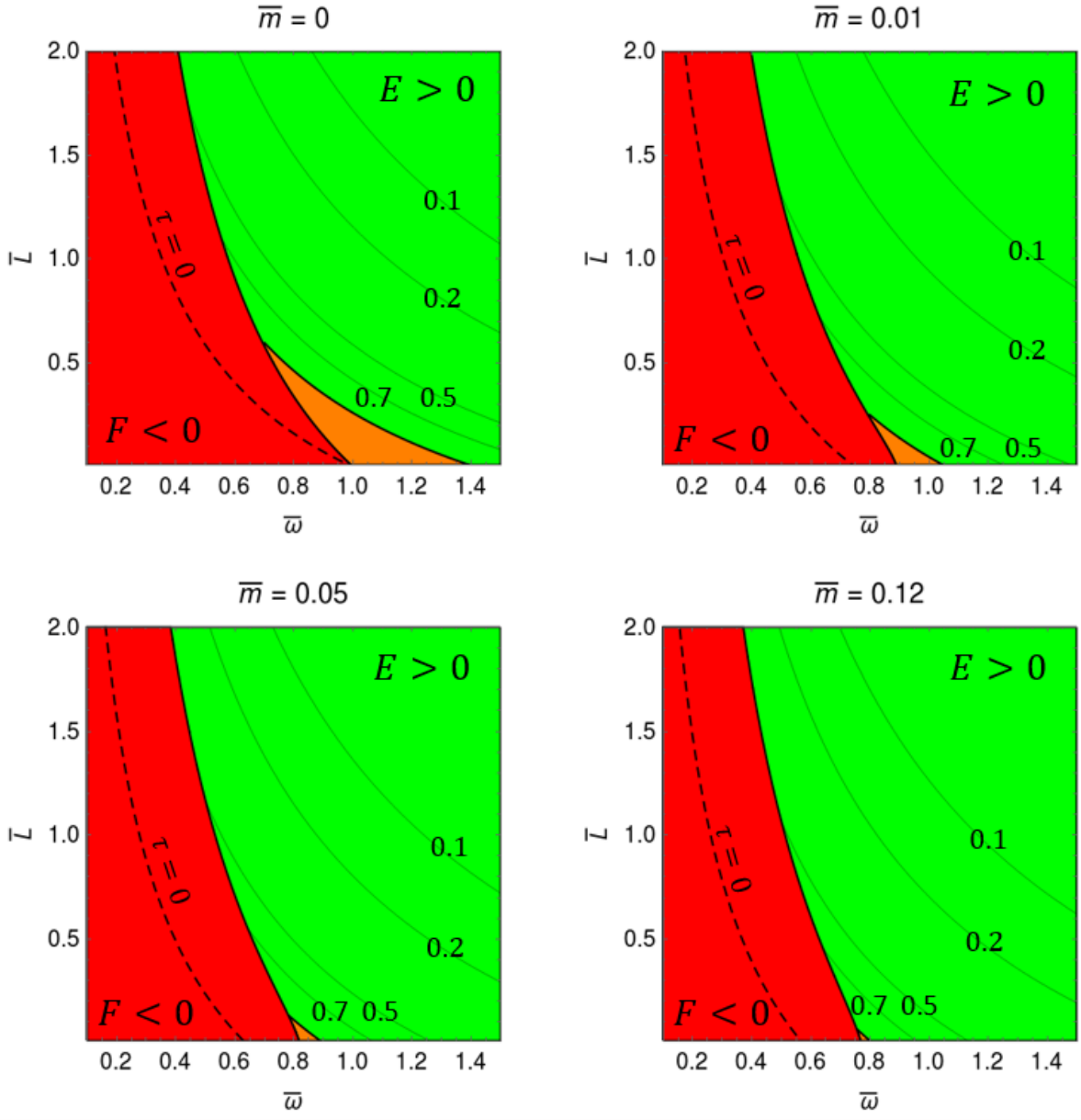

FIGURE 6.6: Regions of secondary escape (green), release to bound orbit (orange) and siphon with negative force (red), as a function of the asteroid velocity $\bar{\omega}$ and the siphon length $\bar{L}$.

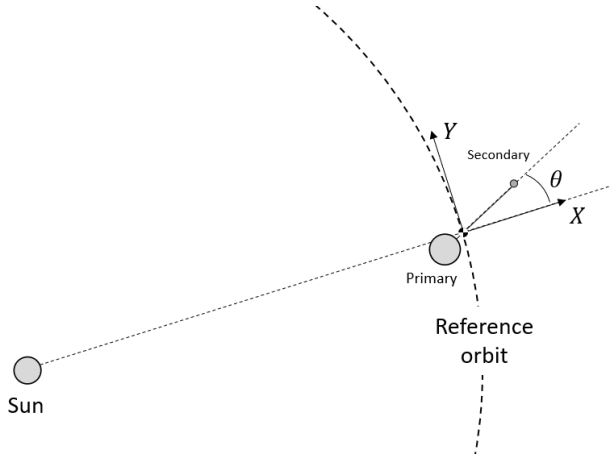

FIGURE 6.7: CW reference frame.

equations for the two masses upon secondary release can be written as

$$\ddot{X}_i = 3\omega_{\text{orb}}^2 X_i + 2\omega_{\text{orb}}\dot{Y}_i + a_{i,X}, \quad i = p,s \tag{6.34a}$$

$$\ddot{Y}_i = -2\omega_{\text{orb}}\dot{X}_i + a_{i,Y}, \qquad i = p,s \tag{6.34b}$$

where $\omega_{\text{orb}} = 2\pi/t_{\text{rev}}$, where t_{rev} is the heliocentric orbit period of the asteroid, and $a_{i,X}, a_{i,Y}$ are the additional accelerations caused by the mutual gravitational interaction between the two masses. Here, the mutual gravitational terms are neglected and the primary is assumed to be released with the appropriate velocity magnitude at the sphere of influence (Eq. (6.29)). Thereby, Eqs. (6.34) can be solved in closed-form to find the state of the the primary as a function of time [29]. Using the scaling factors in Table 3.1:

$$\begin{pmatrix} \bar{X}_p(t) \\ \bar{Y}_p(t) \\ \dot{\bar{X}}_p(t) \\ \dot{\bar{Y}}_p(t) \end{pmatrix} = \begin{pmatrix} 4-3\cos\bar{\omega}_{\text{orb}}\bar{t} & 0 & \frac{1}{\bar{\omega}_{\text{orb}}}\sin\bar{\omega}_{\text{orb}}\bar{t} & \frac{2}{\bar{\omega}_{\text{orb}}}(1-\cos\bar{\omega}_{\text{orb}}\bar{t}) \\ 6(\sin\bar{\omega}_{\text{orb}}\bar{t}-\bar{\omega}_{\text{orb}}\bar{t}) & 1 & -\frac{2}{\bar{\omega}_{\text{orb}}}(1-\cos\bar{\omega}_{\text{orb}}\bar{t}) & \frac{1}{\bar{\omega}_{\text{orb}}}(4\sin\bar{\omega}_{\text{orb}}\bar{t}-3\bar{\omega}_{\text{orb}}\bar{t}) \\ 3\bar{\omega}_{\text{orb}}\sin\bar{\omega}_{\text{orb}}\bar{t} & 0 & \cos\bar{\omega}_{\text{orb}}\bar{t} & 2\sin\bar{\omega}_{\text{orb}}\bar{t} \\ -6n(1-\cos\bar{\omega}_{\text{orb}}\bar{t}) & 0 & -2\sin\bar{\omega}_{\text{orb}}\bar{t} & 4\cos\bar{\omega}_{\text{orb}}\bar{t}-3 \end{pmatrix} \begin{pmatrix} \bar{X}_{0,p} \\ \bar{Y}_{0,p} \\ \dot{\bar{X}}_{0,p} \\ \dot{\bar{Y}}_{0,p} \end{pmatrix} \tag{6.35}$$

where $(\bar{X}_{0,p}, \bar{Y}_{0,p}, \dot{\bar{X}}_{0,p}, \dot{\bar{Y}}_{0,p})$ is the initial state of the primary. The parameter $\sqrt{\bar{X}_p(t)^2 + \bar{Y}_p(t)^2}$ therefore represents the total deflection of the primary at the time $\bar{t}$ away from its unperturbed position. As noted, it is assumed that $\sqrt{\dot{\bar{X}}^2 + \dot{\bar{Y}}^2} = \Delta v_p$. As regards the direction of the velocity vector and the position $X_{0,p}, Y_{0,p}$ it is assumed that: (i) the velocity at the sphere of influence is parallel to the release velocity and (ii) the position vector $(X_{0,p}, Y_{0,p})$ coincides with the release position. It will be shown that the primary trajectory resulting from these approximations does not differ significantly from that obtained by numerical integration of Eq. (6.34), thus making assumptions (i) and (ii) valuable approximations for this preliminary analysis. The primary release position is therefore completely defined by the angle θ between siphon and the X-axis. Here, it is chosen to release the secondary when $\theta = 0$ to ensure that the direction of Δv_p is

parallel to the Y-axis, i.e., in the direction of orbital motion. This changes the period of the resulting orbit and therefore increases the long-term drift with respect to the unperturbed path [4, 32]. Note that, using this model, $\theta = \pi$ would lead to an equivalent deflection trajectory, but symmetric with respect to the X-axis.

6.3.3 Deflection scenarios

Two deflection scenarios are considered: single (SR) and multiple (MR) secondary release. In the SR scenario, a secondary mass m_f is collected at the secondary and released once. The secondary mass m_f and siphon length are selected in order to maximize the effective release velocity of the primary Δv_p. In the second case a smaller Δm (to be chosen) is collected and released multiple times, until the siphon reaches equilibrium ($\bar{f} = 0$, Eq. (6.7)). The siphon length is chosen in order to maximize Δv_p, taken as the sum of the primary hyperbolic excess velocities at each release. In both cases the total deflection that can be achieved in a given time window t_{window} is calculated, for a given asteroid initial angular velocity $\bar{\omega}_0$, siphon linear density μ and heliocentric orbital period (that defines the parameter $\bar{\omega}_{\text{orb}}$).

For a SR release scenario (see Algorithm 1):

1. The time t_{man} (manipulation time) required to collect the secondary mass Δm is computed via Eq. (3.70).

2. If $\theta \neq 0$ at the end of mass collection the system rotates by an additional *phasing time* t_{phasing}, until the siphon is aligned with the X-axis of the CW frame.

3. If $t_{\text{man}} + t_{\text{phasing}} \geq t_{\text{window}}$, the siphon cannot raise the required secondary mass within the allocated time window and the total displacement of the primary is zero. Similarly, if $t_{\text{man}} + t_{\text{phasing}} \leq t_{\text{window}}$ the secondary mass is released and the deflection is computed using Eq. (6.35).

The MR case is analogous, with steps 1 to 3 being iteratively repeated with the selected Δm, until the siphon reaches equilibrium (see Algorithm 2 for more details.) Note that, in the MR scenario, at each release the centre-of-mass of the system instantaneously changes to the centre-of-mass of the primary.

From this point, the total operation time, being the sum of the manipulation time and the phasing time, is indicated with the symbol Δt. Table 6.1 recaps all the time symbols used in this chapter.

As an example, Figures 6.8 shows the deflection trajectory in the CW frame for an asteroid with $\bar{\omega}_0 = 0.65$, $\bar{\mu} = 2.87 \times 10^{-7}$ (this corresponds to a siphon with linear density $150\,\text{kg}\,\text{m}^{-1}$ on an asteroid with radius 250 m) and $\bar{\omega}_{\text{orb}} = 2.66 \times 10^{-4}$ (corresponding to an asteroid with density $\rho = 2000\,\text{kg}\,\text{m}^{-3}$ with an orbital period of 1 year), for a SR (a) and MR case (b). For the SR, the total $\bar{m}_f$ that maximizes the primary release velocity is $\bar{m}_f = 0.027$. In the MR case,

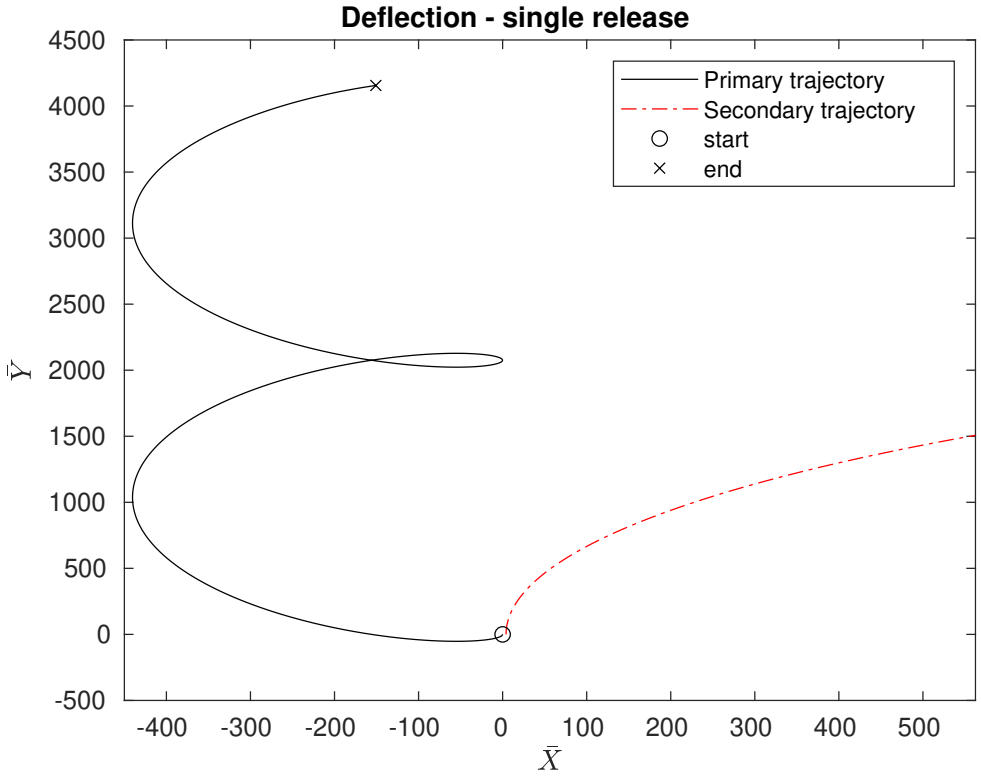

(a)

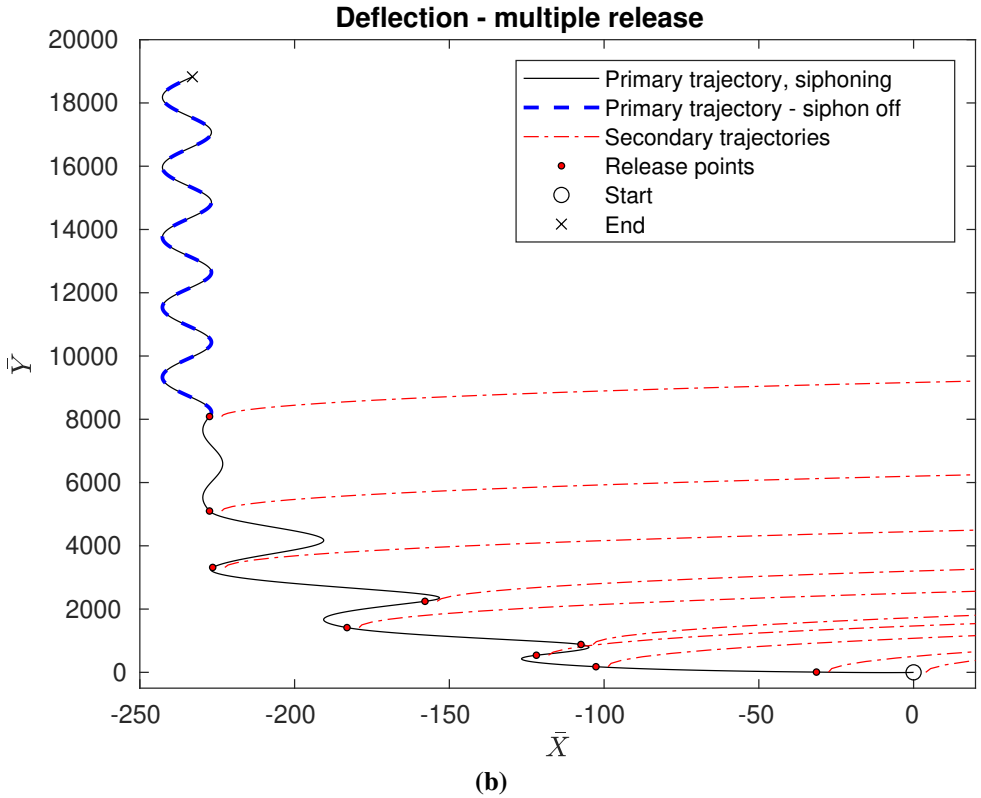

(b)

FIGURE 6.8: Single (a) and multiple (b) release deflection trajectory in relative orbital frame of primary and secondary masses.

input: $\bar{\omega}_0$, $\bar{\omega}_{\text{orb}}$, $\bar{\mu}$

output: deflection

begin

$(X_p, Y_p, \dot{X}_p, \dot{Y}_p) = (0,0,0,0)$;

$t_{\text{man}} \leftarrow$ time to collect m_f ;

if $\mod(\theta, 2\pi) \neq 0$ **then**

$t_{\text{phasing}} \leftarrow$ phasing time required to reach $\mod(\theta, 2\pi) = 0$;

end

$\Delta t = t_{\text{man}} + t_{\text{phasing}}$;

if $\Delta t < t_{window}$ **then**

$(X_{0,p}, Y_{0,p}, \dot{X}_{0,p}, \dot{Y}_{0,p}) = (X_p, Y_p, \dot{X}_p, \dot{Y}_p) + (-x_b, 0, 0, v_{p,\infty})$;

$(X_p, Y_p, \dot{X}_p, \dot{Y}_p) \leftarrow$*Eq.* (6.35) $\leftarrow (X_{0,p}, Y_{0,p}, \dot{X}_{0,p}, \dot{Y}_{0,p})$;

end

deflection $= \sqrt{X_p^2 + Y_p^2}$;

end

Algorithm 1: Single Release deflection.

$\Delta m = 2 \times 10^{-3}$ is chosen. In each case, the initial part of the secondary trajectory is included for completeness.

Figures 6.9 shows the difference between the deflection trajectory calculated using Eq. (6.35) and by numerical integration of Eq. (6.34) taking into account the mutual gravitational acceleration terms. Note that the end points are very close in both cases. The same degree of accuracy can be verified by choosing different values of $\bar{\omega}_0$, $\bar{\mu}$ and $\bar{\omega}_{\text{orb}}$.

6.4 Results

Figure 6.10 shows the quantity of mass that can be collected at the secondary $\bar{m}_f$, given the siphon length $\bar{L}$ and the initial angular velocity of the primary $\bar{\omega}_0$. Each region represents the states $(\bar{m}_f, \bar{L})$ that can be reached for the indicated initial angular velocity intervals. For example, the point $(\bar{m}_f, \bar{L}) = (0.1, 1)$ lies within the region $\bar{\omega}_0 > 1$, meaning it is not possible to collect more than 10% of the initial asteroid mass if the primary is spinning below the critical angular velocity ($\bar{\omega}_0 = 1$). As expected, a larger initial angular velocity is needed to collect larger secondary masses. For an asteroid spinning at its critical angular velocity, ($\bar{\omega}_0 = 1$), the maximum mass fraction that can be collected at the secondary is $\bar{m}_f = 0.08$, which is consistent with the results found in Chapter 3. The minimum angular velocity required for collecting half of the asteroid mass $\bar{m}_f = 0.5$ is approximately $\bar{\omega}_0 = 1.56$. Therefore, an asteroid should spin at more than 56% of its critical angular velocity to enable separation of half of its mass using the orbital siphon. Assuming an asteroid density of $\rho = 2000\,\text{kg}\,\text{m}^{-3}$ this is equivalent to a rotation period of 1.5 h.

input: $\bar{\omega}_0$, $\bar{\omega}_{\text{orb}}$, $\bar{\mu}$

output: deflection

begin

doIterate = True;

$(X_p, Y_p, \dot{X}_p, \dot{Y}_p) = (0,0,0,0)$;

while *doIterate* **do**

$F_{\text{end}} \leftarrow$ siphon force after collection of Δm;

if $F_{end} < 0$ **then**

Reduce Δm such that $F_{\text{end}} = 0$;

doIterate = False;

end

$t_{\text{man}} \leftarrow$ time to collect Δm ;

$\Delta t = \Delta t + t_{\text{man}}$;

if $\mod(\theta, 2\pi) \neq 0$ **then**

$t_{\text{phasing}} \leftarrow$ phasing time required to reach $\mod(\theta, 2\pi) = 0$;

$\Delta t = \Delta t + t_{\text{phasing}}$;

end

if $\Delta t < t_{window}$ **then**

$(X_{0,p}, Y_{0,p}, \dot{X}_{0,p}, \dot{Y}_{0,p}) = (X_p, Y_p, \dot{X}_p, \dot{Y}_p) + (-x_b, 0, 0, v_{p,\infty})$;

$(X_p, Y_p, \dot{X}_p, \dot{Y}_p) \leftarrow$*Eq.* (6.35) $\leftarrow (X_{0,p}, Y_{0,p}, \dot{X}_{0,p}, \dot{Y}_{0,p})$;

else

doIterate = False;

end

end

if $\Delta t < t_{window}$ **then**

$(X_{0,p}, Y_{0,p}, \dot{X}_{0,p}, \dot{Y}_{0,p}) = (X_p, Y_p, \dot{X}_p, \dot{Y}_p)$;

$(X_p, Y_p, \dot{X}_p, \dot{Y}_p) \leftarrow$*Eq.* (6.35) $\leftarrow (X_{0,p}, Y_{0,p}, \dot{X}_{0,p}, \dot{Y}_{0,p})$;

end

deflection = $\sqrt{X_p^2 + Y_p^2}$

end

Algorithm 2: Multiple Release deflection.

TABLE 6.1: Time symbols used in this chapter.

Symbol	Description
t_{man}	Manipulation time required to raise the mass m_f to the secondary in a SR scenario.
t_{phasing}	Phasing time required to align the siphon with the X-axis of the CW frame after the collection of the secondary mass m_f.
Δt	Sum of t_{man} and t_{phasing}.
t_{window}	Maximum allowed Δt.
t_{rev}	Heliocentric orbit period of the asteroid.

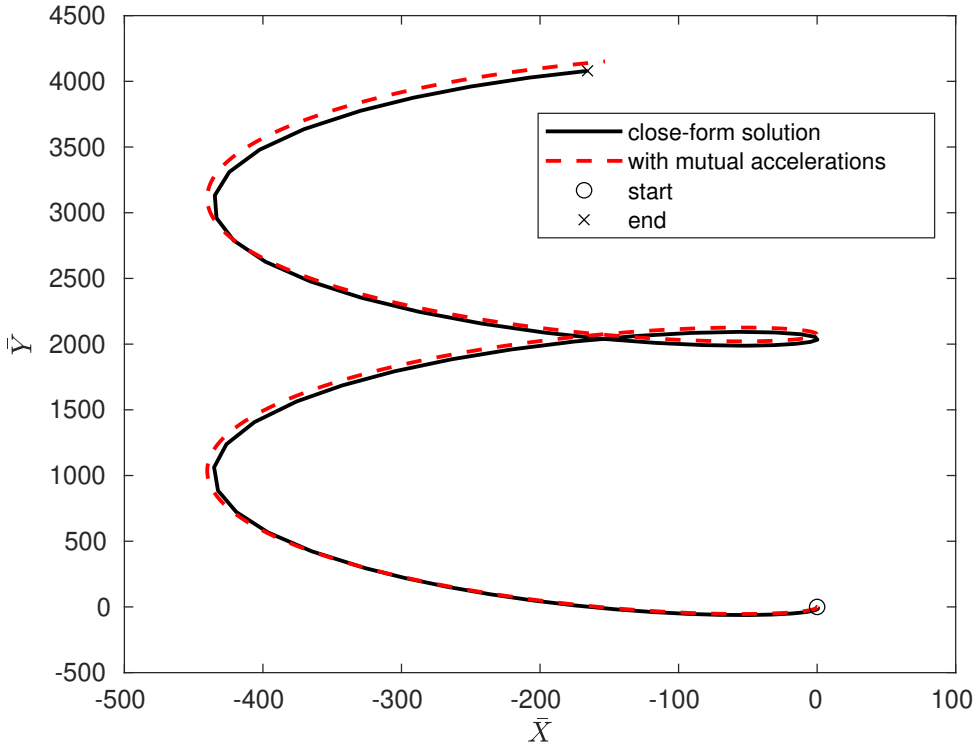

(a)

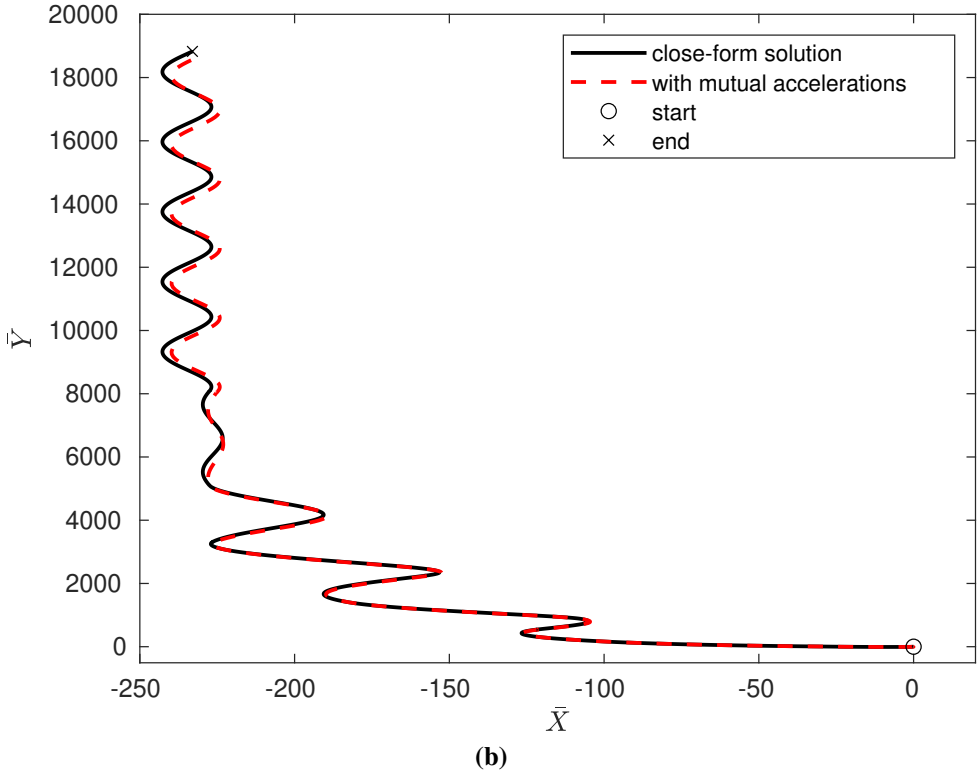

(b)

FIGURE 6.9: Comparison between primary trajectory obtained using Eq. (6.35) (solid black) with respect to numerical solution of Eq. (6.34) (red).

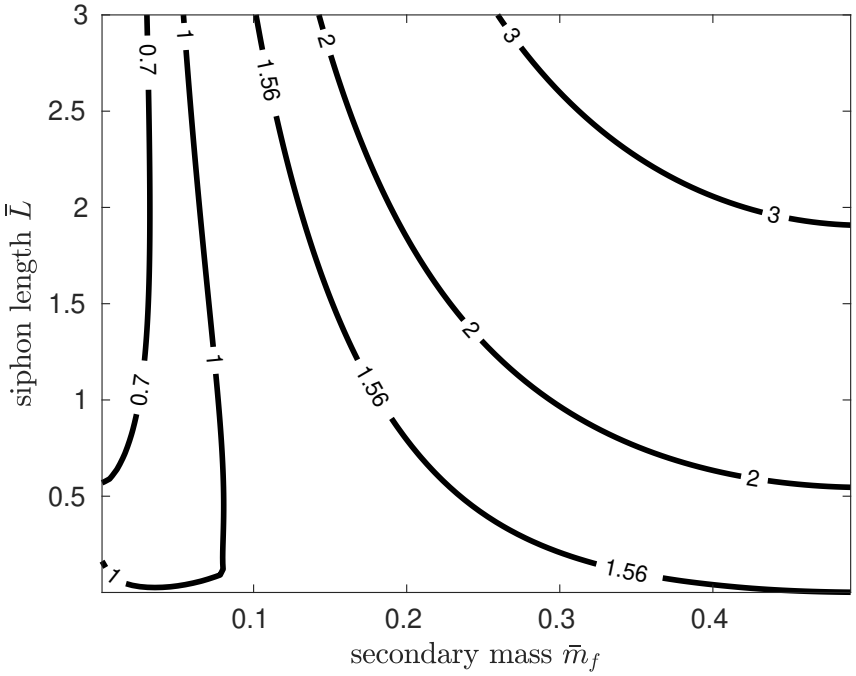

FIGURE 6.10: Isocurves of asteroid initial angular velocity ω_0 as a function of the siphon length and the secondary mass.

Figure 6.11 shows the primary velocity change $\Delta\bar{v}_p$ as a function of the released secondary mass $\bar{m}_f$ and the siphon length for $\bar{\omega}_0 = 0.7$ (a), $\bar{\omega}_0 = 1.56$ (b), in a SR release scenario. In general, a larger secondary mass (and a larger siphon length) enables a larger $\Delta\bar{v}_p$, since the displacement between the primary and the system barycenter increases. At the same time, however, a larger secondary mass (or longer siphon) implies a lower angular velocity of the system $\bar{\omega}$ at the end of the siphon manipulation, thus increasing the gravitational dragging factor (see Eq. (6.31)). Then, the maximum $\Delta\bar{v}_p$ is a tradeoff between these two opposite effects and, in general, the siphon length required to maximize $\Delta\bar{v}_p$ does not match that required to maximize $\bar{m}_f$. For example, in the case $\bar{\omega}_0 = 1.56$, the siphon length needed to approach the half mass separation point ($\bar{m}_f = 0.5$) progressively decreases, thus increasing the gravitational dragging effect at release and reducing $\Delta\bar{v}_p$: the optimal $\Delta\bar{v}_p$ is reached for a siphon length $\bar{L} \approx 0.5$, with a total collected mass $\bar{m}_f = 0.22$.

The black and red contour show the non-dimensional time $\bar{t}_{\text{man}}$ and maximum support tension respectively. Here $\bar{t}_{\text{man}}$ is multiplied by the factor $\bar{\mu}$ to eliminate dependence on the siphon linear density (see Eq. (3.70)). As expected, both time and tension are maximized at the largest $\bar{m}_f$ allowed for the given $\bar{\omega}_0$.

Figure 6.12 compares $\Delta\bar{v}_p$ (a), operation time $\bar{\mu}\Delta\bar{t}$ (b), total released mass (c) and final angular velocity (d) between SR and MR (taking $\Delta\bar{m} = 1 \times 10^{-4}$ for MR), in the condition of maximum $\Delta\bar{v}_p$. It is apparent that the MR scheme enables a larger velocity change in a shorter time. This is due to the fact that, by releasing smaller masses multiple times, rather than a single larger mass once, the gravitational dragging effect is reduced and, even though the total released

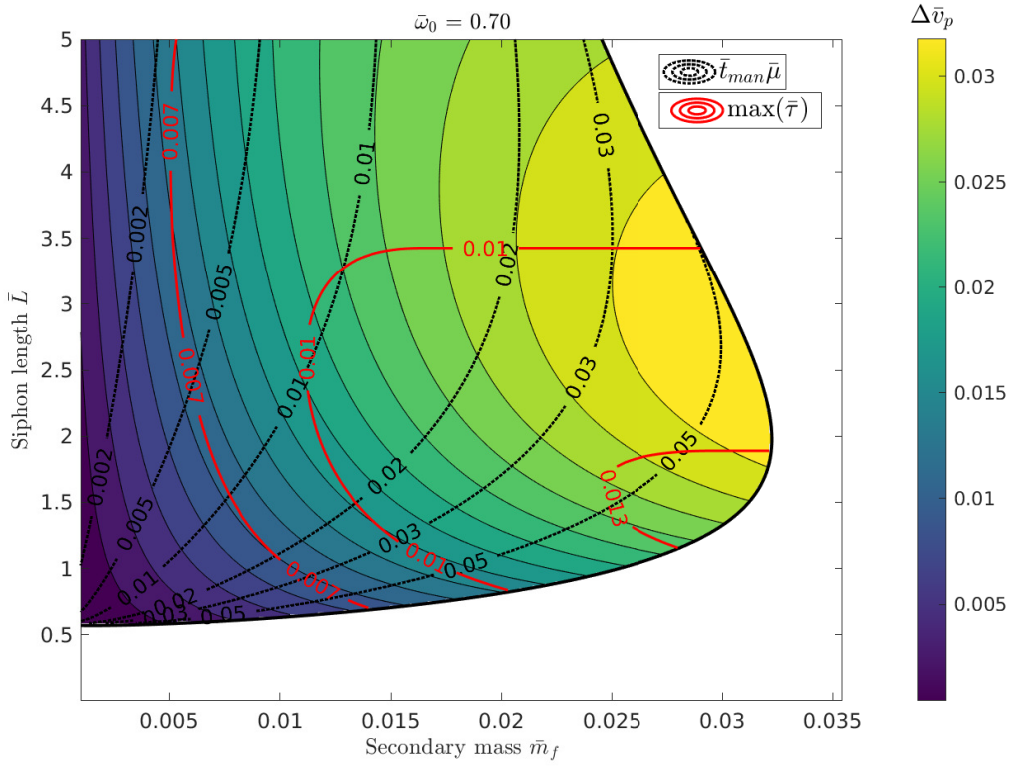

(a)

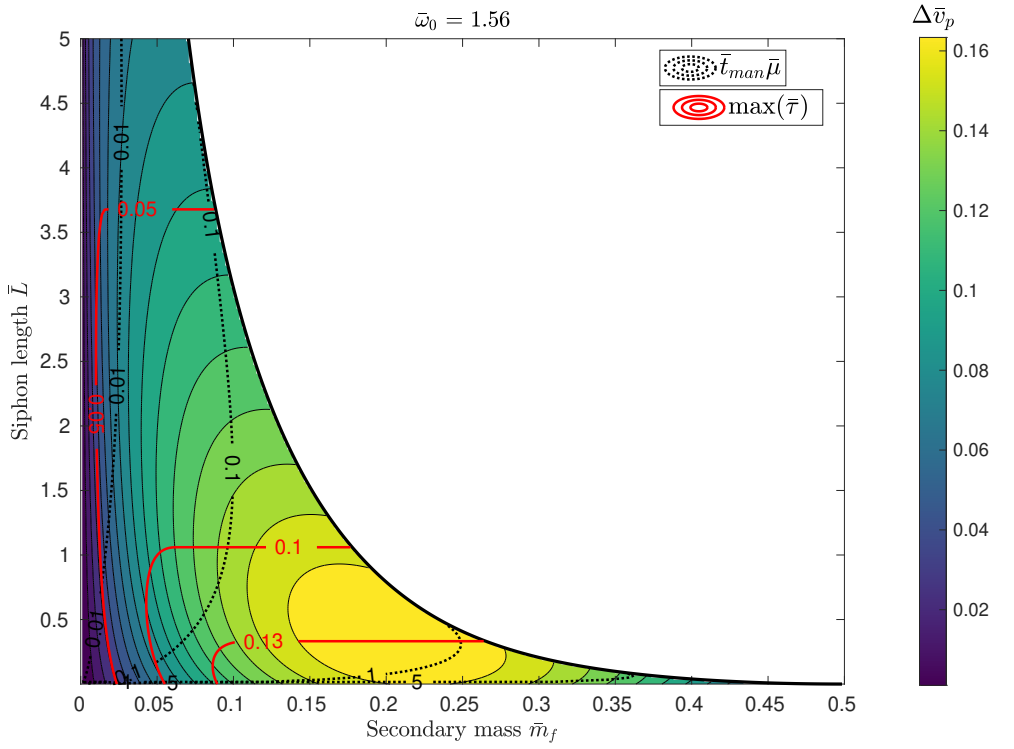

(b)

FIGURE 6.11: Primary release velocity (colored contour), manipulation time $t_{\text{man}}\bar{\mu}$ and maximum support tether tension τ as a function of the secondary mass $\bar{m}_f$ and the siphon length $\bar{L}$.

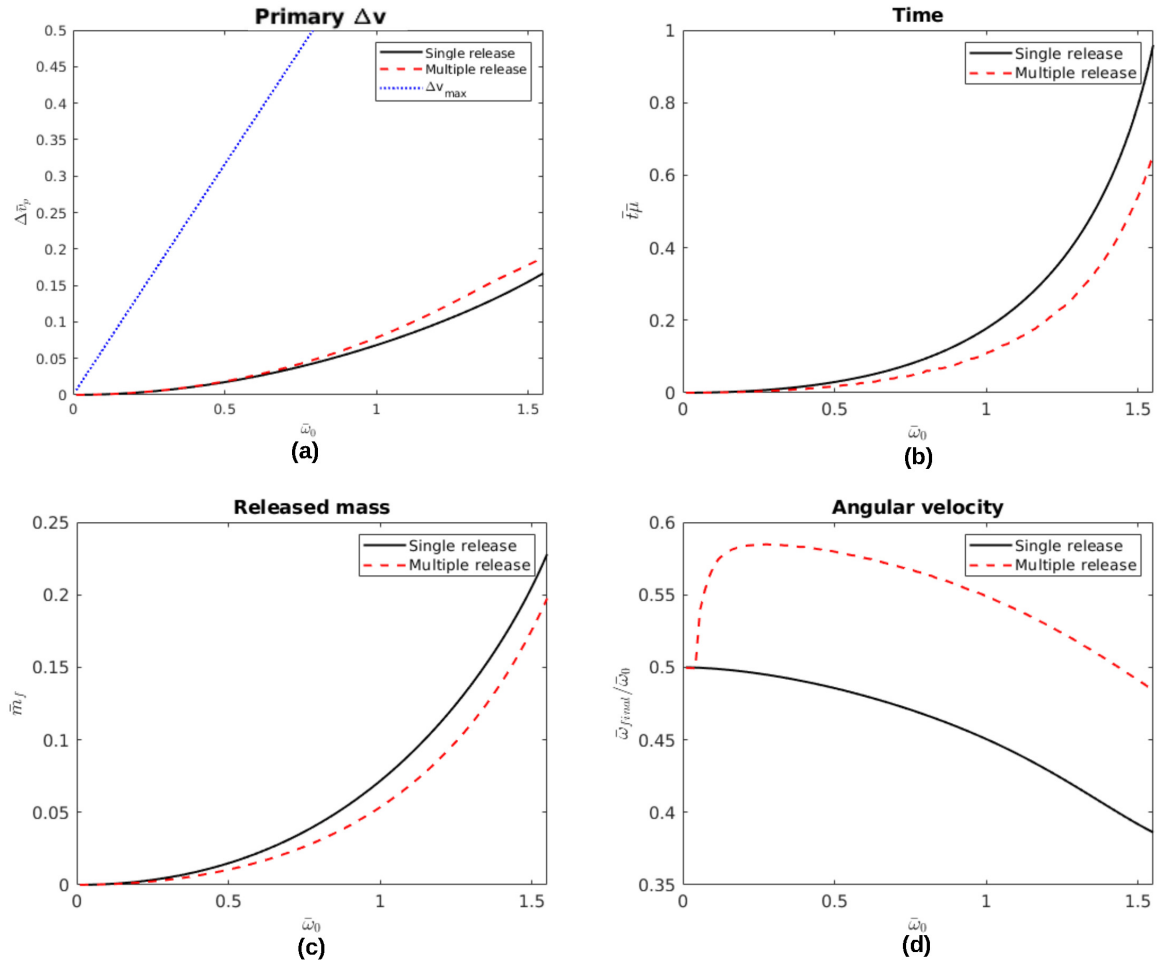

FIGURE 6.12: Primary $\Delta\bar{v}$ (a), time (b), released mass (c) and siphon length (d) as a function of the asteroid non-dimensional angular velocity $\bar{\omega}_0$.

mass is smaller in the MR case (Fig. 6.12c), the overall achievable $\Delta\bar{v}_p$ is larger. The blue dotted line in Fig. 6.12a represents $\Delta\bar{v}_{max}$ (Eq. (6.33)), i.e., the theoretical primary velocity change that would be obtained if the rotational kinetic energy of the asteroid could be entirely converted into transitional kinetic energy. For example, at $\bar{\omega}_0 = 1$ the $\Delta\bar{v}_p$ obtained by a SR siphon is only $0.11\Delta\bar{v}_{\max}$. This difference is due to two unavoidable limits of the proposed strategy: the gravitational dragging at release, and the residual angular velocity of the asteroid at the end of the manipulation process (Fig. 6.12d). In particular, with a fixed length siphon, the asteroid will always retain a final non-zero rotational kinetic energy at the end of the release process, (between 40 and 60 percent of the initial angular velocity, depending on the release scenario and the initial angular velocity) that cannot be further exploited, since the siphon has reached its equilibrium state ($\bar{f} = 0$, Eq. (6.7)).

Figure 6.13 illustrates the dimensional values of the primary Δv_p (a), operation time Δt (b), tension (c) and siphon length (d) as a function of the asteroid initial rotation period, taking an asteroid density $\rho = 2000\,\mathrm{kg\,m^{-3}}$ with radius 250 m (black curves), and 500 m (red curves). Again, each plot refers to the condition of maximum Δv_p. For an asteroid of radius 250 m,

Δv_p varies between 1.5 and 0.3 cm s^{-1} when its period ranges form 2.3 and 6 hours with operation time Δt below 8 years. Note that, from the definition of the scale factors, $\Delta v_p \propto \omega_{\text{crit}} \propto \sqrt{\rho}$ and $t \propto \omega_{\text{crit}}^{-1} \propto 1/\sqrt{\rho}$, i.e., a larger asteroid density increases the Δv of the primary while also increasing the mass transfer time requirements. Figure 6.13c indicates that the support tether tension can vary by several orders of magnitude when comparing the SR and MR methods. For example, an asteroid with radius $R_0 = 250$ m requires a support tether tension $\tau = \mathcal{O}(10^5)$ N for the SR case which drops to $\mathcal{O}(10^3)$ N for the MR case. In general, τ increases with shorter rotational periods and this becomes more noticeable for a larger asteroid radius. Note from the force scaling that $\tau \propto M_0 \omega_c^2 R_0 \propto \rho^2 R_0^4$, hence the tension is strongly influenced by the asteroid density and its radius. Figure 6.13d shows that the siphon length in the MR case is slightly smaller with respect to the SR case. Moreover, in both cases, L is smaller than the radius of the sphere of influence (represented with a dotted line in Fig. 6.13d) and, in general, it can be verified that this holds true even for larger asteroid radii. Therefore, the siphon is always within the sphere of influence of the asteroid, thus justifying the choice of neglecting solar gravitational perturbations in this preliminary analysis. Note that the asteroid density does not influence the siphon length required to maximize $\Delta \bar{v}_p$ and, from the distance scale factor, $L \propto R_0$.

Figure 6.14 shows the siphon linear density required to divert an asteroid by 1 Earth radius within a time window t_{window} of 5 years (first row), 10 years (second row), 15 years (third row), as a function of the asteroid period, for a range of asteroid radii $R_0 = 250$ m (first column), $R_0 = 500$ m (second column), $R_0 = 1000$ m (third column), for the SR case (black line) and the MR case (with $\Delta \bar{m} = 5 \times 10^{-3}$ (red line) and $\Delta \bar{m} = 1 \times 10^{-4}$ (blue line)). The range of allowed μ has been limited to 2×10^3 kg m^{-1}, thus any scenario requiring a larger μ is not represented here. It is apparent that the MR scheme significantly reduces the minimum μ. Moreover, lower values of $\Delta \bar{m}$ further reduce the siphon linear density. For a fixed requirement on the total displacement, larger μ are required in the SR case to increase the mass throughput to the secondary and achieve the required deflection within the given time window. At the same time, however, if the collected mass is too large, the gravitational dragging effect may reduce the overall $\Delta \bar{v}_p$. This explains why the minimum μ can significantly increase for shorter periods in the SR case. In general, lower values of siphon linear density are allowed for smaller asteroids. It is interesting to observe that for a given time window and asteroid radius there is an upper bound on the asteroid period at which $\mu \to \infty$. For example, it is impossible to deflect a 250-metre asteroid by 1 Earth radius in 5 years if its initial period is longer then 3 hours (not even using hypothetical siphon with infinite linear density). Such upper bounds on the asteroid period approaches the critical period (i.e., $2\pi/\omega_{\text{crit}}$) for smaller asteroids.

Figure 6.15 shows the isocurves of minimum siphon linear density to deflect an asteroid by 1 Earth radius (black curve) as a function of the asteroid radius and period, combined with the isocurves of primary release velocity (red dashed curve) and siphon length (blue dot-dashed), for a time window of 10 (a) and 20 (b) years. Note that regions with lower μ are also characterized

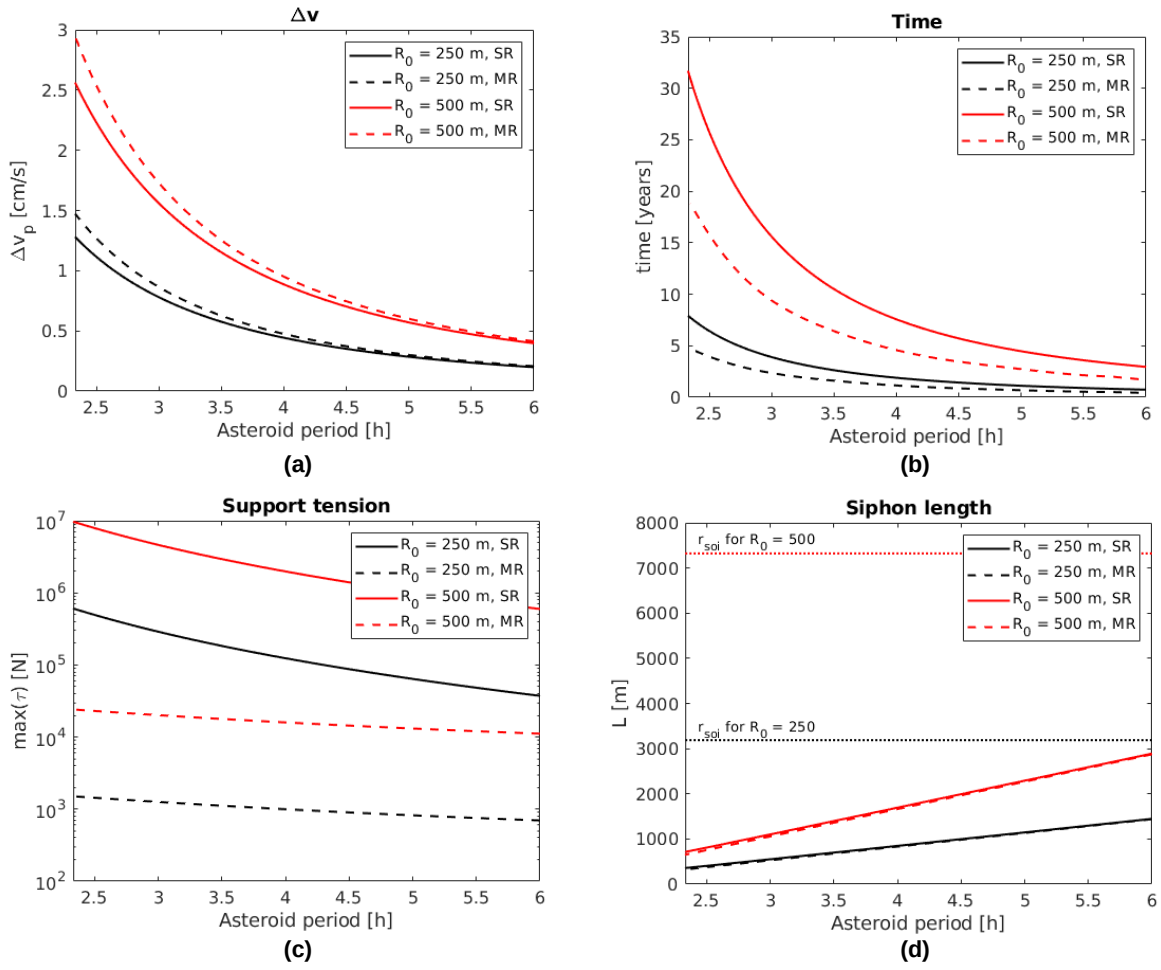

FIGURE 6.13: Primary $\Delta\bar{v}_p$, manipulation time, support tether tension and siphon length as a function of the asteroid period, using dimensional units.

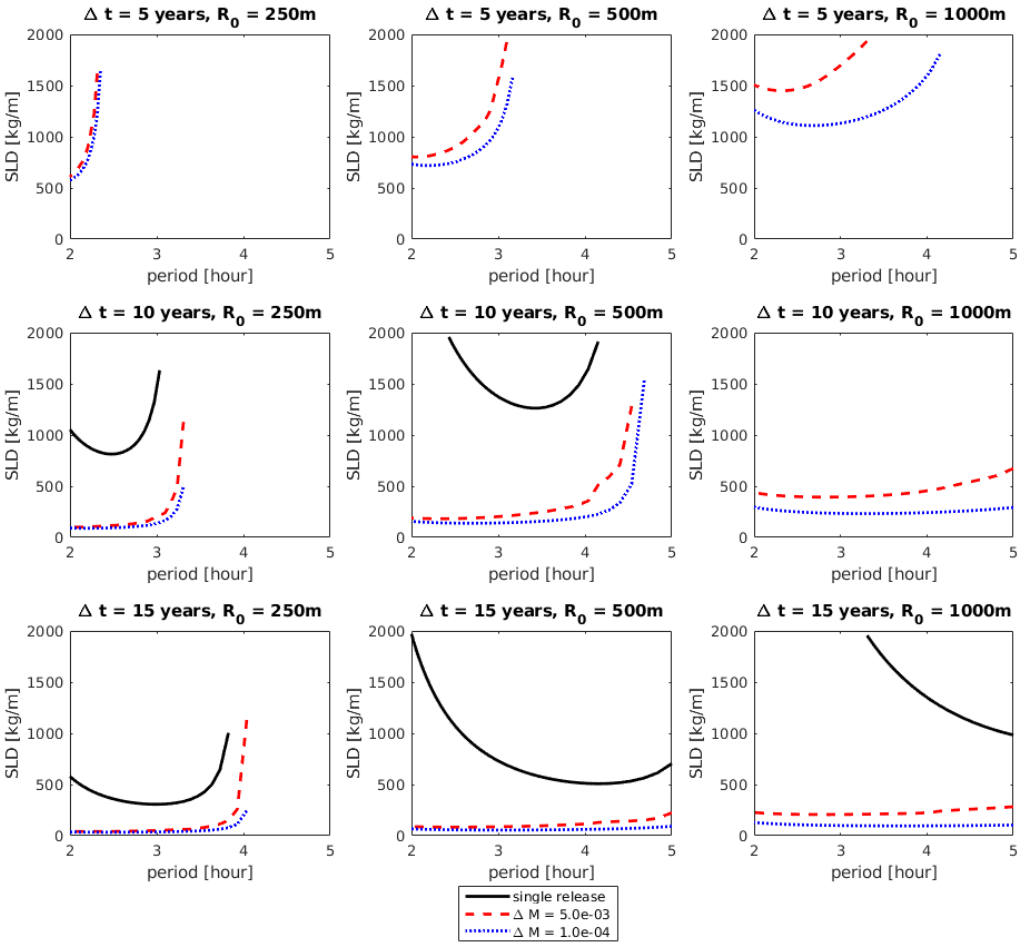

FIGURE 6.14: Required siphon linear density to divert an asteroid by 1 Earth radius, for different asteroid radii and time windows.

TABLE 6.2: Relevant dimensional parameters for the deflection of the asteroid 263976 (2009 KD5) (radius 393 m, period 2.66 hours) by 1 Earth radius in 10 and 20 years, using a MR strategy, with $\Delta\bar{m} = 1 \times 10^{-4}$.

		10 years	20 years
Siphon linear density	[kg/m]	118	24
Total Δv_p	[cm/s]	1.15	0.63
Average Δv_s	[cm/s]	60	54
Average mass rate	[kg/s]	34	8
Number of releases		214	106
Released mass	%	0.0213	0.0105
Siphon length	[m]	670	670
Max tension	[kN]	8.4	8.4

by a smaller siphon length. Figure 6.15 clearly shows that smaller and faster rotating asteroids are preferred candidates for such deflection methods, with a smaller siphon linear density and siphon length requirements.

The siphon linear density is also related to the cross section A of the siphon, with larger μ being associated to larger cross sections (see Eq. (3.22)). For a siphon linear density ranging from 20 to 400 kg/m, $\sqrt{A}$ ranges from 10 cm to 45 cm. Nevertheless, a siphon modelled as a discrete chain of payloads will clearly have a larger cross section, depending on the distance l between consecutive payloads. Assuming that payloads are stored within buckets of cubical shape, it can be shown that the size of the payloads is $\sqrt[3]{\mu l/\rho}$, where, to avoid superposition of consecutive payloads, $l \geq \sqrt{\mu/\rho}$. For example, taking a distance between payloads of $l = 0.5\,\mathrm{m}$, for the same range of μ, the size of the payload ranges from 17 cm to 46 cm. The total number of payloads then depends on the length of the chain.

6.4.1 Case study and discussion

Table 6.2 shows relevant parameter in dimensional units, referred to the MR deflection of the potentially hazardous asteroid 263976 (2009 KD5) (radius 393 m, period 2.66 hours[2]) with $t_{\text{window}} = 10$ years and $t_{\text{window}} = 20$ years by 1 Earth radius, assuming an asteroid density $\rho = 2\,\mathrm{g\,cm^{-3}}$. Figure 6.16 also shows the trajectory in the CW frame for the 10 years deflection case. The siphon linear density drops by approximately one order of magnitude when the time windows are doubled in duration. This implies a reduction of both the siphon cross section and the mass flow rate of material being lifted on the siphon, taken as the ratio between the total released mass and the required time window. The required mass flow rates range from 8 to $34\,\mathrm{kg\,s^{-1}}$ for the scenario presented. Such rates clearly depend upon the technology of the mining units transferring material from the surface of the asteroid to the siphon and the physical properties of the asteroid. For example, surface irregularities, boulders or cavities could inter-

[2]From, https://ssd.jpl.nasa.gov/sbdb.cgi, accessed on 14th May 2020

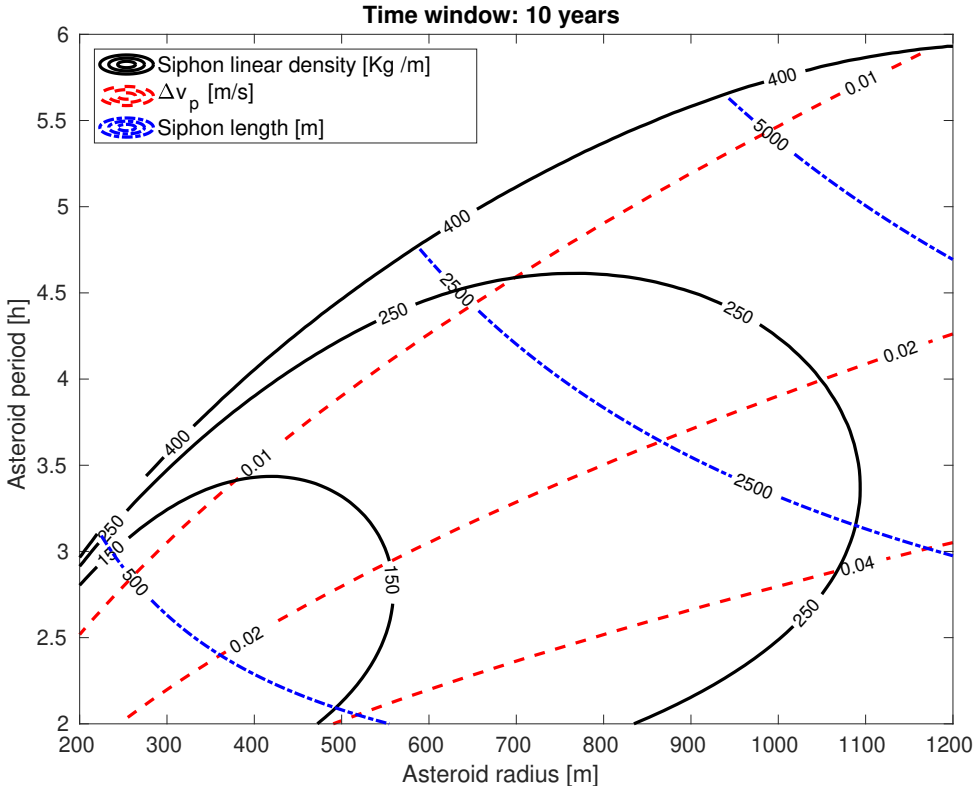

(a)

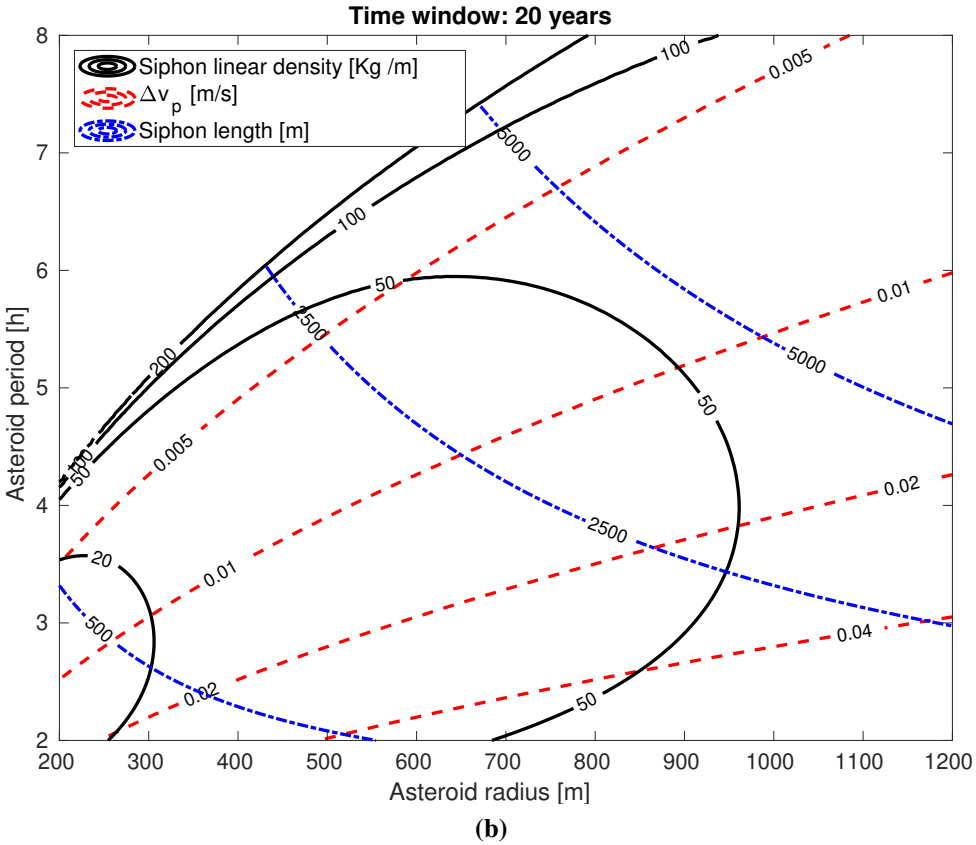

(b)

FIGURE 6.15: Isocurves for siphon linear density (black), Δv_p (dashed red) and siphon length (dot-dashed blue) as a function of the asteroid radius and period, for a MR release scenario, with $\Delta\bar{m} = 1 \times 10^{-4}$ and asteroid density $\rho = 2000\,\mathrm{kg\,m^{-3}}$.

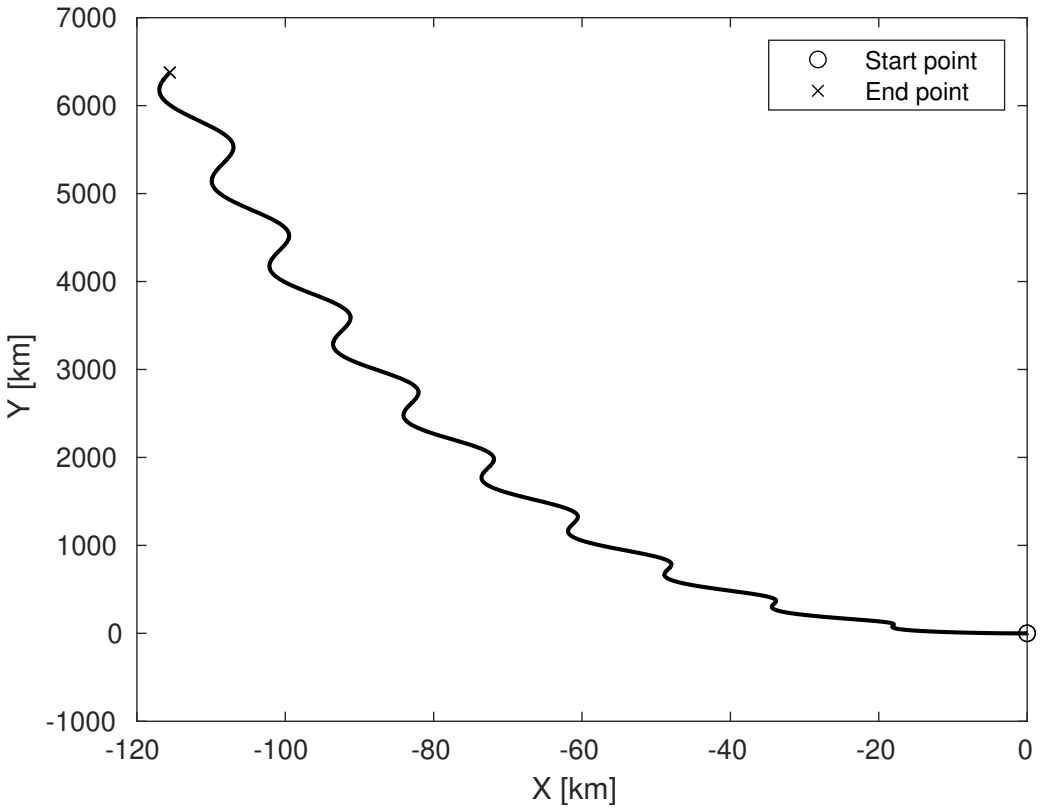

FIGURE 6.16: Primary trajectory for a 10 years deflection of asteroid 263976 (2009 KD5) by 1 Earth radius.

fere with the motion of surface rovers. Use of multiple siphons, anchored at different points on the asteroid equator, would significantly reduce the overall travel distance of surface rovers, thus enabling larger mass throughputs. In any case, the required mass flow rate significantly decreases for larger time windows or, in general, when the required deflection Δv decreases. In cases where an asteroid has a close approach to Earth followed by a later return, the required change in velocity may be orders of magnitude smaller than $1\,\mathrm{cm\,s^{-1}}$ [75], thus significantly reducing the required mass flow rate.

The alignment of the siphon with the local vertical was among the assumptions of the model developed in this chapter. In Chapter 4 it was shown that Coriolis forces due to payload motion actually induce damped oscillations in the equatorial plane and such oscillations are completely damped out when the mass of the secondary is approximately two orders of magnitude larger than the mass of the siphon. In general, the damping timescale is much smaller than the time between consecutive releases. For example, for the 20-years deflection case, it can be shown via Eq. (3.70) that the time required to reach the condition $m = 100\mu L$ is on average just 3% of the time between consecutive releases. Therefore, the timescale for damping out the equatorial oscillations is much smaller than the time between consecutive releases of the secondary mass. It is therefore reasonable to assume that the siphon is aligned with the local vertical for the entire extraction sequence and, in particular, when the secondary is released. A similar ar-

gument can be made for the other case scenario and, more generally, for SR cases and MR cases with $\Delta\bar{m} > 1 \times 10^{-4}$. However, more care must be taken if the parameter $\Delta\bar{m}$ is smaller than 1×10^{-4}: in this case, the time between consecutive releases could decrease to values comparable to the timescale for damping out the equatorial oscillations (since less mass is collected at the secondary for each release) and a more accurate model taking into account Coriolis forces may be required. Equatorial oscillations can also be reduced by using an additional counterweight connected to the top of the siphon via a tether, using a method similar to that described in Ref. [151]. Additionally, as noted in Chapter 4, the minimum mass of the secondary at the beginning of siphon operations cannot be arbitrary small, in order to avoid impact of the siphon with the asteroid surface during the initial oscillation phase. Practically, the minimum initial mass of the secondary should be (approximately) at least one order of magnitude larger than the mass of the siphon (see Sec. 4.5 and Fig. 4.12[3]). In the MR scenario, this requirement can be met by retaining a fraction of the asteroid mass at the secondary at the moment of release, such that the condition $m = 10\mu L$ is always verified at the beginning of each new siphon operation phase.

The maximum support tether tension is 8.4 kN in both cases. A Kevlar tether (density $1440\,\mathrm{kg\,m^{-3}}$, maximum tensile strength 3.6 GPa [6]) with cross section of $1\,\mathrm{cm}^2$ can withstand such tension, with a total tether mass of approximately 10 kg. It must be stressed that the tether tension can vary significantly depending on the asteroid radius, period and the released mass Δm. Therefore a range of very different scenarios and requirements can emerge depending on the asteroid physical characteristics.

The total released mass is approximately 2% and 1% of the asteroid initial mass for a 10 and 20-year deflection scenario respectively. This corresponds to approximately 5×10^6 and 1×10^7 tonnes of material. This reaction mass is much larger than that required by other deflection methods. However, it must be emphasized that the reaction mass is entirely collected *in situ*, and clearly that is one of the main advantages of the orbital siphon deflection method.

An estimate of the size of the buckets can be made using the equations described in the previous section. For example, assuming cubic buckets and a 1 m distance between them, each cubic bucket would have a side length of approximately 39 cm for the 10-year deflection scenario and 23 cm for the 20-year deflection scenario. The mass of the buckets will depend on the selected material and the thickness of each bucket face. However, depending on the average grain size of the asteroid material, buckets can be designed as a wire mesh thus significantly decreasing their mass and therefore the siphon structural mass to be launched from Earth.

Typical secondary escape velocities are between 54 and $60\,\mathrm{cm\,s^{-1}}$, much larger than the total Δv of the primary. Considering the secular term only in the CW equations, the total secondary displacement in time Δt is $3\Delta v_s \Delta t$. Therefore a secondary released with escape velocity $\Delta v_s =$

[3]Fig. 4.12 is related to a slightly oblate asteroid, and not a spherical asteroid as in this model. However, results for a spherical asteroid would not differ significantly from Fig. 4.12 and the same conclusion holds.

$54\,\mathrm{cm\,s^{-1}}$ would be displaced by approximately 8 Earth radii per year. It is therefore reasonable to assume that the secondaries will always miss the Earth. More accurate analysis, taking into account orbital eccentricity and inclination is left for future work.

Chapter 7

Excavation of artificial caverns inside asteroids by leveraging rotational self-energy

7.1 Introduction

This chapter is intended as an extension of Chapter 3, with material mined from the asteroid interior rather than the external surface, to generate an internal cavity. A cavity inside an asteroid would be a natural radiation shield against cosmic radiation [77] for habitation and may also serve as a confined environment for storage of mined material such as water ice or other processed volatiles such as propellants. To this end, it is proposed to use the siphon effect to excavate an artificial cavity in the asteroid interior. An artificial tunnel excavated from a point on the asteroid equator to its centre, contains the orbital siphon which is used to remove material from the asteroid interior to escape. In the first part of this chapter, the maximum quantity of mass that can can be excavated is calculated and compared with results found in Chapter 3 for a siphon anchored at the asteroid surface. In the second part, the variation of the internal asteroid stresses due to the internal void is analysed. Assuming elastic material behaviour, a closed-form solution for the stress tensor is found. Then, using a yield criterion for geological materials, regions inside the asteroid that are more sensitive to structural failure are identified.

7.2 Model

The asteroid is modelled as a sphere with radius R, uniform density ρ and angular velocity ω. An artificial tunnel, excavated from a point on the asteroid equator to its centre, contains the orbital siphon, with length $L > R$ (Fig. 7.1). It is assumed that the cross-section of the tunnel is small compared to the radius of the asteroid, hence the change of asteroid mass and inertia due to the presence of the tunnel can be neglected in this case. As in Chapter 3, the siphon is

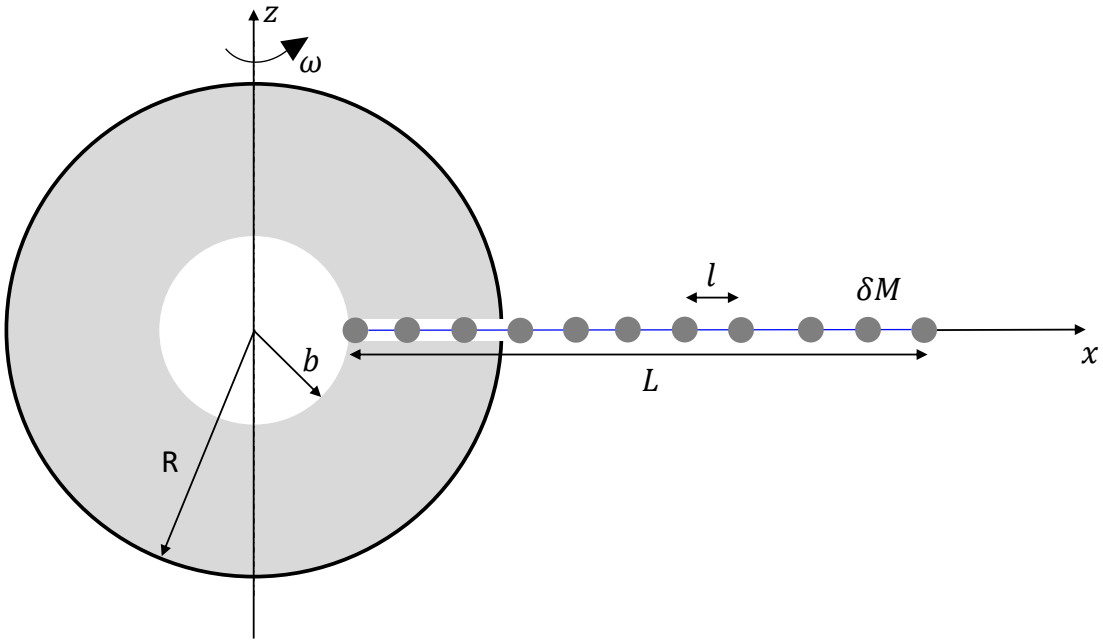

FIGURE 7.1: Orbital siphon model.

modelled as a chain of n tether-connected payloads each with mass δM where the mass of the tethers is neglected. Mining units extract material from the asteroid interior and transfer it to the siphon. For simplicity, the internal cavity is assumed to be spherical, with time varying radius $b < R$. The siphon is assumed to keep a fixed orientation, normal to the asteroid surface. This implies that the masses are sliding without friction on a support structure to avoid rotation of the siphon caused by the Coriolis acceleration resulting from the motion of the chain. Such a support structure can either be a rigid rod or a tether anchored at the base of the siphon and kept in tension via a counterweight, as discussed in previous chapters.

7.2.1 Force on the siphon

Within an asteroid-fixed reference frame, each payload mass is subjected to a gravitational force directed towards the centre of the asteroid and a centrifugal-induced force, in the opposite direction. Let $x_i = b + (i-1)l$ be the distance between the i-th payload mass and the centre of the asteroid, where $l = L/(n-1)$ is the constant length of the tethers connecting consecutive payloads. The gravitational and centrifugal-induced forces can be written respectively as (Sect. 2.2.1):

$$f_{g,i} = \begin{cases} -G\frac{4}{3}\pi\rho\frac{x_i^3 - b^3}{x_i^2}\delta M, & \text{if} \quad x_i \leq R \\ -G\frac{4}{3}\pi\rho\frac{R^3 - b^3}{x_i^2}\delta M, & \text{if} \quad x_i > R \end{cases} \tag{7.1}$$

and

$$f_{c,i} = \delta M \omega^2 x_i \tag{7.2}$$

Then, the total force acting on the siphon will be the sum

$$f = \sum_{i=1}^{n} (f_{g,i} + f_{c,i}) \tag{7.3}$$

Internal tether tensions are not explicitly listed in Eq. (7.3) as they will vanish in a summation to be performed later. From this point Equation (7.3) can then be written in non-dimensional form using the scale factors listed in Table 3.1

$$\bar{f} = \left(\bar{\omega}^2 \bar{x}_i - \sum_{i=1}^{n^*} \frac{\bar{x}_i^3 - \bar{b}^3}{\bar{x}_i^2} - \sum_{i=n^*+1}^{n} \frac{1-\bar{b}^3}{\bar{x}_i^2} \right) \delta \bar{M} \tag{7.4}$$

where the upper bar indicates a non-dimensional variable. The variable n^* represents the number of payload masses below the asteroid surface, i.e., the largest positive integer satisfying:

$$\bar{b} + (n^* - 1)\bar{l} < 1 \tag{7.5}$$

Upon simplification, Eq. (7.4) can be written as:

$$\begin{aligned} \bar{f} = \frac{\delta \bar{M}}{\bar{l}^2} \left[\bar{b}^3 \Psi \left(1 + \frac{\bar{b}}{\bar{l}} \right) + (1 - \bar{b}^3) \Psi \left(n + \frac{\bar{b}}{\bar{l}} \right) - \Psi \left(n^* + \frac{\bar{b}}{\bar{l}} \right) \right] + \\ \frac{\delta \bar{M}}{2} \left[n(\bar{L} + 2\bar{b}) \bar{\omega}^2 - (\bar{l} n^* + 2\bar{b})(n^* - 1) \right] \end{aligned} \tag{7.6}$$

where Ψ is the polygamma function of order 1 (Eq. (3.7)). When the condition

$$\bar{f} = 0 \tag{7.7}$$

is satisfied, the total gravitational and centrifugal-induced forces are balanced and the chain is in equilibrium. Figure 7.2 shows the variation of the function $\bar{f}/\delta\bar{M}$ with respect to the siphon length $\bar{L}$, for an asteroid with $\bar{\omega} = 0.7$, $n = 30$ and a range of inner radii $\bar{b}$. It is apparent that, for a given $\bar{\omega}$, n and $\bar{b}$, two equilibria exist. The smaller equilibrium corresponds to a siphon entirely contained within the tunnel, i.e., with its top mass below the asteroid surface. The larger equilibrium corresponds to a siphon extending outside the asteroid surface. If the radius of the inner void is larger than a certain threshold, which depends on $\bar{\omega}$ and n, the siphon force is always positive and no equilibrium exists. It can be shown that the inner equilibrium is stable in the radial direction whereas the outer equilibrium is unstable. This implies that an orbital siphon effect cannot be generated for a sub-surface orbital siphon. Additionally, a sub-surface orbital siphon would not release the top masses outside the asteroid, and would not be suitable for mass extraction purposes. Therefore, only siphons extending outside the asteroid surface are considered here.

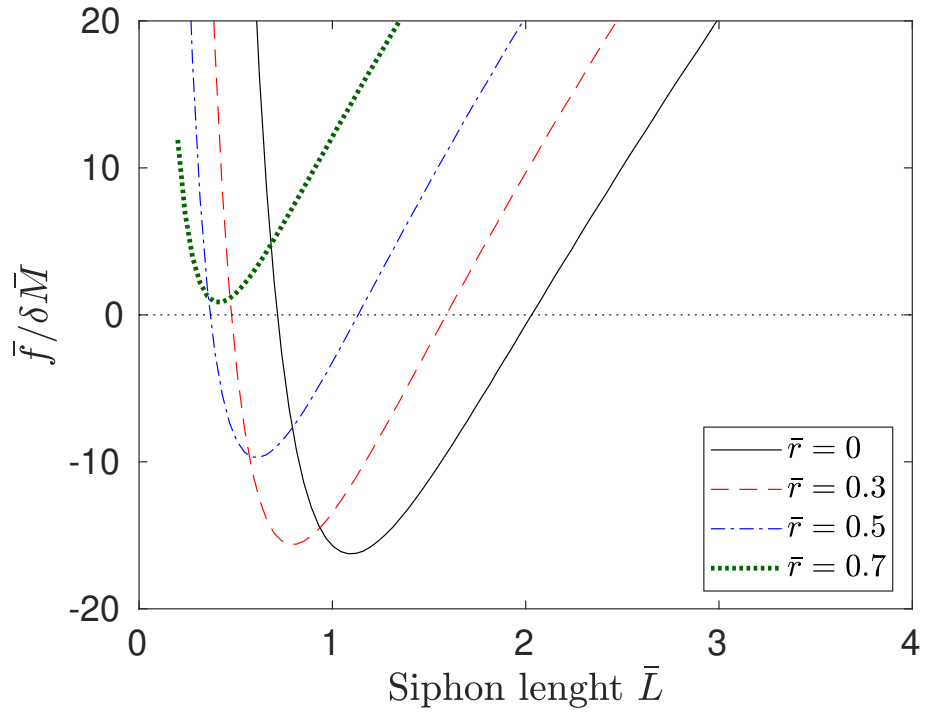

FIGURE 7.2: Non-dimensional siphon force as a function of the siphon length, for $\bar{\omega} = 0.69$, $n = 30$ and a range of inner radii $\bar{b}$.

7.2.2 Approximation for a continuous chain

It is useful for later analyses to rewrite Eq. (7.6) by approximating the siphon with a continuous mass distribution with the same length L and linear density $\mu = n\delta M/L$, as done in Chapter 3. This is obtained by substituting the sum in Eq. 7.3 with an integral over the length of the siphon. It can be shown that, under these conditions, the total force can be written in non-dimensional form as

$$\bar{f}_{\text{cont}} = \frac{1}{2}\left[\frac{(\bar{b}-1)(\bar{b}^2+\bar{b}-2+3\bar{L}(\bar{b}+1))}{\bar{L}+\bar{b}} + \bar{L}(\bar{L}+2\bar{b})\bar{\omega}^2\right]\bar{\mu} \tag{7.8}$$

Figure 7.3 shows the siphon equilibrium length L_{eq} as a function of the non-dimensional asteroid angular velocity $\bar{\omega}$ using the continuous mass distribution approximation (continuous lines), compared with the discrete chain case (dashed lines and dotted lines, corresponding to $n = 10$ and $n = 30$ respectively) for a range of inner radii $\bar{b}$. It is apparent that the equilibrium solution found with the continuous mass distribution approach is an accurate approximation of the discrete chain case. As expected, the equilibrium length increases with a larger asteroid angular velocity. Moreover, a larger internal cavity reduces the asteroid mass and also the gravitational force acting on the chain, thus decreasing the equilibrium length.

7.2.3 Siphon operation: conservation of angular momentum

If the net force on the siphon is positive the chain will lift and an orbital siphon effect can be envisaged, where new payloads are connected at the bottom of the chain while upper payloads

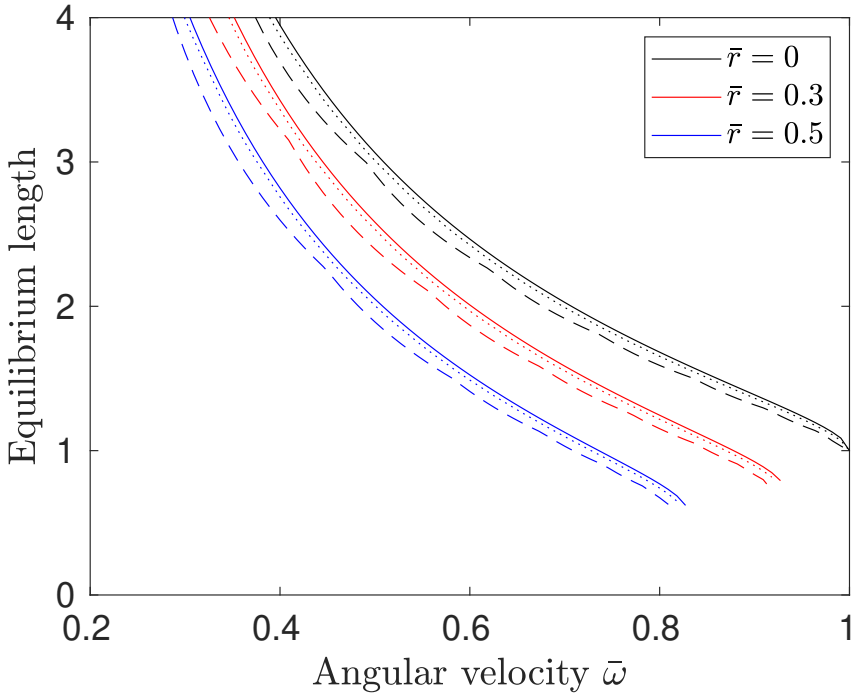

FIGURE 7.3: Equilibrium length (non-dimensional units) of the siphon as a function of the non-dimensional angular velocity $\bar{\omega}$ for a range of inner radii $\bar{b}$, using the continuous mass distribution approximation (continuous lines), compared with the discrete chain case (dashed lines and dotted lines, corresponding to $n = 10$ and $n = 30$)

are released. In analogy with Chapter 3, the extraction of a PM from the asteroid and the subsequent release of the top payload mass from the chain can be modelled through the following four-step sequence (see Fig. 7.4):

1. The chain is initially in the configuration (1) with $x_1 = b$ and will subsequently lift if $f > 0$.

2. The chain is in the configuration (2), with $x_1 = b + l$.

3. A new payload mass δM is connected at the bottom of the siphon. To guarantee conservation of mass, the inner radius b increases by $\delta b > 0$ such that, the mass of the outer shell with thickness δb is equal to δM.

4. The top mass is released from the chain.

This sequence is then repeated. Let b_j, M_j, $I_{A,j}$, $I_{S,j}$ and ω_j be the inner radius, asteroid mass, asteroid inertia, siphon inertia and asteroid angular velocity at the j-th step of the sequence described above. Then:

$$I_{A,j} = \frac{2}{5} M_j \frac{R^5 - b_j^5}{R^3 - b_j^3} \tag{7.9}$$

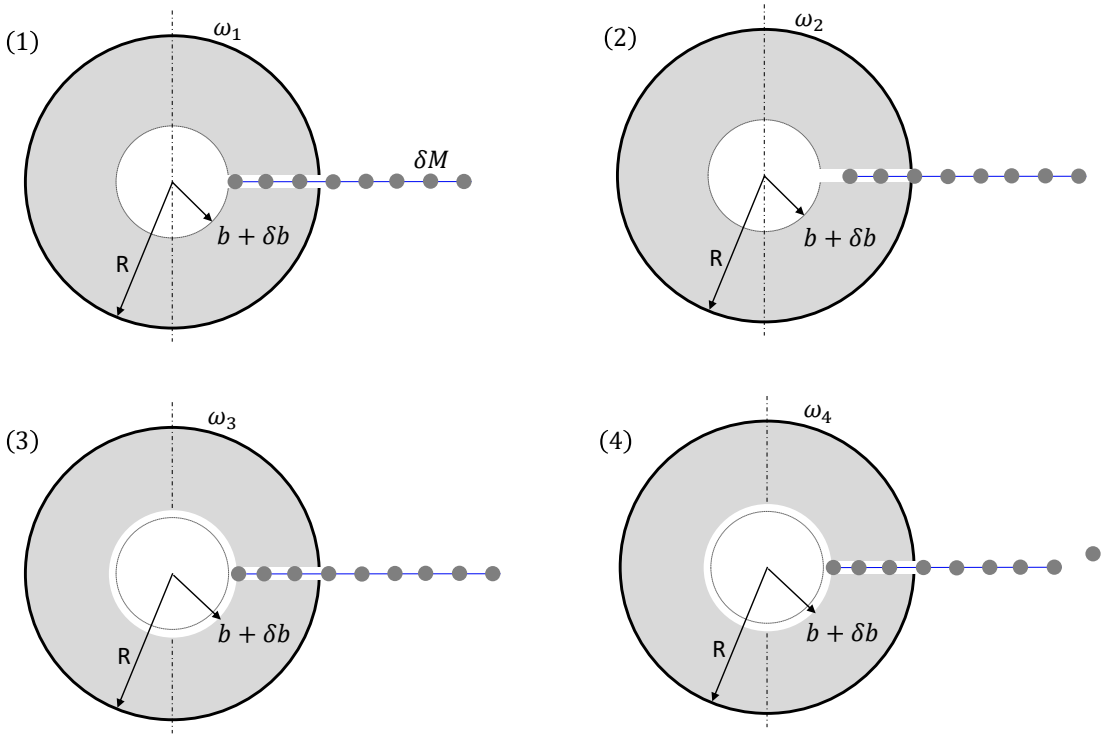

FIGURE 7.4: Siphon operation sequence

and

$$I_{S,j} = \begin{cases} \delta M \sum_{i=1}^{n} (b_j + (i-1)l)^2, & j = 1 \\ \delta M \sum_{i=1}^{n} (b_j + il)^2, & j = 2 \\ \delta M \sum_{i=1}^{n+1} (b_j + (i-1)l)^2, & j = 3 \\ \delta M \sum_{i=1}^{n} (b_j + (i-1)l)^2, & j = 4 \end{cases} \tag{7.10}$$

where $M_1 = M_2 = M$, $M_3 = M_4 = M - \delta M$ and $r_1 = r_2 = b$, $r_3 = r_4 = b + \delta b$.

As no external torques are acting on the asteroid and chain, conservation of angular momentum holds at each step. Therefore:

$$(I_{A,1} + I_{S,1})\omega_1 = (I_{A,2} + I_{S,2})\omega_2 \tag{7.11a}$$

$$(I_{A,2} + I_{S,2})\omega_2 = (I_{A,3} + I_{S,3})\omega_3 \tag{7.11b}$$

$$(I_{A,3} + I_{S,3})\omega_3 = (I_{A,4} + I_{S,4})\omega_4 + \delta M(r_4 + nl)^2\omega_3 \tag{7.11c}$$

Substituting Eqs. (7.9) and (7.10) into Eqs. (7.11) and further simplifying (see Appendix F for

details), Eqs. (7.11) can be written as:

$$\frac{\delta\bar{\omega}_{12}}{\bar{\omega}_1} = 5\frac{\bar{b}^5}{1-\bar{b}^5}\left[\frac{3}{2}\left(1+\frac{\bar{L}}{\bar{b}}\right)^2 - \frac{1}{2}\right]\frac{\delta\bar{b}}{\bar{b}} \tag{7.12a}$$

$$\frac{\delta\bar{\omega}_{23}}{\bar{\omega}_1} = -\frac{5}{2}\frac{\bar{b}^5}{1-\bar{b}^5}\frac{\delta\bar{b}}{\bar{b}} \tag{7.12b}$$

$$\frac{\delta\bar{\omega}_{34}}{\bar{\omega}_1} = 0 \tag{7.12c}$$

where $\delta\bar{\omega}_{12} = \bar{\omega}_2 - \bar{\omega}_1$, $\delta\bar{\omega}_{23} = \bar{\omega}_3 - \bar{\omega}_2$, $\delta\bar{\omega}_{34} = \bar{\omega}_4 - \bar{\omega}_3$ and the higher-order terms are neglected. Again neglecting high-order terms:

$$\frac{\delta\bar{\omega}_{23}}{\bar{\omega}_2} = \frac{\delta\bar{\omega}_{23}}{\bar{\omega}_1 - \delta\bar{\omega}_{12}} \approx \frac{\delta\bar{\omega}_{23}}{\bar{\omega}_1}\left(1+\frac{\delta\bar{\omega}_{12}}{\bar{\omega}_1}\right) \approx \frac{\delta\bar{\omega}_{23}}{\bar{\omega}_1}. \tag{7.13}$$

and equivalently

$$\frac{\delta\bar{\omega}_{34}}{\bar{\omega}_3} \approx \frac{\delta\bar{\omega}_{34}}{\bar{\omega}_1} \tag{7.14}$$

Hence, each contribution given by Eqs. (7.12) can be added to find the overall angular velocity variation $\delta\bar{\omega} = \delta\bar{\omega}_{12} + \delta\bar{\omega}_{23} + \delta\bar{\omega}_{34}$ between step 1 and 4:

$$\frac{\delta\bar{\omega}}{\bar{\omega}} = 5\frac{\bar{b}^5}{1-\bar{b}^5}\left[\frac{3}{2}\left(1+\frac{\bar{L}}{\bar{b}}\right)^2 - 1\right]\frac{\delta\bar{b}}{\bar{b}} \tag{7.15}$$

Note that the right-hand side of Eq. (7.15) only depends on the inner radius $\bar{b}$ and on the length $\bar{L}$ of the chain.

7.2.4 Siphon radial velocity

It was shown in Chapter 3 that the momentum exchange between the mass to be connected to the chain and the rest of the chain induces a deceleration of the siphon which eventually causes the siphon to reach a bound steady state velocity. For a siphon modelled as a continuous mass distribution, the steady state velocity can be written as a function of the radial force and the siphon linear density (Eq. (3.58)). Substituting Eq. (7.8) into Eq. (3.58) yields:

$$\bar{v} = \frac{1}{\sqrt{2}}\sqrt{\frac{(\bar{b}-1)(\bar{b}^2+\bar{b}-2+3\bar{L}(\bar{b}+1))}{\bar{L}+\bar{b}} + \bar{L}(\bar{L}+2\bar{b})\bar{\omega}^2} \tag{7.16}$$

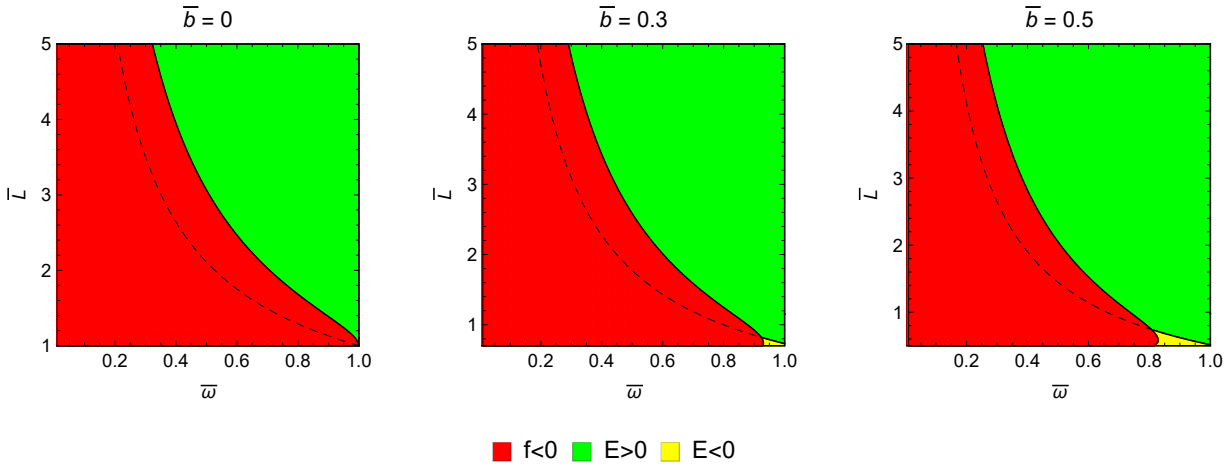

FIGURE 7.5: Regions of positive (green) and negative (yellow) energy of the material released from the siphon for a range of internal radii $\bar{b}$, as a function of the asteroid angular velocity $\bar{\omega}$ and the siphon length $\bar{L}$. Also shown in red is the region associated with negative siphon force, calculated using Eq. (7.8).

7.2.5 Energy of the released material

Following the analysis in Chapter 3, the energy per unit mass $\mathscr{E}$ of the material released at the top of the siphon can be expressed as:

$$\mathscr{E} = -\frac{4}{3}G\rho\pi(R^3 - b^3)\frac{1}{b+L} + \frac{1}{2}\left[\omega^2(b+L)^2 + v^2\right] \tag{7.17}$$

where the two terms represent the gravitational and kinetic energy of the released payload respectively. Equation (7.17) can be conveniently written in non-dimensional form as:

$$\bar{\mathscr{E}} = -\frac{1-\bar{b}^3}{1+\bar{L}} + \frac{1}{2}\left[\bar{\omega}^2(\bar{b}+\bar{L})^2 + \bar{v}^2\right] \tag{7.18}$$

Assuming two-body dynamics upon release, the sign of $\bar{\mathscr{E}}$ determines the fate of the released material, i.e., if it will escape the asteroid or be inserted in orbit around it. Figure 7.5 shows the region of positive (green) and negative (yellow) release energy. Also shown in red is the region where the siphon effect cannot be generated due to a negative radial force, calculated using Eq. (7.8). The dotted black line is the continuation of the contour line $\mathscr{E} = 0$ inside the $f < 0$ region. For $\bar{b} = 0$ material can only be released to escape, whereas for $\bar{b} > 0$, release to a bound orbit is possible only below a maximum siphon length, depending on $\bar{b}$ and the angular velocity of the asteroid.

7.2.6 Maximum internal volume

Equation (7.15) can be integrated from $\bar{\omega}_0$ to $\bar{\omega}_f$ (left-hand side) and from $\bar{b}_0 = 0$ to $\bar{b}_f$ (right-hand side) to obtain the angular velocity variation of the system as a function of the radius of

the internal cavity, such that

$$\frac{\bar{\omega}}{\bar{\omega}_0} = \exp(-\mathscr{I}) \tag{7.19}$$

where

$$\mathscr{I} = \int_0^{\bar{b}_f} 5\frac{\bar{b}^4}{1-\bar{b}^5}\left[\frac{3}{2}\left(1+\frac{\bar{L}}{\bar{b}}\right)^2 - 1\right] d\bar{b} \tag{7.20}$$

Since $\mathscr{I} > 0$ for any $\bar{L} > 0$ and $0 < \bar{b}_f < 1$, the angular velocity of the asteroid exponentially decreases as the radius of the internal cavity increases. If the length of the siphon is constant, Eq. (7.19) admits a closed-form solution, however, due to the length of the resulting expression, it is not explicitly reported here. Then, for a given siphon initial angular velocity $\bar{\omega}_0$ and siphon length $\bar{L}$, the parameter $\bar{b}_{f,max} = \max(\bar{b}_f)$ satisfying the condition $\bar{f} = 0$ (with the angular velocity calculated via Eq. (7.11)) represents the radius of the largest internal spherical cavity that can be excavated by exploiting the orbital siphon effect. Equivalently, $\bar{m}_f = \bar{b}_f^3$ represents the fraction of mass that has been removed, scaled with respect to the initial asteroid mass M_0.

Figure 7.6a shows the extractable mass $\bar{m}_f$ as a function of the siphon length $\bar{L}$ for a range of initial asteroid angular velocities $\bar{\omega}_0$. As for the scenario analysed in Chapter 3, an optimal siphon length which maximizes the extractable mass exists. As expected, the optimal chain increases with decreasing asteroid angular velocity: an asteroid with slower spin rate would require a larger chain to generate enough centrifugal pull to initialize the siphon effect. Figure 7.6b shows the maxima of Fig. 7.6a as a function of the asteroid initial angular velocity and the results are compared with that of Chapter 3, for the case of material extracted from the asteroid outer surface with a siphon anchored at equator. The maximum extractable mass for the internal siphon case is approximately 4.9% of the initial mass of the asteroid for $\bar{\omega}_0 = 1$, corresponding to an internal spherical void of radius $\bar{b} = 0.36$, requiring a siphon length $\bar{L} = 1.28$. The maximum extractable mass for an external siphon is always larger, irrespective of $\bar{\omega}_0$. This is due to the fact that a siphon anchored at the asteroid equator benefits from a larger centrifugal-induced force and therefore the minimum length required to initialize the siphon effect is smaller. Hence the term $\delta\omega/\omega$ is smaller for a siphon anchored at the equator (compare Eq. (7.15) with Eq. (3.32)).

Figure 7.7 shows the non-dimensional energy of the released material as a function of the non-dimensional inner radius $\bar{b}$, for different asteroid initial angular velocities $\bar{\omega}_0$. The siphon length is chosen such that the extractable mass is maximised. It is apparent that for any $\bar{\omega}_0 \leq 1$ material is always released to escape ($\bar{\mathscr{E}} > 0$), i.e., release to bound orbits is not possible.

7.2.7 Timescale

The total time required to extract the mass $\bar{m}_f$ is related to the siphon radial velocity and siphon linear density $\bar{\mu}$ via Eq. (3.70) for a siphon modelled as a continuous mass distribution. Using the velocity equation (7.16) with the conservation of angular momentum (7.19), the integrand of Eq. (3.70) can be written as a function of $\bar{m}$ (or, equivalently, as a function of $\bar{b}$). The resulting

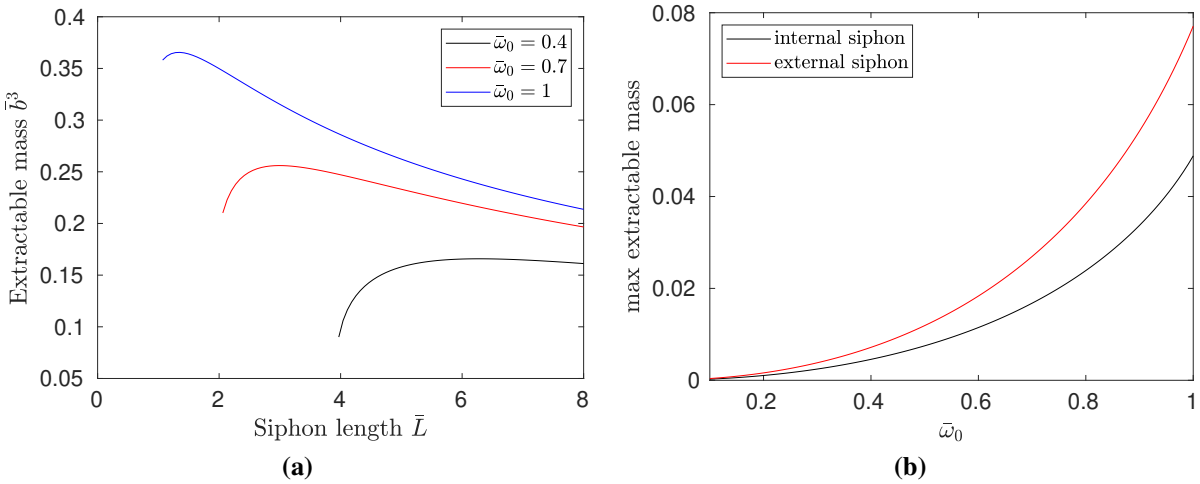

FIGURE 7.6: (a) Extractable mass as a function of the siphon length for a range of initial angular velocities. (b) Maximum extractable mass as a function of the initial angular velocity, compared with the results from Chapter 3, for a siphon anchored at the asteroid equator.

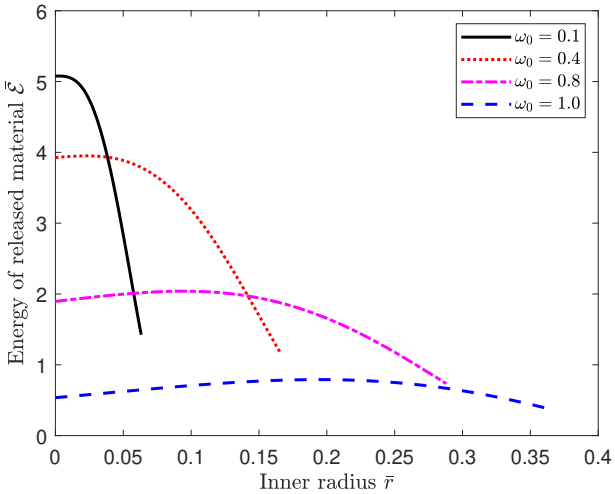

FIGURE 7.7: Non-dimensional energy $\bar{\mathscr{E}}$ of the released material as a function of the non-dimensional inner-radius $\bar{b}$, for different asteroid initial angular velocities $\bar{\omega}_0$. The siphon length is chosen such that the extractable mass is maximised.

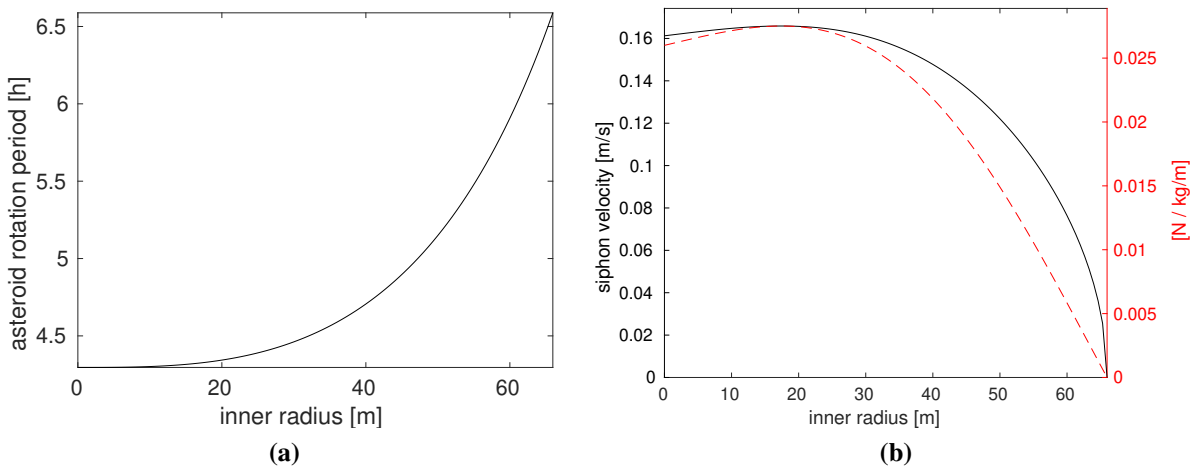

(a) (b)

FIGURE 7.8: (a) Variation of Bennu rotation period as a function of the inner radius. (b) Siphon velocity (black) and force per unit linear density (red) as a function of the inner radius.

integral does not admit a closed-form solution and an approximate solution can be obtained via numerical integration.

7.3 Case study

Relevant results in dimensional units related to the asteroid Bennu are now provided (see Table 2.1 for physical details of the asteroid). The radius of the spherical cavity that can be created inside Bennu by extracting mass using a constant length siphon is $b_{f,max} = 66\,\mathrm{m}$ (approximately one quarter of the outer radius), corresponding to a total extracted mass $m_f = 1.5 \times 10^9\,\mathrm{kg}$ and requiring and optimal siphon length $L = 803\,\mathrm{m}$, approximately three times the radius of the asteroid. Using Eq. (7.17) it can be shown that material is released to escape for all $\bar{b} \in [0, \bar{b}_f]$. Figure 7.8a shows the variation of the asteroid period as a function of the inner radius using the conservation of angular momentum (Eq. (7.11)). The final asteroid rotation period at the end of the manipulation process is approximately 1.5 longer than the initial period.

Figure 7.8b shows the radial velocity of the siphon (Eq. (7.16)) as a function of the radius of the inner cavity (black curve) as well as the siphon force per unit linear density f_{cont}/μ (red). The velocity is on the order of cm/s, comparable with previous results for a siphon anchored at the asteroid surface (Chapter 3). It drops to zero towards the end of the manipulation process, when the radial force on the chain approaches zero and the siphon reaches its equilibrium state.

Figures 7.9a and 7.9b show the time required to generate a cavity with inner radius r and the average mass flow rate as a function of r, for a range of siphon linear densities μ. For example, a 27-meter radius cavity, corresponding to approximately 10^5 tonne of removed material, can be excavated in 6.2 years, for a siphon linear density $\mu = 1\,\mathrm{kg\,m^{-1}}$, or 45 days, for $\mu = 50\,\mathrm{kg\,m^{-1}}$. The required instantaneous mass rates are below $9\,\mathrm{kg\,s^{-1}}$ for $\mu \leq 50\,\mathrm{kg\,s^{-1}}$ (Fig. 3.12). Clearly, such mass rates depend upon the technology of mining units transferring material to the siphon

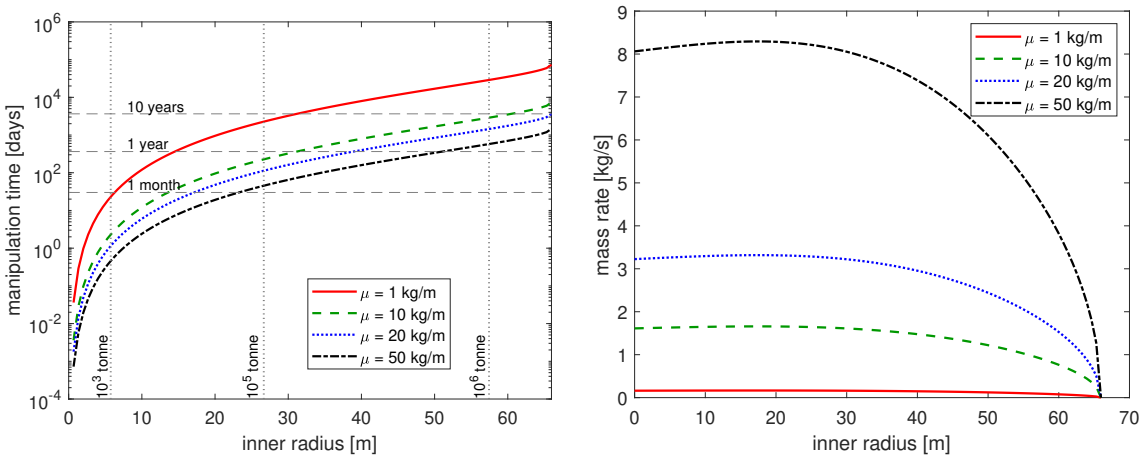

FIGURE 7.9: Manipulation time (a) and instantaneous mass rate of lifted mass (b) as a function of the inner radius r, for a range of siphon linear density μ.

and the physical properties of the asteroid. According to [126], an equipment mass of 5 tonnes could process 1000 tonnes of asteroid regolith per day, or $11.5\,\mathrm{kg\,s^{-1}}$ which is larger than the maximum rate shown in Fig. 7.9b, suggesting that the siphon can be fed with the required mass rates for the test cases considered here.

As noted in Fig. 7.8a, the asteroid retains a residual angular velocity at the end of the manipulation process that cannot be further exploited if the siphon length is constant. However, by allowing the siphon length to increase, it is possible to leverage the residual rotational kinetic energy of the asteroid to further increase the volume of the internal cavity. For example, Fig. 7.10a shows the variation of the asteroid period as a function of the radius of the internal cavity when a siphon of variable length is used. The length L is chosen as a function of the equilibrium length, which increases during siphon operation (see Fig. 7.3). Figure 7.10b shows the length of the siphon as function of the inner radius. The dotted vertical line represents the maximum radius of the inner cavity that can be excavated with a constant-length siphon. As expected, larger cavities can be created in this case. For example, taking $L = 1.2L_{\mathrm{eq}}$, leads to a cavity with a radius of approximately 82 m. Clearly, when L is closer to the equilibrium length, larger cavities can be excavated. However, the case $L = L_{eq}$ represents an ideal limiting scenario, since the siphon would constantly experience zero net force by definition in this case.

The case $L = 1.65L_{eq}$ leads to an equivalent result as the constant length siphon case. Moreover, it should be noted that by changing the shape of the cavity, the angular velocity equation (7.19) would change accordingly, thus in principle changing the maximum extractable mass m_f and therefore the volume of the internal cavity. The key parameter here is the resulting inertia of the spherical asteroid with the internal cavity: if, for a given void volume, this parameter is maximised (or, in turn, the inertia of the cavity is minimised), then the angular velocity of the system comprising the asteroid and the siphon at the end of siphon operation is maximised,

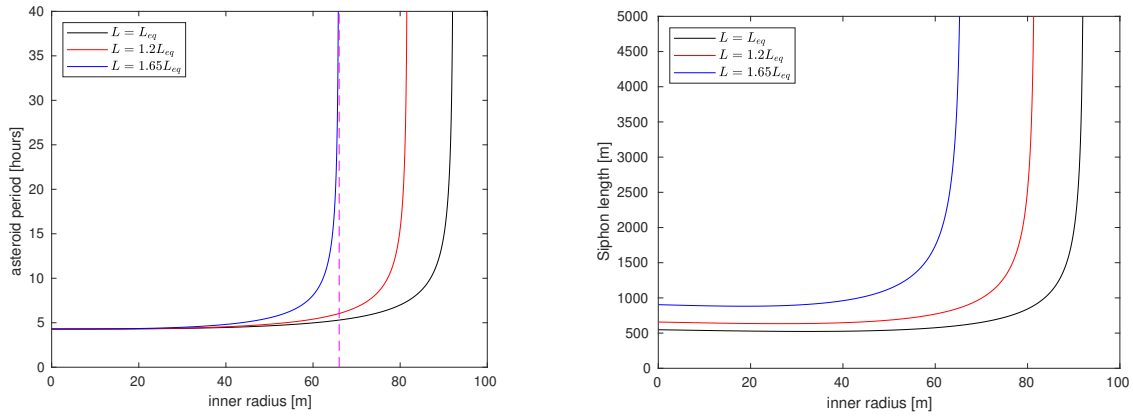

(a) **(b)**

FIGURE 7.10: Variation of asteroid rotation period (a) and siphon length (b) for a variable-length siphon. The dotted vertical green line in Fig. 7.10a indicates the maximum radius of the internal cavity that can be excavated using a constant length siphon.

according to conservation of angular momentum and, therefore, a larger amount of mass can be extracted. For example, a cylinder with height h and cross section diameter d would have half the inertia of a sphere with diameter d if $h = 4/15d$. Although it is expected that the resulting cavity volumes will not change significantly from the values found in the present preliminary analysis for a spherical cavity, further studies are require to apply the present concept to different cavity shapes.

7.4 Analytical modelling of structural failure

As shown in the previous sections, the creation of a void in the interior of the asteroid alters the physical characteristics of the body: its rotation period increases due to conservation of angular momentum and its mass is reduced. Therefore, it is expected that the distribution of internal stresses on the asteroid will change. This section provides a simple analytical model developed using a continuum mechanics approach to explore the variation of internal stresses due to the presence of an artificial cavity of variable size in the interior of the asteroid. Then, using the Druker-Prager failure law [25], the internal regions more sensitive to structural failure are identified.

A set of simplifying assumptions is made such that a closed-form solution for the internal stresses can be found. Firstly, material behaviour is assumed to be elastic-perfectly plastic, and therefore the effect of material hardening after yielding is not taken into account. The same spherical asteroid shape is assumed, as in the previous section. The only two body loads considered are those due to gravity and the asteroid rotation. The effects of the tunnel containing the siphon or that of any anchoring device are not considered in the derivation of the internal stresses. Also, it is assumed that the gradual increase of the inner cavity volume is quasi-static

(so that any time-dependent change of the stress due to additional inertial forces is neglected) and any local variation of internal stress due to the interaction between mining units and the asteroid is not taken into account.

7.4.1 Elastic stress solution

A method described by Barber [8] is adapted to find a closed-form solution for the stress tensor on an axisymmetric body subjected to arbitrary axisymmetric tractions, in this case the self-gravity of the asteroid and centrifugal-induced force due to the asteroid rotation. Barber uses a method that involves harmonic functions to describe the displacement of the body. Eventually, through the stress-strain relationship, such displacements are then linked to the stresses.

Let ϱ, Θ, ϕ define a spherical coordinate system with origin at the asteroid centre-of-mass, where ϱ is the radial distance from the centre, $\Theta \in [0, \pi]$ is the co-latitude (with $\Theta = 0$, $\Theta = \pi$ being the latitude of the poles and $\Theta = \pi/2$ being the latitude of the equator) and $\phi \in [0, 2\pi]$ is the longitude. Let σ_{ij} denote the stress tensor. A sufficiently general solution to σ_{ij} can be written in terms of the body force potential in the form (Ref. [8], pages 259 and 270):

$$\sigma_{\varrho\varrho} = \frac{\nu U}{1-\nu} + \frac{\partial^2 \Gamma}{\partial \varrho^2} + \varrho \cos\Theta \frac{\partial^2 \psi}{\partial \varrho^2} - 2(1-\nu)\frac{\partial \psi}{\partial \varrho}\cos\Theta + \frac{2\nu}{\varrho}\frac{\partial \psi}{\partial \Theta}\sin\Theta \tag{7.21a}$$

$$\sigma_{\phi\phi} = \frac{\nu U}{1-\nu} + \frac{1}{\varrho}\frac{\partial \Gamma}{\partial \varrho} + \frac{\cot\Theta}{\varrho^2}\frac{\partial \Gamma}{\partial \Theta} + \frac{\cos^2\Theta}{\varrho \sin\Theta}\frac{\partial \psi}{\partial \Theta} + (1-2\nu)\frac{\partial \psi}{\partial \varrho}\cos\Theta + \frac{2\nu}{\varrho}\frac{\partial \psi}{\partial \Theta}\sin\Theta \tag{7.21b}$$

$$\sigma_{\Theta\Theta} = \frac{\nu U}{1-\nu} + \frac{1}{\varrho}\frac{\partial \Gamma}{\partial \varrho} + \frac{1}{\varrho^2}\frac{\partial^2 \Gamma}{\partial \Theta^2} + \frac{\cos\Theta}{\varrho}\frac{\partial^2 \psi}{\partial \Theta^2} + (1-2\nu)\frac{\partial \psi}{\partial \varrho}\cos\Theta + \frac{2(1-\nu)}{\varrho}\frac{\partial \psi}{\partial \Theta}\sin\Theta \tag{7.21c}$$

$$\sigma_{\Theta\varrho} = \frac{1}{\varrho}\frac{\partial^2 \Gamma}{\partial \Theta \partial \varrho} - \frac{1}{\varrho^2}\frac{\partial \Gamma}{\partial \Theta} + \cos\Theta \frac{\partial^2 \psi}{\partial \Theta \partial \varrho} + (1-2\nu)\frac{\partial \psi}{\varrho}\sin\Theta - \frac{2(1-\nu)}{\varrho}\frac{\partial \psi}{\partial \Theta}\cos\Theta \tag{7.21d}$$

$$\sigma_{\phi\varrho} = \sigma_{\phi\varrho} = 0 \tag{7.21e}$$

where Γ and ψ are two potential functions satisfying

$$\nabla^2 \Gamma = \frac{(1-2\nu)U}{1-\nu} \tag{7.22a}$$

$$\nabla^2 \psi = 0 \tag{7.22b}$$

and U is the body force potential. The conditions defined by Eqs. (7.22) ensure that the equilibrium equations are satisfied whereas Eqs. (7.21) represent the stress-strain relations, expressed as a function of the potentials Γ and ψ (the interested reader is referred to Ref. [8] for additional details). The body potential U associated with the gravitational and rotational loads is, in

spherical coordinates, given by

$$U = \frac{4}{3} G\pi\rho^2 \left(\frac{1}{2}\, \varrho^2 + \frac{b^3}{\varrho} \right) - \frac{1}{2}\rho\, \varrho^2\, \omega^2 \sin^2\Theta \tag{7.23}$$

Traction-free boundary conditions are imposed at the outer and inner surface, i.e.

$$\sigma_{ij}(\varrho = b, \Theta, \phi)\hat{n} = 0 \tag{7.24a}$$

$$\sigma_{ij}(\varrho = R, \Theta, \phi)\hat{n} = 0 \tag{7.24b}$$

where $\hat{n}$ is the normal to the surface. Therefore, the goal is to identify two harmonic functions Γ and ψ that simultaneously satisfy: (i) the equilibrium equations given by Eqs. (7.22) and (ii) the boundary conditions (Eq. (7.24)) upon substitution of the stress-strain Eqs. (7.21). To this end, first note that the function Γ can be decomposed in the sum $\Gamma_p + \Gamma_h$, representing the particular and homogeneous solution to Eq. (7.22a) respectively. It can easily be verified that the particular solution

$$\Gamma_p = \frac{\varrho^4\, \rho\omega^2(1-2\nu)(5\cos 2\Theta - 3)}{280(1-\nu)} + \frac{4}{3}\pi\rho G\rho^2 \frac{2\nu-1}{\nu-1} \left(\frac{\varrho^4}{40} + \frac{b^3\, \varrho}{2} \right) \tag{7.25}$$

satisfies Eq. (7.22a). In order to find the homogeneous solutions Γ_h and ψ, these are written in terms of spherical harmonics with coefficients to be found in order to satisfy the boundary conditions Eq. (7.24). In particular, the functions Γ_h and ψ can be written as:

$$\Gamma_h = A_1\, \varrho^{-1} + \frac{1+3\cos\Theta}{4}(A_2\, \varrho^2 + A_3\, \varrho^{-3}) + A_4\, \varrho^4\, \frac{9+20\cos 2\Theta + 35\cos 4\Theta}{64} \tag{7.26}$$

$$\psi = \cos\Theta(B_1\, \varrho + B_2\, \varrho^{-2}) + B_3\, \varrho^3\, \frac{3\cos\Theta + 5\cos 3\Theta}{8} \tag{7.27}$$

where A_1, A_2, A_3, A_4, B_1, B_2 and B_3 are coefficients to be determined. The specific spherical harmonics to be used are chosen to enable the boundary conditions to be satisfied. Substituting ψ and $\Gamma = \Gamma_p + \Gamma_h$ into Eqs. (7.21) and then imposing the boundary condition Eq. (7.24) forms a system of 7 linearly independent equations in the 7 unknowns A_1, A_2, A_3, A_4, B_1, B_2 and B_3. Solving for the coefficients and then substituting the potentials Γ, ψ back into Eqs. (7.21) permits the stress tensor σ_{ij} to be found (see Appendix G for intermediate steps). Scaling the stresses by the factor $4/3G\pi\rho^2R^2$, the resulting stress tensor can be written as a function of the asteroid angular velocity $\bar{\omega}$, the Poisson ratio ν, the radial distance $\bar{\varrho}$ and the co-latitude Θ (see Appendix G). Due to the symmetry of the problem, the stress is independent of the longitude ϕ and it is symmetric with respect to the equatorial plane. It is important to note that the particular case of $b = 0$ returns the classical solution for the stress field of an homogeneous elastic rotating

sphere [60]:

$$\sigma_{\varrho\varrho} = \frac{\left(\varrho^2 - 1\right)\left[5\left(2\nu^2+\nu-3\right)\omega^2\cos 2\Theta + 5\nu^2 + \nu\left(7\omega^2-8\right) + 9\omega^2 - 21\right]}{10(\nu-1)(5\nu+7)} \tag{7.28a}$$

$$\sigma_{\phi\phi} = \frac{-5\left(\nu^2-1\right)\,\varrho^2\,\omega^2\cos 2\Theta + \omega^2\left[2\nu(5\nu-1) + (\nu(5\nu+14)+13)\,\varrho^2 - 24\right]}{10(\nu-1) - (5\nu+7)} - \frac{\nu + (3\nu+1)\,\varrho^2 - 3}{10(\nu-1)} \tag{7.28b}$$

$$\sigma_{\Theta\Theta} = \frac{-5\left(2\nu^2+\nu-3\right)\left(\varrho^2-1\right)\omega^2\cos 2\Theta + \omega^2\left[-7\nu + (\nu(10\nu+19)+3)\,\varrho^2 - 9\right]}{10(\nu-1)(5\nu+7)} - \frac{\nu + (3\nu+1)\,\varrho^2 - 3}{10(\nu-1)} \tag{7.28c}$$

$$\sigma_{\Theta\varrho} = -\frac{(2\nu+3)\left(\varrho^2-1\right)\omega^2\sin 2\Theta}{2(5\nu+7)} \tag{7.28d}$$

7.4.2 Failure law

Granular materials have zero or little tensile strength but can withstand considerable shear stress if under pressure. The pressure p is formally the average of the principal stresses $\sigma_1, \sigma_2, \sigma_3$, i.e., $p = (\sigma_1 + \sigma_2 + \sigma_3)/3$. Such pressure dependence is the consequence of the interlocking between the granular particles: in order to trigger failure, particles have to slide over one another and the confining pressure resists such motion [54]. A common pressure-dependent criterion to assess failure of geological material is the Druker-Prager criterion, which is formally an extension of the von-Mises criterion by introducing the influence of the pressure at failure. The Drucker-Prager model states that failure is achieved when [25]:

$$\alpha I_1 + \sqrt{J_2} - s \leq 0 \tag{7.29}$$

where I_1 and J_2 are the stress invariants

$$I_1 = \sigma_1 + \sigma_2 + \sigma_3 \tag{7.30}$$

$$J_2 = \frac{1}{6}\left[(\sigma_1-\sigma_2)^2 + (\sigma_2-\sigma_3)^2 + (\sigma_1-\sigma_3)^2\right] \tag{7.31}$$

Note that I_1 is proportional to the pressure p; the term $\sqrt{J_2}$ is related to the shear stresses [25]. The two coefficients α and s are macroscopic properties of the granular assembly. They can be related to the angle of friction ϕ and the cohesion c via [25] :

$$\alpha = \frac{2\sin\phi}{\sqrt{3}(3-\sin\phi)} \tag{7.32}$$

$$s = \frac{6c\cos\phi}{\sqrt{3}(3-\sin\phi)} \tag{7.33}$$

The cohesion is formally the shear strength at zero pressure. The angle of friction is associated with the interlocking between particles in the granular medium (see Ref. [25]). Similarly to Ref. [53] two types of cohesion are distinguished: the *actual cohesion* and the *critical cohesion* c^*. The former is a macroscopic property of the asteroid while the latter is defined as the value of the cohesion at which Eq. (7.29) is verified with the equality:

$$c^* = \frac{\sqrt{3}(3-\sin\phi)}{6\cos\phi}\sqrt{J_2} + \frac{1}{3}\tan\phi I_1 \tag{7.34}$$

The critical cohesion is an indicator of possible failure: if the actual cohesion c is smaller than c^* at any point on the asteroid interior, the asteroid may structurally fail.

7.4.3 Results

Following Ref. [53] the Poisson ratio is fixed at 0.25 and a range of angles of friction between 20 deg and 45 deg are considered. Figures 7.11 and 7.12 show the distribution of the non-dimensional critical cohesion $\bar{c}^*$ in the xz plane at the beginning (left column) and at the end of siphon operation (right column), taking an angle of friction $\phi = 20$ deg and 45 deg respectively, for a range of initial angular velocities ($\bar{\omega}_0 = 0.6$, $\bar{\omega}_0 = 0.8$, $\bar{\omega}_0 = 1$). The final angular velocity and radius of the internal cavity are calculated with the method described in Sect 7.2.6 assuming a constant and optimal siphon length, and their values are indicated in the title of each figure. The red dotted lines mark the contour lines characterized by $c^* = 0$ and a red dot indicates the location of $\max(\bar{c}^*)$ in the cases where $\max(\bar{c}^*) > 0$. Some relevant information can be inferred. When $b = 0$ the weakest point, i.e. the point with highest $\max(\bar{c}^*)$, is located on the outer surface of the asteroid for lower initial spin rates (at the poles for low angle of friction or at the equator for higher angles of friction) whereas it is at the centre of the asteroid for higher spin rates. At low spin rates and large angles of friction the entire asteroid is characterized by negative stress (such as in the case $\bar{\omega}_0 = 0.6$ and $\phi = 45$ deg), meaning that no cohesion is required for the asteroid to avoid structural failure. At the end of the manipulation process ($b > 0$), the location of the most weak point is on the inner surface, in all the cases represented where $\max(\bar{c}^*) > 0$. At lower angular velocities, the distribution of the stresses does not strongly depend on the latitude. This result is expected since gravity is the predominant body force at slow spin rates. However, at larger angular velocities, the distribution of $\bar{c}^*$ varies significantly with latitude and, for the cases represented here, the equator of the inner cavity is the point with highest sensitivity to failure.

Figure 7.13 shows the magnitude of the maximum critical cohesion (coloured contour curves) on the internal surface $\bar{\varrho} = \bar{b}$ as function of the internal radius $\bar{b}$ and the angular velocity, for $\phi = 25$ deg (a), $\phi = 35$ deg (b), $\phi = 40$ deg (c), $\phi = 45$ deg (d). Here, the critical cohesion is reported in dimensional units, assuming an asteroid with the same density and outer radius R as Bennu (Table 2.1). Also shown as dashed black curves is the variation of the angular velocity

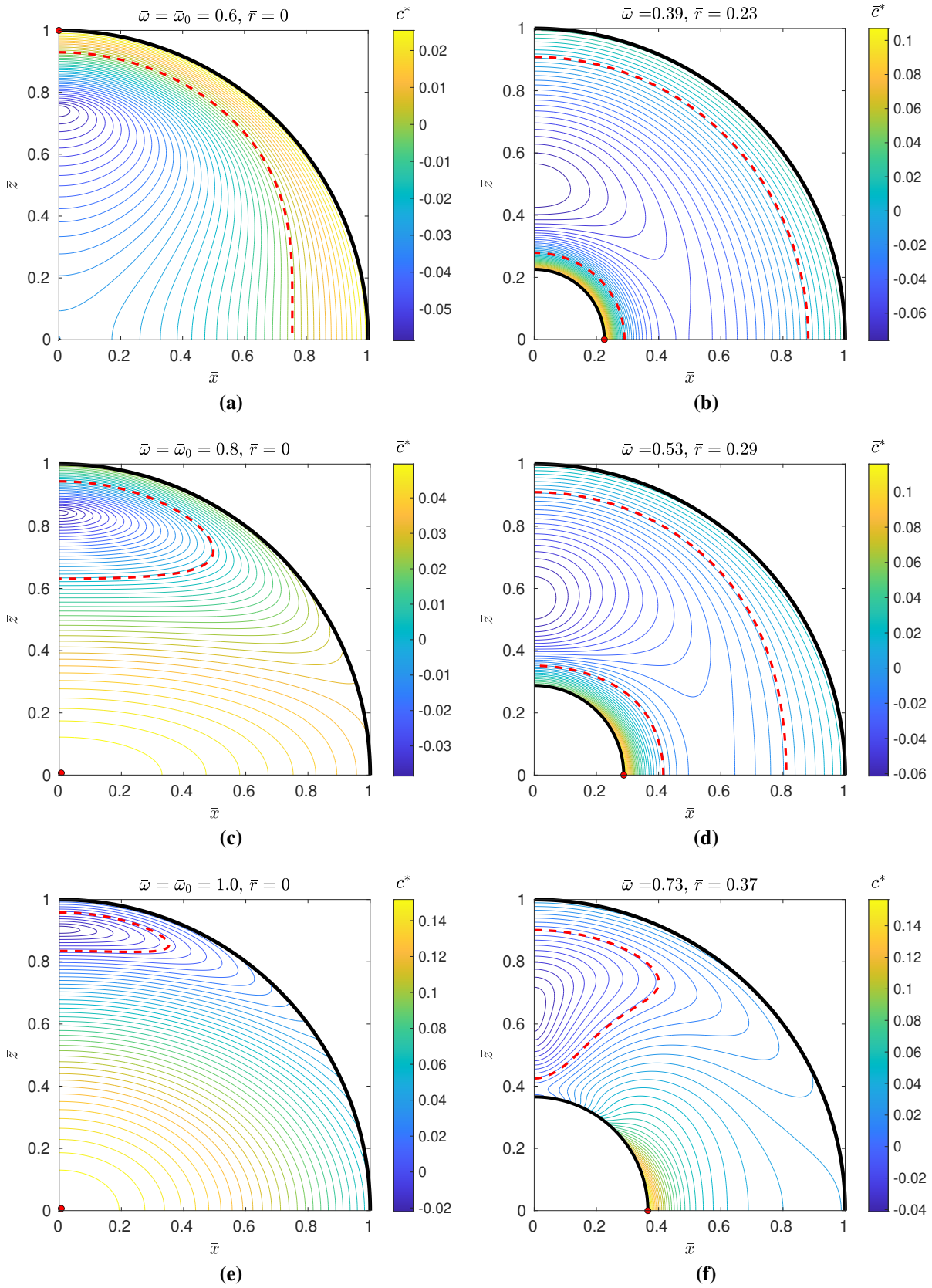

FIGURE 7.11: Non-dimensional critical cohesion $\bar{c}^*$ at the beginning (left column) and the end (right column) of siphon operation, assuming a friction angle $\phi = 20$ deg.

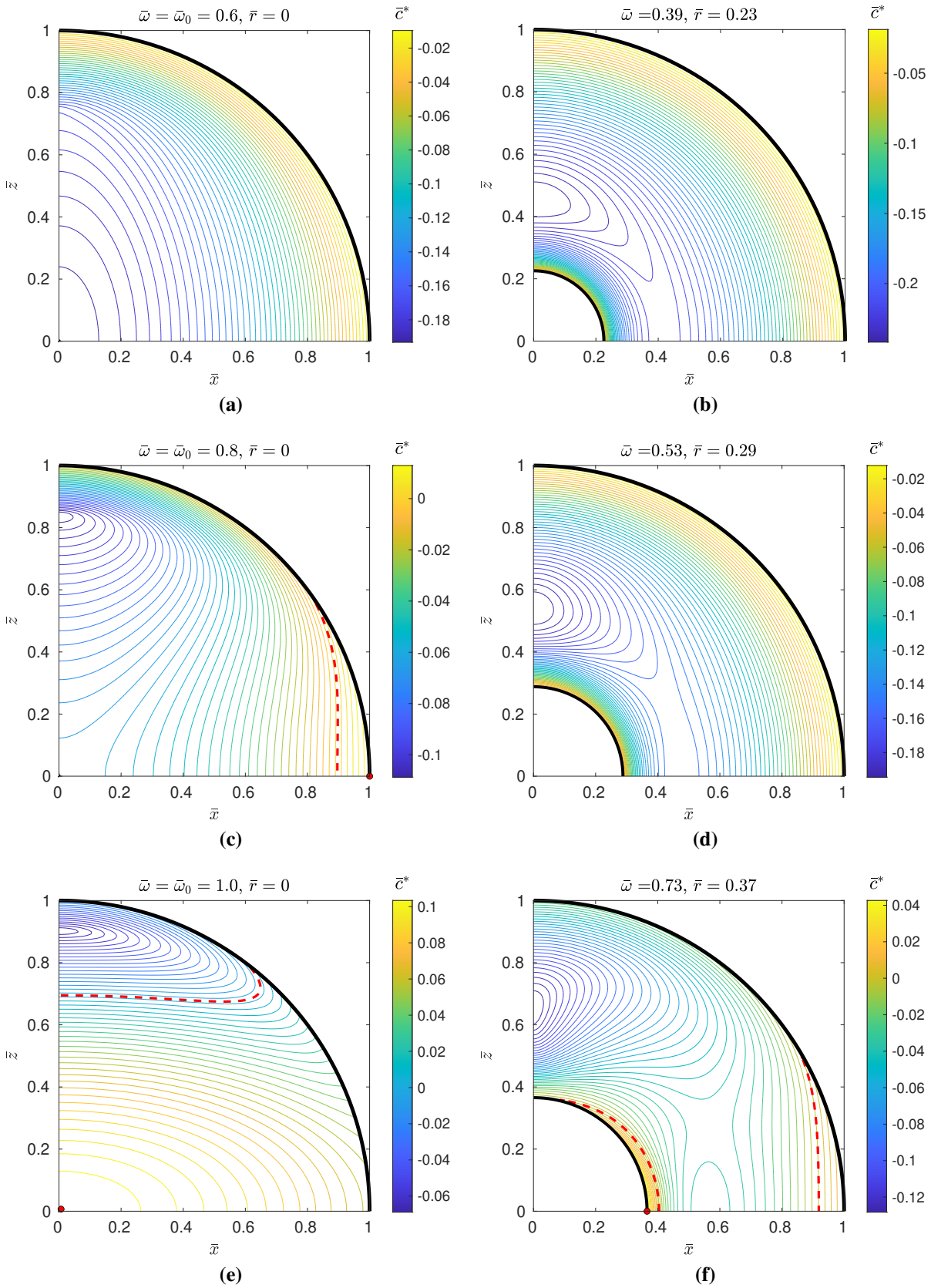

FIGURE 7.12: Non-dimensional critical cohesion $\bar{c}^*$ at the beginning (left column) and the end (right column) of siphon operation, assuming a friction angle $\phi = 45$ deg.

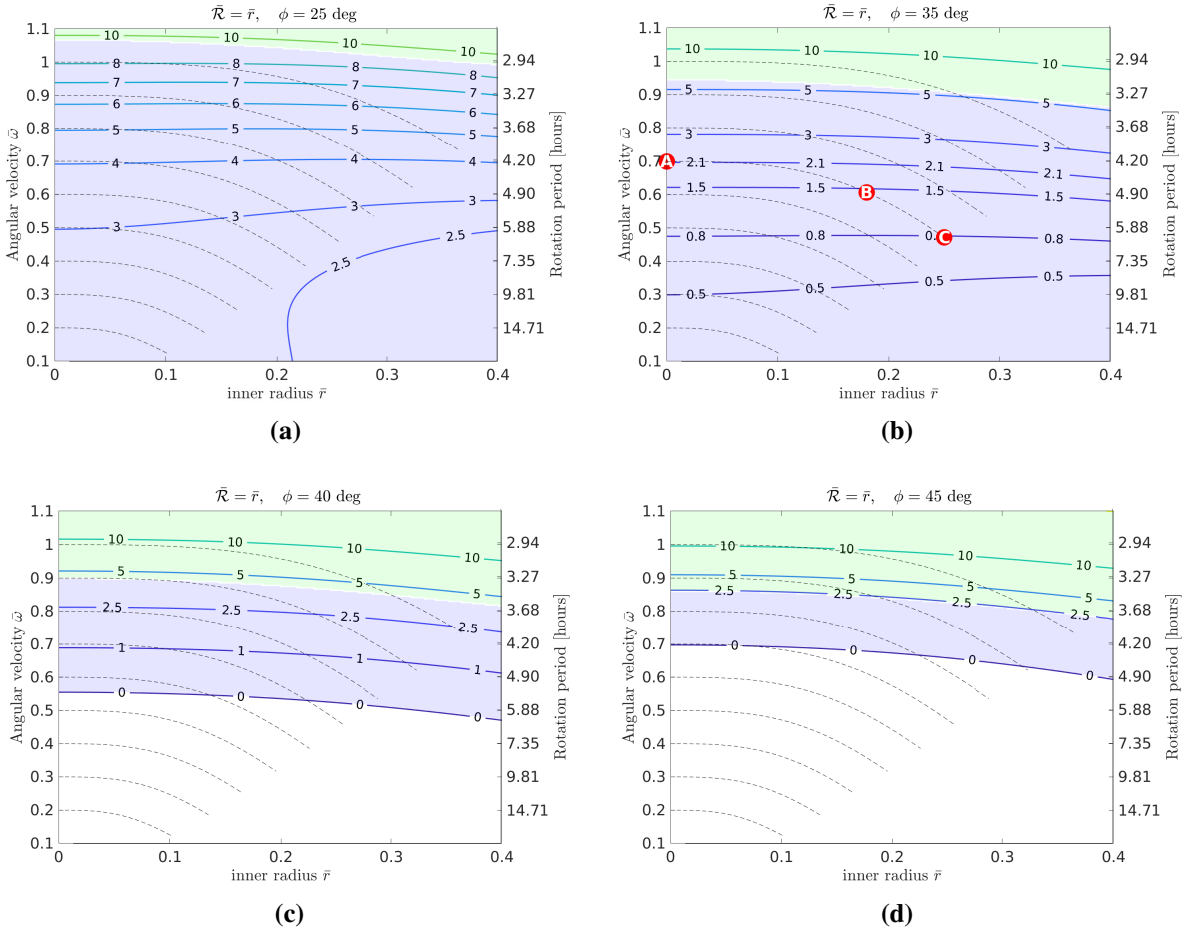

FIGURE 7.13: Contours of the maximum critical cohesion (in Pa) on the surface of the inner cavity $\varrho = b$ as a function of the inner radius and the asteroid angular velocity, for a range of angles of friction, as indicated in the title of each figure. The dashed black curve also show the variation of the asteroid angular velocity as a function of $\bar{b}$, for some values of $\bar{\omega}_0$. The shaded regions indicate the latitude of $\max(c^*)$ ($\max(c^*) > 0$): $\Theta = 0$ (i.e., at the poles) for the green region and $\Theta = \pi/2$ (i.e., at the equator) for the blue region. The right-hand y-axis shows the asteroid rotation period $2\pi/\omega$, taking an asteroid density $\rho = 1260\,\mathrm{kg\,m^{-3}}$.

of the asteroid as a function of the inner radius considering the effect of the orbital siphon, for different initial angular velocities. Each dashed black curve is obtained via Eq. (7.19) taking a constant-length siphon, such that the final radius of the internal cavity is maximized. The right y-axis shows the period of the asteroid (the asteroid period $2\pi/\omega$ is completely defined from $\bar{\omega}$ if the asteroid density is fixed). Also, the shaded regions show the co-latitude at which the maximum critical cohesion is achieved (when $\max(c^* > 0)$): $\Theta = 0$ (i.e., at the poles) for the green region and $\Theta = \pi/2$ (i.e., at the equator) for the blue region. In general, the critical cohesion is not a strong function of the internal radius, since the contour lines are approximately horizontal (with some exceptions for low angular velocities and angles of friction, as in Fig. 7.13a). Therefore, since the angular velocity of the asteroid strictly decreases during siphon operation according to Eq. (7.19) (see the dashed black lines), it follows that the maximum critical co-

hesion c^* in the internal cavity decreases during the material removal process. For example, assuming an initial angular velocity $\bar{\omega}_0 = 0.7$ and $\phi = 35$ deg (Fig. 7.13b) the critical cohesion at the beginning of siphon operation ($\bar{b} = 0$, marker *A*) is approximately 2.1 Pa, then it decreases to 1.5 Pa for $\bar{b} = 0.18$ (marker *B*) and eventually to 0.8 Pa at the end of siphon operation (marker *C*). This is consistent with the fact that both body loads (due to gravity and rotation) decrease during siphon operation and therefore the failure conditions are relaxed at larger b. If the initial asteroid angular velocity is close to the critical spin, the location of the most weak point changes from the poles to the equator of the internal cavity as b increases. This effect is most noticeable at larger angles of friction (see for example the black dashed line in Fig. 7.13c starting from $\bar{\omega} = 1$, intersecting both the green and the blue region). Figure 7.14 is equivalent to however the contour of the maximum critical cohesion is calculated at the outer surface, $\bar{\varrho} = 1$. As already suggested by Fig. 7.13 the maximum critical cohesion on the outer surface is always lower than the $\bar{\varrho} = \bar{b}$ case. It can be verified this is true for any $\bar{b} < \bar{\varrho} \leq 1$, thus confirming that the internal cavity is the most sensitive to failure. In general, at large angles of friction the asteroid equator is more sensitive to failure than the poles. Therefore, since the siphon operation does not increase the critical cohesive strength, the minimum level of cohesive strength the asteroid should have to avoid failure corresponds to the maximum critical cohesive strength for $b = 0$, at the beginning of siphon operation. For example, assuming an initial asteroid period equal to the nominal Bennu period (see Sec. 7.3), a minimum level of cohesion of approximately 4 Pa is required to avoid failure of the internal cavity. This is a conservative value calculated for $\phi = 25$ deg (Fig. 7.13a), however the requirement on the minimum cohesive strength is reduced for higher angles of friction.

Therefore, according to this preliminary model, the presence of the internal cavity does not challenge the structural stability of the asteroid as the cavity is generated. Further studies are then required to verify how external effects that were not taken into account in this model (e.g., siphon anchor forces, plastic behaviour of the asteroid material after yielding, stresses due to the mining rovers, non-spherical asteroid and cavity shape) may change the stress distribution.

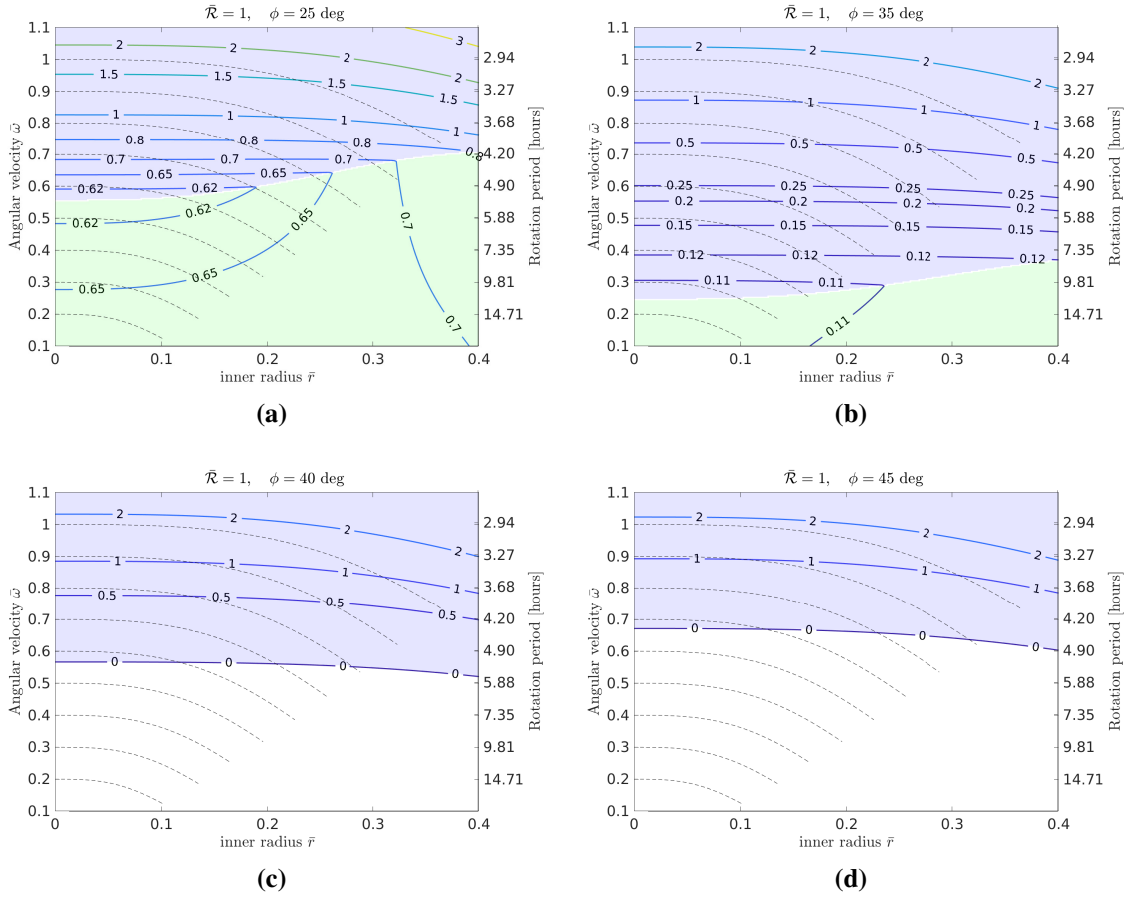

FIGURE 7.14: Contours of the maximum critical cohesion (in dimensional units, Pa) on the asteroid surface $\varrho = R$ as a function of the inner radius and the asteroid angular velocity, for a range of angles of friction, as indicated in the title of each figure. The dashed black curve also show the variation of the asteroid angular velocity as a function of $\bar{b}$, for some values of $\bar{\omega}_0$. The shaded regions indicate the latitude of $\max(c^*)$ ($\max(c^*) > 0$): $\Theta = 0$ (i.e., at the poles) for the green region and $\Theta = \pi/2$ (i.e., at the equator) for the blue region. The right-hand y-axis shows the asteroid rotation period $2\pi/\omega$, taking an asteroid density $\rho = 1260\,\mathrm{kg\,m^{-3}}$.

Chapter 8

Conclusions and future work

In this thesis a novel method for asteroid manipulation, the orbital siphon, has been investigated in detail, and possible applications have been discussed in the context of asteroid mining and deflection. In particular, Chapters 3, 4 and 5 analysed the behaviour of the siphon under different sets of approximations of the asteroid gravitational field and focussing on different operational aspects (e.g., maximum extractable mass, equatorial oscillations, transfer to equilibrium points), whereas Chapters 6, and 7 analysed specific applications. In the following sections, the conclusions drawn from each chapter are reported.

8.1 Chapter 3

In Chapter 3 the analytical mechanics of the orbital siphon has been investigated in detail, with a focus on the maximum quantity of mass that can be disassembled from the asteroid using the siphon effect. It has been shown that a vertical chain of masses can be envisaged to overcome the surface gravity of a rotating body and can be used to lift material collected at the surface without the need for external work to be done. Under specific conditions, the centripetal-induced force on the uppermost masses can be large enough to lift the lower masses. Thus, by releasing the top mass of the chain and adding a new payload mass at the bottom, an orbital siphon mechanism is initialized, and a stream of masses can be released with a range of energies, which depend on the physical characteristics of the asteroid (its angular velocity and density) and the chain (its length). In particular, material can be released into bound orbits around the asteroid and into parabolic or hyperbolic trajectories. However, only fast rotators with an angular velocity larger than approximately 68% of their critical angular velocity can release material into bound motion. It has been observed that the velocity at which payload masses are raised does not diverge, under the assumption that the new payload masses are connected to the siphon at zero velocity in the asteroid rotating frame.

Two strategies of mass extraction have been investigated, involving chains with constant and non-constant length. Optimal chain configurations for these cases have been discussed. In

optimal conditions, the maximum extractable mass is within approximately 8 and 12% of the initial mass of the asteroid, where larger values are possible for fast rotators and variable-length chains. However, it has been noted that longer chains also increase the complexity of the system when considering practical implementation.

8.2 Chapter 4

In this chapter the effect of the Coriolis forces due to the radial motion of the orbital siphon has been considered. Moreover, the effect of the anchor location on the siphon dynamics has been taken into account by modelling the asteroid as an ellipsoid and a collecting spacecraft at the top of the siphon is envisaged for collection of payload masses. It was shown that the siphon effect induces a torque on the chain with respect to the anchor, thus inducing oscillations of the siphon in the equatorial plane with a period comparable to the asteroid period. As more mass is delivered to the collecting spacecraft at the top of the siphon the amplitude of these oscillations is reduced over time, the siphon aligns with the local vertical and the radial velocity of the chain of masses reaches a constant value, which is consistent with the findings in Chapter 3. If material is not transferred to the collecting spacecraft but it is released to orbit or to escape, the siphon does not align with the local vertical, but the amplitude of the oscillations is still damped. Similar dynamical behaviour has been observed in the literature for frictionless pendulums with a sliding mass.

It has been observed that prolate asteroids require a larger minimum chain length if the siphon is anchored at the shortest end. Thus, for a prolate asteroid, the best anchor location for the siphon is the longest equatorial end, where the centrifugal-induced acceleration at the surface is larger.

It is shown that the siphon dynamics can be leveraged to deliver resource payloads to the stable equilibrium points or stable retrograde orbits with a smaller Δv than direct transfer from the asteroid surface using mass drivers, which can be beneficial in a large-scale mining scenario. Such stable points and orbits could serve as gravitational depots for material, waiting to be further processed or stored for later collection, while the siphon keeps raising resources from the surface of the asteroid.

8.3 Chapter 5

In this chapter the siphon was modelled as a set of discrete masses connected by elastic tethers without any support structure and motion is allowed in the three-dimensional space. Moreover, the gravity field is modelled using a polyhedral model of two candidates near-Earth asteroids.

It has been shown that the orbital siphon effect is still generated with the polyhedral models used and the dynamics is similar to that described in Chapter 4 for a rigidly rotating siphon.

This is a key result, as the proposed self-supporting siphon architecture reduces the scale of infrastructure mass with respect to a siphon with a rigid support. However, it has been observed that long structures may cause interference between the two sides of the siphon and this may compromise siphon operation. Moreover, the irregularities of the gravitational potential do not introduce instabilities to the orbital siphon system or irregularly bend the chain in the scenarios analysed. As in previous chapters, the chain average velocity does not diverge but reaches a steady state, due to the constant deceleration accompanying each bucket refilling. It was shown that the period of the oscillations and the velocity at steady state quite accurately match the values found in the previous chapters. Therefore, the models developed in Chapters 3 and 4 can be used as preliminary tools to investigate specific properties of the siphon, such as maximum long-term extractable mass, steady-state radial velocity, transient equatorial oscillations and Δv required for transfers to equilibrium points.

The dynamics of a siphon with a moving anchor base has also been considered. It has been shown that the siphon effect is still generated. This would allow the mining location to be moved without interrupting the flow of material to the collecting spacecraft.

Finally, a preliminary study of the particle release process has been performed, using Discrete Element Method (DEM) simulations. In particular, it has been proposed to exploit the centrifugal-induced force at the collecting spacecraft to sort regolith particles by size. The efficiency of the sorting tower, as the sorting device was named, has been considered for a few test cases, varying the cohesive properties of the asteroid regolith and the centrifugal acceleration on the tower (which depends on the length of the siphon). It has been shown the efficiency of sorting is above 95% in all test cases where the regolith is assumed to be cohesionless. However, non-cohesionless regolith may facilitate the creation of macro-aggregates inside the filter thus reducing the overall performance of the sorting tower. As expected, longer siphons will benefit from a larger centrifugal acceleration thus leading to better performances.

8.4 Chapter 6

In this chapter it was shown that the orbital siphon effect can in principle be exploited for asteroid deflection purposes. In particular, it has been shown that better performance can be achieved when the asteroid mass is released in multiple small fractions, rather than a single release of a larger mass. This allows a reduction of the linear density of material being transported on the siphon and the tether tension for a given time window and deflection distance. A smaller siphon linear density implies a lower siphon bulk mass and a smaller tension reduces the anchor force on the asteroid. The multiple mass release scenario also enables a reduction of the overall volume of the mass collected at the top of the siphon, making the problem of handling the collected material easier. Secondly, although not directly considered here, the repeatability offered by the multiple release scheme offers more margin in case of errors in the release direction.

A typical Δv on the order of $1\,\mathrm{cm\,s^{-1}}$ can be achieved in a time window of a decade, with siphon linear densities on the order of 100 kg/m. Larger Δv can be obtained for fast-rotators and larger asteroids, as they retain more rotational kinetic energy. However, the asteroid size has a direct impact on the time requirements, i.e., larger asteroids can be deflected with a larger Δv but within a longer time window. Contrary to other siphon applications, here the tether tension is much larger, due to the large mass collected at the top of the siphon. For the test cases considered in this chapter, it is suggested that a Kevlar tether with a cross section of $1\,\mathrm{cm}^2$ can withstand the required tension.

8.5 Chapter 7

In this chapter the use the orbital siphon as a conveyor structure to create an artificial spherical cavity inside an asteroid has been proposed. It is shown that, for a Bennu-like asteroid, with a radius of 256 m and rotation period 4.26 hours, a constant length siphon can be used to raise to escape $1.5 \times 10^9\,\mathrm{kg}$ of asteroid material corresponding to an internal cavity with a diameter of 132 m requiring a siphon with a length of 803 m. The time required to complete the manipulation process depends on the siphon linear density. For example, a siphon with a linear density of $20\,\mathrm{kg\,s^{-1}}$ can lift 10^6 tonnes of asteroid material to escape (corresponding to a 57-meter radius cavity) in approximately 10 years, with instantaneous mass rates smaller than $4\,\mathrm{kg\,s^{-1}}$. Assuming that the internal structure of the asteroid behaves elastically and using the Drucker-Prager yield criterion for geological materials, a closed-form solution for the stress tensor for points inside the asteroid was found. It was shown that the internal cavity is the region most sensitive to structural failure. However, as the internal cavity expands during siphon operation, the conditions for failure are relaxed. The required minimum cohesive strength to avoid failure is then evaluated at the beginning of siphon operation, and it is approximately 4 Pa for a Bennu-like asteroid.

8.6 Summary of findings

A detailed and systematic investigation of the orbital siphon dynamics and its interaction with a rotating asteroid has been undertaken. In particular, it is shown that the orbital siphon can be used to raise mined material from the asteroid surface without need for external work. The radial velocity of the siphon does not diverge but reaches a constant value at steady state, on the order of cm/s for candidate asteroids. It is shown that, at most, 8% of the asteroid mass can be lifted from the asteroid surface using a constant length siphon. For a siphon with a $10\,\mathrm{kg\,m^{-1}}$ linear density, approximately $30 \times 10^3\,\mathrm{t}$ of material can be lifted in one year for a Bennu-like asteroid.

Coriolis forces due to the motion of the chain of masses cause the chain to rotate opposite to the direction of the asteroid rotation. However, it is shown that such oscillations are damped.

This effect is beneficial in a real-case mining scenario, as the horizontal anchor forces are reduced. Furthermore, if a collecting spacecraft is used to collect mass at the top of the siphon, the siphon tends to align with the local vertical.

It is demonstrated that the siphon dynamics can be exploited to transfer payload resources to equilibrium points around the asteroid, that may be used as temporary mass depots for material, waiting to be further processed or stored for later collection. The energy required to send material to these equilibria is smaller than that required for direct transfer from the surface using other methods (e.g., mass drivers), which can be beneficial in a large scale mining scenario. Also, granular dynamics simulations showed that the centrifugal-induced forces acting on the collecting spacecraft can be exploited to sort regolith by size. A preliminary model of sorting tower has been proposed and it is shown that cohesion between the particles may affect the efficiency of the sorting process.

It is shown that a bucket-conveyor siphon can operate without any support structure and also the anchor of the siphon can be moved on the surface of the asteroid without interrupting the siphon effect.

It has been proposed to use the orbital siphon as a novel method for asteroid deflection. By releasing the mass collected at the top of the siphon, the asteroid velocity changes. It is shown that a typical heliocentric velocity variation on the order of $1\,\mathrm{cm\,s^{-1}}$ can be achieved (enough to deflect an asteroid in a circular orbit at 1 Astronomical Unit by 1 Earth radius in 10 years), if the siphon linear density is on the order of $100\,\mathrm{kg\,s^{-1}}$.

Finally, use of the orbital siphon for excavation of a cavity inside the asteroid has been proposed. For a Bennu-like asteroid, a cavity with a diameter up to 132 m, using the siphon to lift to escape the mined material. It is shown that the minimum asteroid cohesive strength to avoid possible disruption of the the cavern is approximately 4 Pa for a Bennu-like asteroid. It is proposed to use the cavity for material storage or, more speculatively, to host a space station.

8.7 Future work

The research presented in this thesis has satisfied the objectives outlined in Chapter 1, by investigating in detail the behaviour of the orbital siphon and discussing possible applications in the context of asteroid manipulation. However, simplifications were often used to allow an easier mathematical treatment of the problem. Moreover, many aspects of the orbital siphon applications were just preliminarily outlined. Therefore, directions for future research are discussed here.

Mining strategies. In Chapter 3 the effects of long-term siphon operation have been discussed assuming that a spherical asteroid is uniformly mined along its entire surface, such that its spherical shape is retained. This choice permitted a significant simplification of the problem and

a closed-form expression for the variation of the asteroid angular velocity as a function of the extracted mass was found. However, in a real scenario, only a fraction of the asteroid surface might be mined, for example only material within a given range from the asteroid anchor, in order to minimize the locomotion of mining rovers transporting material to the siphon. In this case, the variation of the asteroid angular velocity as a function of the extracted mass may be different from that found in Chapter 3 due to fact that the asteroid inertia changes depending on the shape of the mined region. Moreover, it would be interesting to identify the geometry of the mined region that minimizes the loss of asteroid rotational kinetic energy (thus maximizing the extractable mass) or that minimizes the energy required for material transportation, as a function of the power available to the mining units and their number. Ideally, in a scenario where the extractable mass has to be maximised, mining of material in proximity of the poles should be avoided, since transportation of large quantities of mass from the vicinity of the spin axis to the equator would further reduce the rotational kinetic energy of the asteroid. Additionally, use of multiple siphons anchored at different positions along the equator could be considered. This would reduce the energy required by the locomotion units to deliver material to the siphon base. Similarly, in relation to the excavation of internal cavities, another interesting development would be to consider non-spherical cavities, such as cylindrical cavities and examine how this changes the inertia of the asteroid during siphon operation.

Material transfer to the siphon. In general, the problem of transferring material to the siphon base should be carefully considered, since this will influence the mass flow rate of material that can be raised by the siphon (thus impacting on extraction time-scales). Although it was suggested in Chapter 5 that the siphon base could be moved to different surface locations, specific conditions might arise where locomotion of the entire siphon might compromise its stability (e.g., due to large boulders on the surface or other obstacles). Key variables for future analysis would include: number of mining rovers/locomotion units, volume of material that each unit can transport, energy required for moving material from different asteroid locations or to fragment the material if required (for example, in case a large boulder has to be lifted but it does not fit within a siphon bucket) and the maximum velocity of the locomotion units on the asteroid surface.

Orbital siphon at irregularly rotating asteroids. The effect of procession and nutation of the asteroid on the siphon dynamics has not been considered in this thesis, justified by the fact that most asteroids are in a uniform rotational state about the axis of maximum inertia. However, it would be of interest to consider the effect of non-uniform asteroid rotation in the siphon dynamics and verify if the siphon effect is still guaranteed under these conditions. Non-equatorial oscillations will likely arise with non-uniform asteroid rotation, and self-supporting siphons may experience interference between the ascending and descending side of the bucket

conveyor. The use of damping mechanisms at the anchor should be considered to minimize unwanted oscillations.

Granular dynamics simulations. Chapter 5 preliminarily investigated the problem of material release to the collecting spacecraft and material sorting, using DEM simulations. However, results were provided for a few test cases: additional work is required to verify the feasibility of sorting material by considering different geometrical configurations of the sorting tower and using non-spherical particles models. Additionally, further work is required to understand the role of cohesion in granular material flows in microgravity.

DEM simulations can be extensively exploited for other purposes within the context of this thesis. Possible applications include the analysis of the regolith dynamics inside the buckets, and its coupling with the siphon dynamics. Moreover, the problem of filling the buckets at the siphon base should be thoroughly considered using granular simulations. Key aspects of this problem will include the careful examination of the regolith-bucket interaction, while the bucket is moving along with the siphon. The filling process must be optimised in order to avoid any loss of material, by considering different refilling options and bucket shapes. DEM simulations can also be used to investigate the behaviour of large agglomerations of regolith at equilibrium points, expanding the work undertaken in Chapter 4. In particular, it may be interesting to verify the maximum size of a large agglomerate of regolith at an equilibrium point, such that it does not scatter into orbit but it is kept together by self-gravity and cohesive forces. Eventually, in the context of internal asteroid cavities, the entire asteroid could be modelled as a collection of particles and extraction of material from the asteroid interiors would be modelled as a discrete removal spherical particles. DEM simulations can also be used to validate the analytical results obtained in Chapter 7.

Appendix A

Gravitational potential of a constant density ellipsoid

The main steps to obtain the gravitational potential due to an ellipsoidal mass distribution are outlined here. The interested reader is referred to [76] for a exhaustive and comprehensive derivation.

The gravitational potential at a point outside the asteroid can be obtained by first calculating the potential for an *interior* point and then using Ivory's theorem [128] to extend the potential to exterior points. Computation of the potential for interior points is explained here and then the technique to extend it to exterior points is briefly outlined.

Let the surface of the ellipsoid be defined by the equation

$$\frac{\xi^2}{\alpha^2}+\frac{\eta^2}{\beta^2}+\frac{\zeta^2}{\gamma^2}=1. \tag{A.1}$$

Also let $\mathbf{r}=\{x,y,z\}$ be the position vector of a point P interior to the asteroid at which the potential has to be computed and s,ϕ,θ a set of polar coordinates with origin in P, such that:

$$\begin{cases}\xi = x+s\cos\phi\cos\theta\\ \eta = y+s\cos\phi\cos\theta\\ \zeta = z+s\sin\phi\end{cases} \tag{A.2}$$

Then, from the definition of the gravitational potential (Eq. (2.3)):

$$\begin{aligned} V &= -\rho\int\frac{dm}{s}\\ &= -\rho\int_{-\pi/2}^{\pi/2}\int_0^{2\pi}\int_0^{s_1}\cos\phi\, d\theta d\phi ds\end{aligned} \tag{A.3}$$

The upper limit s_1 defines the distance between P and the points on the surface of the ellipsoid,

and it therefore varies with the angles θ, ϕ. The parameter s_1 can then be evaluated by substituting Eqs.(A.2) into Eq. (A.1). Upon substitution and simplification, Eq. (A.2) reduces to a second-degree equation in s_1. The solution of interest is

$$s_1 = \frac{-B + \sqrt{B^2 - AC}}{A} \tag{A.4}$$

where

$$\begin{cases} A = \dfrac{\cos^2\theta\cos^2\phi}{\alpha^2} + \dfrac{\cos^2\theta\cos^2\phi}{\beta^2} + \dfrac{\sin^2\theta}{\gamma^2} \\ B = x\dfrac{\cos^2\theta\cos^2\phi}{\alpha^2} + y\dfrac{\cos^2\theta\cos^2\phi}{\beta^2} + z\dfrac{\sin^2\theta}{\gamma^2} \\ C = \dfrac{x^2}{\alpha^2} + \dfrac{y^2}{\beta^2} + \dfrac{z^2}{\gamma^2} - 1 \end{cases} \tag{A.5}$$

Therefore Eq. (A.3) becomes:

$$V = -\frac{1}{2}\rho \int_{-\pi/2}^{\pi/2}\int_0^{\pi} \frac{2B^2 - AC - 2B\sqrt{B^2 - AC}}{A^2}\cos\theta \; d\theta \; d\phi \tag{A.6}$$

Substituting Eqs. (A.5) into Eq. (A.6) yields:

$$\begin{aligned} V = &-\rho \int_{-\pi/2}^{\pi/2}\int_0^{\pi} \left(\frac{\cos^2\theta\cos^2\phi}{\alpha^2}\frac{x^2}{\alpha^2} + \frac{\cos^2\theta\cos^2\phi}{\beta^2}\frac{y^2}{\beta^2} + \frac{\sin^2\theta}{\gamma^2}\frac{z^2}{\gamma^2} \right) \frac{\cos\theta}{A^2} d\theta d\phi \\ &+ \frac{1}{2}\rho C \int_{-\pi/2}^{\pi/2}\int_0^{\pi} \frac{\cos\theta}{A} d\theta d\phi \end{aligned} \tag{A.7}$$

By defining:

$$V_0 = \frac{1}{2}\rho \int_{-\pi/2}^{\pi/2}\int_0^{\pi} \frac{\cos\theta}{A} d\theta d\phi \tag{A.8}$$

then V can be rewritten as

$$V = \frac{1}{\alpha}\frac{\partial F}{\partial \alpha}x^2 + \frac{1}{\beta}\frac{\partial F}{\partial \beta}y^2 + \frac{1}{\gamma}\frac{\partial F}{\partial \alpha}z^2 - CV_0 \tag{A.9}$$

Note that by substituting $x = y = z = 0$ into Eq. (A.9) yields, $V = V_0$, i.e., V_0 represents the potential at the center of the asteroid. Equation Eq. (A.8) can then be further manipulated and simplified

$$V_0 = \pi\alpha\beta\gamma \int_0^{\infty} \frac{ds}{\sqrt{(\alpha^2 + s)^2 + (\beta^2 + s)^2 + (\gamma^2 + s)^2}} \tag{A.10}$$

such that the potential V finally becomes:

$$V = \frac{3\mu}{4}\int_0^{\infty} \Theta(x, y, z, s)\frac{ds}{\Delta(s)} \tag{A.11}$$

with

$$\Theta(x,y,z,s) = \frac{x^2}{\alpha^2+s} + \frac{y^2}{\beta^2+s} + \frac{z^2}{\gamma^2+s} - 1 \tag{A.12}$$

$$\Delta(s) = \sqrt{(\alpha^2+s)^2 + (\beta^2+s)^2 + (\gamma^2+s^2)} \tag{A.13}$$

and $\mu = 4/3\rho\pi\alpha\beta\gamma$ is the gravitational parameter. Equation (A.11) represents the potential at a point at the interior of the asteroid. If the point P is exterior to the asteroid, the potential can then be obtained using Ivory's theorem. The idea is to consider an ellipsoid confocal to the original ellipsoid passing through the point where the potential is evaluated. A one-to-one correspondence between the two ellipsoids can then be defined such that the potential at the exterior of the body can be written as:

$$V = \frac{3\mu}{4}\int_{\kappa}^{\infty} \Theta(x,y,z,s)\frac{ds}{\Delta(s)} \tag{A.14}$$

where κ is the largest root of the equation:

$$\Theta(x,y,z,\kappa) = 0 \tag{A.15}$$

and depends on the point where the potential is evaluated.

The partial derivative of the potential can then be computed by applying Leibniz's rule. For example, the derivative with respect to x:

$$V_x = \frac{3\mu x}{4}\int_{\kappa}^{\infty} \frac{ds}{(\alpha^2+s)\Delta(s)} - \frac{3\mu}{4}\Theta(x,y,z,\kappa)\frac{\kappa_x}{\Delta(\kappa)} \tag{A.16}$$

however note that $\Theta(x,y,z,\kappa) = 0$ by definition, and therefore the derivatives become:

$$V_x = \frac{3\mu x}{4}\int_{\kappa}^{\infty} \frac{ds}{(\alpha^2+s)\Delta(s)} \tag{A.17}$$

$$V_y = \frac{3\mu y}{4}\int_{\kappa}^{\infty} \frac{ds}{(\beta^2+s)\Delta(s)} \tag{A.18}$$

$$V_z = \frac{3\mu z}{4}\int_{\kappa}^{\infty} \frac{ds}{(\gamma^2+s)\Delta(s)} \tag{A.19}$$

Appendix B

Gravitational potential of a constant density polyhedron

The gravitational potential of a constant-density polyhedron (Eq. (2.20)) derived here, highlighting the main steps in the derivation presented by Werner and Scheeres [155]. For a more detailed insight, the reader is referred to the cited paper.

Recall the definition of the gravitational potential given by Eq. (2.3) and let $\mathbf{s} = \mathbf{r} - \tilde{\mathbf{r}}$ be a vector from the field point $\mathbf{r}$ to a point on the mass distribution $\tilde{\mathbf{r}}$. Using the identity

$$\operatorname{div}\left(\frac{1}{2}\hat{\mathbf{s}}\right) = \frac{1}{s} \tag{B.1}$$

where $\hat{\mathbf{s}} = \mathbf{s}/s$ and $s = |\mathbf{s}|$ and using the divergence theorem, Eq. (2.3) can be rewritten as

$$\begin{aligned} V &= -\frac{1}{2}G\rho \iiint_{\mathscr{V}} \operatorname{div} \hat{\mathbf{s}}\, dV \\ &= -\frac{1}{2}G\rho \iint_{S} \hat{\mathbf{n}} \cdot \hat{\mathbf{s}}\, dS \end{aligned} \tag{B.2}$$

where S is the boundary of the region $\mathscr{V}$ and $\hat{\mathbf{n}}$ is the normal to the surface S. Hence, thanks to the divergence theorem, the integral over the volume of the mass distribution is substituted by an integral over the boundary of the volume. Now, for the case of a polyhedron, the integral can be expressed as a sum of integrals over the faces of the polyhedron, such that:

$$\begin{aligned} V &= -\frac{1}{2}G\rho \sum_{f \in \text{faces}} \iint_{f} \hat{\mathbf{n}}_f \cdot \hat{\mathbf{s}}\, dS \\ &= -\frac{1}{2}G\rho \sum_{f \in \text{faces}} \iint_{f} \hat{\mathbf{n}}_f \cdot \frac{\mathbf{s}}{s}\, dS \end{aligned} \tag{B.3}$$

where $\hat{\mathbf{n}}_f$ is the normal to the face f. Now define a triad of unit vectors, $\hat{\mathbf{i}}, \hat{\mathbf{j}}, \hat{\mathbf{k}}$, such that $\hat{\mathbf{k}}$ is aligned with $\hat{\mathbf{n}}_f$ and the direction of the two remaining unit vectors is not relevant. Let $\mathbf{s} =$

$\Delta x\hat{\mathbf{i}} + \Delta y\hat{\mathbf{j}} + \Delta z\hat{\mathbf{k}}$. Then, the product $\hat{\mathbf{n}}_f \cdot \mathbf{s}$ is constant over the face and equal to Δz. Therefore, it can be taken out of the integral:

$$V = -\frac{1}{2}G\rho \sum_{f\in\text{faces}} \hat{\mathbf{n}}_f \cdot \mathbf{s}_f \iint_f \frac{1}{r} dS \tag{B.4}$$

where $\mathbf{s}_f$ is the position vector from the field point to any point on the face (recall that any point can be selected, where $\hat{\mathbf{n}}_f \cdot \mathbf{s}$ is constant, for example a point on the edge).

The integral $\iint dS/s$ can then be written as:

$$\begin{aligned} \iint_S \frac{1}{s} &= \iint_S \left(\frac{1}{s} + \frac{\Delta z^2}{s^3}\right) - \iint_S \frac{\Delta z^2}{s^3} \\ &= \iint_S \left(\frac{s^2 - \Delta x^2}{s} + \frac{s^2 - \Delta y^2}{s}\right) dS - \Delta z \iint_S \frac{\Delta z}{s^3} \end{aligned} \tag{B.5}$$

Using Green's theorem and noting that $\hat{\mathbf{n}}_f \cdot \mathbf{s}_f = \Delta z$:

$$\begin{aligned} \iint_S \frac{1}{s} &= \iint_S \left(\frac{\partial}{\partial \Delta x}\frac{\Delta x}{s} + \frac{\partial}{\partial \Delta y}\frac{\Delta y}{s}\right) dS - \hat{\mathbf{n}}_f \cdot \mathbf{s}_f \gamma_f \\ &= \oint_C \frac{1}{s}\left(\Delta x d\Delta y - \Delta y d\Delta x\right) - \hat{\mathbf{n}}_f \cdot \mathbf{s}_f \gamma_f \end{aligned} \tag{B.6}$$

where C is the boundary of the face and $\gamma_f = \Delta z \iint_S \Delta z/s^3$ is the solid angle subtended by the planar region S when viewed from the field point. The parameter γ_f can be written as a function of the distances between the field point and the vertexes of the face, as indicated by Eq. (2.26) (see [155], Section 2.5 for the proof.)

Consider the first term in the sum. Being an integral over each contour on each face, it can be written as a sum of integrals over each edge e

$$\oint_C \frac{1}{s}\left(\Delta x d\Delta y - \Delta y d\Delta x\right) = \sum_{e\in\text{face's edges}} \int_e \frac{1}{s}\left(\Delta x d\Delta y - \Delta y d\Delta x\right) \tag{B.7}$$

The coordinates $(\Delta x, \Delta y)$ of a point on the edge can be written as $(\Delta x_e + \sigma\cos\alpha_e, \Delta y_e + \sigma\sin\alpha_e)$, where Δx_e and Δy_e are the coordinates of a fixed point along the edge, σ is the distance from such a fixed point and α_e is the angle between the edge and the face $\hat{\mathbf{i}}$ axis, such that $\sin\alpha_e = \hat{\mathbf{n}}_e^f \cdot \hat{\mathbf{i}}$. The unit vector $\hat{\mathbf{n}}_e^f$ is the normal to the edge e and the face f. With these substitutions:

$$\begin{aligned} \sum_{e\in\text{face's edges}} \int_e \frac{1}{s}\left(\Delta x d\Delta y - \Delta y d\Delta x\right) &= \sum_{e\in\text{face's edges}} \left(\Delta x_e \sin\alpha_e - \Delta y_e \cos\alpha_e\right) \int_e \frac{1}{s} ds \\ &= \sum_{e\in\text{face's edges}} \hat{\mathbf{n}}_e^f \cdot \hat{\mathbf{r}}_e^f \int_e \frac{1}{s} d\sigma \end{aligned} \tag{B.8}$$

where $\hat{\mathbf{r}}_e^f$ is the vector from the field point to the fixed point on the edge e of face f. The

integral $\int_e 1/s d\sigma$ is the potential of a straight one-dimensional wire and its value is known from MacMillan [76]:

$$L_e^f = \int_e \frac{1}{s} d\sigma = \ln \frac{a+b+e_e}{a+b-e_e} \tag{B.9}$$

where a and b are the distances from the field point to the two edges and e_e is the length of the edge. Therefore, summing up:

$$\iint_S \frac{1}{s} dS = \sum_{e \in \text{face's edges}} L_e^f \hat{\mathbf{n}}_e^f \cdot \mathbf{s}_e^f - \gamma_f \hat{\mathbf{n}}_f \cdot \mathbf{s}_f \tag{B.10}$$

and, substituting back into Eq. (B.4):

$$\begin{aligned} V &= -\frac{1}{2} G\rho \sum_{f \in \text{faces}} \hat{\mathbf{n}}_f \cdot \mathbf{s}_f \iint_f \frac{1}{s} dS \\ &= -\frac{1}{2} G\rho \sum_{f \in \text{faces}} \hat{\mathbf{n}}_f \cdot \mathbf{s}_f \left[\left(\sum_{e \in \text{face's edges}} L_e^f \hat{\mathbf{n}}_e^f \cdot \mathbf{s}_e^f - \gamma_f \hat{\mathbf{n}}_f \cdot \mathbf{s}_f \right) - \gamma_f \hat{\mathbf{n}}_f \cdot \mathbf{s}_f \right] \end{aligned} \tag{B.11}$$

After some algebraic manipulation involving simplifications over common edges of two different faces (see [155] pages 322 - 325), Eq. (B.11) can be further reduced to:

$$V = -\frac{1}{2} G\rho \left(\sum_{e \in \text{edges}} L_e \mathbf{s}_e \cdot \mathbf{E}_e \mathbf{s}_e - \sum_{f \in \text{faces}} \gamma_f \mathbf{s}_f \cdot \mathbf{F}_f \mathbf{s}_f \right) \tag{B.12}$$

where $\mathbf{E}_e = \hat{\mathbf{n}}_f \hat{\mathbf{n}}_e^f + \hat{\mathbf{n}}_{f'} \hat{\mathbf{n}}_e^{f'}$, and where f, f' are the two faces associated with the edge e, $\hat{\mathbf{n}}_f$, $\hat{\mathbf{n}}_{f'}$ are the two normals to that face and $\hat{\mathbf{n}}_e^f$, $\hat{\mathbf{n}}_{f'}$ are the normal to the edge and parallel to the faces f and f' respectively. The dyad $\mathbf{F}_f$ is defined for each face as the product $\mathbf{F}_f = \hat{\mathbf{n}}_f \hat{\mathbf{n}}_f$.

Appendix C

Carlson elliptic integrals

The gravitational potential for a constant density homogeneous ellipsoid (Eq. (2.14)) can be re-written as:

$$V = \frac{3\mu}{4}\int_0^\infty \left[\frac{x^2}{\alpha^2+\kappa+s}+\frac{x^2}{\beta^2+\kappa+s}+\frac{x^2}{\gamma^2+\kappa+s}\right]\frac{ds}{\Delta(\kappa+s)} \tag{C.1}$$

with $\Delta(\kappa+s)$ is defined according to Eq. (2.15). The required Carlson's elliptic integrals are R_F and R_D, defined as [22]:

$$R_F(x,y,z) = \frac{1}{2}\int_0^\infty \frac{ds}{\sqrt{(x+s)(y+s)(z+s)}} \tag{C.2}$$

$$R_D(x,y,z) = \frac{3}{2}\int_0^\infty \frac{ds}{(z+s)\sqrt{(x+s)(y+s)(z+s)}} \tag{C.3}$$

Then, the potential V can be written as a function of the elliptic integrals R_F and R_D:

$$\begin{aligned} V = &\frac{1}{2}\mu x^2 R_D(\beta^2+\kappa,\gamma^2+\kappa,\alpha^2+\kappa)+\frac{1}{2}\mu y^2 R_D(\gamma^2+\kappa,\alpha^2+\kappa,\beta^2+\kappa) \\ &+\frac{1}{2}\mu z^2 R_D(\alpha^2+\kappa,\beta^2+\kappa,\gamma^2+\kappa)-\frac{3}{2}\mu R_F(\alpha^2+\kappa,\beta^2+\kappa,\gamma^2+\kappa) \end{aligned} \tag{C.4}$$

Similarly, the potential derivatives can be written as:

$$V_x = xR_D(\beta^2+\kappa,\gamma^2+\kappa,\alpha^2+\kappa) \tag{C.5a}$$

$$V_y = yR_D(\gamma^2+\kappa,\alpha^2+\kappa,\beta^2+\kappa) \tag{C.5b}$$

$$V_z = zR_D(\alpha^2+\kappa,\beta^2+\kappa,\gamma^2+\kappa) \tag{C.5c}$$

The algorithms for computing the functions R_F and R_D can be found in Ref. [103].

Appendix D

Impact condition for released material

Let $v_\perp$ and v_r be the radial and tangential velocities at release respectively. Then $v_\perp = \bar{\omega}R$ and v_r is given (in its normalized form) from Eq. (3.43). If material is released into an orbit with eccentricity e and semi-major axis a then:

$$\mathscr{E} = -\frac{GM}{2a} = \frac{v_\perp^2 + v_r^2}{2} - \frac{GM}{R+L} < 0 \tag{D.1}$$

where $\mathscr{E}$ is the (constant) specific energy of the orbit and a its semi-major axis. At the periapsis r_p:

$$\mathscr{E} = \frac{h^2}{2r_p^2} - \frac{GM}{r_p} \tag{D.2}$$

where $h = v_p r_p$ is the angular momentum per unit mass of the orbit and v_p is the velocity at the periapsis. Since $r_p = \frac{h^2}{GM}\frac{1}{1+e}$ [136], Eq. (D.2) becomes:

$$\mathscr{E} = -\frac{1}{2}\frac{(GM)^2}{h^2}(1-e^2). \tag{D.3}$$

The angular momentum per unit mass is also equal to the product $h = v_\perp(R+d)$, hence Eq. (D.3) can be written as:

$$\mathscr{E} = -\frac{1}{2}\frac{(GM)^2}{v_\perp^2(R+L)^2}(1-e^2). \tag{D.4}$$

Moreover, the periapsis r_p of the orbit can be expressed as a function of the semi-major axis and the eccentricity:

$$r_p = a(1-e). \tag{D.5}$$

Solving Eq. (D.1) and (D.4) for a and e respectively and substituting into Eq. (D.5) yields, after simplifications:

$$\bar{r}_p = -\frac{\bar{R}}{2\bar{\mathscr{E}}}\sqrt{1 + 2\bar{\mathscr{E}}\bar{\omega}^2(1+\bar{L})^4} \tag{D.6}$$

where the non-dimensional scale factors are those listed in Table 3.1. Then, if $\bar{r}_p \leq 1$ material will impact the asteroid.

Appendix E

Modelling payload refilling

The radial velocity of the chain after the top payload is released and a new one is connected at the surface bucket is calculated, modelling the refilling event as an inelastic collision.

Figure E.1 shows the chain configuration before (a) and after (b) the refilling event, for a chain with $n = 4$. The absolute velocity of each mass on the siphon before (superscript I) and after (superscript II) the refilling event is:

$$\bar{\mathbf{v}}_i^{\mathrm{I}} = \dot{s}^{\mathrm{I}}\hat{\mathbf{u}}_r + \bar{\boldsymbol{\omega}} \times \bar{\mathbf{r}}_i \tag{E.1a}$$

$$\bar{\mathbf{v}}_i^{\mathrm{II}} = \dot{s}^{\mathrm{II}}\hat{\mathbf{u}}_r + \bar{\boldsymbol{\omega}} \times \bar{\mathbf{r}}_i \tag{E.1b}$$

where $\mathbf{r}_i$ is the distance between the i-th mass and the centre of the asteroid. Similarly, the absolute velocity of the waiting payload (wp) and the released payload (rp) are

$$\bar{\mathbf{v}}_{wp} = \bar{\boldsymbol{\omega}} \times \bar{\mathbf{r}}_{wp} \tag{E.2a}$$

$$\bar{\mathbf{v}}_{rp} = \dot{s}^{\mathrm{I}}\hat{\mathbf{u}}_r + \bar{\boldsymbol{\omega}} \times \bar{\mathbf{r}}_{rp} \tag{E.2b}$$

where it is assumed that the waiting payload is at rest on the asteroid surface. Then, conservation

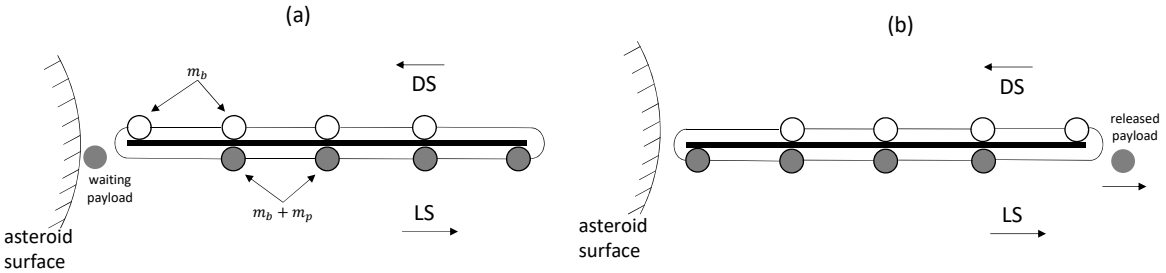

FIGURE E.1: Chain with $n = 4$ before (a) and after (b) the surface bucket is refilled with a payload.

of linear momentum dictates:

$$\bar{m}_{wp}\bar{\mathbf{v}}_{wp} + \sum_{i=1}^{2n} \bar{m}_i \bar{\mathbf{v}}_i^{\mathrm{I}} = \bar{m}_{rp}\bar{\mathbf{v}}_{rp} + \sum_{i=1}^{2n} \bar{m}_i \bar{\mathbf{v}}_i^{\mathrm{II}} \tag{E.3}$$

where the masses of the waiting payload and released payload are the same $\bar{m}_{wp} = \bar{m}_{rp} = \bar{m}_p$, whereas $\bar{m}_i = \bar{m}_b + \bar{m}_p$ for a mass on the LS and $\bar{m}_i = \bar{m}_b$. Substituting Eqs. (E.1a) and (E.2a) into Eq. (E.3), performing a scalar product with $\hat{\mathbf{u}}_r$ on both sides and using non-dimensional variables yields:

$$n\dot{s}^{\mathrm{I}} + Dn\dot{s}^{\mathrm{I}} = n\dot{s}^{\mathrm{II}} + (1-D)\dot{s}\mathrm{I} + nD\dot{s}^{\mathrm{II}} \tag{E.4}$$

Then, further simplifying:

$$\dot{s}^{\mathrm{II}} = \frac{n-1}{n}\dot{s}^{\mathrm{I}} \tag{E.5}$$

Note that the result is independent of the mass ratio D.

Appendix F

Conservation of angular momentum

- Step $1 \rightarrow 2$ (Eq. (7.11a)). Substituting Eqs.(7.9) and (7.10) into Eq. (7.11a) and collecting MR^2 on both sides yields:

$$\frac{2}{5}\frac{1-\bar{r}^5}{1-\bar{r}^3}+\frac{\delta M}{M}\sum_{i=1}^{n}\bar{x}_i^2=\left[\frac{2}{5}\frac{1-\bar{r}^5}{1-\bar{r}^3}+\frac{\delta M}{M}\sum_{i=1}^{n}(\bar{l}+\bar{x}_i)^2\right]\left(1-\frac{\delta\omega}{\omega}\right) \tag{F.1}$$

From $M=4/3\rho\pi(R^3-r^3)$, it follows by differentiation:

$$\frac{\delta M}{M}=3\frac{\bar{r}^3}{1-\bar{r}^3}\frac{\delta\bar{r}}{\bar{r}} \tag{F.2}$$

Substituting Eq. (F.2) into (F.1), neglecting higher order terms and further simplifying yields:

$$\frac{\delta\omega_{12}}{\omega_1}=5\frac{\bar{r}^5}{1-\bar{r}^5}\left[\frac{3}{2}\left(1+\frac{n\bar{l}}{\bar{r}}\right)^2-\frac{1}{2}\right]\frac{\delta\bar{r}}{\bar{r}} \tag{F.3}$$

Assuming that the number of payloads is larger the term $n\bar{l}$ effectively represents the total length $\bar{L}$ of the siphon:

$$\frac{\delta\omega_{12}}{\omega_1}=5\frac{\bar{r}^5}{1-\bar{r}^5}\left[\frac{3}{2}\left(1+\frac{\bar{L}}{\bar{r}}\right)^2-\frac{1}{2}\right]\frac{\delta\bar{r}}{\bar{r}} \tag{F.4}$$

- Step $2 \rightarrow 3$ (Eq. (7.11b)). Substituting Eqs. (7.9) and (7.10) into Eq. (7.11b) and collecting MR^2 on both sides yields:

$$\frac{2}{5}\frac{1-\bar{r}^5}{1-\bar{r}^3}+\frac{\delta M}{M}\sum_{i=1}^{n}\bar{x}_i^2=\left[\frac{2}{5}\left(1-\frac{\delta M}{M}\frac{1-\bar{r}^5\left(1+\frac{\delta\bar{r}}{\bar{r}}\right)^5}{1-\bar{r}^3\left(1+\frac{\delta\bar{r}}{\bar{r}}\right)^3}\right)+\frac{\delta M}{M}\sum_{i=1}^{n+1}(\delta\bar{r}+\bar{x}_i)^2\right]\left(1-\frac{\delta\omega}{\omega}\right) \tag{F.5}$$

Under the assumption $\delta\bar{r}/\bar{r} << 0$ it follows that

$$\frac{1-\bar{r}^5\left(1+\frac{\delta\bar{r}}{\bar{r}}\right)^5}{1-\bar{r}^3\left(1+\frac{\delta\bar{r}}{\bar{r}}\right)^3} = \frac{1-\bar{r}^5}{1-\bar{r}^3}\left[1+\left(3\frac{\bar{r}^3}{1-\bar{r}^3}-5\frac{\bar{r}^5}{1-\bar{r}^5}\right)\frac{\delta\bar{r}}{\bar{r}}\right]+o\left(\frac{\delta\bar{r}}{\bar{r}}\right) \tag{F.6}$$

Substituting Eqs.(F.2), (F.6) into Eq.(F.5), neglecting the higher order terms and further simplifying yields:

$$\frac{\delta\omega_{23}}{\omega_1} = -\frac{5}{2}\frac{\bar{r}^5}{1-\bar{r}^5}\frac{\delta\bar{r}}{\bar{r}} \tag{F.7}$$

- Step $3 \rightarrow 4$ (Eq. (7.11c)). The results follows immediately noting that $I_{A,3} = I_{A,4}$ and $I_{C,4} = I_{C,3} - \delta M(\bar{r}+(n-1)\bar{l})^2$:

$$\frac{\delta\omega_{34}}{\omega_1} = 0 \tag{F.8}$$

Appendix G

Stress tensor

Substituting the potentials $\Gamma = \Gamma_p + \Gamma_h$ (Eqs. (7.25) (7.26)) and ψ (Eq. (7.27)) into Eqs. (7.21) yields (note that all variables here are non-dimensional although the upper bar notation is removed to improve the readability):

$$\begin{aligned}\sigma_{\varrho\varrho} =& \frac{1}{560(\nu-1)\,\varrho^5}\left\{20\cos(2\Theta)\left\{\varrho^2\left[\varrho^3\left(42A_1(\nu-1)+\varrho^2\left(105A_4(\nu-1)+42B_3(\nu-1)\nu+(5\nu-6)\omega^2\right)\right.\right.\right.\right.\\ &\left.\left.\left.\left.+28B_1\left(2\nu^2-3\nu+1\right)\right)-28B_2\left(\nu^2-6\nu+5\right)\right]+252A_2(\nu-1)\right\}\\ &+280A_1\nu\,\varrho^5-280A_1\,\varrho^5+1680A_2\nu-1680A_2+1120A_3\nu\,\varrho^2-1120A_3\,\varrho^2+\\ &+525(\nu-1)\,\varrho^7\cos(4\Theta)(7A_4+4B_3\nu)+945A_4\nu\,\varrho^7-945A_4\,\varrho^7-560b^3\nu\,\varrho^4-560B_1\nu\,\varrho^5+560B_1\,\varrho^5\\ &-1680B_2\nu^2\,\varrho^2+4480B_2\nu\,\varrho^2-2800B_2\,\varrho^2+420B_3\nu^2\,\varrho^7-420B_3\nu\,\varrho^7-4\nu\,\varrho^7\,\omega^2+56\nu\,\varrho^7\\ &+72\,\varrho^7\,\omega^2-168\,\varrho^7\Big\}\end{aligned} \tag{G.1}$$

$$\begin{aligned}\sigma_{\phi\phi} =& \frac{1}{140(\nu-1)\,\varrho^5}\left\{\varrho^2\left\{\varrho^2\left[\varrho\left(-140A_1(\nu-1)+\varrho^2\left(-315A_4(\nu-1)-210B_3\left(\nu^2-1\right)+13\nu\omega^2\right.\right.\right.\right.\right.\\ &\left.\left.\left.\left.\left.-42\nu+11\omega^2-14\right)-280B_1(\nu-1)\nu\right)-70b^3\right]-140A_3(\nu-1)+70B_2\left(2\nu^2-5\nu+3\right)\right\}\\ &-5\cos(2\Theta)\left(105A_2(\nu-1)+\varrho^2\left(\varrho^5\left(105A_4(\nu-1)+42B_3\left(3\nu^2-2\nu-1\right)+(5\nu+1)\omega^2\right)\right.\right.\\ &\left.\left.-42B_2\left(2\nu^2-3\nu+1\right)\right)\right)-315A_2(\nu-1)\Big\}\end{aligned} \tag{G.2}$$

$$\begin{aligned}\sigma_{\Theta\Theta} =& -\frac{1}{560(\nu-1)\,\varrho^5}\left\{140\cos(2\Theta)\left(\varrho^2\left(\varrho^3\left(6A_1(\nu-1)+4B_1\left(2\nu^2-3\nu+1\right)+\varrho^2\left(6B_3\left(\nu^2+\nu-2\right)+\nu\omega^2\right)\right)\right.\right.\right.\\ &\left.\left.\left.+B_2\left(-4\nu^2+6\nu-2\right)\right)+21A_2(\nu-1)\right)-280A_1\nu\,\varrho^5+280A_1\,\varrho^5+420A_2\nu-420A_2+560A_3\nu\,\varrho^2\\ &-560A_3\,\varrho^2+525(\nu-1)\,\varrho^7\cos(4\Theta)(7A_4+4B_3\nu)-315A_4\nu\,\varrho^7+315A_4\,\varrho^7+280b^3\,\varrho^4+560B_1\nu\,\varrho^5\\ &-560B_1\,\varrho^5-1680B_2\nu^2\,\varrho^2+3080B_2\nu\,\varrho^2-1400B_2\,\varrho^2+420B_3\nu^2\,\varrho^7-420B_3\nu\,\varrho^7-92\nu\,\varrho^7\,\omega^2\\ &+168\nu\,\varrho^7-24\,\varrho^7\,\omega^2+56\,\varrho^7\Big\}\end{aligned} \tag{G.3}$$

$$\begin{aligned}\sigma_{\Theta\varrho} = \frac{1}{28(\nu-1)\,\varrho^5}\Big\{&\sin(\Theta)\cos(\Theta)\Big(\varrho^2\Big(\varrho^3\Big(-84A_1(\nu-1)+3\,\varrho^2\,(-35A_4(\nu-1)-28B_3\\&\left(\nu^2-1\right)+2(1-2\nu)\omega^2\right)-56B_1\left(2\nu^2-3\nu+1\right)\Big)+56B_2\left(\nu^2-1\right)\Big)\\&+336A_2(\nu-1)-105(\nu-1)\,\varrho^7\cos(2\Theta)(7A_4+4B_3\nu)\Big)\Big\}\end{aligned} \tag{G.4}$$

The boundary conditions (Eq. (7.24)) can be written as:

$$\sigma_{\varrho\varrho}(\varrho = b) = 0 \tag{G.5a}$$

$$\sigma_{\varrho\varrho}(\varrho = 1) = 0 \tag{G.5b}$$

$$\sigma_{\Theta\varrho}(\varrho = b) = 0 \tag{G.5c}$$

$$\sigma_{\Theta\varrho}(\varrho = 1) = 0 \tag{G.5d}$$

Equations (G.5) can then be written as the following set of linearly independent equations (these are obtained upon substitution of Eqs. (G.1), (G.2), (G.3), (G.4) into Eq. (G.5) and then equating the coefficients of the trigonometric terms to zero):

$$\begin{cases}
\begin{aligned}&280A_1(\nu-1)+1680A_2(\nu-1)+1120A_3(\nu-1)+945A_4(\nu-1)-560B_1(\nu-1)\\&-560B_2\left(3\nu^2-8\nu+5\right)+420B_3(\nu-1)\nu-4\left(\nu\left(140r^3+\omega^2-14\right)-18\omega^2+42\right)\end{aligned} & = 0\\[2ex]
\begin{aligned}&+280A_1(\nu-1)r^5+1680A_2(\nu-1)+1120A_3(\nu-1)r^2+945A_4(\nu-1)r^7-560B_1(\nu-1)r^5\\&-560B_2\left(3\nu^2-8\nu+5\right)r^2+420B_3(\nu-1)\nu r^7-4r^7\left(\nu\left(\omega^2+126\right)-18\omega^2+42\right)\end{aligned} & = 0\\[2ex]
\begin{aligned}&42A_1(\nu-1)+252A_2(\nu-1)+105A_4(\nu-1)+28B_1\left(2\nu^2-3\nu+1\right)\\&-28B_2\left(\nu^2-6\nu+5\right)+42B_3(\nu-1)\nu+(5\nu-6)\omega^2\end{aligned} & = 0\\[2ex]
\begin{aligned}&42A_1(\nu-1)r^5+252A_2(\nu-1)+105A_4(\nu-1)r^7++42B_3(\nu-1)\nu r^7+\\&28B_1\left(2\nu^2-3\nu+1\right)r^5-28B_2\left(\nu^2-6\nu+5\right)r^2+(5\nu-6)r^7\omega^2\end{aligned} & = 0\\[2ex]
\begin{aligned}&-84A_1(\nu-1)+336A_2(\nu-1)-105A_4(\nu-1)-56B_1\left(2\nu^2-3\nu+1\right)\\&+56B_2\left(\nu^2-1\right)-84B_3\left(\nu^2-1\right)+6(1-2\nu)\omega^2\end{aligned} & = 0\\[2ex]
\begin{aligned}&336A_2(\nu-1)-105A_4(\nu-1)r^7-84A_1(\nu-1)r^5-84B_3\left(\nu^2-1\right)r^7\\&-56B_1\left(2\nu^2-3\nu+1\right)r^5+56B_2\left(\nu^2-1\right)r^2+6(1-2\nu)r^7\omega^2\end{aligned} & = 0\\[2ex]
7A_4+4B_3\nu & = 0
\end{cases} \tag{G.6}$$

Solving the system of equations (G.6) for A_1, A_2, A_3, A_4, B_1, B_2, B_3, substituting the results into Eqs. (G.1), (G.2), (G.3), (G.4) and further simplifying yields (this computation can be easily performed

with a symbolic algebra software, e.g., Mathematica):

$$
\begin{aligned}
\sigma_{\varrho\varrho} = & \frac{-10\left(\varrho^2-1\right)\nu b^6+3\left(\varrho^3-1\right)c_{60}b^5+\left(-3\,\varrho^5+\left(\varrho^2\left(\varrho^3-10\,\varrho+10\right)-1\right)\nu+3\right)b^3-\varrho^3\left(\varrho^2-1\right)c_{59}}{10\,\varrho^3\,c_{53}c_{65}} \\
& + \frac{1}{10\,\varrho^5\,c_{53}c_{64}c_{66}c_{69}}\Big\{\omega^2\left(-c_{31}\,\varrho^5+c_{33}\,\varrho^2+30c_{29}\right)b^{13} \\
& \quad -2\omega^2\left(c_{31}\,\varrho^5-c_{33}\,\varrho^2-30c_{29}\right)b^{12} \\
& \quad +\omega^2\left(c_{31}\,\varrho^7-3c_{31}\,\varrho^5+c_{32}\,\varrho^2+60c_{29}\right)b^{11} \\
& \quad -\omega^2\left(c_{39}\,\varrho^7+3c_{40}\,\varrho^5+c_{37}\,\varrho^2-30c_{29}\right)b^{10} \\
& \quad -3\,\varrho^2\,\omega^2\left(-c_{31}\,\varrho^5+5c_{34}\,\varrho^3+56c_{59}\right)b^9 \\
& \quad -2\omega^2\left(c_{38}\,\varrho^7+c_{35}\,\varrho^5+15c_{29}\right)b^8 \\
& \quad +\omega^2\left(c_{41}\,\varrho^7-c_{31}\,\varrho^5+168c_{59}\,\varrho^2-60c_{29}\right)b^7 \\
& \quad +\omega^2\left(6c_{36}\,\varrho^7+c_{31}\,\varrho^5+c_{37}\,\varrho^2-60c_{29}\right)b^6 \\
& \quad -2\omega^2\left(3c_{36}\,\varrho^7-c_{35}\,\varrho^5+c_{33}\,\varrho^2+15c_{29}\right)b^5 \\
& \quad +\varrho^2\,\omega^2\left(-c_{41}\,\varrho^5+15c_{34}\,\varrho^3-c_{32}\right)b^4 \\
& \quad +\varrho^2\,\omega^2\left(2c_{38}\,\varrho^5+3c_{40}\,\varrho^3-c_{33}\right)b^3 \\
& \quad -3\,\varrho^5\left(\varrho^2-1\right)\omega^2 c_{31}b^2 \\
& \quad -2\,\varrho^5\left(\varrho^2-1\right)\omega^2 c_{31}b \\
& \quad -\varrho^5\left(\varrho^2-1\right)\omega^2 c_{31} \\
& \quad -5(b-\varrho)(\varrho-1)\omega^2\cos(2\beta)\left[\left(-c_{16}\,\varrho^4-c_{16}\,\varrho^3-c_{16}\,\varrho^2+18c_{29}\,\varrho+18c_{29}\right)b^9\right. \\
& \qquad +(\varrho+2)\left(-c_{16}\,\varrho^4-c_{16}\,\varrho^3-c_{16}\,\varrho^2+18c_{29}\,\varrho+18c_{29}\right)b^8 \\
& \qquad +\left(-2c_{16}\,\varrho^5-5c_{16}\,\varrho^4+10c_{42}\,\varrho^3+10c_1\,\varrho^2+72c_{29}\,\varrho+36c_{29}\right)b^7 \\
& \qquad +\left(-3c_{16}\,\varrho^5+6c_2\,\varrho^4+c_7\,\varrho^3+2c_6\,\varrho^2+72c_{29}\,\varrho+36c_{29}\right)b^6 \\
& \qquad +\left(c_4\,\varrho^5+6c_3\,\varrho^4+4c_5\,\varrho^3+2c_6\,\varrho^2+72c_{29}\,\varrho+36c_{29}\right)b^5 \\
& \qquad +\left(15c_8\,\varrho^5+6c_3\,\varrho^4+c_7\,\varrho^3+10c_1\,\varrho^2+54c_{29}\,\varrho+18c_{29}\right)b^4 \\
& \qquad +\varrho\left(c_4\,\varrho^4+6c_2\,\varrho^3+10c_{42}\,\varrho^2+2c_3\,\varrho+18c_{29}\right)b^3 \\
& \qquad -\varrho^2\left(3\,\varrho^3+5\,\varrho^2+3\,\varrho+1\right)c_{16}b^2 \\
& \qquad -\varrho^3\left(2\,\varrho^2+3\,\varrho+1\right)c_{16}b \\
& \qquad \left.-\varrho^4\left(\varrho+1\right)c_{16}\right]c_{65}\Big\}
\end{aligned}
\tag{G.7}
$$

$$\sigma_{\Theta\Theta} = \frac{-10\left(\varrho^2+\nu\right)b^6+3\left(2\,\varrho^3+1\right)c_{60}b^5+\left(c_{59}-2\,\varrho^2\left(3\nu\,\varrho^3+\varrho^3+10\nu\,\varrho-5\right)\right)b^3+2\,\varrho^3\left(c_{60}\,\varrho^2+c_{59}\right)}{20\,\varrho^3\,c_{53}c_{65}}$$
$$+\frac{1}{20\,\varrho^5\,c_{53}c_{64}c_{66}c_{69}}\left\{-\omega^2\left(2c_{31}\,\varrho^5+c_{68}\,\varrho^2+15c_{29}\right)b^{13}\right.$$
$$-2\omega^2\left(2c_{31}\,\varrho^5+c_{68}\,\varrho^2+15c_{29}\right)b^{12}$$
$$-2\omega^2\left(c_{10}\,\varrho^7+3c_{31}\,\varrho^5+c_{68}\,\varrho^2+15c_{29}\right)b^{11}$$
$$-\omega^2\left(4c_{10}\,\varrho^7+6c_{40}\,\varrho^5+c_{13}\,\varrho^2+15c_{29}\right)b^{10}$$
$$+6\,\varrho^2\,\omega^2\left(-c_{10}\,\varrho^5-5c_{34}\,\varrho^3+28c_{59}\right)b^9$$
$$+\omega^2\left(4c_9\,\varrho^7-4c_{35}\,\varrho^5+15c_{29}\right)b^8$$
$$+2\omega^2\left(c_{12}\,\varrho^7-c_{31}\,\varrho^5-84c_{59}\,\varrho^2+15c_{29}\right)b^7$$
$$+\omega^2\left(12c_{43}\,\varrho^7+2c_{31}\,\varrho^5+c_{13}\,\varrho^2+30c_{29}\right)b^6$$
$$+\omega^2\left(-12c_{43}\,\varrho^7+4c_{35}\,\varrho^5+2c_{68}\,\varrho^2+15c_{29}\right)b^5$$
$$-2\,\varrho^2\,\omega^2\left(c_{12}\,\varrho^5-15c_{34}\,\varrho^3-c_{68}\right)b^4$$
$$+\varrho^2\,\omega^2\left(-4c_9\,\varrho^5+6c_{40}\,\varrho^3+c_{68}\right)b^3$$
$$-6\,\varrho^5\,\omega^2c_{62}\left(c_{30}\,\varrho^2+c_{63}\right)b^2$$
$$-4\,\varrho^5\,\omega^2c_{62}\left(c_{30}\,\varrho^2+c_{63}\right)b$$
$$-2\,\varrho^5\,\omega^2c_{62}\left(c_{30}\,\varrho^2+c_{63}\right)+$$
$$5\omega^2\cos(2\beta)\left[\left(-2c_{16}\,\varrho^5-5c_{42}\,\varrho^2-21c_{29}\right)b^{10}\right.$$
$$+2\left(-2c_{16}\,\varrho^5-5c_{42}\,\varrho^2-21c_{29}\right)b^9$$
$$-2\left(-c_{16}\,\varrho^7+c_{15}\,\varrho^5+5c_{42}\,\varrho^2+21c_{29}\right)b^8$$
$$-2\left(-2c_{16}\,\varrho^7+c_{14}\,\varrho^5+5c_{42}\,\varrho^2+21c_{29}\right)b^7$$
$$-2\left(-3c_{16}\,\varrho^7+5c_{16}\,\varrho^5+5c_{42}\,\varrho^2+21c_{29}\right)b^6$$
$$-\left(6c_{18}\,\varrho^7+10c_{16}\,\varrho^5+10c_{42}\,\varrho^2+21c_{29}\right)b^5$$
$$-10\,\varrho^2\left(c_{17}\,\varrho^5+c_{16}\,\varrho^3+c_{42}\right)b^4$$
$$+\left(-6c_{18}\,\varrho^7-8c_{16}\,\varrho^5-5c_{42}\,\varrho^2\right)b^3$$
$$+6\,\varrho^5\left(\varrho^2-1\right)c_{16}b^2$$
$$+4\,\varrho^5\left(\varrho^2-1\right)c_{16}b$$
$$\left.+2\,\varrho^5\left(\varrho^2-1\right)c_{16}\right]c_{65}\Big\} \tag{G.8}$$

$$
\begin{aligned}
\sigma_{\phi\phi} = & \frac{-10b^6\left(\nu+\varrho^2\right)+3b^5c_{60}\left(2\,\varrho^3+1\right)+b^3\left(c_{59}-2\,\varrho^2\left(3\nu\,\varrho^3+\varrho^3+10\nu\,\varrho-5\right)\right)+2\,\varrho^3\left(c_{60}\,\varrho^2+c_{59}\right)}{20c_{53}c_{65}\,\varrho^3} \\
& + \frac{1}{20c_{53}c_{64}c_{66}c_{69}\,\varrho^5}\left\{b^{13}\omega^2\left(4c_{24}\,\varrho^5+c_{19}\,\varrho^2-45c_{29}\right)\right. \\
& + 2b^{12}\omega^2\left(4c_{24}\,\varrho^5+c_{19}\,\varrho^2-45c_{29}\right) \\
& - 2b^{11}\omega^2\left(-c_{22}\,\varrho^7-6c_{24}\,\varrho^5-c_{19}\,\varrho^2+45c_{29}\right) \\
& - b^{10}\omega^2\left(-4c_{22}\,\varrho^7-12c_{21}\,\varrho^5+c_{20}\,\varrho^2+45c_{29}\right) \\
& + 6b^9\,\varrho^2\,\omega^2\left(c_{22}\,\varrho^5+10c_{45}\nu\,\varrho^3+28c_{59}\right) \\
& + b^8\omega^2\left(4c_{27}\,\varrho^7+8c_{23}\,\varrho^5+45c_{29}\right) \\
& + 2b^7\omega^2\left(c_{28}\,\varrho^7+2c_{24}\,\varrho^5-84c_{59}\,\varrho^2+45c_{29}\right) \\
& + b^6\omega^2\left(24c_{46}\,\varrho^7-4c_{24}\,\varrho^5+c_{20}\,\varrho^2+90c_{29}\right) \\
& + b^5\omega^2\left(-24c_{46}\,\varrho^7-8c_{23}\,\varrho^5-2c_{19}\,\varrho^2+45c_{29}\right) \\
& - 2b^4\,\varrho^2\,\omega^2\left(c_{28}\,\varrho^5+30c_{45}\nu\,\varrho^3+c_{19}\right) \\
& - b^3\,\varrho^2\,\omega^2\left(4c_{27}\,\varrho^5+12c_{21}\,\varrho^3+c_{19}\right) \\
& - 6b^2c_{62}\,\varrho^5\,\omega^2\left(c_{47}\,\varrho^2+c_{44}\right) \\
& - 5c_{65}\omega^2\cos(2\beta)\left[15b^{10}c_{29}\left(c_{54}\,\varrho^2+1\right)\right. \\
& \quad + 30b^9c_{29}\left(c_{54}\,\varrho^2+1\right) \\
& \quad + 2b^8\left(c_{67}\,\varrho^7+15c_{42}\,\varrho^2+15c_{29}\right) \\
& \quad + 2b^7\left(2c_{67}\,\varrho^7+15c_{42}\,\varrho^2+15c_{29}\right) \\
& \quad + 6b^6\left(c_{67}\,\varrho^7+5c_{42}\,\varrho^2+5c_{29}\right) \\
& \quad + 3b^5\left(2c_{26}\,\varrho^7+10c_{42}\,\varrho^2+5c_{29}\right) \\
& \quad + 30b^4\,\varrho^2\left(c_{25}\,\varrho^5+c_{42}\right) \\
& \quad + 3b^3\left(2c_{26}\,\varrho^7+5c_{42}\,\varrho^2\right) \\
& \quad + 6b^2c_{67}\,\varrho^7 \\
& \quad + 4bc_{67}\,\varrho^7 \\
& \quad \left.+2c_{67}\,\varrho^7\right] \\
& \left.-4bc_{62}\,\varrho^5\,\omega^2\left(c_{47}\,\varrho^2+c_{44}\right)-2c_{62}\,\varrho^5\,\omega^2\left(c_{47}\,\varrho^2+c_{44}\right)\right\}
\end{aligned}
\tag{G.9}
$$

$$
\begin{aligned}
\sigma_{\Theta\varrho} = -\frac{1}{c_{69}\,\varrho^5}\Big\{\omega^2\sin(\beta)\cos(\beta)\Big[b^{10}\left(-c_{48}\,\varrho^5+5c_{50}\,\varrho^2-12(2\nu+3)\right)\\
+b^9\left(-2c_{48}\,\varrho^5+10c_{50}\,\varrho^2-24(2\nu+3)\right)\\
+b^8\left(c_{48}\,\varrho^7-3c_{48}\,\varrho^5+10c_{50}\,\varrho^2-24(2\nu+3)\right)\\
+2b^7\left(c_{48}\,\varrho^7-2c_{48}\,\varrho^5+5c_{50}\,\varrho^2-12(2\nu+3)\right)\\
+b^6\left(3c_{48}\,\varrho^7-5c_{48}\,\varrho^5+10c_{50}\,\varrho^2-24(2\nu+3)\right)\\
+b^5\left(3c_{52}\,\varrho^7-5c_{48}\,\varrho^5+10c_{50}\,\varrho^2-12(2\nu+3)\right)\\
+5b^4\,\varrho^2\left(3c_{51}\,\varrho^5-c_{48}\,\varrho^3+c_{49}\right)\\
+b^3\left(3c_{52}\,\varrho^7-4c_{48}\,\varrho^5+5c_{50}\,\varrho^2\right)\\
+3b^2c_{48}\,\varrho^5\left(\varrho^2-1\right)\\
+2bc_{48}\,\varrho^5\left(\varrho^2-1\right)\\
+c_{48}\,\varrho^5\left(\varrho^2-1\right)\Big]\Big\}
\end{aligned}
\tag{G.10}
$$

with:

$$
\begin{aligned}
c_1 &= \nu^3+9\nu^2+\nu-12\\
c_2 &= 10\nu^3-3\nu^2-19\nu+12\\
c_3 &= 10\nu^3+9\nu^2-13\nu-6\\
c_4 &= 30\nu^3+9\nu^2-48\nu+9\\
c_5 &= 10\nu^3+27\nu^2-4\nu-33\\
c_6 &= 10\nu^3+63\nu^2+14\nu-87\\
c_7 &= 40\nu^3+72\nu^2-34\nu-78\\
c_8 &= 2\nu^3+3\nu^2-2\nu-3\\
c_9 &= 50\nu^3+175\nu^2-127\nu+6\\
c_{10} &= -50\nu^3-25\nu^2+118\nu+21\\
c_{11} &= -150\nu^3-50\nu^2+259\nu\\
c_{12} &= 50\nu^3+625\nu^2-154\nu+87\\
c_{13} &= 150\nu^3+50\nu^2-343\nu+279\\
c_{14} &= -40\nu^3+36\nu^2+88\nu-84\\
c_{15} &= -30\nu^3+27\nu^2+66\nu-63\\
c_{16} &= -10\nu^3+9\nu^2+22\nu-21\\
c_{17} &= 6\nu^3-39\nu^2-30\nu+63\\
c_{18} &= 10\nu^3-37\nu^2-36\nu+63\\
c_{19} &= 50\nu^3-50\nu^2-91\nu+123\\
c_{20} &= -50\nu^3+50\nu^2+7\nu+129\\
c_{21} &= 25\nu^3-40\nu^2-39\nu+42\\
c_{22} &= 25\nu^3+35\nu^2-33\nu-91\\
c_{23} &= 25\nu^3-40\nu^2-32\nu+21\\
c_{24} &= 25\nu^3-40\nu^2-53\nu+84\\
c_{25} &= \nu^3-19\nu^2+7\nu+11\\
c_{26} &= 5\nu^3-51\nu^2+15\nu+31\\
c_{27} &= 25\nu^3+65\nu^2+213\nu-199\\
c_{28} &= 25\nu^3+155\nu^2+951\nu-523\\
c_{29} &= 2\nu^2+\nu-3\\
c_{30} &= 10\nu^2+19\nu+3\\
c_{31} &= 35\nu^2-4\nu-63\\
c_{32} &= -50\nu^2-68\nu+54\\
c_{33} &= -25\nu^2-34\nu+27\\
c_{34} &= 7\nu^2-12\nu+21\\
c_{35} &= 35\nu^2-46\nu+63\\
c_{36} &= 10\nu^2-9\nu+27\\
c_{37} &= 25\nu^2+118\nu-279\\
c_{38} &= -65\nu^2+31\nu-18\\
c_{39} &= -70\nu^2+8\nu+126\\
c_{40} &= 35\nu^2-32\nu+21
\end{aligned}
$$

$$c_{41} = 155\nu^2 - 112\nu + 261$$
$$c_{42} = 4\nu^3 - 7\nu + 3$$
$$c_{43} = 50\nu^2 - 3\nu + 9$$
$$c_{44} = 10\nu^2 - 2\nu - 24$$
$$c_{45} = 5\nu^2 - 8\nu - 5$$
$$c_{46} = 5\nu^2 + 41\nu - 18$$
$$c_{47} = 5\nu^2 + 14\nu + 13$$
$$c_{48} = 10\nu^2 + \nu - 21$$
$$c_{49} = 4\nu^2 + 10\nu + 6$$
$$c_{51} = 2\nu^2 + 5\nu + 3$$
$$c_{52} = 2\nu^2 - 3\nu - 9$$
$$c_{53} = 10\nu^2 - 7\nu - 33$$
$$c_{54} = (\nu - 1)$$
$$c_{55} = (2\nu - 1)$$
$$c_{56} = 5\nu^2 + 7$$
$$c_{57} = 25\nu^2 - 49$$
$$c_{58} = 25\nu^2 - 7$$
$$c_{59} = 50\nu$$
$$c_{60} =^2 -98$$
$$c_{61} = (\nu - 3)$$
$$c_{62} = (3\nu + 1)$$
$$c_{63} = 5\nu^3 - 7\nu^2$$
$$c_{64} = (5\nu - 7)$$
$$c_{65} = (-7\nu - 9)$$
$$c_{66} = (b - 1)$$
$$c_{67} = b^3 - 1$$
$$c_{68} = b^2 + b + 1$$
$$c_{69} = 5\nu^3 - 7\nu^2 - 5\nu + 7$$

Bibliography

[1] ABRAMOWITZ, M. AND STEGUN, I. A. *Handbook of mathematical functions: with formulas, graphs, and mathematical tables*, vol. 55. Courier Corporation (1964). ISBN 0-486-61272-4.

[2] ADACHI, M. AND KAWAMOTO, H. Electrostatic sampler for large regolith particles on asteroids. *Journal of Aerospace Engineering*, **30** (2017), 04016098. Available from: https://doi.org/10.1061%2F%28asce%29as.1943-5525.0000701, doi:10.1061/(asce)as.1943-5525.0000701.

[3] ADACHI, M., MAEZONO, H., AND KAWAMOTO, H. Sampling of regolith on asteroids using electrostatic force. *Journal of Aerospace Engineering*, **29** (2016), 04015081. Available from: https://doi.org/10.1061%2F%28asce%29as.1943-5525.0000583, doi:10.1061/(asce)as.1943-5525.0000583.

[4] AHRENS, T. J. AND HARRIS, A. W. Deflection and fragmentation of near-Earth asteroids. *Nature*, **360** (1992), 429. doi:10.1038/360429a0.

[5] AND, A. V. R. On a particle motion along the leier fixed in a precessing rigid body. *Nelineinaya Dinamika*, (2011), 295. Available from: https://doi.org/10.20537%2Fnd1102007, doi:10.20537/nd1102007.

[6] ARAVIND, P. K. The physics of the space elevator. *American Journal of Physics*, **75** (2007), 125. doi:10.1119/1.2404957.

[7] ARTSUTANOV, Y. V kosmos na elektrovoze. *Komsomolskaya Pravda*, **31** (1960), 946.

[8] BARBER, J. R. *Elasticity*. Springer (2002). doi:10.1007/0-306-48395-5.

[9] BATCHELOR, G. K. *An Introduction to Fluid Dynamics*. Cambridge University Press (2000). Available from: https://doi.org/10.1017%2Fcbo9780511800955, doi:10.1017/cbo9780511800955.

[10] BLOUNT, P. AND ROBISON, C. J. One small step: The impact of the US Commercial Space Launch Competitiveness Act of 2015 on the exploitation of resources in outer space. *NCJL & Tech.*, **18** (2016), 160.

[11] BOMBARDELLI, C. Nonexplosive approach to fragment subkilometer asteroids with a tether centrifuge. *Journal of Guidance, Control, and Dynamics*, **30** (2007), 1546. Available from: https://doi.org/10.2514%2F1.29413, doi:10.2514/1.29413.

[12] BOMBARDELLI, C. Artificial spin-up and fragmentation of sub-kilometre asteroids. *Acta Astronautica*, **65** (2009), 1162. Available from: https://doi.org/10.1016%2Fj.actaastro.2009.03.030, doi:10.1016/j.actaastro.2009.03.030.

[13] BOMBARDELLI, C., URRUTXUA, H., MERINO, M., PELÁEZ, J., AND AHEDO, E. The ion beam shepherd: A new concept for asteroid deflection. *Acta Astronautica*, **90** (2013), 98. Available from: https://doi.org/10.1016%2Fj.actaastro.2012.10.019, doi:10.1016/j.actaastro.2012.10.019.

[14] BONITZ, R. The brush wheel sampler: A sampling device for small-body touch-and-go missions. In *2012 IEEE Aerospace Conference*. IEEE (2012). Available from: https://doi.org/10.1109%2Faero.2012.6187049, doi:10.1109/aero.2012.6187049.

[15] BOTTKE JR, W. F., CELLINO, A., PAOLICCHI, P., AND BINZEL, R. P. An overview of the asteroids: the asteroids iii perspective. *Asteroids III*, **1** (2002), 3.

[16] BRACK, D. N. AND MCMAHON, J. W. Dynamical behavior of an asteroid undergoing material removal. In *2018 Space Flight Mechanics Meeting*. American Institute of Aeronautics and Astronautics (2018). doi:10.2514/6.2018-0954.

[17] BRACK, D. N. AND MCMAHON, J. W. Active mass ejection for asteroid manipulation and deflection. *Journal of Spacecraft and Rockets*, **57** (2020), 413. Available from: https://doi.org/10.2514%2F1.a34631, doi:10.2514/1.a34631.

[18] BROWNLEE, D. The Stardust mission: Analyzing samples from the edge of the Solar System. *Annual Review of Earth and Planetary Sciences*, **42** (2014), 179. Available from: https://doi.org/10.1146%2Fannurev-earth-050212-124203, doi:10.1146/annurev-earth-050212-124203.

[19] BUROV, A. A., GERMAN, A. D., AND KOSENKO, I. I. On plane oscillations of a pendulum with variable length suspended on the surface of a planet's satellite. **52**, 289. Available from: https://link.springer.com/article/10.1134/S0010952514040029, doi:10.1134/S0010952514040029.

[20] BUROV, A. A., GUERMAN, A. D., KOSENKO, I. I., AND NIKONOV, V. I. Dynamics of a pendulum anchored to a rotating asteroid. *IFAC-PapersOnLine*, **51** (2018), 867. Available from: https://doi.org/10.1016%2Fj.ifacol.2018.04.023, doi:10.1016/j.ifacol.2018.04.023.

[21] BUROV, A. A., GUERMAN, A. D., KOSENKO, I. I., AND NIKONOV, V. I. Tethered spacecraft in asteroid gravitational environment. *Acta Astronautica*, **143** (2018), 126. Available from: https://doi.org/10.1016%2Fj.actaastro.2017.11.018, doi:10.1016/j.actaastro.2017.11.018.

[22] CARLSON, B. C. Numerical computation of real or complex elliptic integrals. *Numerical Algorithms*, **10** (1995), 13. Available from: https://doi.org/10.1007%2Fbf02198293, doi:10.1007/bf02198293.

[23] CARRY, B. Density of asteroids. *Planetary and Space Science*, **73** (2012), 98. Available from: https://doi.org/10.1016%2Fj.pss.2012.03.009, doi:10.1016/j.pss.2012.03.009.

[24] CASTILLO-ROGEZ, J. C., PAVONE, M., NESNAS, I. A. D., AND HOFFMAN, J. A. Expected science return of spatially-extended in-situ exploration at small solar system bodies. In *2012 IEEE Aerospace Conference*. IEEE (2012). Available from: https://doi.org/10.1109%2Faero.2012.6187034, doi:10.1109/aero.2012.6187034.

[25] CHEN, W.-F. AND HAN, D.-J. *Plasticity for structural engineers*. J. Ross Publishing (2007).

[26] CHERSTON, J., STROHMEIER, P., AND PARADISO, J. A. Grappler: Array of bistable elements for pinching net-like infrastructure to low gravity bodies. In *AIAA Scitech 2019 Forum*. American Institute of Aeronautics and Astronautics (2019). Available from: https://doi.org/10.2514%2F6.2019-0871, doi:10.2514/6.2019-0871.

[27] CHESLEY, S. R. Direct detection of the Yarkovsky Effect by radar ranging to asteroid 6489 Golevka. *Science*, **302** (2003), 1739. Available from: https://doi.org/10.1126%2Fscience.1091452, doi:10.1126/science.1091452.

[28] CLARKE, A. C. Space elevator:" thought experiment," or key to the universe. *Advances in Earth Oriented Applied Space Technologies*, **1**, 39.

[29] CLOHESSY, W. AND WILTSHIRE, R. Terminal guidance system for satellite rendezvous. *Journal of the Aerospace Sciences*, **27** (1960), 653. doi:https://doi.org/10.2514/8.8704.

[30] COHEN, S. AND MISRA, A. K. Static deformation of space elevator tether due to climber. *Acta Astronautica*, **111**, 317. Available from: http://www.sciencedirect.com/science/article/pii/S0094576515000703, doi:10.1016/j.actaastro.2015.02.017.

[31] COVEY, S. An electromagnetic asteroid regolith excavator—preliminary results. In *Earth and Space 2016: Engineering for Extreme Environments*, pp. 523–529. American Society of Civil Engineers Reston, VA (2016).

[32] CUARTIELLES, J. P. S., COLOMBO, C., VASILE, M., AND RADICE, G. A multi-criteria assessment of deflection methods for dangerous NEOs. In *AIP Conference Proceedings*. AIP (2007). doi:10.1063/1.2710065.

[33] CUNDALL, P. A. A computer model for simulating progressive, large-scale movement in blocky rock system. In *Proceedings of the International Symposium on Rock Mechanics, 1971* (1971).

[34] CUNDALL, P. A. AND HART, R. D. Numerical modelling of discontinua. *Engineering Computations*, **9** (1992), 101. Available from: https://doi.org/10.1108%2Feb023851, doi:10.1108/eb023851.

[35] DORRINGTON, S. AND OLSEN, J. Mining requirements for asteroid ore extraction. In *68th Int. Astronautical Congress IAC-17, D4, 5, 2, Adelaide, Australia, 25–29 September* (2017).

[36] DREYER, C. B., SERCEL, J., GERTSCH, L., LAMPE, A., CANNEY, T. J., AND ABBUD-MADRID, A. Exploration and utilization of extra-terrestrial bodies. In *Earth and Space 2016*. American Society of Civil Engineers (2016). Available from: https://doi.org/10.1061%2F9780784479971.047, doi:10.1061/9780784479971.047.

[37] ĎURECH, J., ET AL. Detection of the YORP effect in asteroid (1620) Geographos. *Astronomy & Astrophysics*, **489** (2008), L25. Available from: https://doi.org/10.1051%2F0004-6361%3A200810672, doi:10.1051/0004-6361:200810672.

[38] EDWARDS, B. C. Design and deployment of a space elevator. *Acta Astronautica*, **47**, 735. Available from: http://www.sciencedirect.com/science/article/pii/S0094576500001119, doi:10.1016/S0094-5765(00)00111-9.

[39] FITZGIBBONS, T. C., GUTHRIE, M., SHI XU, E., CRESPI, V. H., DAVIDOWSKI, S. K., CODY, G. D., ALEM, N., AND BADDING, J. V. Benzene-derived carbon nanothreads. *Nature Materials*, **14** (2014), 43. Available from: https://doi.org/10.1038%2Fnmat4088, doi:10.1038/nmat4088.

[40] FRENCH, D. B. AND MAZZOLENI, A. P. Asteroid diversion using long tether and ballast. *Journal of Spacecraft and Rockets*, **46** (2009), 645. doi:10.2514/1.40828.

[41] GATES, M., MAZANEK, D., MUIRHEAD, B., STICH, S., NAASZ, B., CHODAS, P., MCDONALD, M., AND REUTER, J. NASA's Asteroid Redirect Mission concept development summary. In *2015 IEEE Aerospace Conference*. IEEE (2015). Available from: https://doi.org/10.1109%2Faero.2015.7119163, doi:10.1109/aero.2015.7119163.

[42] GIBBINGS, A. AND VASILE, M. A smart cloud approach to asteroid deflection. In *62nd International Astronautical Congress 2011* (2011).

[43] GIBBINGS, A., VASILE, M., WATSON, I., HOPKINS, J.-M., AND BURNS, D. Experimental analysis of laser ablated plumes for asteroid deflection and exploitation. *Acta Astronautica*, **90** (2013), 85. Available from: https://doi.org/10.1016%2Fj.actaastro.2012.07.008, doi:10.1016/j.actaastro.2012.07.008.

[44] GLASSMEIER, K.-H., BOEHNHARDT, H., KOSCHNY, D., KÜHRT, E., AND RICHTER, I. The Rosetta mission: Flying towards the origin of the Solar System. *Space Science Reviews*, **128** (2007), 1. Available from: https://doi.org/10.1007%2Fs11214-006-9140-8, doi:10.1007/s11214-006-9140-8.

[45] GOROVE, S. Interpreting article ii of the outer space treaty. *Fordham L. Rev.*, **37** (1968), 349.

[46] GRIEVE, R. A. Logan Medallist 4. Large-scale impact and Earth history. *Geoscience Canada*, **44** (2017), 1. Available from: https://doi.org/10.12789%2Fgeocanj.2017.44.113, doi:10.12789/geocanj.2017.44.113.

[47] GUCKENHEIMER, J. AND HOLMES, P. *Nonlinear oscillations, dynamical systems, and bifurcations of vector fields*, vol. 42. Springer Science & Business Media (2013). ISBN 978-1-4612-1140-2.

[48] GUNDLACH, B. AND BLUM, J. A new method to determine the grain size of planetary regolith. *Icarus*, **223** (2013), 479. Available from: http://www.sciencedirect.com/science/article/pii/S0019103512004939.

[49] HADJIDEMETRIOU, J. D. Analytic solutions of the two-body problem with variable mass. **5**, 34. Available from: http://www.sciencedirect.com/science/article/pii/0019103566900066, doi:10.1016/0019-1035(66)90006-6.

[50] HAMPTON, D. L., BAER, J. W., HUISJEN, M. A., VARNER, C. C., DELAMERE, A., WELLNITZ, D. D., A'HEARN, M. F., AND KLAASEN, K. P. An overview of the instrument suite for the Deep Impact mission. *Space Science Reviews*, **117** (2005), 43.

[51] HARRIS, L. R., HERPERS, R., HOFHAMMER, T., AND JENKIN, M. How much gravity is needed to establish the perceptual upright? *PLoS ONE*, **9** (2014), e106207. Available from: https://doi.org/10.1371%2Fjournal.pone.0106207, doi:10.1371/journal.pone.0106207.

[52] HELFENSTEIN, P., ET AL. Galileo photometry of asteroid 243 Ida. *Icarus*, **120** (1996), 48. Available from: https://doi.org/10.1006%2Ficar.1996.0036, doi:10.1006/icar.1996.0036.

[53] HIRABAYASHI, M. Failure modes and conditions of a cohesive, spherical body due to YORP spin-up. *Monthly Notices of the Royal Astronomical Society*, **454** (2015), 2249. Available from: https://doi.org/10.1093%2Fmnras%2Fstv2017, doi:10.1093/mnras/stv2017.

[54] HOLSAPPLE, K. A. Spin limits of solar system bodies: From the small fast-rotators to 2003 EL61. *Icarus*, **187** (2007), 500. Available from: https://doi.org/10.1016%2Fj.icarus.2006.08.012, doi:10.1016/j.icarus.2006.08.012.

[55] HOWELL, K. C. Three-dimensional, periodic, halo orbits. *Celestial Mechanics*, **32** (1984), 53. Available from: https://doi.org/10.1007%2Fbf01358403, doi:10.1007/bf01358403.

[56] HUDSON, R. AND OSTRO, S. Physical model of asteroid 1620 Geographos from radar and optical data. *Icarus*, **140** (1999), 369. Available from: https://doi.org/10.1006%2Ficar.1999.6142, doi:10.1006/icar.1999.6142.

[57] ICHIRO WATANABE, S., TSUDA, Y., YOSHIKAWA, M., TANAKA, S., SAIKI, T., AND NAKAZAWA, S. Hayabusa2 mission overview. *Space Science Reviews*, **208** (2017), 3. Available from: https://doi.org/10.1007%2Fs11214-017-0377-1, doi:10.1007/s11214-017-0377-1.

[58] IIJIMA, S. Helical microtubules of graphitic carbon. *Nature*, **354** (1991), 56. Available from: https://doi.org/10.1038%2F354056a0, doi:10.1038/354056a0.

[59] JIANG, Y., BAOYIN, H., LI, J., AND LI, H. Orbits and manifolds near the equilibrium points around a rotating asteroid. *Astrophysics and Space Science*, **349** (2013), 83. Available from: https://doi.org/10.1007%2Fs10509-013-1618-8, doi:10.1007/s10509-013-1618-8.

[60] KADISH, J., BARBER, J., AND WASHABAUGH, P. Stresses in rotating spheres grown by accretion. *International Journal of Solids and Structures*, **42** (2005), 5322. Available from: https://doi.org/10.1016%2Fj.ijsolstr.2004.11.009, doi:10.1016/j.ijsolstr.2004.11.009.

[61] KANG, J. AND ZHU, Z. H. A unified energy-based control framework for tethered spacecraft deployment. *Nonlinear Dynamics*, **95** (2018), 1117. Available from: https://doi.org/10.1007%2Fs11071-018-4619-x, doi:10.1007/s11071-018-4619-x.

[62] KANG, J., ZHU, Z. H., WANG, W., WANG, C., AND LI, A. Dynamics and de-spin control of massive target by single tethered space tug. *Chinese Journal of Aeronautics*, **32** (2019), 653. Available from: https://doi.org/10.1016%2Fj.cja.2019.01.002, doi:10.1016/j.cja.2019.01.002.

[63] KANTSIPER, B., CHENG, A., AND REED, C. The Double Asteroid Redirection test mission. In *2016 IEEE Aerospace Conference*. IEEE (2016). Available from: https://doi.org/10.1109%2Faero.2016.7500625, doi:10.1109/aero.2016.7500625.

[64] KAWAKUBO, M., MORISHITA, H., MATUNAGA, S., OKAMOTO, C., AND YANO, H. Examination of sampling mechanism for installing in the next asteroid explorer. *The Proceedings of the Space Engineering Conference*, **2009.18** (2010), 1. Available from: https://doi.org/10.1299%2Fjsmesec.2009.18.1, doi:10.1299/jsmesec.2009.18.1.

[65] KLOSS, C., GONIVA, C., HAGER, A., AMBERGER, S., AND PIRKER, S. Models, algorithms and validation for opensource DEM and CFD–DEM. *Progress in Computational Fluid Dynamics, an International Journal*, **12** (2012), 140.

[66] KNUDSEN, S. AND GOLUBOVIĆ, L. Rotating space elevators: Physics of celestial scale spinning strings. *The European Physical Journal Plus*, **129** (2014). Available from: https://doi.org/10.1140%2Fepjp%2Fi2014-14242-8, doi:10.1140/epjp/i2014-14242-8.

[67] KNUDSEN, S. AND GOLUBOVIĆ, L. Modeling the physics of sliding objects for rotating space elevators. *The European Physical Journal Plus*, **131** (2016). Available from: https://doi.org/10.1140%2Fepjp%2Fi2016-16400-4, doi:10.1140/epjp/i2016-16400-4.

[68] KULCHITSKY, A. V., JOHNSON, J. B., AND REEVES, D. M. Resistance forces during boulder extraction from an asteroid. *Acta Astronautica*, **127** (2016), 424. Avail-

able from: https://doi.org/10.1016%2Fj.actaastro.2016.06.027, doi:10.1016/j.actaastro.2016.06.027.

[69] KWON, H. J. AND LEE, C. E. Reliability analysis for probability of pipe breakage in water distribution system. *Journal of Korean Society of Water and Wastewater*, **22** (2008), 609.

[70] LAURETTA, D. S., ET AL. OSIRIS-REx: Sample return from asteroid (101955) Bennu. *Space Science Reviews*, **212** (2017), 925. Available from: https://doi.org/10.1007%2Fs11214-017-0405-1, doi:10.1007/s11214-017-0405-1.

[71] LEMKE, E. On a lunar space elevator. *Acta Astronautica*, **12** (1985), 385. Available from: https://doi.org/10.1016%2F0094-5765%2885%2990044-x, doi:10.1016/0094-5765(85)90044-x.

[72] LI, C., ET AL. The Chang'e 3 mission overview. *Space Science Reviews*, **190** (2015), 85. Available from: https://doi.org/10.1007%2Fs11214-014-0134-7, doi:10.1007/s11214-014-0134-7.

[73] LIESKE, J. Galilean satellites and the Galileo space mission. *International Astronomical Union Colloquium*, **165** (1997), 13. Available from: https://doi.org/10.1017%2Fs0252921100046327, doi:10.1017/s0252921100046327.

[74] LOGSDON, T. *Orbital mechanics: theory and applications*. John Wiley & Sons (1998).

[75] LU, E. T. AND LOVE, S. G. Gravitational tractor for towing asteroids. *Nature*, **438** (2005), 177.

[76] MACMILLAN, W. D. *The theory of the potential*. Dover (1958). ISBN 978-0486604862.

[77] MAINDL, T. I., MIKSCH, R., AND LOIBNEGGER, B. Stability of a rotating asteroid housing a space station. *Frontiers in Astronomy and Space Sciences*, **6** (2019). Available from: https://doi.org/10.3389%2Ffspas.2019.00037, doi:10.3389/fspas.2019.00037.

[78] MALLICK, S. AND RAJAGOPALAN, R. P. If space is «the province of mankind», who owns its resources? the potential of space mining and its legal implications. *Orf Occasional Paper*, (2019). Available from: https://www.orfonline.org/research/if-space-is-the-province-of-mankind-who-owns-its-resources-47561/.

[79] MASHAYEKHI, M. AND MISRA, A. Tether assisted near earth object diversion. *Acta Astronautica*, **75** (2012), 71. doi:10.1016/j.actaastro.2011.12.018.

[80] MASHAYEKHI, M. J., MISRA, A. K., AND KESHMIRI, M. Dynamics of a tether system connected to an irregularly shaped celestial body. *The Journal of the Astronautical Sciences*, **63** (2016), 206. Available from: https://link.springer.com/article/10.1007/s40295-016-0088-y, doi:10.1007/s40295-016-0088-y.

[81] MATUNAGA, S., YAMANAKA, T., FUJIWARA, K., MAENO, M., NISHIDA, J., IKEDA, T., YANO, H., MAKABE, T., AND MORI, O. Result of micro-gravity experiment using parabolic

flight for tethered recovery in tethered sampling method. *Transactions of the Japan Society for Aeronautical and Space Sciences*, **7** (2009), Pk_23. Available from: https://doi.org/10.2322%2Ftstj.7.pk_23, doi:10.2322/tstj.7.pk_23.

[82] MCINNES, C. Harvesting near Earth asteroid resources using solar sail technology. *Fourth International Symposium on Solar Sailing (ISSS 2017), Kyoto, Japan, 17-20 Jan 2017*, (2017), 7.

[83] MCINNES, C. R. Deflection of near-Earth asteroids by kinetic energy impacts from retrograde orbits. *Planetary and Space Science*, **52** (2004), 587.

[84] MCINNES, C. R. Dynamics of a particle moving along an orbital tower. *Journal of Guidance, Control, and Dynamics*, **28** (2005), 380. doi:10.2514/1.13505.

[85] MCINNES, C. R. AND DAVIS, C. Novel payload dynamics on space elevator systems. *56th International Astronautical Congress, IAC-05-D4.2-07*, (2005). doi:10.2514/6.iac-05-d4.2.07.

[86] MCINNES, C. R. AND DAVIS, C. The orbital siphon: A new space elevator concept. *JBIS, Journal of the British Interplanetary Society*, **59** (2006), 368.

[87] MCMAHON, J., MITCHELL, S. K., OGURI, K., KELLARIS, N., KUETTEL, D., KEPLINGER, C., AND BERCOVICI, B. Area-of-effect softbots (AoES) for asteroid proximity operations. In *2019 IEEE Aerospace Conference* (2019). doi:10.1109/aero.2019.8741680.

[88] MICHEL, P., ET AL. European component of the AIDA mission to a binary asteroid: Characterization and interpretation of the impact of the DART mission. *Advances in Space Research*, **62** (2018), 2261. Available from: https://doi.org/10.1016%2Fj.asr.2017.12.020, doi:10.1016/j.asr.2017.12.020.

[89] MORISHITA, H., MORII, S., MATSUNAGA, S., YANO, H., AND OKAMOTO, C. Study and evaluation experiments of adhesive based sampling system for the next minorbody exploration. In *Space Engineering Conf*, vol. 19 (2010).

[90] MOTTOLA, S., ET AL. Physical model of near-earth asteroid 6489 Golevka (1991 JX) from optical and infrared observations. *The Astronomical Journal*, **114** (1997), 1234. doi:10.1086/118557.

[91] NALLAPU, R. T., THOESEN, A., GARVIE, L., ASPHAUG, E., AND THANGAVELAUTHAM, J. Optimized bucket wheel design for asteroid excavation. *arXiv preprint arXiv:1701.07547*, (2017).

[92] NEWTON, I. *Philosophiae naturalis principia mathematica*, vol. 1. G. Brookman (1687).

[93] NOLAN, M. C., ET AL. Shape model and surface properties of the OSIRIS-REx target asteroid (101955) Bennu from radar and lightcurve observations. *Icarus*, **226** (2013), 629. doi:10.1016/j.icarus.2013.05.028.

[94] NOMURA, S., TOMOOKA, M., AND FUNASE, R. Initial design and analysis of a system extracting and collecting water from temporarily captured orbiters. In *10th Symposium on Space Resource Utilization*. American Institute of Aeronautics and Astronautics (2017). Available from: https://doi.org/10.2514%2F6.2017-0651, doi:10.2514/6.2017-0651.

[95] NOZETTE, S. AND SHOEMAKER, E. M. Back to the Moon, on to an asteroid - The Clementine mission. *Planetary Report*, **13** (1993), 11.

[96] OLDS, J., CHARANIA, A., AND SCHAFFER, M. G. Multiple mass drivers as an option for asteroid deflection missions. In *2007 Planetary Defense Conference, Washington, DC, Paper*, pp. S3–7 (2007).

[97] O'NEILL, G. K. AND O'LEARY, B. *Space-Based Manufacturing from Nonterrestrial Materials*. American Institute of Aeronautics and Astronautics (1977). doi:10.2514/4.865312.

[98] OSTRO, S. J. Radar observations of asteroid 216 Kleopatra. *Science*, **288** (2000), 836. Available from: https://doi.org/10.1126%2Fscience.288.5467.836, doi:10.1126/science.288.5467.836.

[99] OSTRO, S. J., ET AL. Radar observations of asteroid 1620 Geographos. *Icarus*, **121** (1996), 46. Available from: https://doi.org/10.1006%2Ficar.1996.0071, doi:10.1006/icar.1996.0071.

[100] PARK, S.-Y. AND MAZANEK, D. D. Deflection of earth-crossing asteroids/comets using rendezvous spacecraft and laser ablation. *The Journal of the Astronautical Sciences*, **53** (2005), 21. Available from: https://doi.org/10.1007%2Fbf03546392, doi:10.1007/bf03546392.

[101] PEARSON, J. Konstantin Tsiolkovski and the origin of the space elevator. In *48th IAF, International Astronautical Congress, Turin, Italy*, vol. 10, pp. 6–10.

[102] PEARSON, J. The orbital tower: A spacecraft launcher using the earth's rotational energy. *Acta Astronautica*, **2** (1975), 785. Available from: https://doi.org/10.1016%2F0094-5765%2875%2990021-1, doi:10.1016/0094-5765(75)90021-1.

[103] PERRIN, C. L. Numerical recipes in Fortran 90: the art of scientific computing. *Journal of the American Chemical Society*, **119** (1997), 8748. Available from: https://doi.org/10.1021%2Fja965936f, doi:10.1021/ja965936f.

[104] PRAVEC, P. AND HARRIS, A. W. Fast and slow rotation of asteroids. *Icarus*, **148** (2000), 12. doi:10.1006/icar.2000.6482.

[105] PUGNO, N., SCHWARZBART, M., STEINDL, A., AND TROGER, H. On the stability of the track of the space elevator. *Acta Astronautica*, **64** (2009), 524.

[106] PUGNO, N. M. On the strength of the carbon nanotube-based space elevator cable: from nanomechanics to megamechanics. *Journal of Physics: Condensed Matter*, **18**, S1971. Available from: http://stacks.iop.org/0953-8984/18/i=33/a=S14, doi:10.1088/0953-8984/18/33/S14.

[107] RAMÍREZ-ARAGÓN, C., ORDIERES-MERÉ, J., ALBA-ELÍAS, F., AND GONZÁLEZ-MARCOS, A. Comparison of cohesive models in EDEM and LIGGGHTS for simulating powder compaction. *Materials*, **11** (2018), 2341. Available from: https://doi.org/10.3390%2Fma11112341, doi:10.3390/ma11112341.

[108] RAYMAN, M. D., VARGHESE, P., LEHMAN, D. H., AND LIVESAY, L. L. Results from the Deep Space 1 technology validation mission. *Acta Astronautica*, **47** (2000), 475.

[109] RICHARDSON, J. E., MELOSH, H. J., LISSE, C. M., AND CARCICH, B. A ballistics analysis of the Deep Impact ejecta plume: Determining comet Tempel 1's gravity, mass, and density. *Icarus*, **191** (2007), 176.

[110] ROSS, S. D. Near-Earth asteroid mining. *Caltech Internal Report*, (2001). Available from: http://www.dept.aoe.vt.edu/~sdross/papers/.

[111] RUSSELL, C. T. AND RAYMOND, C. A. The dawn mission to vesta and ceres. In *The Dawn Mission to Minor Planets 4 Vesta and 1 Ceres*, pp. 3–23. Springer New York (2011). Available from: https://doi.org/10.1007%2F978-1-4614-4903-4_2, doi:10.1007/978-1-4614-4903-4_2.

[112] SAGAN, C. AND OSTRO, S. J. Dangers of asteroid deflection. *Nature*, **368** (1994), 501. doi:10.1038/368501a0.

[113] SANCHEZ, J. AND MCINNES, C. Assessment on the feasibility of future shepherding of asteroid resources. *Acta Astronautica*, **73** (2012), 49. doi:10.1016/j.actaastro.2011.12.010.

[114] SANCHEZ, J. P. AND COLOMBO, C. Impact hazard protection efficiency by a small kinetic impactor. *Journal of Spacecraft and Rockets*, **50** (2013), 380. doi:10.2514/1.a32304.

[115] SÁNCHEZ, P. AND SCHEERES, D. J. The strength of regolith and rubble pile asteroids. *Meteoritics & Planetary Science*, **49** (2014), 788. Available from: https://doi.org/10.1111%2Fmaps.12293, doi:10.1111/maps.12293.

[116] SAYLOR, J., ZOLENSKY, M., BODNAR, R., LE, L., AND SCHWANDT, C. Fluid inclusions in carbonaceous chondrites. *Lunar and Planetary Science XXXII*, **1** (2001).

[117] SCHEERES, D., HARTZELL, C., SÁNCHEZ, P., AND SWIFT, M. Scaling forces to asteroid surfaces: The role of cohesion. *Icarus*, **210** (2010), 968. doi:10.1016/j.icarus.2010.07.009.

[118] SCHEERES, D. AND SCHWEICKART, R. The mechanics of moving asteroids. 2004 Planetary Defense Conference: Protecting Earth from Asteroids (2004). ISBN 978-1-62410-162-5. doi:10.2514/6.2004-1446.

[119] SCHEERES, D., ET AL. The geophysical environment of Bennu. *Icarus*, **276** (2016), 116. Available from: https://doi.org/10.1016%2Fj.icarus.2016.04.013, doi:10.1016/j.icarus.2016.04.013.

[120] SCHEERES, D. J. Dynamics about uniformly rotating triaxial ellipsoids: Applications to asteroids. *Icarus*, **110** (1994), 225. doi:10.1006/icar.1994.1118.

[121] SCHEERES, D. J. *Orbital Motion in Strongly Perturbed Environments*. Springer Berlin Heidelberg (2012). doi:10.1007/978-3-642-03256-1.

[122] SCHEERES, D. J., ET AL. The dynamic geophysical environment of (101955) Bennu based on OSIRIS-REx measurements. *Nature Astronomy*, **3** (2019), 352. Available from: https://doi.org/10.1038%2Fs41550-019-0721-3, doi:10.1038/s41550-019-0721-3.

[123] SERCEL, J. Apis: Asteroid provided in-situ supplies. *NIAC Phase I Report*, (2016). Available from: https://www.nasa.gov/sites/default/files/atoms/files/niac_sercel_phase_i_final_report_tagged.pdf.

[124] SERCEL, J. C., DREYER, C. B., ABBUD-MADRID, A., BRITT, D., JEDICKE, R., GERTSCH, L., AND LOVE, S. G. A coordinated research program to develop the technology to optical mine asteroids. In *Earth and Space 2016: Engineering for Extreme Environments*, pp. 507–522. American Society of Civil Engineers Reston, VA (2016).

[125] SHEPARD, M. K., ET AL. A revised shape model of asteroid (216) Kleopatra. *Icarus*, **311** (2018), 197. Available from: https://doi.org/10.1016%2Fj.icarus.2018.04.002, doi:10.1016/j.icarus.2018.04.002.

[126] SONTER, M. The technical and economic feasibility of mining the near-Earth asteroids. *Acta Astronautica*, **41** (1997), 637. Available from: https://doi.org/10.1016%2Fs0094-5765%2898%2900087-3, doi:10.1016/s0094-5765(98)00087-3.

[127] SPITALE, J. N. Asteroid hazard mitigation using the Yarkovsky effect. *Science*, **296** (2002), 77. doi:10.1126/science.1069577.

[128] STACHEL, H. AND WALLNER, J. Ivory's theorem in hyperbolic spaces. *Siberian Mathematical Journal*, **45** (2004), 785. Available from: https://doi.org/10.1023%2Fb%3Asimj.0000035839.90234.45, doi:10.1023/b:simj.0000035839.90234.45.

[129] STERN, A. AND SPENCER, J. New horizons: The first reconnaissance mission to bodies in the Kuiper belt. In *The First Decadal Review of the Edgeworth-Kuiper Belt*, pp. 477–482. Springer (2004).

[130] STEWART, M. Material requirements: piping materials. In *Surface Production Operations*, pp. 159–192. Elsevier (2016). Available from: https://doi.org/10.1016%2Fb978-1-85617-808-2.00003-1, doi:10.1016/b978-1-85617-808-2.00003-1.

[131] SZYSZKOWSKI, W. AND STILLING, D. On damping properties of a frictionless physical pendulum with a moving mass. *International Journal of Non-Linear Mechanics*, **40** (2005), 669. Available from: https://doi.org/10.1016%2Fj.ijnonlinmec.2004.09.001, doi:10.1016/j.ijnonlinmec.2004.09.001.

[132] TARDIVEL, S. *The deployment of scientific packages to asteroid surfaces*. Ph.D. thesis, Université Nice Sophia Antipolis (2014).

[133] THOMAS, P. Sizes, shapes, and derived properties of the saturnian satellites after the Cassini nominal mission. *Icarus*, **208** (2010), 395. Available from: https://doi.org/10.1016%2Fj.icarus.2010.01.025, doi:10.1016/j.icarus.2010.01.025.

[134] TRICARICO, P. The near-Earth asteroid population from two decades of observations. *Icarus*, **284** (2017), 416. Available from: https://doi.org/10.1016%2Fj.icarus.2016.12.008, doi:10.1016/j.icarus.2016.12.008.

[135] TSIOLKOVSKY, K. *Dreams of Earth and Sky*. The Minerva Group, Inc. ISBN 1-4147-0163-2.

[136] VALLADO, D. A. *Fundamentals of astrodynamics and applications*, vol. 12. Springer Science & Business Media. ISBN 0-7923-6903-3.

[137] VASILE, M. AND COLOMBO, C. Optimal impact strategies for asteroid deflection. *Journal of Guidance, Control, and Dynamics*, **31** (2008), 858. Available from: https://doi.org/10.2514%2F1.33432, doi:10.2514/1.33432.

[138] VASILE, M., GIBBINGS, A., WATSON, I., AND HOPKINS, J.-M. Improved laser ablation model for asteroid deflection. *Acta Astronautica*, **103** (2014), 382. Available from: https://doi.org/10.1016%2Fj.actaastro.2014.01.033, doi:10.1016/j.actaastro.2014.01.033.

[139] VASILE, M. AND MADDOCK, C. A. On the deflection of asteroids with mirrors. *Celestial Mechanics and Dynamical Astronomy*, **107** (2010), 265. Available from: https://doi.org/10.1007%2Fs10569-010-9277-3, doi:10.1007/s10569-010-9277-3.

[140] VASILE, M. AND MADDOCK, C. A. Design of a formation of solar pumped lasers for asteroid deflection. *Advances in Space Research*, **50** (2012), 891. Available from: https://doi.org/10.1016%2Fj.asr.2012.06.001, doi:10.1016/j.asr.2012.06.001.

[141] VASILE, M., ET AL. Light-touch2: a laser-based solution for the deflection, manipulation and exploitation of small asteroids. In *IAA Planetary Defense Conference*, pp. Paper–IAA (2013).

[142] VASILKOVA, O. Three-dimensional periodic motion in the vicinity of the equilibrium points of an asteroid. **430**, 713. doi:10.1051/0004-6361:20034414.

[143] VERGAAIJ, M., MCINNES, C. R., AND CERIOTTI, M. Economic assessment of high-thrust and solar-sail propulsion for near-earth asteroid mining. *Advances in Space Research*, (2020). Available from: https://doi.org/10.1016%2Fj.asr.2020.06.012, doi:10.1016/j.asr.2020.06.012.

[144] VETRISANO, M., COLOMBO, C., AND VASILE, M. Asteroid rotation and orbit control via laser ablation. *Advances in Space Research*, **57** (2016), 1762. Available from: https://doi.org/10.1016%2Fj.asr.2015.06.035, doi:10.1016/j.asr.2015.06.035.

[145] VEVERKA, J., ET AL. The landing of the NEAR-Shoemaker spacecraft on asteroid 433 Eros. *Nature*, **413** (2001), 390. Available from: https://doi.org/10.1038%2F35096507, doi:10.1038/35096507.

[146] VIALE, A., CERIOTTI, M., AND MCINNES, C. Dynamics of an orbital siphon anchored to a rotating ellipsoidal asteroid for resource exploitation. *Acta Astronautica*, (2020). Available from: https://doi.org/10.1016%2Fj.actaastro.2020.08.001, doi:10.1016/j.actaastro.2020.08.001.

[147] VIALE, A., MCINNES, C., BAILET, G., AND CERIOTTI, M. Asteroid deflection by leveraging rotational self-energy. *Journal of Spacecraft and Rockets*, (2021). doi:https://doi.org/10.2514/1.A34889.

[148] VIALE, A., MCINNES, C., BAILET, G., AND CERIOTTI, M. Excavation of artificial caversns inside asteroids by leveragin rotational self-energy. *Advances in Space Research*, (2021). Available from: https://doi.org/10.1016/j.asr.2021.02.021.

[149] VIALE, A., MCINNES, C., AND CERIOTTI, M. Analytical mechanics of asteroid disassembly using the orbital siphon effect. *Proceedings of the Royal Society A: Mathematical, Physical and Engineering Sciences*, **474** (2018), 20180594. doi:10.1098/rspa.2018.0594.

[150] VIALE, A., MCINNES, C., AND CERIOTTI, M. Dynamics of a nonrigid orbital siphon at a near-earth asteroid. *Journal of Guidance, Control, and Dynamics*, (2020), 1. Available from: https://doi.org/10.2514%2F1.g004894, doi:10.2514/1.g004894.

[151] VIALE, A., MCINNES, C. R., AND CERIOTTI, M. Disassembly of near earth asteroids by leveraging rotational self energy. *69th International Astronautical Congress, IAC-18-D4.3-18*, (2018), 13608. Available from: http://eprints.gla.ac.uk/168724/.

[152] WALSH, K. J., RICHARDSON, D. C., AND MICHEL, P. Rotational breakup as the origin of small binary asteroids. *Nature*, **454** (2008), 188. Available from: https://doi.org/10.1038%2Fnature07078, doi:10.1038/nature07078.

[153] WANG, Z.-K., FAN, Y.-H., CUI, N.-G., AND LIU, D. Non-equatorial space elevator design approach. *Proceedings of the Institution of Mechanical Engineers, Part G: Journal of Aerospace Engineering*, **233** (2018), 3235. Available from: https://doi.org/10.1177%2F0954410018797879, doi:10.1177/0954410018797879.

[154] WEINSTEIN, L. M. Space colonization using space-elevators from Phobos. In *AIP Conference Proceedings*. AIP (2003). Available from: https://doi.org/10.1063%2F1.1541423, doi:10.1063/1.1541423.

[155] WERNER, R. AND SCHEERES, D. Exterior gravitation of a polyhedron derived and compared with harmonic and mascon gravitation representations of asteroid 4769 Castalia. *Celestial Mechanics and Dynamical Astronomy*, **65** (1997). doi:10.1007/bf00053511.

[156] WIE, B. Dynamics and control of gravity tractor spacecraft for asteroid deflection. *Journal of Guidance, Control, and Dynamics*, **31** (2008), 1413.

[157] WIE, B. Astrodynamic fundamentals for deflecting hazardous near-Earth objects. *60th International Astronautical Congress, IAC-09-C1.3.1*, **3** (2009), 12.

[158] WILLIAMS, P. Dynamic multibody modeling for tethered space elevators. *Acta Astronautica*, **65**, 399. Available from: http://www.sciencedirect.com/science/article/pii/S0094576509001209, doi:10.1016/j.actaastro.2008.11.016.

[159] WOO, P. AND MISRA, A. K. Dynamics of a partial space elevator with multiple climbers. *Acta Astronautica*, **67**, 753. Available from: http://www.sciencedirect.com/science/article/pii/S0094576510001530, doi:10.1016/j.actaastro.2010.04.023.

[160] WOO, P. AND MISRA, A. K. Mechanics of very long tethered systems. *Acta Astronautica*, **87**, 153. Available from: http://www.sciencedirect.com/science/article/pii/S0094576513000568, doi:10.1016/j.actaastro.2013.02.008.

[161] YÁRNOZ, D. G., CUARTIELLES, J. P. S., AND MCINNES, C. R. Passive sorting of asteroid material using solar radiation pressure. *Journal of Guidance, Control, and Dynamics*, **37** (2014), 1223. doi:10.2514/1.62412.

[162] YOSHIKAWA, M., FUJIWARA, A., AND KAWAGUCHI, J. Hayabusa and its adventure around the tiny asteroid Itokawa. *Proceedings of the International Astronomical Union*, **2** (2006), 323. Available from: https://doi.org/10.1017%2Fs174392130701085x, doi:10.1017/s174392130701085x.

[163] ZACNY, K., COHEN, M. M., JAMES, W. W., AND HILSCHER, B. Asteroid mining. In *AIAA SPACE 2013 Conference and Exposition*. American Institute of Aeronautics and Astronautics (2013). Available from: https://doi.org/10.2514%2F6.2013-5304, doi:10.2514/6.2013-5304.

[164] ZHANG, J., YANG, K., AND QI, R. Dynamics and offset control of tethered space-tug system. *Acta Astronautica*, **142** (2018), 232. doi:10.1016/j.actaastro.2017.10.020.

[165] ZHAO, Z., WANG, S., LI, D., WANG, H., WANG, Y., AND ZHAO, J. Development of an anchoring system for the soft asteroid landing exploration. *International Journal of Aerospace Engineering*, **2019** (2019), 1. doi:10.1155/2019/1257038.

[166] ZHONG, R. AND WANG, Y. Research on the tether assisted observation of an asteroid. *Acta Astronautica*, **123** (2016), 310. doi:10.1016/j.actaastro.2016.03.027.

[167] ZHONG, R. AND WANG, Y. Dynamics and control of a probe tethered to an asteroid. *Journal of Guidance, Control, and Dynamics*, **41** (2018), 1585. doi:10.2514/1.g003386.